Numéro d'ordre: 40951

Ecole doctorale : Sciences de la Matière, du Rayonnement et de l'Environnement

Université Lille 1 Sciences et Technologies

Thèse

présentée pour obtenir le grade de

Docteur en Physique de l'Université Lille I

Laboratoire de Physique des Lasers, Atomes et Molécules

dans la spécialité

Optique et Lasers, Physico-chimie, Atmosphère

ÉTUDE THÉORIQUE DE LA RÉACTIVITÉ DE L'HYDROGÈNE AVEC CO, H_2CO ET H_3COH À LA SURFACE DES GRAINS INTERSTELLAIRES

par

Phillip Peters

Soutenue le 29 novembre 2012 devant la commission d'examen :

H. Fraser, Senior Lecturer The Open University (Royaume Uni)	Rapporteur
M. C. Bacchus, Chargé de recherche- Université Claude-Bernard Lyon I	Rapporteur
C. Ceccarelli, Astronome - Université Joseph-Fourier Grenoble 1	Examinateur
F. Spiegelman, Directeur de recherche - Université Paul-Sabatier Toulouse III	Examinateur
L. Krim, Professeur - Université Pierre et MArie Curie Paris VI	Examinateur
D. Duflot, Maître de conférences - Université Lille I	Directeur
L. Wiesenfeld, Chargé de recherche - Université Joseph-Fourier Grenoble I	Co-directeur
C. Toubin, Maître de conférences - Université Lille I	Co-encadrant

A THEORETICAL STUDY OF THE REACTION OF HYDROGEN WITH CO, H_2CO, AND CH_3OH ON THE SURFACES OF INTERSTELLAR DUST GRAINS

a

Thesis

by

Phillip Peters

within the
Physics of Lasers, Atoms and Molecules Laboratory
and the
The science of matter, light and the atmosphere doctoral school
within the discipline of
Optics, lasers, physical chemistry, and the atmosphere
at the
University Lille 1 Science and Technology

is presented to obtain the title of

Doctor of Physics of the University Lille 1

Defended on the 29th of November 2012 before the examination committee comprised of:

H. Fraser, Senior Lecturer The Open University (UK)	Reporter
M. C. Bacchus, Researcher- University Claude-Bernard Lyon I	Reporter
C. Ceccarelli, Astronomer - University Joseph-Fourier Grenoble 1	Examiner
F. Spiegelman, Director of Research - University Paul-Sabatier Toulouse III	Examiner
L. Krim, Professor- University Pierre and Marie Curies Paris VI	Examiner
D. Duflot, Assistant Professor - University Lille I	Supervisor
L. Wiesenfeld, Researcher - University Joseph-Fourier Grenoble I	Co-supervisor
C. Toubin, Assistant Professor - University Lille I	Co-supervisor

ABSTRACT

Throughout this work high level quantum chemistry methods have been used to investigate reactive processes involving: H, D, CO, H_2CO, H_3COH and H_2O on model interstellar grain surfaces.

This study has mainly focused upon the formation of the two most abundant Complex Organic Molecules (COMS), H_2CO and H_3COH. For the first time, all of the hydrogenation steps have been considered and treated with reliable methods in the gas phase, and in particular making use of multi-reference approaches such as MRCI+Q and MRMP2.

Following the characterization of all the reactions in the gas phase, the same processes have been investigated within small molecular clusters using various density functionals and MP2. This was done as a preliminary attempt to model the icy grain mantles of interstellar dust grains. For some of the steps, such as the formation of HCO, the activation energy does not vary significantly between the gas phase and the clusters. In contrast, for other processes, such as the formation of COH, and H_3CO, the activation energy is lowered and the exothermicity/endothermicity of the reaction changes. In addition, the isomerizations of some species, for example HCOH to H_2CO, are also strongly affected by the presence of water. From the cluster calculations, we conclude that the arrangement of the surface molecules and the H flux may have a significant influence on the chemical routes leading to H_2CO and H_3COH.

Finally, we have also discussed how these results may be incorporated into astrophysical models, as our results suggest that the current route, that is considered, may not include all of the possible steps which may contribute to the actual formation of these COMs.

RÉSUMÉ

L'objectif de ce mémoire de thèse est de caractériser par des méthodes de chimie quantique de haute qualité les processus réactionnels impliquant H, CO, H_2CO, H_3COH et H_2O à la surface des grains interstellaires. En effet, H_2CO et H_3COH, sont parmi les molécules organiques dites complexes (COM: Complex Organic Molecules en anglais) les plus abondantes dans les nuages moléculaires du milieu interstellaire. Ce travail théorique est la première étude s'attachant à décrire toutes les étapes et les intermédiaires réactionnels intervenant dans la séquence de réactions conduisant au méthanol par hydrogénations successives de CO. Pour la phase gazeuse, des méthodes multi-références (MRCI+Q et MRMP2) ont été appliquées afin d'avoir la description la plus juste des systèmes. Les calculs montrent que certaines étapes cruciales de la synthèse (formation de HCO) en phase gazeuse mettent en jeu des barrières d'activation significatives dans les conditions du milieu interstellaire. La possibilité de réaction par effet tunnel a aussi été envisagée.

Les mêmes processus réactionnels ont ensuite été étudiés sur des agrégats d'eau ou de CO. Ces agrégats ont été choisis comme surfaces modèles pour les grains interstellaires. Compte-tenu de la taille du système, les calculs ont été menés en utilisant la théorie de la fonctionnelle densité et la méthode perturbative MP2. Pour certaines réactions, telle que la formation de HCO, la présence d'un agrégat ne modifie pas l'énergie d'activation. En revanche, pour d'autres (formation de COH et H_3CO), l'énergie d'activation est réduite et l'endothermicité/exothermicité de la réaction change. De plus, l'isomerisation de certains composés, HCOH en H_2CO, est rendue possible en présence d'agrégats d'eau. Les résultats obtenus sur les agrégats indiquent que l'état de surface et le flux d'atomes H peuvent avoir une influence notable sur la séquence réactionnelle, ouvrant d'autres voies non envisageables en phase gazeuse.

Enfin, les résutats de ces calculs seront intégrées dans le modèle astrophysique GRAIN-OBLE, ce qui permettra de prendre en compte les différents intermédaires qui pourraient potentiellement participer à la synthèse de ces deux molécules ainsi qu'à celle de molécules plus complexes.

CONTENTS

LIST OF FIGURES

LIST OF TABLES

ACRONYMS

ABMO	Anti-bonding Molecular Orbital
AIM	Atoms in Molecules
AO	Atomic Orbital
BMO	Bonding Molecular Orbital
BO	Born-Oppenheimer
CASSCF	Complete Active Space Self-Consistent Field theory
CASPT2	Complete Active Space with second order perturbation
CC	Coupled Cluster theory
CCD	CC including double excitations only
CCSD	CC including Single and Double excitations
CCSDT	CCSD with full treatment of Triple excitations, where the T is written as (T) the triple excitations have been included perturbativly
CI	Configuration Interaction
CID	CI including Double excitations only
CISD	CI including Single and Double excitations only
COM	Complex Organic Molecule
DFT	Density Functional Theory
FCI	Full Configuration Interaction
FORCOMS	FORmation of Complex Organic Molecules in Space
GGA	Generalised Gradient Approximation
HF	Hartree-Fock Theory
IRC	Intrinsic Reaction Coordinate
LCAO	Linear Combination of Atomic Orbitals
LDA	Local Density Approximation
LSDA	Local Spin Density Approximation
MCSCF	Multi-Configurational Self-Consistent Field theory
MEP	Minimum Energy Pathway

MO	Molecular Orbital
MP2	Møller Plesset Perturbation Theory to second order
MPPT	Møller Plesset Perturbation Theory
MRCI	Multi-Reference Configuration Interaction
MRMP2	Multi-Reference MP2
PAH	Polyaromatic Hydrocarbon
PES	Potential Energy Surface
QC	Quantum Chemistry
QM	Quantum Mechanics
RS2	Second order Rayleigh-Scrödinger Perturbation Theory
RS2C	see RS2
SCF	Self-Consistent Field theory
SD	Slater Determinant
SE	Schrödinger Equation
TID	Time Independent Dynamics
TS	Transition State
WFT	Wavefunction Theory
WKB	Wentzel-Kramer-Brillouin
VDW	Van der Waals
ZPE	Zero Point Energy

Chapter I

INTRODUCTION

1 INTRODUCTION

The formation of low mass stars, like the Sun, is accompanied by a chemical evolution from atoms to large molecules, and ultimately to the complex structures of proteins and enzymes we find here on Earth. Throughout this evolution, it is believed interstellar dust plays a crucial role. With this in mind, within this chapter we explore the various physical and chemical changes which accompany star formation and what role the dust has at each stage. We therefore begin in the next section with a discussion of star formation, which will then be followed by discussions of the chemistry at each stage, the composition of the dust, and finally how the dust influences the chemistry we observe.

1.1 FROM MOLECULAR (ATOMIC) CLOUDS TO STARS

1.1.1 *Clouds, Clumps and Cores*

It is our current understanding that low mass stars like the Sun form in cold dark clouds. These clouds range in size up to a maximum of 15 pc[1]. They show complex irregular and filamentary structures. Within these clouds, we find so called embedded clumps which have a higher particle density than the surrounding cloud and a maximum size of 3 pc. In addition, smaller cores have also been observed, which show a higher particle density than the clumps and are typically no larger than 0.2 pc. It is believed that these so called cold cores are the first stages of star formation. This is due to their coexistence with starless cores in the same region of the cloud [1]. As a result of this, they are commonly referred to as prestellar cores. These cores typically have particle densities greater than $1x10^5$ cm^{-3} and the temperature can be as low as 8 K at the centre. Table 1 shows the typical physical conditions of these objects.

Table 1: Typical physical conditions within dark clouds, embedded clumps and prestellar cores

	Clouds	Clumps	Cores
Size (pc)	$3-15$	$0.3-3$	$0.03-0.2$
Mean particle density $\left(cm^{-3}\right)$	$<5x10^2$	10^3-10^4	10^4-10^5
Temperature (K)	$10-30$	$10-20$	$8-12$

1.1.2 *From a prestellar core to a star*

In 1977, Shu [2] proposed that a core undergoes collapse to form a star when it exceeds a certain mass known as the Bonnor-Ebert mass [3, 4]. This mass is given by:

$$M_{BE} = \frac{1.18 v_T^4}{P_0^{\frac{1}{2}} G^{\frac{3}{2}}} \quad (1)$$

1 1 parsec(pc) = 3.2615 light years (ly) = $3.085678x10^{16}$ m

where v_T, the isothermal sound speed, is given by:

$$v_T = \sqrt{\frac{\gamma k_b T}{m}} \tag{2}$$

In equation 1, p_0 is the external gas pressure, and G is the gravitational constant. In equation 2, k_b and T are the Boltzmann constant and the Temperature respectively, γ is the ratio of the specific heat capacity of the gas under constant pressure, C_p, to the specific heat capacity of the gas in a constant volume, C_V, and m is the mass of the particles in the gas phase. It is believed that this criteria is normally met 10^5 years after the core has formed.

Star formation is separated into several stages based upon the time since initial collapse of the core, its size, and the type of objects which surround the forming star.

The first stage is the formation of a class 0 protostar. These objects are more commonly referred to as "hot corinos". During this phase, which occurs ~ 10000 years [5, 6] after initial collapse, the central star is formed and accretes mass from its surroundings. At this stage, the object is typically identified by its surrounding envelope, as most of the objects mass is within the envelope and not the central star. These objects are typically around 1000 AU in size[2]. At their centre, they exhibit temperatures in excess of 100 K and particle densities of greater than 10^9 [7]. At the outermost regions, the temperature drops to around 10 K and the particle density has decreased to ~ 10^5 cm^{-3}.

Overtime, the star heats its surroundings and after approximately 10000 years, since the collapse began, the star now has more mass than its surrounding envelope. It has increased its density and temperature but remains roughly the same size. At this stage, most of the envelope is gone, since it has either been accreted into the star or into the protoplanetary disk which now surrounds the star. The object is now known as a Class I protostar.

The temperature continues to rise and the envelope has all but disappeared and the disk has evolved considerably. Deuterium fusion begins within the core of the star, which is characteristic of this Class II star. Class II objects are also known as classical T-Tauri stars, after the prototypical example star.

During the final stages of formation, the disk dissipates either by accretion into the star or by the formation of planetesimals. This Class III object will now continue to evolve onto the main sequence and ultimately, when it dies it will go on to eject its outer envelope to become a white dwarf at the centre of a new diffuse cloud.

1.2 WHAT ABOUT THE CHEMISTRY?

Every stage of stellar evolution is accompanied by a stepwise increase in chemistry. This chemistry, which begins life as an atomic/diatomic gas in dark clouds, then forms what we shall call simple "Complex" Organic Molecules[3] (COMs) in hot corinos. This strange notion of a simple "Complex" molecule arises, as we shall see in tables 2 and 3, due to the definition of a COM. The accepted astrophysical definition is that an organic molecule is complex if it contains 5 or more atoms. A rigorous enforcement of this definition would class nearly 70% of the detected organic species as complex.

2 1 Astronomical Unit (AU) is the mean distance between the Earth and the Sun. It is therefore equal to 1.495979×10^{11} m, or 1.581×10^{-5} ly.

3 As per the IUPAC definition an organic species must contain carbon, but the following compounds are always considered as inorganic: cyanides, simple oxides of carbon, carbonates, carbides, and allotropes of carbon. They note however that the distinction between organic and inorganic is somewhat arbitrary.

Table 2: Table of detected organics in the interstellar and circumstellar objects with up to 6 atoms [8]. c- and n- denote the molecule is cyclic or linear respectively.

2 atoms	3 atoms	4 atoms	5 atoms	6 atoms
CH	HCP	c-C_3H	C_4H	C_5H
CH^+	CCP	n-C_3H	C_4Si	n-H_2C_4
CN	HNC	C_3N	n-C_3H_2	C_2H_4
CP	OCS	C_3O	c-C_3H_2	CH_3CN
CS	HOC^+	C_3S	H_2C_2N	CH_3NC
CF^+	HCS^+	C_2H_2	CH_4	CHOH
	HCO^+	HCCN	HC_3N	CH_3SH
	HCO	$HCNH^+$	HC_2NC	HC_3NH^+
	CH_2	HNCO	HCOOH	HC_3HO
	C_2S	HNCS	H_2CNH	NH_2CHO
	C_2O	CH_3	H_2C_2O	C_5N
	C_2H	C_3N^-	H_2N_2C	c-H2C3O
	HCN	HNCO	HNC_3	H_2C_2NH
		HOCN	H_2COH^+	C_5N^-
		HSCN	C_4H^-	
		H_2CO	HC(O)CN	

Table 3: Table of detected organics in the interstellar and circumstellar objects with 7 or more atoms [8]. c- and n- denote the molecule is cyclic or linear respectively.

7 atoms	8 atoms	9 atoms	10 atoms	11 atoms or greater
C_6H	CH_3C_3N	CH_3C_4H	CH_3C_5N	HC_9N
CH_2CHCN	$HC(O)OCH_3$	CH_3CH_2CN	$(CH_3)_2CO$	CH_3C_6H
CH_3C_2H	CH_3COOH	$(CH_3)_2O$	$(CH_2OH)_2$	C_2H_5OCHO
HC_5N	C_7H	CH_3CH_2OH	CH_3CH_2CHO	c-C_6H_6
CH_3CHO	H_2C_6	HC_7N		$C_2H_5OCH_3$
CH_3NH_2	CH_2OHCHO	C_8H		n-C_3H_7CN
c-C_2H_4O	n-HC_6H	$CH_3C(O)NH_2$		n-C_3H_7CN
H_2CCHOH	CH_2CHCHO	C_8H^-		$HC_{11}N$
C_6H^-	CH_2C_2HCN	C_3H_6		
	H_2NCH_2CN			

As tables 2 and 3 illustrate, the chemistry is very diverse, in terms of the molecular functionality. Though it should be noted that we know very little about how many of these species are formed.

Our current understanding is that within dark clouds, the atomic gas becomes slowly molecular due to the low UV flux [9]. The formation of molecules such as CO is then brought

about by cosmic ray induced ion neutral reactions [10]. At the same time, ices, composed mainly of water, begin to form on dust grains. As the clouds density begins to increase and the temperature drops, CO then begins to freeze out onto the grains as well. It is at this point that molecules such as H_2CO and CH_3OH are believed to start forming.

From here, as the collapse to form a protostar begins, the temperature starts to increase and lighter molecules start to desorb from the grains. At the same time, the heavier species become more mobile on the grain surfaces and are believed to form larger molecules such as methylformate. This gradual heating eventually causes all of the ice to desorb at ~ 100 K [11], which leads to the diverse chemistry which is then observed in the gas phase [11, 12].

During star formation, material is progressively brought towards the centre; these molecules must then do the same. At this point, they can refreeze onto the grains in the midplane of the disc, be photodissociated by the increased photon flux from the star, or perhaps undergo gas phase reactions to form second generation molecules [13, 14].

As the circumstellar disc collapses to form a solar system, comets and meteorites form. Observations of comets have shown the same chemistry as observed in hot corinos [15], which suggests that at least some of the chemistry is preserved throughout the entire process. However, composition and abundance differ from comet to comet suggesting they undergo different processing within their lifetimes. [16].

1.3 DUST AND ICE: THE CHEMICAL INDUSTRY OF THE INTERSTELLAR MEDIUM

In the previous section, we highlighted the fact that it is currently accepted that several important species are formed on dust grains encased within ices [17]. So we are left asking what are these dust grains composed of and what is the chemical composition of these ices? In the following sections, we explore these two questions.

1.3.1 *Dust composition*

In general, the dust is considered to be of one of two broad types, namely: silicates and carbonaceous [18, 19]. The silicate grains are typically amorphous in nature. Generally, these silicates incorporate small fractions of iron and magnesium, as is common for the crystalline silicates like olivine. The carbonaceous grains are considered to be made of any material which is carbon rich. As such this includes: diamond, graphite, amorphous carbon, hydrogenated amorphous carbon, Polyaromatic Hydrocarbons (PAHs), and long chain hydrocarbons. As we see, whilst there are two broad categories which cover the composition of the grains, it is difficult to know the nature of these grains precisely.

1.3.2 *So what of these ices then?*

Numerous studies have been conducted to determine the composition of the ices [20–23]. They have revealed that interstellar ices are mainly water, but also contain other species. These include CO, CO_2, and methanol in significant quantities. In addition, infrared adsorption bands have indicated the presence of other species such as CH_4, NH_3, and XCN [21]. The XCN feature is currently assigned to OCN^-, but it is not an unambiguous assignment [21, 23]. Table 4 shows some of the ice components deduced from observations [23–27] and their

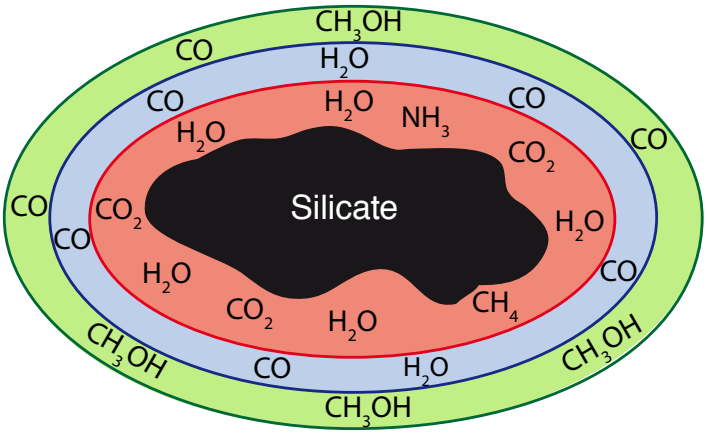

Figure 1: Cartoon representation of a typical interstellar ice deduced from infrared observational studies. The red component represents the water rich mixture, the blue component the CO rich ice and the green ice represents the ice thought to be mostly composed of CO and CH_3OH.

relative abundance to H_2O and figure 1 provides a schematic illustration of our current idea of how the ices are segregated upon the grains.

Table 4: Median abundances as a percentage relative to water for various components of interstellar ice analogues [23] for low mass and high mass stars, as well as prestellar cores.

Component	Abundance relative to H_2O		
	Low mass	High mass	Prestellar Core
CO_2	29	13	38
CO	21	13	31
CH_3OH	7	8	8
NH_3	5	16	-
CH_4	5	16	-

Whilst we have been able to deduce the most abundant components of the ices from the observations, the structure of the ice remains an open question, though it is generally agreed that the ice is amorphous. Moreover, it should be noted that the observations support mixing of these components in various ratios. This gives rise to regions dominated by mixtures of H_2O and CO_2, the other regions consisting of CO_2 and CO. This is further complicated by the fact that the microscopic structure is dependent upon the physical conditions, on a local scale when the ice is forming. The quantities needed to describe such processes are difficult to determine from observations.

We shall however attempt to offer a qualitative structure for the ice based upon what we know. The first question, that arises is where does the water come from? It has been suggested that the water is formed on the grain surface by the hydrogenation of O, O_2, and O_3 [28]. This mechanism has recently been proven, experimentally, to be efficient at low temperatures [29–31]. Similar reactions in which carbon and nitrogen atoms are hydrogenated are thought to produce the ammonia and methane ices [32].

Following the formation of the water ice, it is generally accepted that CO then freezes out. Once this occurs, the chemistry necessary to build some of the simpler COMs can begin. In addition, the formation of CO_2 also requires CO to be frozen on the grains [33].

1.4 HOW DO WE CONSIDER THIS HETEROGENEOUS SURFACE CHEMISTRY? FROM ASTROPHYSICS TO CHEMISTRY

1.4.1 *Experiments*

As seen in the previous section, methanol is one of the most abundant molecules in the interstellar medium and one of the most abundant molecules after, water, CO, and CO_2, within the ices. Indeed, methanol and formaldehyde are typically the two most abundant COMs detected around low mass stars, as can be seen in table 5. As such, understanding how they form is crucial.

Table 5: The abundances of some of the most abundant COMs in the objects listed. Abundances for methanol and formaldehyde are given with respect to the total density of hydrogen nuclei. The abundances for the other species are given relative to methanol.

Molecule	IRAS16293	IRAS4A	IRAS4B	IRAS2A	Ref.
H_2CO	$1x10^{-7}$	$2x10^{-8}$	$3x10^{-6}$	$2x10^{-7}$	[34–36]
CH_3OH	$1x10^{-7}$	$< 1x10^{-8}$	$7x10^{-7}$	$3x10^{-7}$	[37]
HCOOH	0.62	> 0.46	< 1.4	< 0.4	[11, 35, 38]
$HCOOCH_3$	1.7	> 3.4	1.6	< 2.2	[11, 35, 38]
CH_3OCH_3	0.1	-	0.4	0.1	[11, 35, 38, 39]
CH_3CN	0.1	> 0.16	0.13	0.029	[11, 35, 38]
C_2H_5CN	0.12	-	1.1	< 0.33	[11, 35, 38]

The most widely accepted route to the formation of methanol and formaldehyde is through the sequential hydrogenation of CO. This is believed to follow the route:

$$H + CO \rightarrow HCO \xrightarrow{+H} H_2CO \xrightarrow{+H} H_3CO \xrightarrow{+H} H_3COH \tag{3}$$

Since the hydrogen is initially in the gas phase and the CO is frozen out onto the grains, clearly this chemistry is heterogeneous in nature. Due to this, the chemistry has to be considered to contain three main steps. These are:

1. Adsorption of hydrogen on the surface
2. Diffusion of hydrogen across the surface
3. Reaction with species already adsorbed on the grain

The latter is known as the Langmuir-Hinshelwood mechanism [40] and is the most common mechanism considered for grain surface processes. However, another possibility is the Eley-Rideal mechanism [40] where an incoming hydrogen "hits" or is adsorbed directly at the reaction site. This mechanism is not as widely considered due to the exceptionally low probability of its occurrence. This can be rationalised by relating the probability of reaction

to the cross section of the grain in its entirety to the cross section of a specific species: since the whole grain is considerably larger at low surface coverage then clearly there is a greater probability of landing at any location on the surface rather than a specific site. Of course, with high surface coverage, the reverse is true.

Experiments by several groups [41–44] have shown that bombarding an ice containing CO can indeed lead to the formation of H_2CO and CH_3OH.

For example, in the experiments of Watanabe and Kouchi [45–47], both pure CO and mixed ices of CO and H_2O were irradiated with hydrogen atoms. During these experiments, both formaldehyde and methanol were detected. However, the authors were unable to detect the reactive intermediates so were not able to fully confirm the hydrogenation scheme proposed in equation 3. Following on from the initial studies, the group then proceeded to consider the effects of ice thickness and temperature on the reaction.

In considering the temperature effects, they note that initial temperature increases between 10 and 15 K, lead to an increase in the rate of formation of both formaldehyde and methanol. They postulate that this brought about as a result of the increased mobility of atomic hydrogen on the surface. With the increase in mobility being a result of the increase in temperature. They note however that the rate reaches a maximum limit within this temperature range as at higher temperatures the hydrogen readily desorbs before it can react. As the thickness of the ice increases, the amount of CO converted decreases relative to its initial abundance. In other words, although with a thicker ice you have more CO, it is not necessarily entirely converted into hydrogenated species. The rationale behind this is that hydrogen is unable to penetrate more than 1 or 2 monolayers of the ice. Consequently, any CO that lies deeper in the ice cannot be converted.

The work was then continued by Hidaka et al [47] who deduced that the rate of conversion of H_2CO to CH_3OH was approximately half of the rate of conversion of CO to H_2CO. Further to this, by replacing the hydrogen with deuterium, they showed that it was possible to form the deuterated isotopologues of formaldehyde and methanol in this manner. By comparison with the hydrogenation experiments, they note that the deuteration rate was approximately 10 times slower, indicating that quantum effects are clearly implicit within the reaction mechanism.

In addition, more recent results form Hidaka et al and Nagoaka et al [48–50] have shown that when deuterium is added to ices already containing H_2CO and CH_3OH, it can effectively substitute itself for a hydrogen atom. Interestingly, they observe that on reaction with H_2CO, it is possible to produce HDCO and D_2CO, but for CH_3OH no deuterated species are detected where the OH functional group has been replaced by an OD group.

Similar experiments have also been performed by Iopollo et al [51]. These experiments confirm the previous results. In addition they also indicate that the formation of CH_3OH is dependent on the flux of hydrogen atoms hitting the surface. In addition, these experiments have also been performed by Pirim et al [42–44] with a slightly different experimental method being employed through the co-deposition of hydrogen, CO, and H_2O at low temperatures. There results also confirm that formaldehyde and methanol can be formed in this way, and that the rate is increased in the presence of water. Further to this, at 3 K, the reaction does not proceed past HCO.

We see from the experiments that it is possible to obtain rates of formation for formaldehyde and methanol but astrophysical models require more than this to model abundances of COMs. Since from experiments it is not possible to deduce accurate mechanisms, rates or activation energies for these processes, astrophysicists turn to quantum chemists to obtain

the data they need. In the next section, we discuss the calculations which have been carried out previously for these molecules and the approach we shall take.

1.4.2 *Quantum Chemistry for Astrophysicists*

Whilst the experiments have clearly shown that formaldehyde and methanol can be formed by the sequential hydrogenation of CO, they are unable to deduce the exact mechanism. The experiments are also able to provide the total reaction rates for the formation of the two species, but these total reaction rates are complex quantities which include all of the surface processes that took place to produce them. Whilst this is useful for the astrophysical models, these rates need to be broken down into the components due to diffusion and reaction. This is not possible experimentally and so quantum chemistry is used to determine the energetics and as far as possible the rates of reaction for all species involved within the mechanism.

If we now consider the specifics of the route to formaldehyde and methanol, there are a variety of ways one can begin modelling the reactions. Firstly, one can consider only the reactions which are known to have activation barriers and those intermediates which lead directly to formaldehyde and through formaldehyde to methanol in the gas phase, these are then:

$$H + CO \rightarrow HCO \tag{4}$$

and

$$H + H_2CO \rightarrow H_3CO \tag{5}$$

This is the approach taken by Woon [52], Andersson et al [53], and Goumans [54]. Indeed Woon benchmarked reaction 4 using a variety of methods and basis sets to obtain an activation energy for the reaction of ~ 4 kcal.mol^{-1}. Further to this, Woon then modelled reactions 4 and 5 in small water clusters and found that the activation energy is not strongly affected by the presence of water. Andersson et al have more recently published 1st order rate constants for reaction 4 using Harmonic Quantum Transition State Theory (HQTST) using the potential energy surface (PES) of Werner et al [55, 56]. In the gas phase, the activation energy was scaled to fit the experimental value of 2.0 ± 0.4 kcal.mol^{-1} [57]. However, this experimental value has been called into question by Friedrichs et al [58] and by Zhao et al [59]. Both studies suggest that the barrier is infact larger than the value obtained by Wang. However, both give different values in the range 2.5 to 3.8 kcal.mol^{-1}. Goumans work on reaction 5 was performed both in the gas phase and in small clusters of water in a similar fashion to Woon. He notes that whilst there is no change in the activation energy for the process, the addition of water to the reaction complex decreases the rate of hydrogen abstraction from H_2CO and thus leads to a higher relative rate for the addition.

The second approach which can be taken, and indeed is taken by us, is to consider all of the possible addition reactions and treat them with the same level of theory. This involves computing all of the reactions listed below.

$$H + CO \rightarrow HCO \quad (6)$$
$$H + CO \rightarrow COH \quad (7)$$
$$COH \rightleftharpoons HCO \quad (8)$$
$$H + HCO \rightarrow H_2CO \quad (9)$$
$$H + HCO \rightarrow HCOH \quad (10)$$
$$H + COH \rightarrow HCOH \quad (11)$$
$$HCOH \rightleftharpoons H_2CO \quad (12)$$
$$H + H_2CO \rightarrow H_3CO \quad (13)$$
$$H + HCOH \rightarrow H_2COH \quad (14)$$
$$H + HCOH \rightarrow H_2COH \quad (15)$$
$$H_3CO \rightleftharpoons H_2COH \quad (16)$$
$$H + H_3CO \rightarrow H_3COH \quad (17)$$
$$H + H_2COH \rightarrow H_3COH \quad (18)$$

This approach enables us to determine which reactions may actually be participating in the formation of formaldehyde and methanol. In addition to considering each of these reactions in the gas phase, we will also consider them in molecular clusters.

Moreover, since the experiments highlight the importance of the abstraction of hydrogen by deuterium from formaldehyde and methanol we shall also investigate all of the channels within these processes in the gas phase.

The data from the experiments and calculations are then combined and used in astrophysical models.

1.4.3 *Astrophysical Models: the final step*

As part of the FORCOMS project, the GRAINOBLE model has been developed by Taquet et al [60]. Since our results are to be added to the model, we shall outline some of the key features of the model. We shall also briefly discuss the models of Hasegawa et al [61] and the continuous time random walk (CTRW) model of Chang, Cuppen, and Herbst [62–66]. The Grainoble model [60] treats both gas phase and grain surface chemistry. The model considers four main processes on the grains:

1. Accretion of species onto the grains from the gas phase
2. Diffusion of particles across the grain surface through thermal hopping
3. Reaction of adsorbed species as described by the Langmuir-Hinshelwood process
4. Desorption by either thermal processing or cosmic ray bombardment

These processes are illustrated in figure 2.

The model also includes parameters to describe the surface structure. This is done through the inclusion of two types of sites within the model: the first considered as non-porous and the second as porous. In addition, it also considers a multi-layer approach by distinguishing between sites within the bulk and those at the surface.

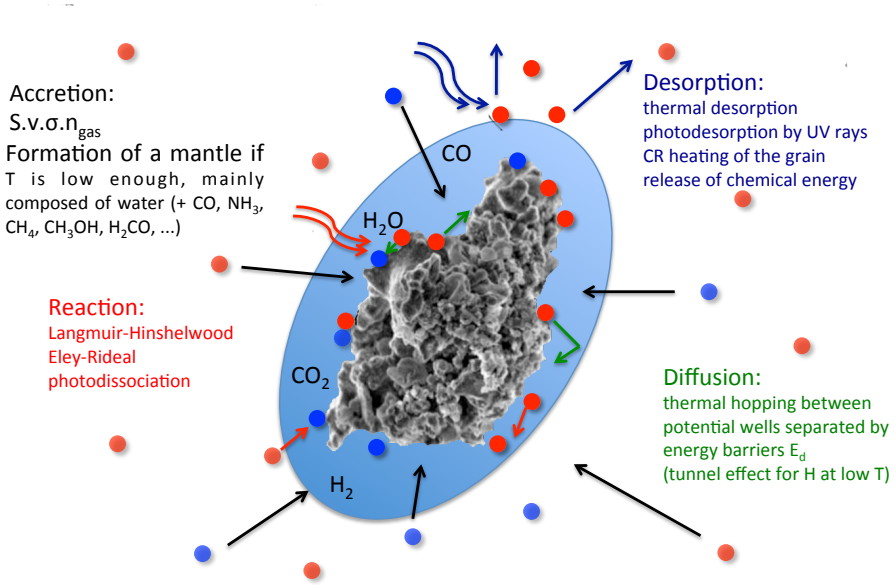

Figure 2: Schematic illustrating the various processes included within the Grainoble model.

This segregation of the bulk and the surface is achieved by considering a single layer at a time. In this case, a layer encompasses a number of sites, both porous and non-porous, into which species can undergo the processes listed above. This processing continues until the total number of particles within a layer is equal to the number of sites. At this point, the layer is considered inert and a new surface layer is started. Currently, the model does not allow for exchanges between the layers. The model then solves a series of rate equations for a number of time steps to monitor the chemical composition of the layers. The final composition is determined by the activation energies, binding energies, and reaction probabilities for the chemical network chosen. It is here that the data from experiments and from calculations are used as input parameters.

In comparison, the model of Hasegawa [61] uses three sets of differential equations to consider the gas phase, grain surface, and bulk chemistries. The chemistry of the bulk and the surface are linked via a term which is proportional to the growth rate of the ice mantle. As a result, surface species are continuously incorporated into the bulk. As such, this model does allow for chemistry to occur between the surface and the bulk unlike the Grainoble model. However, as with the Grainoble model, it uses chemical networks to deduce the final composition of the ice and the chemistry which takes place. Despite the fact that the Hasegawa model includes the additional chemistry, the results of both models appear to be similar.

The CTRW model [62–66] is another multilayer grain model which models the chemistry on a microscopic level. This is achieved by considering the interaction energies between all particles on the surface. In contrast, the macroscopic approach of the Grainoble model considers only the binding energy of particles with the surface. Unlike the other two models which use differential equations and rate equations, the CTRW model uses a Monte Carlo approach to determine the final chemistry and composition. In spite of this difference, it still requires data from chemical networks for this determination. Once again, by comparison with the Grainoble model for similar initial conditions and chemical networks, both models give similar results. For a more detailed comparison of the two models the reader is directed

to reference [60]. In addition, full details of all the models can be obtained from the references cited.

Due to the manner in which chemistry is incorporated into these models, they are highly dependent upon the chemical network considered. Therefore, accurate knowledge of reaction mechanisms is critcal to the relative success or failure of the model in reproducing the observed abundances of COMs. As such, we intend to use quantum chemistry to offer new insights into the formation of formaldehyde and methanol for use within these models. This thesis is arranged as follows:

Chapter 2 presents the theory behind the methods we employ during this work. In addition, it outlines the tunnelling methodologies employed for the calculation of rate constants, when possible. Finally, it also discusses some elements of thermochemistry which will be used to evaluate the possible entropic contribution to the processes.

Chapter 3 presents the gas phase results for the formation of HCO and COH and compares them to previous studies. This is done in several sections, first evaluating the relative electronic and zero point corrected energies of the stationary points within these two reactions. The discussion then moves to the role of a potential Van der Waals complex. Finally, the role entropy may play in the formation of HCO under the relevant conditions is discussed.

Chapter 4 is dedicated to "grain" surface primary model by considering the formation of HCO and COH in clusters of CO molecules and H_2O molecules. Once again, we commence with a discussion of the energetics followed by an Atoms In Molecules (AIM) analysis of the clusters to assess the relative strengths of the interactions within the clusters.

Chapter 5 presents the gas phase results for the formation of HCOH and H_2CO. The discussion then continues by considering the effect of water on the isomerisation of *trans*-HCOH to H_2CO. This process has been studied in some detail using a variety of methods and AIM analysis has also been performed on the clusters.

Chapter 6 presents the gas phase results for the final two hydrogenation steps, with consideration of the formation of CH_2OH, CH_3O from H_2CO and HCOH in the gas phases and clusters of water. In addition, it presents the results for the hydrogen abstractions from H_2CO and CH_3OH.

In chapter 7 we discuss the implications of this work for the astrophysical models. Finally, in chapter 8, we conclude our findings and present how this work can be built upon in the future.

Chapter II

THEORY

2 THEORY

Throughout this work, theoretical methods have been used in order to obtain molecular properties and energies. In all cases, this requires the selection of appropriate models of the chemistry. In order to give a full description of these, it is necessary to start from our most basic approximations. For reference, these are outlined in the following sections beginning with the use of the Schrödinger equation [67] and developing into the methods we use to solve this formidable problem.

2.1 ELECTRONIC STRUCTURE THEORY

2.1.1 *The Schrödinger Equation, the molecular hamiltonian and the Born-Oppenheimer approximation*

The chief purpose of all electronic structure methods is to solve the time independent version of the Schrödinger equation (SE), 19.

$$\hat{H}\Psi = E\Psi \tag{19}$$

Where Ψ is the total molecular wavefunction and $\hat{H}$ is the molecular hamiltonian which is defined as:

$$\hat{H} = T_N + T_e + V \tag{20}$$

T_N and T_e are the kinetic energy of the nuclei and the electrons respectively and are expressed in atomic units for an ensemble of nuclei, $A = 1$ to N, and a set of electrons, $i = 1$ to n, as:

$$T_N = -\sum_{A}^{N} \frac{\Delta_A}{2M_A} \tag{21}$$

$$T_e = -\sum_{i}^{n} \frac{\Delta_i}{2} \tag{22}$$

The V term in equation 20 corresponds to the total potential energy of the system. This encompasses the electrostatic attraction between the electrons and the nuclei, V_{Ne}, plus the two repulsive terms from electron-electron, V_{ee}, and nuclear-nuclear interactions,V_{NN}. These quantities, expressed in atomic units, are:

$$V_{Ne} = -\sum_{i}^{n}\sum_{A}^{N}\frac{Z_A}{r_{iA}} \tag{23}$$

$$V_{ee} = \sum_{i}^{n}\sum_{j>i}^{n}\frac{1}{r_{ij}} \tag{24}$$

$$V_{NN} = \sum_{A}^{N}\sum_{B>A}^{N}\frac{Z_A Z_B}{R_{AB}} \tag{25}$$

Where Z_A and Z_B refer to the charge of nucleus A and B respectively, $r_{ij}$the distance between two electrons i and j, r_{iA} is the distance between nucleus A and the electron i and R_{AB} is the internuclear distance between the two nuclei. Formally, this equation encompasses all the information we may wish to know about a molecule within the wavefunction, Ψ. This includes the energy of the system and all other properties. However, Ψ is a function of both the nuclear and electronic motions and this problem quickly becomes intractable once one has more than one nucleus [68]. For this reason, a first approximation is introduced: it surmises that given the difference in mass of the nuclei and the electrons, we may partition the wave function into a nuclear part and an electronic one. Following this, we may then solve the SE at a given nuclear configuration. The approximation was first introduced by Born and Oppenheimer and consequently bears their names [69–71]. Using this approximation the electronic hamiltonian becomes:

$$\hat{H}^e = T_e + V_{Ne} + V_{ee} = -\sum_{i}^{n}\frac{\Delta_i}{2} - \sum_{i}^{n}\sum_{A}^{N}\frac{Z_A}{r_{iA}} + \sum_{i}^{n}\sum_{j>i}^{n}\frac{1}{r_{ij}} \tag{26}$$

2.1.2 *Potential energy (hyper)Surface (PES)*

The chief consequence of expressing the hamiltonian in this fashion is that now we only solve equation 19 for the potential energy of the nuclei and not their kinetic energy. This leads to the very useful concept of a potential energy (hyper)surface. This surface shows how the potential energy of the nuclei evolves as a function of their configuration and consequentialy has 3N dimensions. As with any function, by analysis of the change in energy with respect to the nuclear coordinates, we can predict how the system will respond to change. Such an analysis also enables us to find configurations corresponding to stationary points of the energy. That is to say those points where:

$$\forall Q_A \quad \left.\frac{\partial E}{\partial Q_A}\right|_{Q_0} = 0 \tag{27}$$

$$\forall Q_A \quad \left.\frac{\partial^2 E}{\partial Q_A^2}\right|_{Q_0} > 0 \quad \text{minima} \tag{28}$$

$$\exists Q_A \quad \left.\frac{\partial^2 E}{\partial Q_A^2}\right|_{Q_0} < 0 \quad \text{maxima} \tag{29}$$

Care must be taken here in the definition of Q_A, the nuclear coordinates, since there are many ways one may chose to define them and indeed obtain their derivative. The coordinates Q_0 are a subset of Q_A which correspond to the stationary points. Normally, we define

molecular geometries in terms of internal coordinates. These coordinates consist of the various bond lengths, angles, and dihedral angles which exist between the nuclei and define the molecular geometry. This coordinate system is useful since it explicitly relates to the degrees of freedom, ν, the molecule has. This means for a non-linear molecule, $\nu = 3N - 6$ and for a linear system $\nu = 3N - 5$, where N is the number of atoms. In choosing this coordinate system, we may now take the derivative of the energy (and the second derivative) with respect to each degree of freedom. This is extremely useful since now, we can define two key types of stationary points from all others: minima and 1st order maxima. 1st order maxima are those points which have only one second derivative which is less than zero. These points correspond to the transition states which are accessible in chemical reactions. In addition, the minima correspond to the equilibrium geometries which can be detected experimentally, at least in principle

In order to evaluate the second derivatives, we must introduce our second approximation: the PES about these stationary points can be fitted approximately by a harmonic function. In addition to allowing us to more easily compute second derivatives, it also enables us to compute the harmonic vibrational frequencies of the molecule. This is achieved by relating the derivative matrix, more commonly referred to as the hessian matrix, $\mathcal{H}_{AA}$, to the molecular force constants.

This matrix is then diagonalised to produce a set of eigenvalues which are then mass weighted. Since the matrix is a 3Nx3N matrix from diagonalisation, one obtains 3N eigenvalues from which the 6 (or 5 for linear molecules) zero eigenvalues due to global rotations and translations are removed. Once this has been done, one may then compute the harmonic vibrational frequencies, ω_A:

$$\mathcal{H}_{AA} = |\frac{\partial^2 E}{\partial Q_A^2}| = |k_A| \Rightarrow \omega_A = \sqrt{\frac{k_A}{\mu_A}} \tag{30}$$

k_A and μ_A are the force constant and reduced mass associated with the molecular motion described by ω_A.

Figure 3 shows the relationship between the two types of stationary point schematically. The quantities marked with ZPE refer to those where the harmonic zero point energy has been included. The zero point energy is defined as:

$$E_{ZPE} = \sum_{i=1}^{\nu} \frac{\omega_i}{2} \tag{31}$$

Here the summation is from $i = 1$ to ν. For this summation, only positive values of the frequencies, ω_i are considered.

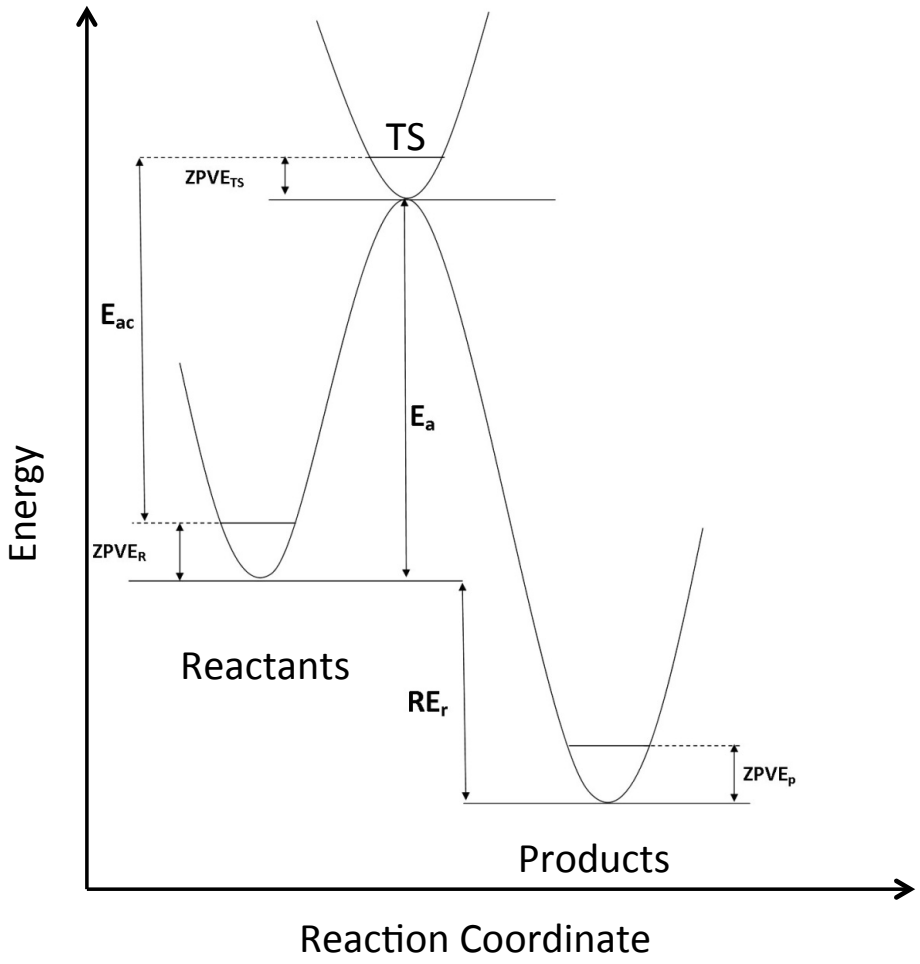

Figure 3: Schematic of the different types of stationary points which are of chemical interest on a PES. The various quantities shown are: the activation energy, E_a, the zero point corrected activation energy, E_{ac}, the zero point vibrational energies for the reactants, $ZPVE_r$, transition state, $ZPVE_{TS}$, and the product, $ZPVE_P$. In addition, the relative energy of the reactants is given by RE_r. This schematic also shows the intrinsic reaction coordinate (IRC) for the process when the reaction coordinate is given in mass weighted units.

In addition, the path shown in figure 3 corresponds to the minimum energy pathway (MEP) which connects the reactants to the products through the transition state. In this case, this pathway is also called an intrinsic reaction coordinate (IRC) [72] since the reaction coordinate is given in mass weighted cartesian coordinates. Whilst it is also possible to determine MEPs without using mass weighted coordinates, these may not then be considered as IRCs.

In order to evaluate the energetics of a system, we must attempt to solve equation 19. As outlined above, we simplify this by separating the nuclear and electronic motions. However, this still only permits us to solve the SE exactly for molecules with only one electron. This is known as the quantum many-body problem for which there are many different methods available, offering approximate solutions for systems with more than 1 electron and more than a single nucleus. These will now be discussed under the two broad headings of wave-function theory (WFT) and density functional theory (DFT).

In order to assess the quality of these methods, we compare them to 3 criteria that we would like a given method to have and also with the size of the problem to be solved. It

should be noted however, that in practice we typically use the highest level of theory we can afford, based on the computational cost.

The properties we would like our approximate solution to have are as follows:

1. The method should be variational, meaning the energy obtained from the approximate wavefunction should always be above the exact energy of the system.
2. The method should ideally be size extensive, meaning the calculated energy should become proportional to the number of electrons, n, in the limit $n \to \infty$.
3. The method should be size consistent, meaning that the energy of an ensemble of atoms at infinite distance should be the same as the sum of the energy of all of the atoms within the ensemble, computed one by one. This property guarantees that when one breaks a bond within a molecule, the energy will asymptotically converge to the sum of the energies of the fragments.

2.1.3 *Wavefunction Theory (WFT)*

We commence our discussion with those methods, which optimise the wavefunction, Ψ, within the BO approximation. Indeed the methods we shall focus on here are those, that are commonly referred to as *ab initio* methods, since they are attempts to solve the SE without the use of experimental or empirical data.

2.1.3.1 *Hartree-Fock theory*

The simplest of these methods is the Hartree-Fock (HF) model, first proposed in 1928 by Hartree [73, 74]. His idea was to express the total electronic hamiltonian, $\hat{H}^e$, as a summation of mono-electronic hamiltonians:

$$\hat{H}^e \approx \sum_{i=1}^{n} h_i = \sum_{i=1}^{n} \left\{ \frac{-\Delta_i}{2} + \sum_{A=1}^{N} \frac{-Z_A}{|\mathbf{R}_A - \mathbf{r}_i|} + V_c(r_i) \right\} \tag{32}$$

In order to take into account the effect the other electrons, j, have on the electron i, h_i contains a term, V_c, which is a coulombic potential created by all the electrons $j \neq i$:

$$V_c(r_i) = \sum_{j \neq i}^{n} \frac{1}{r_{ij}} \tag{33}$$

In this way, each electron, i, is associated with a wavefunction ϕ_i. Then, the solution to the mono-electronic Hartree equations takes the form:

$$h_i \phi_i = \varepsilon_i \phi_i \tag{34}$$

Where ϕ_i is a function known as a spin-orbital, which depends on both the electron spin, α or β, and a spatial part, ψ_i. This separation is justified by the fact that the hamiltonian does not depend on the spin. This is of course only true in the non-relativistic scheme, which is all we consider here. By computing these mono-electronic functions, and energies, via equation 34, the total energy can be expressed merely as a summation of all of the mono-electronic energies:

$$E_0 = \sum_{i=1}^{n} \varepsilon_i \tag{35}$$

The corresponding total wavefunction can be expressed then as the product of all of the mono-electronic orbitals, ϕ_i. However, this wavefunction does not allow for the fact that under the Pauli exclusion principle [75], two electrons may not occupy the same spatial orbital if they have the same spin. This then requires a wavefunction which is antisymmetrical with respect to the permutation of two electrons. In order to allow for this anti-symmetry in the total wavefunction, Slater [76] proposed that it should be expressed as a determinant:

$$\Phi_0 = \frac{1}{\sqrt{n!}} \begin{vmatrix} \phi_1(1) & \dots & \phi_n(1) \\ \vdots & & \vdots \\ \phi_1(n) & \dots & \phi_n(n) \end{vmatrix} \tag{36}$$

In which each column represents a spin orbital and each row an electron. In practice, this means there are many determinants which could describe the electronic configuration of a molecule.

Fock [77, 78] first introduced the Pauli principle into the Hartree model. It is for this reason that the method is now referred to as Hartree-Fock theory. The basic idea is to write a mono electronic hamiltonian with the Fock operator for electron j:

$$F(j) = h^c(j) + V^{HF}(j) = h^c(j) + \sum_{i=1}^{n} [\mathbb{J}_i(j) - \mathbb{K}_i(j)] \tag{37}$$

where

$$h^c(j) = -\frac{\Delta_j}{2} + \sum_{A=1}^{N} \frac{-Z_A}{|\mathbf{R}_A - \mathbf{r}_j|} \tag{38}$$

$$\mathbb{J}_i(1) = \iiint_{(2)} \phi_i^*(2) \frac{1}{r_{12}} \phi_i(2)\, d\tau_2 \tag{39}$$

$$\mathbb{K}_i(1)\phi_j(1) = \phi_i(1) \iiint_{(2)} \phi_i^*(2) \frac{1}{r_{12}} \phi_j(2)\, d\tau_2 \tag{40}$$

$\mathbb{J}$ and $\mathbb{K}$ are known as the Coulomb and exchange operators respectively. The operator $\mathbb{K}$ is fully non-local since it depends on the value of $\phi_i(1)$ over all space. The Hartree Fock equations take the form:

$$F\phi_i = \varepsilon_i \phi_i \tag{41}$$

where ε_i is:

$$\varepsilon_i = h_{ii}^c + V^{HF} = h_{ii}^c + \sum_{j=1}^{n} J_{ij} - K_{ij} \tag{42}$$

Here we introduce the matrix elements of the core hamiltonian and the Coulomb, J_{ij}, and exchange, K_{ij}, integrals.

$$h_{ii}^{c} = \iiint_{(1)} \phi_i(1) h^{c}(1) \phi_i(1) d\tau_1 = \langle \phi_i | h^{c} | \phi_i \rangle \tag{43}$$

$$\begin{aligned} J_{ij} &= \iiint \phi_i^*(1) \phi_j^*(2) \frac{1}{r_{12}} \phi_i(1) \phi_j(2) d\tau_1 d\tau_2 \\ &= \left\langle \phi_i(1)\phi_j(2) \left| \frac{1}{r_{12}} \right| \phi_i(1)\phi_j(2) \right\rangle = \langle ij|ij\rangle \end{aligned} \tag{44}$$

$$\begin{aligned} K_{ij} &= \iiint \phi_i^*(1) \phi_j^*(2) \frac{1}{r_{12}} \phi_i(2) \phi_j(1) d\tau_1 d\tau_2 \\ &= \left\langle \phi_i(1)\phi_j(2) \left| \frac{1}{r_{12}} \right| \phi_i(2)\phi_j(1) \right\rangle = \langle ij|ji\rangle \end{aligned} \tag{45}$$

From this, we get the final expression of the Hartree Fock energy to be:

$$\begin{aligned} E_{HF} &= \sum_{i=1}^{n} \varepsilon_i - \frac{1}{2} \sum_{i=1}^{n} \sum_{j=i}^{n} (J_{ij} - K_{ij}) \\ &= \sum_{i=1}^{n} \varepsilon_i - \frac{1}{2} \sum_{i=1}^{n} \sum_{j=i}^{n} (\langle ij|ij\rangle - \langle ij|ji\rangle) \end{aligned} \tag{46}$$

Since the Hartree Fock method only considers a single Slater determinant, it is known as a single-reference method. Typically, these equations are solved self consistently since the orbital energies have a dependence upon the orbitals. It should be noted that the HF method is variational, that is to say E_{HF} is always greater than the exact energy.

2.1.3.2 *Linear Combination of Atomic Orbitals* (LCAO)

Typically, we solve the HF equations within the Linear Combination of Atomic Orbitals (LCAO) approach. This method is an approximate way of generating the molecular orbitals (MOs), and it is widely used within Chemistry. The idea is that when two atoms form a bond, their atomic orbitals mix to generate a set of molecular orbitals, such that the mixing of m atomic orbitals generates m molecular orbitals.

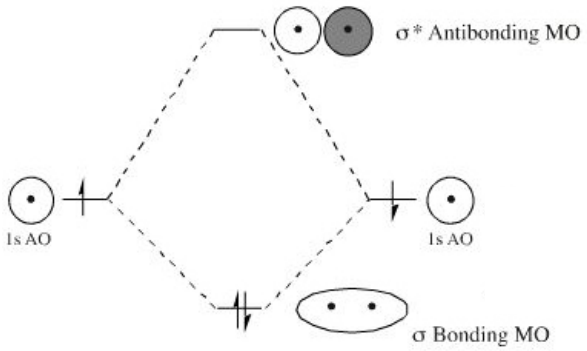

Figure 4: Schematic of the linear combination of the 1s orbitals of two hydrogen atoms to form the bonding and antibonding orbitals of H_2

This is shown pictorially in figure 4 for H_2. We see that the two 1s orbitals of the hydrogen atoms combine to give us 1 MO which is more stable and one which is less. These are more

commonly referred to as a bonding orbital (BMO) and an anti-bonding orbital (ABMO). As such, this approximation allows us to build the MO's using atomic orbitals, and thus we can use a set of functions centred on atoms to build the molecular functions we need. In most QC calculations, these atomic basis sets consist of gaussian functions of the form:

$$S(N, m, \alpha) = Ne^{-\alpha r^2} Y_L^m(\Theta, \Psi) \tag{47}$$

In this way there are two commonly used basis set types: the Dunning sets [79, 80] and the Pople sets [81–94]. They differ in the number of gaussian functions used for each atom and the exponents used for the various gaussians used in describing the atomic s, p, d, and f shells[1]. It should be noted that for the most acurrate calculations possible we would like to use as large a basis set as we can. However, the computational cost increases considerably with the basis set size.

2.1.3.3 *Correlation Energy*

The HF approximation is typically used within the SCF-LCAO-MO approach, for molecules, and has been since the 1950's. It had remarkable success in describing simple diatomic and triatomic species. One of the most frequent applications was in obtaining the equilibrium configurations of molecules, with good agreement compared to experiment. However, there were certain systems where, even with large basis sets, only a qualitative description was possible. An example of this is shown in figure 5, which is taken from a figure produced by I. Csizmadia [95] to show that there was a portion of the exact energy missed by the HF method, in the case of CO.

1 It should be noted that some large basis sets include functions for the description of f and higher orbitals as well.

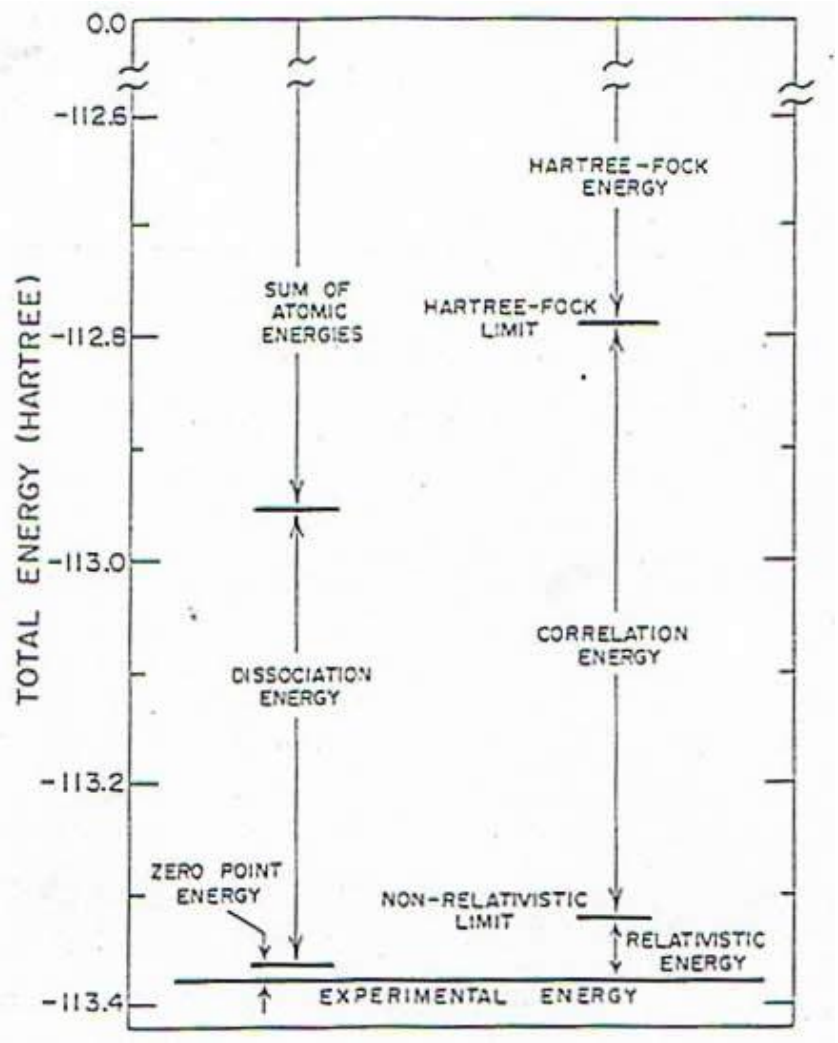

Figure 5: Schematic of the energy contributions to the total energy of CO compared to the experimental value [95].

The correlation problem arises due to the fact that within the mean field approximation, the probability of finding two electrons of opposite spin in the same region of space is not 0. To show this, we shall now consider the case where two electrons are in two spin orbitals ϕ_1 and ϕ_2. We can then express the Slater determinant as:

$$\Phi(1,2) = |\phi_1\phi_2| = \frac{1}{\sqrt{2}}[\phi_1(1)\phi_2(2) - \phi_1(2)\phi_2(1)] \tag{48}$$

The probability of finding electron 1 at $\mathbf{r}_1$ and electron 2 at $\mathbf{r}_2$ is:

$$P(\mathbf{r}_1,\mathbf{r}_2) = |\Phi(1,2)|^2 d\mathbf{r}_1 d\mathbf{r}_2 \tag{49}$$

So now, if we consider that electrons 1 and 2 have the same spin:

$$\begin{cases} \phi_i(1) = \psi_i(\mathbf{r}_1) \\ \phi_i(2) = \psi_i(\mathbf{r}_2) \end{cases} \quad \forall i \tag{50}$$

After integration with respect to the spin we have:

$$P(\mathbf{r}_1,\mathbf{r}_2) = \frac{1}{2}\left[\psi_1^2(\mathbf{r}_1)\psi_2^2(\mathbf{r}_2) + \psi_1^2(\mathbf{r}_2)\psi_2^2(\mathbf{r}_1) - 2\psi_1(\mathbf{r}_1)\psi_2(\mathbf{r}_2)\psi_1(\mathbf{r}_2)\psi_2(\mathbf{r}_1)\right] \tag{51}$$

If $\mathbf{r}_1 = \mathbf{r}_2$ then $P(\mathbf{r}_1,\mathbf{r}_2) = 0$. In this way, the probability of finding two electrons of the same spin at the same position is zero. This result is unsurprising since a Slater determinant is constructed such that it respects the Pauli exclusion principal. Now, if we consider the case where electrons 1 and 2 have different spins α and β, where ψ_i and $\overline{\psi_i}$ are the spatial orbitals associated with the α and β spins, respectively, we have:

$$\begin{cases} \phi_i(1) = \psi_i(\mathbf{r}_1) \\ \phi_i(2) = \overline{\psi_i}(\mathbf{r}_2) \end{cases} \quad \forall i \tag{52}$$

After integration:

$$P(\mathbf{r}_1,\mathbf{r}_2) = \frac{1}{2}\left[\psi_1^2(\mathbf{r}_1)\psi_2^2(\mathbf{r}_2) + \psi_1^2(\mathbf{r}_2)\psi_2^2(\mathbf{r}_1)\right] = P(\mathbf{r}_1)P(\mathbf{r}_2) \tag{53}$$

as electrons 1 and 2 are indistinguishable. If $\mathbf{r}_1 = \mathbf{r}_2$ then $P(\mathbf{r}_1,\mathbf{r}_2) \neq 0$ which is clearly unphysical. Consequently Wigner [96] and subsequently Löwdin [97] introduced/reintroduced the idea of the correlation energy, E_c, as the difference between the exact energy of a system, E, and the HF energy, E_{HF}:

$$E_c = E - E_{HF} \tag{54}$$

As a consequence of the variational nature of the HF method, E_{HF} is always greater than E so E_c is always negative.

2.1.3.4 *Perturbative Treatment of Electron Correlation*

One of the simplest methods which is commonly used in quantum chemistry is Møller Plesset Perturbation Theory (MPPT) [98, 99]. In this case, one takes the HF solution as a reference function and the correlation energy is merely a perturbation of the HF solution. From this viewpoint, the hamiltonian can be partitioned into two parts: a zero order part, $\hat{H}_0$, and a perturbation, $\hat{V}$:

$$\hat{H} = \hat{H}_0 + \hat{V} \tag{55}$$

This allows us to express the energy as an expansion of the order of perturbation included. Now, by imposing the condition that all functions with $n \neq 0$, where n is the order of perturbation, are orthogonal to the zero order functions, we get:

$$E^1 = \langle \Psi^0 | \hat{V} | \Psi^0 \rangle \tag{56}$$

$$E^2 = \langle \Psi^0 | \hat{V} | \Psi^1 \rangle \tag{57}$$

$$\vdots$$

to

$$E^n = \langle \Psi^0 | \hat{V} | \Psi^{n-1} \rangle \tag{58}$$

The correction to the energy then becomes:

$$E_{MPPTn} = E^0 + E^1 + E^2 + \cdots + E^n \tag{59}$$

This expression can then be truncated to any order to give the MPn methods. Typically, it is truncated to 2nd order, giving the MP2 method where E^0 is the HF energy and $\hat{H}_0$ is the HF hamiltonian. This truncation to the second order is most common as the cost of the higher order corrections is significant with often little gain in accuracy.

2.1.3.5 *Configuration Interaction (CI)*

The next method to evaluate E_c was the Configuration Interaction (CI) method [100]. The principal idea was, that instead of writing the total wavefunction using a single determinant, as in the HF case, one now writes the wavefunction as a linear combination of determinants. Each determinant corresponds to electronic excitations of one or more electrons from the HF reference.

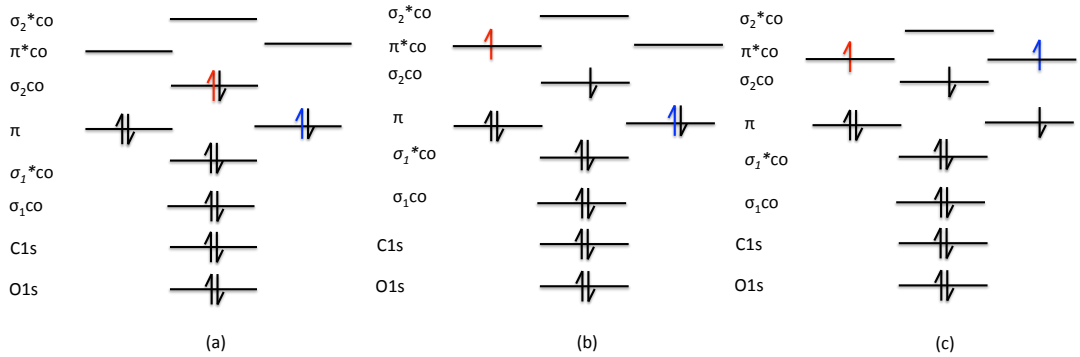

Figure 6: Schematic illustration of three different electronic configurations of CO where (a) corresponds to a typical HF reference, (b) corresponds to a single electronic excitation, and (c) corresponds to a double electronic excitation.

Figure 6 shows 3 such determinants where the 2nd and 3rd determinants correspond to single/mono, double/di electronic excitations from the initial determinant. In the case of full-CI (FCI), the wavefunction involves inclusion of all single (1 e^-), double (2 e^-), triple (3e^-), ..., k-tuple (k e^-) excitations. As such, the wavefunction is expressed as:

$$|\Phi_{FCI}\rangle = c_0|\Phi_0\rangle + \sum_M c_M|\Phi_M\rangle + \sum_D c_D|\Phi_D\rangle + \sum_T c_T|\Phi_T\rangle + \cdots = \sum_K c_K|\Phi_K\rangle \tag{60}$$

The c_0, c_M, c_D, c_T, c_K are the excitation coefficients which correspond to the reference, monoexcited, doubly excited, triply excited, up to k-tuply excited wavefunctions respectively.

The SE takes the form:

$$H|\Phi^{FCI}\rangle = E^{FCI}|\Phi^{FCI}\rangle \tag{61}$$

By applying variational theory we obtain:

$$\sum_K \left(H_{IK} - E^{FCI}\delta_{IK}\right) c_K = 0 \tag{62}$$

with

$$H_{IK} = \langle\Phi_I|H|\Phi_K\rangle \tag{63}$$

Where the $|\Phi_K\rangle$ are linear combinations of Slater determinants which satisfy any spatial symmetry and any spin constraints of the wavefunction. Each $|\Phi_K\rangle$ is now referred to as a

Configuration State Function (CSF). In principle, the matrix equation 62 provides the exact energy of the ground state and all excited states of a system. However, even for small molecules with only a few electrons, the CI matrix is very large. Consequently, FCI is not often used as it is much too costly. Typically, the CI matrix is truncated to only include Single and Double excitations and in this case, it is referred to as CISD. However, this truncation now means the CI treatment is no longer size consistent [101]. This has consequently led to CI no longer being used.

2.1.3.6 *Coupled Cluster Theory (CC)*

The most accurrate correlation method based on the HF solution is Coupled Cluster theory (CC) [102, 103]. This method is similar to CI but it was however initially developed in nuclear physics [104–106]. The chief concept here is that the HF solution contributes over 90% of the total CI wavefunction, in most cases, and then the double excitations are the next most important contribution, followed by the quadruple excitations, with the triples being negligible. We can then approximate the coefficients for quadruple excitations, c_{abcd}^{rstu}, as a product of two double excitations $c_{ab}^{rs}c_{cd}^{tu}$ which are equivalent to the diexcitation coefficients c_{ab}^{rs} and c_{cd}^{tu}. As such, we can rewrite the FCI wavefunction as:

$$|\Phi_{FCI}\rangle = e^{T}|\Phi_0\rangle \tag{64}$$

where T is the sum:

$$T = T_1 + T_2 + T_3 + \cdots + T_N = \sum_{n=1}^{N} T_N \tag{65}$$

with T_1, T_2, T_3 corresponding to configurations with mono, di, and triple excitations with respect to $|\Phi_0\rangle$. For example:

$$T_2 = \sum_{abrs} t_{ab}^{rs} a_r^\dagger a_s^\dagger a_a a_b |\Phi_{ab}^{rs}\rangle \tag{66}$$

Where the t_{ab}^{rs} operators corresponding to the creation of holes and particles respectively and $a_r^\dagger$, $a_s^\dagger$, a_a, a_b are referred to as amplitudes. If we take the complete form of T, we obtain the FCI wavefunction. In practice, the sum of operators is truncated for the calculation to remain feasible. For example, in a CCSD calculation one has $T \cong T_1 + T_2$. In this case the CC approximation has an advantage over the CI form. If we now consider only the CCD expansion where $T \cong T_2$ by using a Taylor expansion of the e^{T_2} operator:

$$|\Phi_{CCD}\rangle = e^{T_2}|\Phi_0\rangle = \left[1 + T_2 + \frac{T_2^2}{2!} + \frac{T_2^3}{3!} + \ldots\right]|\Phi_0\rangle = \sum_{i=1}^{\infty}\frac{T_2}{i!} \tag{67}$$

The $1 + T_2$ term corresponds to the CID expression. However, in the CCD expression, we have the T_2^2 which corresponds to a class of quadruple exciteations which are a product of diexcitations. In this way, we say that the T_2^2 term contains the unlinked quadruple excitations. The linked terms correspond to the terms in T_4 which includes the excitations which are not products of double excitations. In the same way, the T_2^3 term includes contributions from hexaexcitations. It is the absence of these terms in the CID case which causes the truncated CI wavefunction to lack size consistency.

The determination of the excitation amplitudes included in T requires us to solve the SE:

$$He^{T}|\Phi_0\rangle = Ee^{T}|\Phi_0\rangle \tag{68}$$

To do this, one multiplies the left hand side by e^{-T}

$$e^{-T}He^{T}|\Phi_{CC}\rangle = E|\Phi_{CC}\rangle \Longrightarrow E = \left\langle \Phi_{CC} \left| e^{-T}He^{T} \right| \Phi_{CC} \right\rangle \tag{69}$$

In practice, the solution of this is very complicated and the method scales as O^6, where O is the number of basis functions, for the CCSD calculation. In addition, the energy is evaluated iterativly but it is not variational. This means that using a larger basis set does not mean that one will improve the result. A full CCSDT calculation scales as M^8, where M corresponds to the number of basis functions. As such, it quickly becomes impractical. In this case, the triple excitations are introduced in a perturbative manner and it is referred to as CCSD(T) [107]. The CCSD(T) method is often referred to as the gold standard of quantum chemistry. But it is only precise where the HF wavefunction is a good approximation. The effectiveness of this description can be evaluated with the T_1 diagnostic proposed by Lee and Taylor [108]:

$$T_1 = \frac{\|\mathbf{t}_1\|}{n} \tag{70}$$

Here $\mathbf{t}_1$ is the vector of single excitation amplitudes and n is the number of electrons. Typically a value of T_1 greater than 0.02 indicates that the HF reference is not a good approximation. In this case, a reference should be used which includes more than one Slater determinant. Methods which do this are called Multi-reference methods and they are described in the next section.

2.1.3.7 *Single-reference vs Multi-reference*

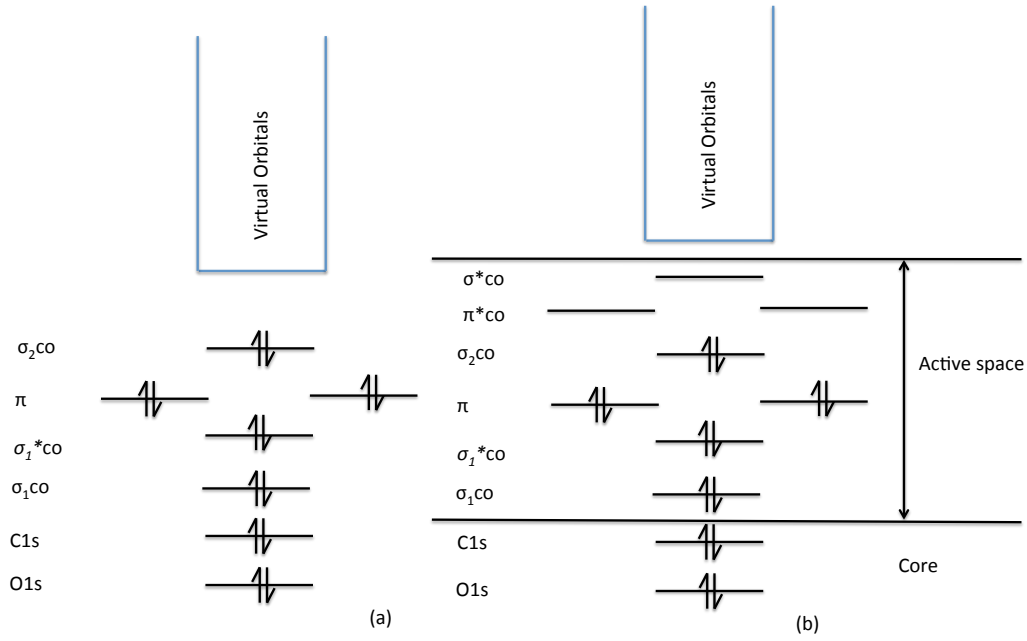

Figure 7: Schematic illustration of (a) HF Slater determinant for CO showing the occupied and virtual orbitals, (b) CASSCF reference determinant for a full valence active space of CO.

In the common *ab initio* methods, a single Slater determinant is used as they are based upon the HF wavefunction. This leads to the partitioning of the molecular orbitals into two types: occupied orbitals and unoccupied or virtual orbitals. These single-reference methods have been shown to be deficient in describing open shelled species, where there are degenerate states, with an odd number of electrons. This behaviour is typical for heavy elements and transition metals.

In the multi-reference picture, the electronic orbitals are partitioned differently, figure 7. In this approach, one defines two types of occupied and two types of unoccupied or virtual orbitals. In the case of the occupied, they are partitioned into core and active orbitals whereby the core orbitals usually denote the 1s orbitals of elements heavier than hydrogen and the active orbitals consist, in a full valence case, of all of the bonding orbitals and any lone pairs. In addition, the active space includes an equivalent number of orbitals to the bonding ones to represent the anti bonding orbitals of a molecular system which are naturally unoccupied initially. All other unoccupied orbitals are attributed to the virtual orbitals and left out of the active space.

Within the active space, a full-CI calculation is performed taking into account any spin and symmetry conditions for the total wavefunction. This leads to more than one configuration, so we are now able to compute the energy of the system using more than one reference. This then becomes known as a multi-reference treatment. One possible reference from this active space description for CO is shown in figure 7. This partitioning into an active space is not unlike the chemical idea of Frontier orbitals whereby one considers that a chemical process is dominated by the exchange of electrons from key orbitals. This can be readily seen in using CASSCF (Complete Active Space Self Consistent Field) [109–114], when looking at bond breaking reactions, since this clearly requires the promotion of electrons from a bonding situation to an anti bonding one.

It should be noted that CASSCF is a special case of the more general MCSCF (Multi-Configurational Self Consistent Field) method [115–117]. CASSCF is used more widely than MCSCF since it is more computationally efficient. The additional efficiency of CASSCF arises from the FCI treatment, making it possible to treat the gradient evaluations analytically, instead of by finite differences. The key difference between the normal FCI treatment and the MCSCF or CASSCF approach is that one optimises both the orbitals and the CSFs, whereas in the CI treatment only the CSFs are optimised.

In addition to CASSCF, there are several high level multi reference methods which use the CAS references to carry out a more complete correlation treatment. The two main variants are CASPT2 (Complete Active Space Perturbation Theory of the second order) [118–120] and MRCI (Multi reference Configuration Interaction) [121, 122] which are multi-reference versions of their single reference counterparts (MP2, and CISD). Also, there are a variety of treatments for multi-reference coupled cluster methods, but at the time of writing, these are not widely used. It should be noted that certain software packages use RS2 [123] or RS2C [124] (Rayleigh Schrödinger Perturbation theory) or MRMP [125] (multi-reference Møller Plesset perturbation) which are formally equivalent, but not identical to CASPT2.

As can be seen through this discussion, there are many wavefunction methods available so the question is which one is most suitable for a given problem?

Table 6 shows how some of the methods commonly used compare with the desirable properties outlined previously. What we see is in fact only three methods have all of these desired properties, HF, FCI, and CASSCF. The problem that arises however is that FCI is only tractable on small systems and both HF and CASSCF fail to account for all of the correlation

energy. As such, we are forced into using the other methods for chemically relevant systems. This is not to say that even all of these are available for every system. In order to choose the most appropriate method, a hierarchy exists based upon the accuracy of the method whereby as the accuracy increases, the size of the system we can treat in a reasonable time decreases. This hierachy is shown in figure 8.

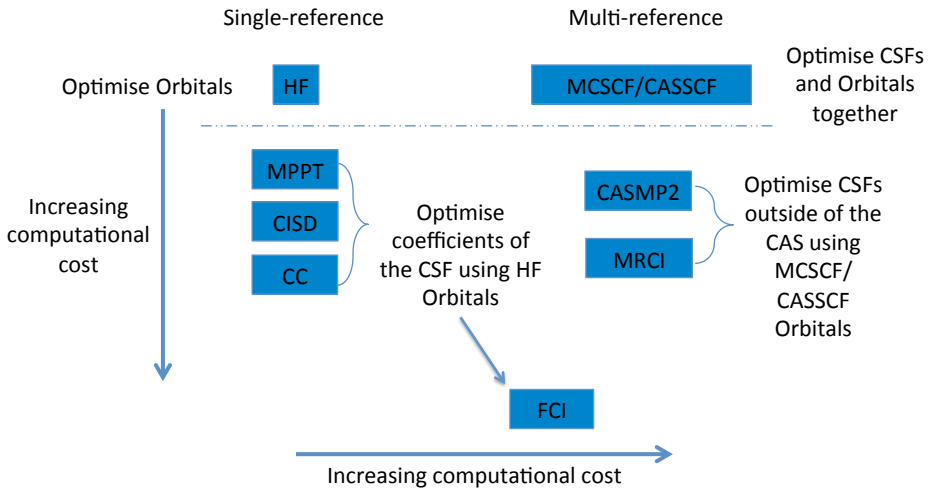

Figure 8: Scheme showing the hierarchy of various single and multi-reference methods along with the quantities optimised during their energy evaluations. We also note that the computational cost of the various methods increases as you move down each strand and as you go from left to right. In addition, it should be noted that FCI is not placed in either group since it is a special case, and it is placed at the bottom of the figure as it is the most computationally intensive.

Table 6: Comparison of some of the WFT methods with respect to the properties of variation, size extensivity and size consistency.

Method	Variational	Size Extensive	Size Consistent
HF	✓	✓	✓
CISD	✓	-	-
Full-CI	✓	✓	✓
CCSD(T)	-	✓	✓
MP2	-	✓	-
CASSCF	✓	✓	✓
CASPT2	-	✓	✓
MRCI	✓	-	-

2.1.4 *Density Functional Theory (DFT)*

Another approach to obtaining the total energies of molecules is instead of computing the wavefunction, one attempts to compute something more observable. A good candidate for

this is the total electronic density, ρ. If one integrates the total density over all space one obtains the total number of electrons, n:

$$n = \int \rho(\mathbf{r})\, d\mathbf{r} \tag{71}$$

In the case where the nuclei are represented by point charges, their positions correspond to the maxima of ρ. Also by the theorem of Kato [126, 127], the nuclear charge Z_A is related to the maximum density by the relation:

$$\frac{\delta \bar{\rho}(r_A)}{\delta x}|_{r_A=0} = -2Z_a \bar{\rho}(r_A) \tag{72}$$

Where $\bar{\rho}(r_A)$ is the average density of a sphere. At long distance, in the asymptotic region, the density allows us to obtain the ionization energy, I [128]:

$$\rho(\mathbf{r}) \xrightarrow[r\to\infty]{} e^{-\sqrt{2I}r} \tag{73}$$

We see that in principal, it is possible to write a hamiltonian for a given density $\rho(\mathbf{r})$, and we note that the density is itself a function of a function, or a functional. The electronic hamiltonian is now expressed as:

$$H[\rho(\mathbf{r})] = T_e[\rho(\mathbf{r})] + V_{Ne}[\rho(\mathbf{r})] + V_{ee}[\rho(\mathbf{r})] \tag{74}$$

where

$$V_{Ne}[\rho(\mathbf{r})] = \sum_{A=1}^{N} \int \frac{Z_A}{|\mathbf{R}_A - \mathbf{r}|} \rho(\mathbf{r})\, d\mathbf{r} \tag{75}$$

$$V_{ee}[\rho(\mathbf{r})] = \frac{1}{2} \iint \frac{\rho(\mathbf{r}_1)\,\rho(\mathbf{r}_2)}{|\mathbf{r}_1 - \mathbf{r}_2|} d\mathbf{r}_1\, d\mathbf{r}_2 \tag{76}$$

We note that the terms T and V depend on the density and also the spatial coordinates. The term V_{Ne} is the potential exerted between the nuclei and the electrons and it is known as the external potential, $V(\mathbf{r})$. The term V_{ee} corresponds to a classical coulombic interaction between the electrons. The kinetic energy term T_e is difficult to evaluate and for this reason, Thomas [129] and Fermi [130] first proposed to simplify the problem by studying a system which they called jellium. Jellium is simply a uniform electron gas, which consists of an infinite number of electrons that occupy an infinite space. This space is further characterized by having a uniform positive charge density. Consequently, the electronic density is then constant. By using the statistical theory of fermions, the kinetic energy of the electrons, T_e^{ug}, can then be expressed as:

$$T_e^{ug}[\rho(\mathbf{r})] = \frac{3}{10}\left(3\pi^2\right)^{\frac{2}{3}} \int \rho^{\frac{2}{3}}(\mathbf{r})\, d\mathbf{r} \tag{77}$$

It was shown that the Thomas-Fermi functional works well for atoms and metals but not for molecules, since molecules evidently do not consist of a uniform positive charge density. However, it should also be noted that the Thomas-Fermi approach lacks terms for exchange and correlation of the electrons. In 1951, Slater [131] proposed that the effects of exchange were more important than the effects of correlation and therefore, the correlation could be

neglected. The exchange term is estimated by supposing that the Fermi hole, the region about an electron into which no other can enter, could be modeled by a spherical potential whose radius depended upon the density. In this case, the exchange energy can be expressed as:

$$E_x[\rho(\mathbf{r})] = -\frac{9\alpha}{8}\left(\frac{3}{\pi}\right)^{\frac{1}{3}}\int \rho^{\frac{4}{3}}(\mathbf{r})\,d\mathbf{r} \tag{78}$$

Slater found α to be equal to 1 whereas Bloch [132] and Dirac [133] had previously obtained a value of $\alpha = \frac{2}{3}$. A generalization of the method, called Xα, exists where α is varied empirically. In addition, it should be noted that there is no known exact solution for the correlation energy of a uniform electron gas, but a solution is known for the extremes of low and high densities.

In the 1960's, DFT was further developed by Hohenberg, Kohn and Sham [134]. Principally, they proposed two theorems, the first of which was to prove that all of the properties of the ground state (non degenerate) of a molecule could be determined from the electronic density $\rho(\mathbf{r})$. By use of the *reductio ad absurdum* principal, we suppose that there exists two potentials, $V_a(\mathbf{r})$ and $V_b(\mathbf{r})$ and their corresponding hamiltonians H_a and H_b. Each hamiltonian is associated with an energy E_0 and a wavefunction Ψ_0. After application of the variation theorem, we have:

$$E_{0,a} < \langle \Psi_{0,b} | H_a | \Psi_{0,b} \rangle \tag{79}$$

$$E_{0,b} < \langle \Psi_{0,a} | H_b | \Psi_{0,a} \rangle \tag{80}$$

Following on logically, we can write:

$$E_{0,a} < \langle \Psi_{0,b} | H_a - H_b + H_b | \Psi_{0,b} \rangle \tag{81}$$

$$E_{0,a} < \langle \Psi_{0,b} | H_a - H_b | \Psi_{0,b} \rangle + \langle \Psi_{0,a} | H_b | \Psi_{0,a} \rangle \tag{82}$$

$$E_{0,a} < \langle \Psi_{0,b} | H_a - H_b | \Psi_{0,b} \rangle + E_{0,b} \tag{83}$$

We can follow the same development for $E_{0,b}$ to obtain:

$$E_{0,b} < \langle \Psi_{0,a} | H_b - H_a | \Psi_{0,a} \rangle + E_{0,a} \tag{84}$$

We can then express the external potentials as:

$$E_{0,a} < \int [V_a(\mathbf{r}) - V_b(\mathbf{r})]\,\rho(\mathbf{r})\,d\mathbf{r} + E_{0,b} \tag{85}$$

$$E_{0,b} < \int [V_b(\mathbf{r}) - V_a(\mathbf{r})]\,\rho(\mathbf{r})\,d\mathbf{r} + E_{0,a} \tag{86}$$

If we now add 85 and 86 we obtain:

$$E_{0,a} + E_{0,b} < \int [V_a(\mathbf{r}) - V_b(\mathbf{r})]\,\rho(\mathbf{r})\,d\mathbf{r} + E_{0,b} + \int [V_b(\mathbf{r}) - V_a(\mathbf{r})]\,\rho(\mathbf{r})\,d\mathbf{r} + E_{0,a}$$

$$E_{0,a}+E_{0,b} < \int [V_a(\mathbf{r}) - V_b(\mathbf{r}) + V_b(\mathbf{r}) - V_a(\mathbf{r})]\,\rho(\mathbf{r})\,d\mathbf{r} + E_{0,a} + E_{0,b}$$

$$E_{0,a} + E_{0,b} < E_{0,a} + E_{0,b} \tag{87}$$

Since the expression given in equation 87 is clearly impossible, our hypothesis that two potentials may describe the same density is false. Therefore, we can say the density of the ground state uniquely determines the external potential, the hamiltonian, and the wavefunction of the system. This applies for the first spin state and spatial symmetry of the molecule. The second theorem simply proves the density obeys the variational principal like the wavefunction. However, the theorems do not show how to obtain the energy without computing the wavefunction. A solution to this problem was first proposed in 1965 by Kohn and Sham [135]. The idea was that the problem is simple to solve if the hamiltonian corresponds to a system of non-interacting particles. In this case, the hamiltonian is a sum of mono electronic operators. As a result, one may then use a Slater determinant consisting of suitable functions. The key point is, within this fictitious system, where there are no interactions, the density is identical to a real system where the electrons do interact. In this way, we can rewrite our hamiltonian as the difference between the real system and this fictitious one:

$$H[\rho(\mathbf{r})] = T_{ni}[\rho(\mathbf{r})] + V_{Ne}[\rho(\mathbf{r})] + V_{ee}[\rho(\mathbf{r})] + \Delta T[\rho(\mathbf{r})] + \Delta V_{ee}[\rho(\mathbf{r})] \tag{88}$$

Where T_{ni} is the kinetic energy of the electrons without interaction, ΔT is the difference in the kinetic energy of the non-interacting and the real system ($\Delta T = T_e - T_{ni}$) and ΔV_{ee} contains all of the non-classical corrections to the interactions between the electrons. Within the LCAO formalism, the total energy is expressed as:

$$\begin{aligned} E[\rho(\mathbf{r})] = &\sum_{i=1}^{n} \left\langle \theta_i \left| \frac{-\Delta_i}{2} \right| \theta_i \right\rangle - \sum_{i=1}^{n} \left\langle \theta_i \left| \sum_{A=1}^{N} \frac{Z_A}{|\mathbf{R}_A - \mathbf{r}|} \right| \theta_i \right\rangle \\ &+ \sum_{i=1}^{n} \left\langle \theta_i \left| \int \frac{\rho\left(\mathbf{r}'\right)}{|\mathbf{r}_i - \mathbf{r}'|} d\mathbf{r}' \right| \theta_i \right\rangle + E_{xc}[\rho(\mathbf{r})] \end{aligned} \tag{89}$$

where the density is:

$$\rho = \sum_{i=1}^{n} \langle \theta_i | \theta_i \rangle \tag{90}$$

The terms which are most difficult to calculate, ΔT_{ee} and ΔV_{ee}, are grouped together in the exchange correlation term, E_{xc}. For most of the time, the kinetic energy term is neglected. Now we have obtained a problem which depends only on single electrons, much like the HF method, where in this case:

$$h_i^{KS}\theta_i = \varepsilon_i \theta_i \tag{91}$$

where:

$$h_i^{KS} = \frac{-\Delta_i}{2} \sum_{A=1}^{N} \frac{Z_A}{|\mathbf{R}_A - \mathbf{r}|} + \int \frac{\rho\left(\mathbf{r}'\right)}{|\mathbf{r}_i - \mathbf{r}'|} d\mathbf{r}' + V_{XC} \tag{92}$$

and

$$V_{XC} = \frac{\delta E_{XC}[\rho]}{\delta \rho(\mathbf{r})} \tag{93}$$

V_{XC} is the derivative of the exchange correlation functional. In practice the Kohn-Sham functions, θ_i, are obtained by using the LCAO approximation and use of gaussian functions. This type of calculation runs in a very similar fashion to a HF calculation but with one important difference: DFT is essentially exact in its formalism unlike HF.

In practice, however, DFT is not exact as the exact form of the exchange correlation functional is not known. As a result, it is necessary to approximate it. Consequently, there are a large variety of density functionals which all treat the exchange correlation term differently. It should be noted that this fact is something which, as is highlighted in a recent review by Burke [136], developers love and users hate. From a development perspective, it means one can simply continue to make new functionals and write about how they perform better than others on given test sets. However, from a users perspective, this generates the problem that it is not possible to know *a priori* how well a given functional will work for your problem.

It should also be noted that DFT is only strictly variational when the exact E_{XC} functional is used. As such, all practical implementations of DFT are non variational, but they are however size consistent and size extensive. Another key benefit of DFT is the fact it is able to capture some of the correlation energy for the same cost as a HF calculation. For this reason, it is often the only real choice one has for systems with a reasonable number of electrons and low spatial symmetry, and certainly it is the only method, aside from HF, which is available for problems involving the solid state.

As discussed, there are several ways the exchange correlation term is handled and the exact contributions from the density used in each of the various approaches is summarized in table 7. It should be noted that hybrid DFT requires only the inclusion of some of the density terms and a contribution from HF exchange and not necessarily all of the contributions from the density listed. Equation 94 show the contributions in the very popular B3LYP [137] hybrid functional. The coefficients a_0, a_x, and a_c are parameters which have been fitted to the experimental dissociation energies of various molecules. They are equal to 0.20, 0.72, and 0.81 respectively. E_x^{LSDA} is the contribution from the LSDA exchange functional (the spin adapted version of LDA), E_x^{HF} is the contribution from the HF exchange, and E_x^{B88} is the contribution from the B88 exchange functional. Finally, E_c^{VWN}, and E_c^{LYP} are the contributions from the VWN and LYP correlation functionals:

$$E_x^{B3LYP} = (1 - a_0 - a_x) E_x^{LSDA} + a_0 E_x^{HF} + a_x E_x^{B88} + (1 - a_c) E_c^{VWN} + a_c E_c^{LYP} \tag{94}$$

In addition some functionals include an empirical correction for long range effects [138–142]. This is done by adding a correction to the energy of the form:

$$E_{disp} = -s_6 \sum_{i=1}^{N-1} \sum_{j=i+1}^{N} \frac{C_6^{ij}}{R_{ij}^6} f_{dmp}(R_{ij}) \tag{95}$$

Where, s_6 is a global scaling factor, N is the number of atoms in the system being studied, C_6^{ij} is the dispersion coefficient for the atom pair ij, and R_{ij} is the interatomic distance between atoms i and j. f_{dmp} is a damping function, which depends upon the van der Waals radii of the atoms.

Table 7: Classification of some density functionals based upon the properties of the density used within their parameterisation.

Contributions of $\rho(\mathbf{r})$ included in V_{XC}	Classification	Example functional
$\rho(\mathbf{r})$	Local Density Approximation (LDA)	SVWN
$\nabla\rho(\mathbf{r})$	Generalised Gradient Approximation (GGA)	BLYP, B97D
$\nabla^2\rho(\mathbf{r})$	meta-GGA	M06, M05
HF exchange, $\nabla\rho(\mathbf{r})$, $\rho(\mathbf{r})$, $\nabla^2\rho(\mathbf{r})$	Hybrid	B3LYP, M06-L, M06-2X, BHLYP

2.1.5 *Composite methods*

Finally, there exists a set of methods where the geometry and frequencies are computed at a relativly low level and then the energy is corrected using higher levels. One example of such a method that we have used is the Gaussian 4 or G4 theory [143]. Here the geometry is optimised at the $B3LYP/6-31G(2df,p)$ level and the frequencies are also computed at this level. The frequencies and zero point energy are then scaled using an empirical factor of 0.9854.

The energy of the structure is then computed at the HF level, $\Delta E(HF)$, with two modified dunning basis sets prior to extrapolation to the CBS limit using the extrpolation formula:

$$E_{HF/aug-cc-pVnZ} = E_{HF/limit} + Bexp^{-\alpha n} \tag{96}$$

Here n is either the quadruple or pentuple zeta basis set, α is taken as 1.63. Following the extrapolation a series of single point enrgies are performed to assess both basis set and correlation effects. These tests include tests for polarisation, $\Delta E(2df,p)$, and diffuse functions, $\Delta E(+)$, computed at the MP4 level, and a test for the use of larger basis sets, $\Delta E(Large)$ computed at the MP2 level. Finally, the test for correllation beyond MP4 is included by a single point calculation at the CCSD(T) level. All of these energies are then combined in the following way:

$$E(combined) = E[CCSD(T)/6-31G(d)] + \Delta E(+) + \Delta E(2df,p) + \Delta E(Large) + \Delta E(HF) \tag{97}$$

A second empirical correction is made known as the HLC correction. This correction has a dependence on the number of α and β electrons within the system of study. It is computed using the following formula for neutral molecules.

For closed shell species

$$-An_\beta \tag{98}$$

where A has the value of 6.947 mhartree and n_β is the number of β electrons.
For open shelled systems

$$-A'n_\beta - B\left(n_\alpha - n_\beta\right) \tag{99}$$

where A′ has the value 7.128 mhartree, B has the value 2.441 mhartree, and n_α is the number of α electrons assuming that $n_\alpha > n_\beta$.

There are additional parameters for atoms and ions. The G4 electronic energy is then computed as:

$$E_e(G4) = E(combined) + E(HLC) \tag{100}$$

The 0 K enthalpy, also called the G4 energy, is then the sum of $E_e(G4)$ and the zero point energy.

2.2 SOFTWARE USED FOR THE WFT AND DFT COMPUTATIONS

Throughout this work the Gaussian [144, 145], Gamess [146, 147], Molpro [148], and Turbomole [149] software packages have been used to perform the QC calculations. Table 8 shows the type of calculations which were performed with each software.

The choice of the software was based upon both the type of calculation required and the methods available within each package. This meant that all DFT computations were performed with Gaussian, because it offers the largest choice of functionals and the ability to compute gradients and hessians analytically. This improves the efficiency of optimisation and frequency calculations.

For the cluster calculations at the MP2 level, Turbomole was used as its implementation of the RI [150] approximation makes it considerably more efficient than any of the other software packages at this level. However, due to its limited transition state searching options and its inability to compute IRCs, Gaussian had to be used to compute them at the MP2 level, in spite of the increased computational cost.

In order to carry out computations at the MRCI+Q level, at present one has no choice but to use Molpro. Whilst Molpro does compute minimum energy pathways (MEPs) these are not equivalent to IRCs as outlined in section 2.1.2. As such IRCs using multi-reference methods had to be obtained at the CASSCF/MRMP2 level with GAMESS.

In addition for the H_3CO, CH_2OH, and CH_3OH systems, it was necessary to switch to the use of RS2 as the computational cost of the MRCI+Q was too considerable. This increased cost arises for these systems due to the larger number of electrons and low symmetry of the systems.

2.3 ATOMS IN MOLECULES (AIM) ANALYSIS

So far we have discussed the idea that the SE may be partitioned into its nuclear and electronic components using the BO approximation. However, this does not provide a simple way to interpret the interactions which exist between the nuclei apart from their distance from one another. With this in mind, Richard Bader proposed that if instead of viewing just the wavefunction, one visualises the electronic density, $\rho(\mathbf{r})$.

$$\rho(\mathbf{r}) = \langle \Psi | \hat{\rho}(\mathbf{r}) | \Psi \rangle \tag{101}$$

Table 8: The software used throughout this work and what it has been used for. [a]MRMP covers the algorithm specific adaptations of CASPT2 for GAMESS and Molpro which are MRMP2 and RS2 respectivly.

Calculation Type	Gaussian [144, 145]	Gamess [146, 147]	Molpro [148]	Turbomole [149]
Optimisation (minima)	✓	✓	✓	✓
Optimisation (TS)	✓	✓	✓	...
Frequency	✓	✓	✓	✓
IRC	✓	✓	...	...
DFT	✓	...	...	...
MP2	✓	...	...	✓
CC	✓	...	✓	...
CASSCF	...	✓	✓	...
MRMP[a]	...	✓	✓	...
MRCI+Q	...	...	✓	...

One may map onto it the atomic densities of each nuclei within a molecule. In this way, any differences between the molecular and atomic densities arise due to the interactions between the atoms. In conducting this type of analysis, several key points arise which have special characteristics that can be directly linked back to atoms.

The first of these points is a density maxima in all 3 dimensions. It was observed that these points are typically found close to the nucleus. This is not surprising, since if one considers the electronic distribution as a function of the distance from the nucleus, one finds it is maximal at the nucleus and decays exponentially as you move away. These points have subsequently become known as nuclear critical points (NCP) for this reason.

The second type of point exists between pairs of critical points and it is in fact a maxima in all dimensions apart from the one in which the two nuclei sit, where it is a minimum. These points are more commonly known as bond critical points (BCP) as they are indicative of the interaction between two bound nuclei. For covalenty bound systems, this can be visualised as the build up of electronic density between two atoms being brought together, shown pictorially for a simple homonuclear diatomic molecule in figure 9.

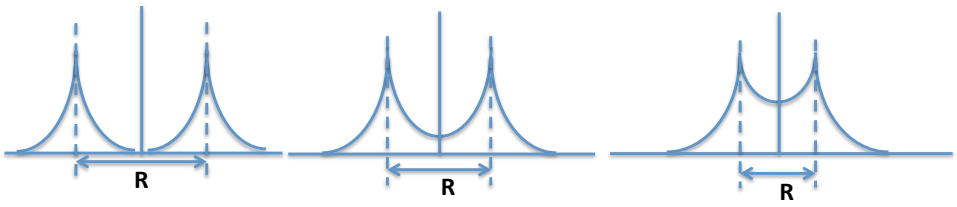

Figure 9: Schematic view of the change in the electronic density as a function of the interatomic distance, **R**, as two atoms are brought together

There are two other types of critical points within the electronic density. Though these points are only found where the nuclei exist in certain geometrical arrangements. The first of these is the ring critical point (RCP), which exists where the nuclei enclose an area of space and all nuclei have bond critical points between pairs. The final type of critical point is the

cage critical point (CCP), which exists where the nuclei enclose a volume of space such that each face contains a ring critical point.

Another useful property obtained from this analysis is a qualitative picture of the type of bonding between two nuclei. This is obtained using the density, $\rho(\mathbf{r})$ and the laplacian of the density, $\nabla^2\rho(\mathbf{r})$. At the bond critical point, a general picture can be obtained from table 9.

Whilst we are able to identify the type of interaction, we can not explicitly distinguish between single, double, and triple covalent bonds since it is not possible to attribute a specific value of $\rho(\mathbf{r})$ to a particular degree of bonding.

Table 9: Qualitative relation between $\rho(\mathbf{r})$, $\nabla^2\rho(\mathbf{r})$, and the type of bonding interaction between nuclei

$\rho(\mathbf{r})$	$\nabla^2\rho(\mathbf{r})$	Type of bonding
$0 < \rho(\mathbf{r}) \leqslant 1$	$\leqslant 0$	Covalent
≈ 0	$\geqslant 0$	Ionic
$0 \lesssim \rho(\mathbf{r}) \ll 1$	$\geqslant 0$	Hydrogen bonding

The AIM analysis throughout this work has been conducted using the AIM2000 package [151–153].

2.4 TUNNELING

Another property exhibited by the consideration of wavefunctions, is that, within the formulation of quantum mechanics, particles may enter classically forbidden regions. This property allows reactions with activation energies greater than the thermal energy to proceed.

This occurs as a result of the wave formulation within quantum mechanics. As one approaches a finite barrier, the probability of the density does not decay to zero. Consequently, there is a finite probability that a particle with energy less than the barrier height may be transmitted through it. This phenomenon known as tunnelling is both strange and important. It is strange because it presents the idea that somehow particles, be that electrons, protons, H atoms or small molecules can behave like moles and burrow through a barrier by somehow "borrowing" energy. Nevertheless, as strange as it may seem, it does happen and here we shall discuss some of the basic concepts using the simplest example possible, the 1D square barrier. Then we shall develop the more rigorous treatments used throughout this work to calculate the probabilities for H atoms to be transmitted through the barriers we compute.

2.4.1 *Square Barrier*

The discussion here is for illustrative purposes and consequently will be somewhat limited. The reader is therefore directed to read more in depth texts on Quantum Mechanics such as the book by Messiah [154]. Let us commence our discussion by considering the potential shown in figure 10 where we have partitioned the potential into 3 regions: Region I $-\infty \leqslant x \leqslant 0$ where the potential $U_{(x)} = 0$, Region II, $0 \leqslant x \leqslant L$, where $U_{(x)} = U$, and Region III $L \leqslant x \leqslant +\infty$ where $U_{(x)} = 0$.

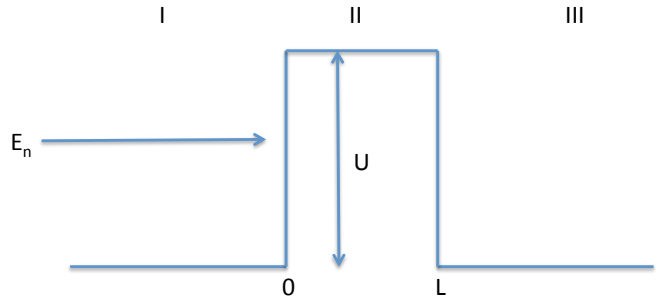

Figure 10: Ilustration of a model square barrier

Considering a particle with a mass of μ and Energy E approaching the barrier through region I we obtain a wavefunction, $\Phi(x)$, for the particle in region I of the form:

$$\Phi(x) = Ae^{ikx} + Be^{-ikx} \tag{102}$$

where

$$k = \frac{\sqrt{2\mu E}}{\hbar} \tag{103}$$

In this case Ae^{ikx} corresponds to the wave propagating towards the barrier and Be^{-ikx} corresponds to the reflected wave. Using this definition, we can define the reflection probability as:

$$R(E) = \frac{|\Phi_{reflected}|^2}{|\Phi_{incident}|^2} = \frac{|B|^2}{|A|^2} \tag{104}$$

If we now consider the wavefunction in region III, but only consider particles moving away from the barrier, then we obtain $\Phi(x)$ to be:

$$\Phi(x) = Ge^{ikx} \tag{105}$$

As such we have a transmission coefficient T of the form:

$$T(E) = \frac{|\Phi_{transmitted}|^2}{|\Phi_{incident}|^2} = \frac{|G|^2}{|A|^2} \tag{106}$$

such that $T + R = 1$, due to the energy conservation principle.
Now if we consider motion in the classically forbidden region II, the SE is:

$$\frac{\hbar^2}{2\mu}\frac{\partial^2}{\partial x^2}\Phi(x) = (E - U)\,\Phi(x) \tag{107}$$

This gives us a solution for $\Phi(x)$ of

$$\Phi(x) = Ce^{-\eta x} + De^{\eta x} \tag{108}$$

where

$$\eta = \frac{\sqrt{2\mu(U - E)}}{\hbar} \tag{109}$$

In order to solve this problem we must impose two boundary conditions these are:

1. $\Phi(x)$ must be a continuous function in the range $-\infty \leqslant x \leqslant +\infty$
2. the first derivative of $\Phi(x)$ must be continuous in the range $-\infty \leqslant x \leqslant +\infty$

By enforcing these conditions at $x = 0$ we obtain:

$$Ae^{ikx} + Be^{-ikx} = Ce^{-\eta x} + De^{\eta x} \tag{110}$$

$$A + B = C + D \tag{111}$$

and

$$ikAe^{ikx} - ikBe^{-ikx} = \eta De^{\eta x} - \eta Ce^{-\eta x} \tag{112}$$

$$ikA - ikB = \eta D - \eta C \tag{113}$$

now by doing the same at $x = L$, we obtain:

$$Ce^{-\eta L} + De^{\eta L} = Ge^{ikL} \tag{114}$$

and

$$-\eta Ce^{-\eta L} + \eta De^{\eta L} = ikGe^{ikL} \tag{115}$$

by manipulation of these 4 equations, we obtain the transmission coeffcient T to be:

$$T(E) = \left[1 + \frac{1}{4}\frac{U^2}{E(U-E)}\sinh^2(\eta L)\right]^{-1} \tag{116}$$

Thus, as can be seen by equation 116 the final transmission probability depends upon: the barrier height, U, the reduced mass of the particle, μ, the energy of the approaching particle, E, and the barrier width, L. Whilst this simple 1D square barrier serves to both illustrate and introduce the phenomenon, it is not accurrate enough for the computation of rate constants. For this reason we have employed the Eckart [155], and the Wentzel-Kramer-Brillouin (WKB) [156, 157] methods, to obtain more acurate transmission probabilities. These methods are outlined in the following sections.

2.4.2 *Eckart model*

The Eckart model involves fitting the stationary points of the reaction to an analytical potential of the form:

$$U(x) = \frac{A\exp[(x-x_0)/l]}{1+\exp[(x-x_0)/l]} + \frac{B\exp[(x-x_0)/l]}{1+\exp[(x-x_0)/l]^2} \tag{117}$$

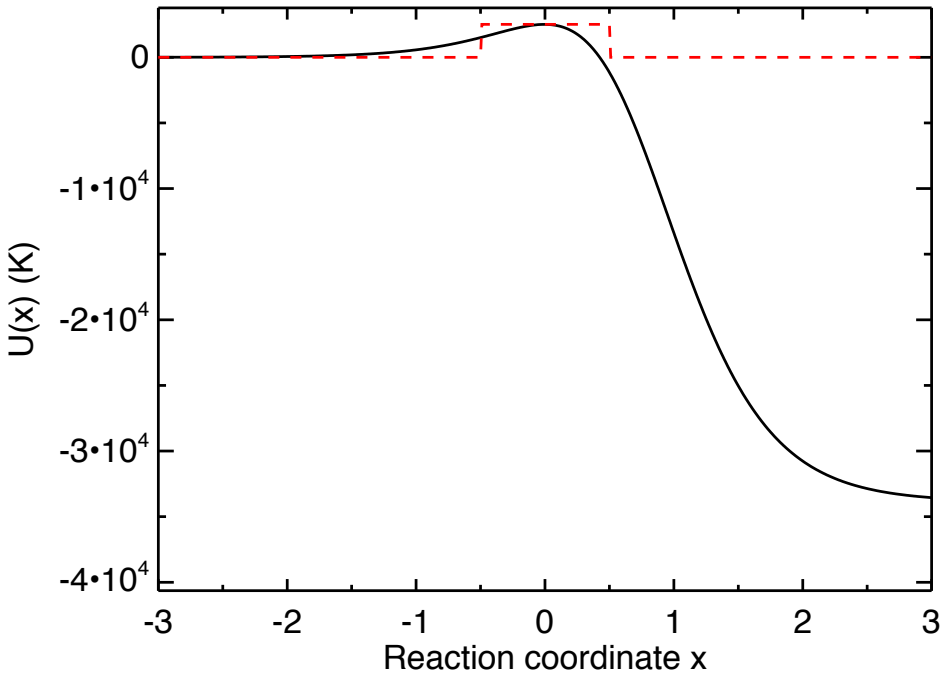

Figure 11: Illustration of the difference between the square barrier (red dashed line) as previously employed and an asymmetric Eckart potential (solid black line). Figure taken from ref. [226]

with parameters of the form:

$$A = V_f - V_r \tag{118}$$

$$B = \left(\sqrt{V_f} + \sqrt{V_r}\right)^2 \tag{119}$$

$$l = \frac{1}{\nu^*}\sqrt{\frac{2}{\mu}}\left(\frac{1}{\sqrt{V_f}} + \frac{1}{\sqrt{V_r}}\right)^{-1} \tag{120}$$

Here, V_f and V_r correspond to the forward and reverse activation energies respectively, μ is the reduced mass corresponding to the motion of the transferring atom in the frequency ν^*, which is given by the absolute value of the imaginary mode of the TS. Whilst l is dependent on the barrier heights, mass, and frequency terms, it represents the width of the barrier. Figure 11 shows how the Eckart potential differs from the square barrier where the forward barrier heights are the same.

From this, it is possible to calculate the tunnelling probability $P(E_n)$, of a particle with energy E_n from:

$$P(E_n) = \frac{\cosh(\alpha+\beta) - \cosh(\alpha-\beta)}{\cosh(\alpha+\beta) + \cosh\delta} \tag{121}$$

where

$$\alpha = \frac{4\pi}{h\nu^*}\sqrt{E_n}\left(\frac{1}{\sqrt{V_f}}+\frac{1}{\sqrt{V_r}}\right)^{-1} \tag{122}$$

$$\beta = \frac{4\pi}{h\nu^*}\sqrt{E_n - V_f + V_r}\left(\frac{1}{\sqrt{V_f}}+\frac{1}{\sqrt{V_r}}\right)^{-1} \tag{123}$$

$$\delta = 4\pi\sqrt{\frac{V_f V_r}{(h\nu^*)^2}-\frac{1}{16}} \tag{124}$$

E_n is the vibrational energy of the harmonic oscillator, $E_n = h\nu_0(n+1/2)$, with ν_0 the harmonic frequency corresponding to motion along the reaction pathway within the reactant complex.

2.4.3 *Wentzel-Kramer-Brillouin (WKB) method*

The WKB method on the other hand requires computing the action integral θ over the full intrinsic reaction coordinates (IRC) [72] curve. This action integral θ takes the form:

$$\theta(E_n) = \frac{\sqrt{2}}{\hbar}\int_{s_1}^{s_2}\sqrt{\mu(U(s)-E_n)}\ ds \tag{125}$$

Formally ds has units of length only, but more typically when conducting an IRC calculation ds will have units of bohr $amu^{\frac{1}{2}}$. In this case, the integral is modified to:

$$\theta(E_n) = \frac{\sqrt{2}}{\hbar}\int_{s_1^*}^{s_2^*}\sqrt{(U(s^*)-E_n)}\quad ds^* \tag{126}$$

$$P(E_n) = e^{-2\theta(E_n)} \tag{127}$$

As with the Eckart model, E_n corresponds to the energy levels of the harmonic oscillator with frequency ν_0. In addition, it should be noted that $P(E_n)$ is equivalent to $T(E)$.

These methods have been employed throughout for the computation of rate constants. In the following section, we shall deal with the treatment used to compute first order rate constants from these probabilities.

2.4.4 *Converting transmission probabilities to rate constants*

In the simplest treatment, we can consider that the rate constant may be determined by multiplying the transmission/tunnelling probability by a physical quantity which has the correct units for the rate constant and corresponds to some physical process which would lead to reaction.

With this in mind, throughout this work, the first order rate constants have been computed by considering this quantity to be the vibrational mode, ν_0, which corresponds to motion towards the barrier. The reason for this choice is that by definition, it has units of s^{-1}. Using this hypothesis, the tunnelling rate $k(E_n)$ is then given by:

$$k(E_n) = \nu_0 P(E_n) \tag{128}$$

these $k(E)$ values are then summed over a Boltzmann population distribution to compute $\kappa(T)$:

$$\kappa(T) = \frac{\sum_{n=0}^{\infty} k(E_n) e^{\gamma}}{\sum_{n=0}^{\infty} e^{\gamma}} \tag{129}$$

where

$$\gamma = \frac{-nh\nu_0}{k_b T} \tag{130}$$

Our discussion now moves to the realms of thermochemistry. Here will shall discuss the role entropy may play in our reactive processes in order to determine the free energies.

2.5 THERMOCHEMISTRY

Within this section, we shall discuss the quantities needed to make a thermochemical correction to the energies. For a more detailed derivation of some of these quantities, the reader is directed to the book by McQuarrie and Simon [158].

Within the realms of thermochemistry, one is primarily interested in assessing the quantities of enthalpy, H, and entropy, S, and how they summarily affect a reactive process. These quantities are usually analysed together by consideration of the Gibbs free energy, G, which relates the two quantities by:

$$G = H - TS \tag{131}$$

Since it is not possible to experimentally determine S, one normally considers changes in free energy. As such, one considers the free energy change of activation, $\Delta G^{\ddagger}$, which looks at the difference in free energies of the TS and the reactants, and the free energy of reaction, ΔG_r, which considers the change in free energy between the products and reactants. They are typically evaluated for a given temperature and pressure. The quantities, $\Delta^{\ddagger} G^{\theta}$ and $\Delta_r G^{\theta}$, are the free energy of activation and reaction under so called standard conditions. Standard conditions are defined as a temperature of 298.15 K and a pressure of 1 atmosphere for gas phase processes. However, as we saw in Chapter 1, the conditions we will be dealing with are quite far from the standard ones.

Therefore, one might think, not unreasonably, that the corrections at such low temperatures will be small. This will of course be true for entropic contributions which depend on temperature alone, and indeed the thermal correction to the energy will be small. However, we must consider the contributions to the entropy from all molecular motions. As such, we shall now look at the dependence of the partition functions for translation, rotation, vibration and electronic motion on temperature and pressure.

We commence by considering the translational partition function, q_T:

$$q_T = \left(\frac{2\pi m k_B T}{h^2}\right)^{\frac{3}{2}} \frac{k_b T}{P} \tag{132}$$

here m is the total mass of the system, k_B is the Boltzmann constant, T is the ambient temperature, and P is the external pressure. We see here that q_T is inversely proportional to the pressure. We can therefore conclude that under interstellar conditions, it will be large. As such, any process where translational motion changes during the reaction process will have a significant change in entropy. If we now consider the rotational partition function for an asymmetric top in the so called high temperature limit[2], q_r is approximated by (if $T >> \Theta_r$) as:

$$q_r = \frac{\pi^{\frac{1}{2}}}{\sigma_r}\left(\frac{T^{\frac{3}{2}}}{\Theta_{r,x}\Theta_{r,y}\Theta_{r,z}}\right) \tag{133}$$

Where σ_r is the symmetry number of the species and is related to its point group[3], $\Theta_{r,x}\Theta_{r,y}\Theta_{r,z}$ are the rotational temperatures for rotations about the respective axis. We note that the rotational partition function depends only upon temperature and so will be small. However, it must be stated that under interstellar conditions, out temperature will not be much greater than the rotational temperature and as such, we probably overestimate this quantity.

If we now consider contributions from vibrational motion, the partition function q_v is defined as:

$$q_v = \prod_K \frac{e^{\frac{-\Theta_{vK}}{2T}}}{1 - e^{\frac{-\Theta_{vK}}{T}}} \tag{134}$$

Here, the quantity Θ_{vK} is the vibrational temperature for a given mode K. As with the rotational partition function, it depends on the temperature alone and its contribution would be small, except for process which involve a vibrational excitation.

Finally, we come to the contributions from electronic motions. The electronic partition function q_e is defined as:

$$q_e = g_0 e^{\frac{\varepsilon_0}{k_B T}} + g_1 e^{\frac{\varepsilon_1}{k_B T}} + \ldots \tag{135}$$

Here the g_n quantities are the degeneracy of the state n, with $n = 0$ being defined as the ground state and $n = 1$ the first excited state and so on. The ε_n quantities are the energies of the various electronic states. It is conventional to define ε_0 to be energy zero. In this way all the other ε_n quantities become the energy difference between state n and the ground state. As such, we note that under the conditions we will be considering, and indeed almost all conditions, ε_1 is much larger than $k_B T$ and as such q_e is truncated to the first term only, and since ε_0 is set to zero, q_e is now:

$$q_e = g_0 \tag{136}$$

We note therefore that q_e has no dependence on pressure or temperature under these conditions, and as such, unless the degeneracy of the ground state changes in the reaction process, there will be no contribution to the entropy from electronic motion.

We therefore conclude that the largest contribution to the entropy under interstellar conditions will be from translational motion. This may be accompanied by small contributions from rotation and vibration, but we suspect that there will be no contribution from electronic motion.

2 The high temperature limit is defined such that $T \gg \Theta_r$

3 For the C_1, C_s, $C_{\infty V}$ groups σ_r is equal to 1 and for the C_{2V} group it is equal to 2

Having outlined the theoretical approaches considered throughout this work, the following chapters will discuss the results obtained by application of these methods.

Chapter III

REACTION OF HYDROGEN ATOMS WITH CO IN THE GAS PHASE

3

REACTION OF HYDROGEN ATOMS WITH CO IN THE GAS PHASE

3.1 INTRODUCTION

The addition of H to CO can be considered to form one of two possible products, HCO or COH. Since this reaction may afford either product, this provides an additional reaction which is the interconversion of COH to HCO. With this in mind, we will now look in more detail at the formation of both isomers and their interconversion.

The formation of HCO has been studied previously by many people. Table 10 lists values for the activation energy with and without the inclusion of zero point energy obtained in previous studies. We note, that other than the DFT results of Jursic [159], all of the other methods predict a barrier height which is at least 1.5 kcal.mol^{-1} higher than the experimental value of Wang et al [57]. In contrast the DFT results are below the experimental value of 2.0 ± 0.4 kcal.mol^{-1} by at least 1.0 kcal.mol^{-1}.

However, more recent experimental works [58, 59, 160] have called into question the value obtained by Wang et al. Indeed, in the newer results, all of the available data has been fitted and with inclusion of the experimental error the experimental range is from 2 to 6 kcal.mol^{-1}.

Table 10: Activation Energies E_A with and without ZPE for the formation of HCO. Energies are given in kcal mol^{-1}

Method	Basis set	E_a	E_a + ZPE	Ref.
MRCI+Q	aug-cc-pVTZ	3.50	3.93	This work
MP2	cc-pVTZ	4.76	5.27	[52]
RCCSD	cc-pVTZ	4.76	5.29	[52]
RCCSD(T)	cc-pVTZ	4.22	4.73	[52]
RCCSD(T)	aug-cc-pVTZ	3.71	4.22	[52]
MRCI	cc-pVTZ	4.89	5.40	[52]
MRCI+Q	cc-pVTZ	4.01	4.49	[52]
B3LYP	6-311G**	0.6	1.0	[159]
B3LYP	6-311++G**	0.1	1.1	[159]
MRCI+Q	cc-pVQZ	3.9	-	[53, 55]
MRCI+Q	cc-pVQZ	3.46	-	[161]
CISD	cc-pVDZ	3.64	3.9	[162]

In addition to the activation barrier in the formation of HCO, two recent studies [53, 163] have suggested that there is a Van der Waals complex prior to the TS. This complex is reported to have a stability of around 0.01 kcal.mol^{-1}, a CH bond length between 3.6 and 3.8 Å, and a HĈO angle of 72°. Owing to the discrepancy in the estimated CH bond length we shall also try to find this VDW complex.

3.2 COMPUTATIONAL METHODS

Most of the calculations were performed using the MOLPRO programme [148]. Dunning's correlation consistent basis sets, with (aug-cc-pVXZ) and without (cc-pVXZ) diffuse functions have been employed [79, 80, 164], with X=D, T, Q, 5, and 6, and using spherical contractions. Complete active space self-consistent field (CASSCF) [109–114] calculations, using a full valence space, were performed. The resulting CAS wavefunction served as the reference for an internally contracted multi-reference configuration interaction calculation (MRCI) [121, 122] calculation. In contrast to Woon's work [52], the oxygen 2s orbital was included in the MRCI calculation. Finally. Davidson's correction [165] (MRCI+Q) was included. The geometries of the minima and saddle points were optimized at the MRCI+Q level, using the Gaussian convergence criteria. In order to spare computational time, due to the fact that MOLPRO does not use symmetry during numerical evaluation of the hessian, vibrational frequencies of the stationary points were obtained by calculating the energy on a grid of 36 points, centred at the equilibrium geometry and using 0.05 Å and 5° steps. Harmonic vibrational frequencies were obtained by fitting the resulting energies. For minima, anharmonic contributions were also obtained, by fitting the grid points with fourth-order polynomials and third-degree cross terms. This was done with the SURFIT program [166]. No appreciable difference was observed between the minimum geometries obtained with MOLPRO and SURFIT. The (unscaled) frequencies and zero-point energies (ZPE) were evaluated using the masses: $m_C = 12.0$, $m_O = 15.994915$, $m_H = 1.007825$, and $mD = 2.014102$ amu.

In order to test core-valence correlation effects, additional calculations were conducted using the cc-pCVXZ family of basis sets [167, 168], up to X=5. The computational methodology was similar to that described in the previous paragraph, except that the core 1s orbitals of carbon and oxygen atoms were included in the CASSCF active space. These two orbitals were also allowed to be excited in the subsequent MRCI+Q calculation. In order to include a relatavistic correction the recontracted Dunning basis sets were used [169] in conjuction with the DKH 2 algoritm in Molpro [170, 171]. For isolated hydrogen atom, the energy was calculated at the ROHF level for each basis set. For CO, the ground state potential energy curve was calculated using a grid of 48 points which was then fitted with a 47 degree polynomial.

With a full set of basis sets results, it is natural to perform a Complete Basis Set (CBS) extrapolation. In the present work, the final MRCI+Q energy was extrapolated using the double exponential formula of Peterson [172]:

$$E_n = E_{CBS} + A\exp^{-(n-1)} + B\exp^{-(n-1)^2} \tag{137}$$

In addition to the *ab initio* computations a DFT benchmark was carried out. This was carried out by using the aug-cc-pVTZ basis set in conjunction with the B3LYP [137], B971 [173], KMLYP [174], PBEPBE1 [175], BHLYP [176], KMLYP-mod [177], TPSSH6 [178], and B97D [142] functionals. The KMLYP-mod differs from the KMLYP functional in that the contribution to correlation from the VWN functional is reduced.

Since previous works [53] have indicated that there is a van der Waals complex present prior to the TS, we have performed a relaxed scan of the CH bond length from 0.8 to 4.4 Å at the MRCI+Q/aug-cc-pVQZ level. In addition a relaxed scan was performed scanning both the $H\hat{C}O$ bond angle from 80° to 110°, whilst scanning the CH bond length between 3.0 and 4.4 Å.

In order to compare the formation and interconversion of COH and HCO all geometries were computed and optimised at the MRCI+Q/aug-cc-pVTZ level. For consistency the thermochemical analysis was also performed at this level.

For the computation of rate constants, an IRC was required for the COH to HCO isomerisation. Due to the fact that Molpro does not compute IRCs, it was necessary to compute this at the MRMP2/aug-cc-pVTZ level with GAMESS [125, 146, 147]. Within GAMESS the fourth order Runge-Kutta algorithm was used to obtain the IRC.

For all calculations we have only considered the lowest doublet electronic state, since previous computations have shown that the doublet-quartet gap is greater than 130 kcal.mol^{-1} [179–181].

3.3 THE GLOBAL PICTURE: FORMATION AND ISOMERISATION OF COH AND HCO

The HCO formation route is characterized by a saddle point having an activation energy of 3.50 kcal.mol^{-1} without ZPE correction and 3.93 kcal.mol^{-1} with ZPE included, figure 12. Whilst this barrier is lower than that found by many of the previous studies, table 10, it is still considerably higher than the gas phase experimental result of Wang et al [57] which predicts a barrier of at most 2.0 ± 0.4 kcal.mol^{-1} [57].

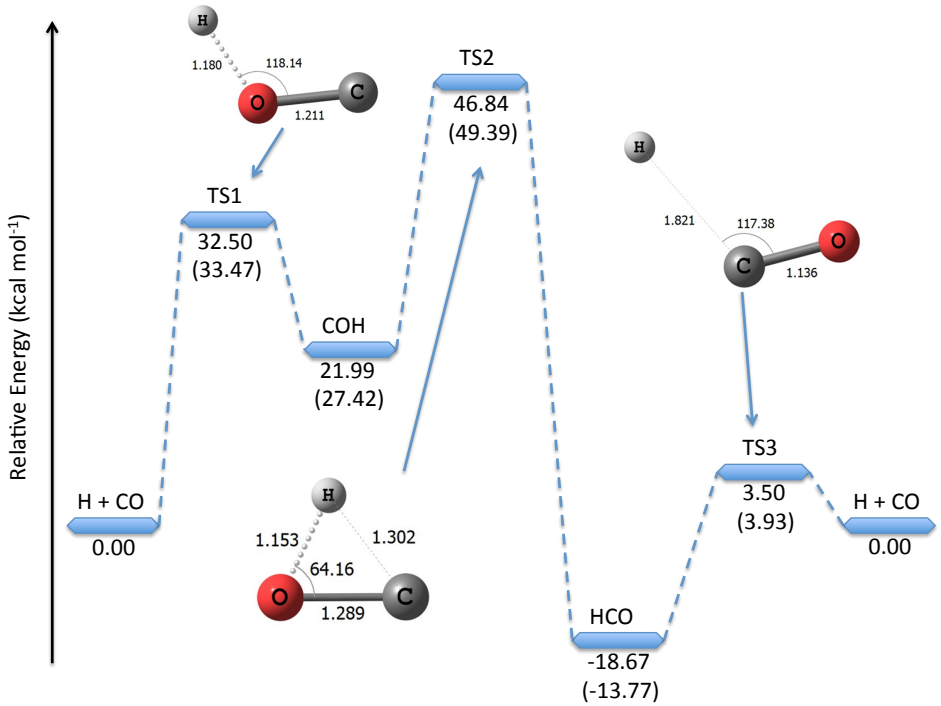

Figure 12: Stationary point analysis for the reaction of H with CO. Energies are given relative to the dissociated fragments at infinite separation and were computed at the MRCI+Q/aug-cc-pvtz level. Geometries shown are for the transition states where distances are given in angstroms and angles in degrees.

If we now consider figure 12, we see that the formation of COH shows two features which allow us to immediately rule out this route. Firstly the barrier height is almost 10 times larger than that of the formation of HCO. Secondly, the reaction is endothermic by more than 20 kcal.mol^{-1}. We can therefore reasonably assume that at temperatures between 10 and 20 K

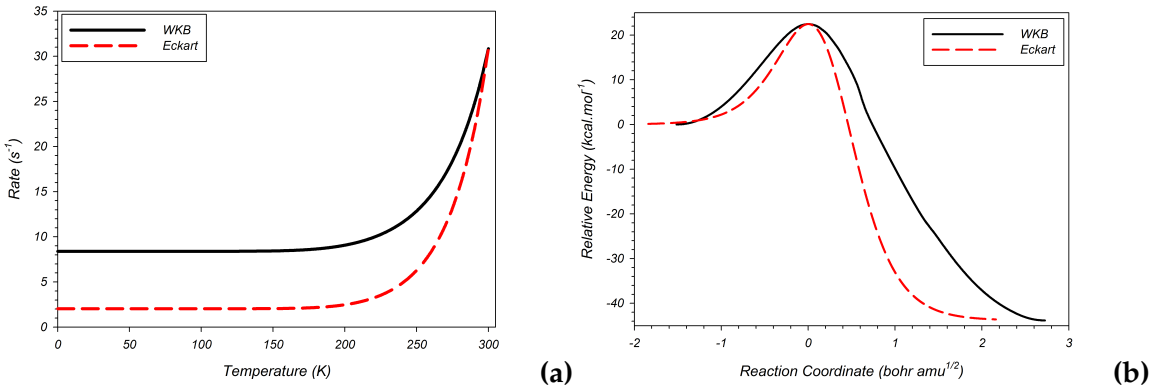

Figure 13: (a)Rate constants as a function of temperature for the COH to HCO isomerisation.(b) MRMP2 IRC and Eckart potential for the COH to HCO isomerisation.

it will not be formed. However, for completeness we have also calculated the isomerisation TS for the conversion of COH to HCO. We note, with reference to figure 12, that the barrier is in excess of 20 kcal.mol^{-1} and the process is exothermic by more than 40 kcal.mol^{-1}. This interconversion is thus of little importance in the gas phase, due to the fact we are not likely to form COH. With this in mind, we now proceed to benchmark the formation of HCO in the gas phase in order to rationalise the discrepancy between the experiments of Wang et al [57] and the theoretical calculations.

3.3.1 *Tunnelling rates for the isomerisation*

Whilst the isomerisation of COH to HCO may be of little consequence in the gas phase, figure 13 shows the rate constants obtained with the tunnelling methods discused in Chapter 2 along with the Eckart potential and the IRC used by the WKB method.

From the global picture we see that the most likely product of the reaction of hydrogen atoms with CO in the gas phase is HCO. However, the barrier height is still considerably above the experimental value. As such we now proceed with the results for the *ab initio* benchmark.

3.4 HCO BENCHMARK

3.4.1 *Geometries*

We shall commence this analysis by considering the basis set effects upon the geometry of HCO, table 11 and figures 14 to 16. Firstly, when considering the effect of diffuse functions, we see that for all of the basis sets, except the DZ, there is no significant change in the geometry by adding these functions. This is not surprising since they are designed to add gaussian functions which have a small exponent to better describe long range interactions. Since in the minimum all of the distances are relatively short, these functions provide no extra benefit to the geometrical parameters over the valence basis sets. A possible reason for the significant change in the geometry with the DZ basis sets is that the cc-pVDZ basis set is too small to correctly describe the MOs, which leads to bond lengths that are too short.

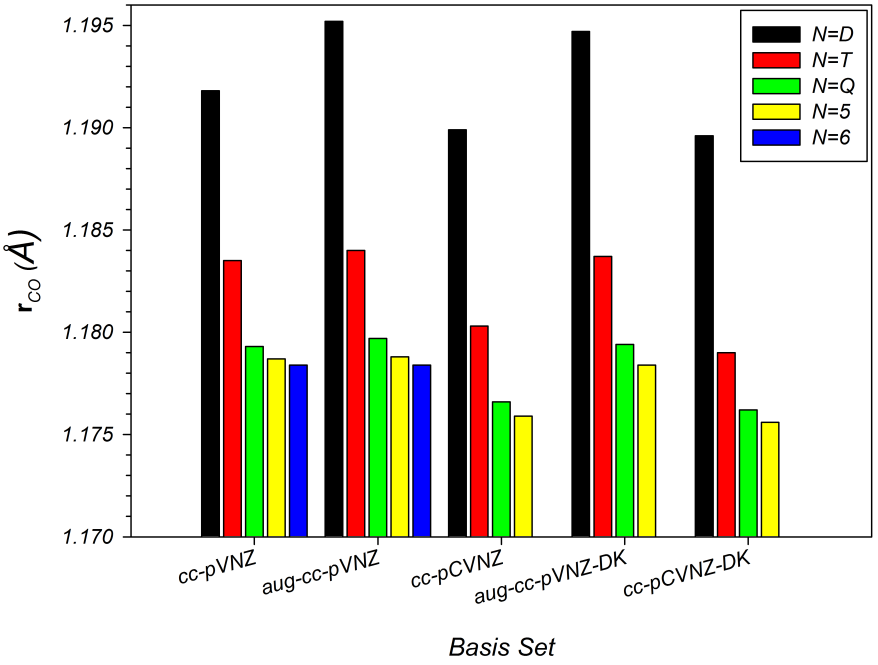

Figure 14: Chart showing the variation in the CO bond length within HCO with respect to the basis set.

In contrast, the inclusion of the functions necessary to consider core valence effects show a greater change. We see in all cases a shortening of the bond lengths and an increase in the HĈO angle. The shorter bond lengths are likely due to an increase in the binding energy as a consequence of the additional correlation. The shorter bond lengths require the increased bond angle to minimise the steric strain.

Finally, with reference to the scalar relativistic basis sets, aug-cc-pVNZ-DK and cc-pCVNZ-DK, we see that in both cases, they are in good agreement with their non relativistic counterparts. This suggests that the relativistic correction to the geometry is small, ~ 0.0003 Å for $\mathbf{r}_{CO}$, in comparison to the correction due to core valence effects, ~ 0.02 Å.

If we now compare our results to the equilibrium gemoetries determined experimentally we see that for the two bond lengths results from all the QZ or larger basis sets are in excellent agreement with two of the three experiments, table 11. With respect to the angle we see good agreement between the computations and the experimental values of Hirota at al [182], 124.43°, but relativly poor agreement with the experiemntal value of Austin et al [183], 127.0°.

We see the same effects for the TS geometry, table 12 and figures 17 to 19. We also note once again the discrepancy of the DZ basis sets with the other sets. This further supports the case that the DZ basis sets are too small to accurately describe the geometry, and are therefore more likely to show a greater deviation in the energies, with respect to the other basis sets.

3.4.2 *Energetics*

Next we consider the basis set effects on the zero point energies of HCO, DCO, their respective transistion states, and CO. For the minima and CO, we shall also compare the size of the

Table 11: Geometrical parameters for HCO at the MRCI+Q level with the basis sets given. Distances are in Angstroms and angles are in degrees. [a]Ref.[52] [b]Ref.[168] [c]Ref.[180] [d]Ref.[55] [e]Ref.[181] [f] Ref.[162] [g]Ref.[182] [h]Ref.[184] [i]Ref.[183]

Basis set	$\mathbf{r}_{CO}$	$\mathbf{r}_{CH}$	$H\hat{C}O$
cc-pVDZ	1.1918	1.1462	123.79
cc-pVTZ	1.1835	1.1271	124.24
cc-pVQZ	1.1793	1.1256	124.35
cc-pV5Z	1.1787	1.1248	124.36
cc-pV6Z	1.1784	1.1248	124.36
aug-cc-pVDZ	1.1952	1.1412	124.00
aug-cc-pVTZ	1.1840	1.1261	124.34
aug-cc-pVQZ	1.1797	1.1253	124.38
aug-cc-pV5Z	1.1788	1.1248	124.37
aug-cc-pV6Z	1.1784	1.1248	124.37
cc-pCVDZ	1.1899	1.1405	123.91
cc-pCVTZ	1.1803	1.1195	124.44
cc-pCVQZ	1.1766	1.1169	124.60
cc-pCV5Z	1.1759	1.1161	124.62
aug-cc-pVDZ-DK	1.1947	1.1412	123.96
aug-cc-pVTZ-DK	1.1837	1.1262	124.31
aug-cc-pVQZ-DK	1.1794	1.1254	124.33
aug-cc-pV5Z-DK	1.1784	1.1250	124.31
cc-pCVDZ-DK	1.1896	1.1406	123.86
cc-pCVTZ-DK	1.1790	1.1190	124.42
cc-pCVQZ-DK	1.1762	1.1170	124.55
cc-pCV5Z-DK	1.1756	1.1161	1254.57
MRCI+Q/cc-pVTZ[a]	1.1818	1.1246	124.26
R-UCCSD(T)/aug-cc-pVQZ[b]	1.1789	1.1194	124.48
CASPT2/VTZ2P+f[c]	1.183	1.112	124.9
MRCI+Q/cc-pVQZ[d]	1.182	1.118	124.5
EE-CCSDT/6-311++G**[e]	1.184	1.126	124.6
SDCI+Q/DZP[f]	1.195	1.120	124.5
Exp.[g]	1.1754	1.1191	124.43
Exp.[h]	1.17708	1.1514	123.01
Exp.[i]	1.17	1.11	127.0

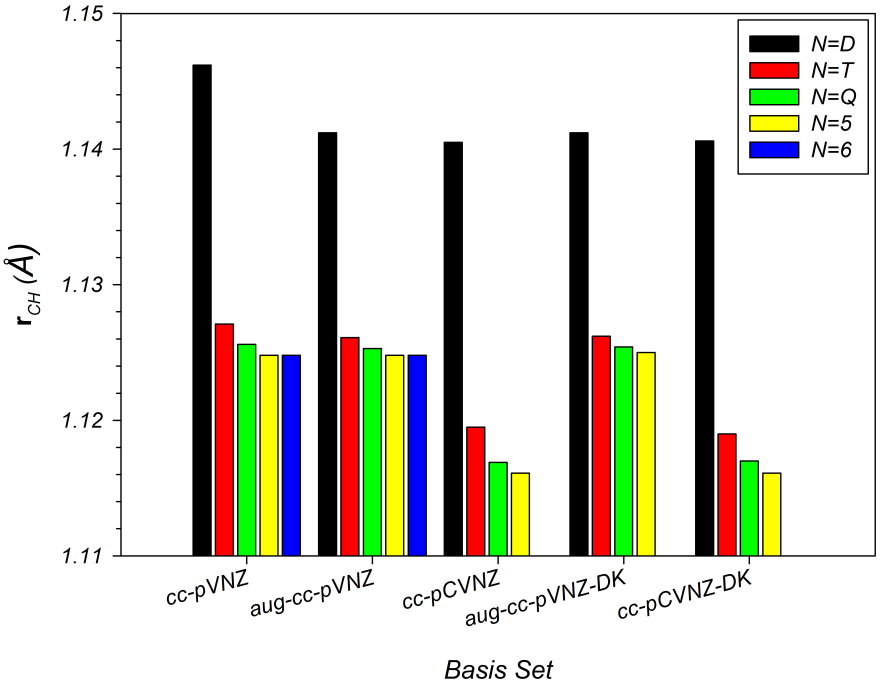

Figure 15: Chart showing the variation in the CH bond length within HCO with respect to the basis set.

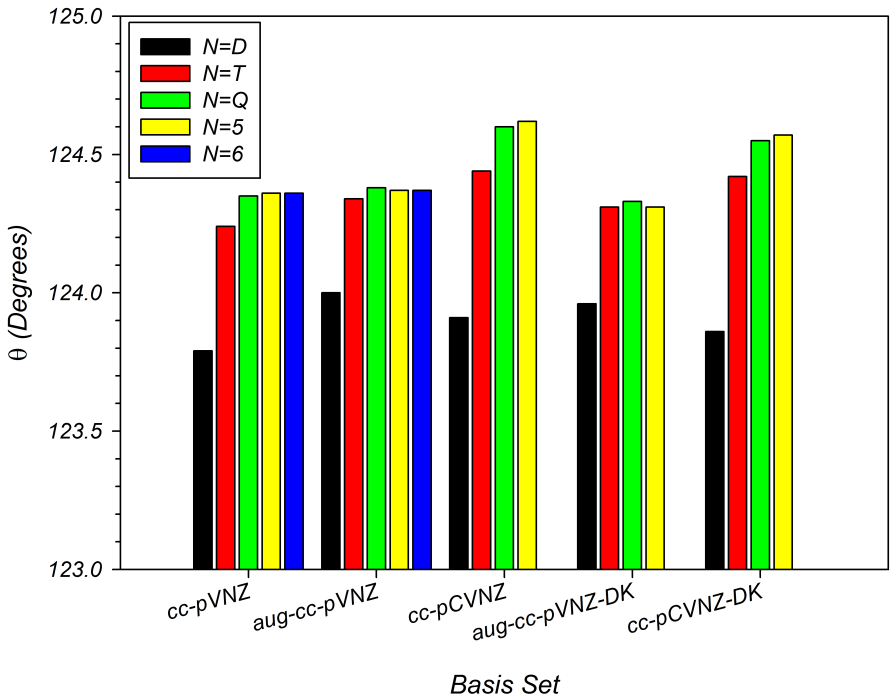

Figure 16: Chart showing the variation in the HCO bond angle, Θ, within HCO with respect to the basis set.

Table 12: Geometrical parameters for the TS in the formation of HCO at the MRCI+Q level with the basis sets given. Distances are in Angstroms and angles are in degrees. [a] Ref.[52] [b] Ref.[55] [c] Ref.[56] [d] Ref.[162]

Basis set	$\mathbf{r}_{CO}$	$\mathbf{r}_{CH}$	$H\hat{C}O$
cc-pVDZ	1.1511	1.8321	117.93
cc-pVTZ	1.1418	1.8690	117.47
cc-pVQZ	1.1373	1.8748	117.34
cc-pV5Z	1.1366	1.8767	117.18
cc-pV6Z	1.1364	1.8768	117.13
aug-cc-pVDZ	1.1538	1.8634	117.06
aug-cc-pVTZ	1.1420	1.8769	117.27
aug-cc-pVQZ	1.1377	1.8778	117.16
aug-cc-pV5Z	1.1368	1.8773	117.11
aug-cc-pV6Z	1.1365	1.8771	117.11
cc-pCVDZ	1.1489	1.8181	117.87
cc-pCVTZ	1.1379	1.8432	117.51
cc-pCVQZ	1.1341	1.8481	117.32
cc-pCV5Z	1.133	1.8495	117.18
aug-cc-pVDZ-DK	1.1533	1.8594	117.08
aug-cc-pVTZ-DK	1.1416	1.8740	117.28
aug-cc-pVQZ-DK	1.1374	1.8710	117.09
aug-cc-pV5Z-DK	1.1364	1.8742	117.12
cc-pCVDZ-DK	1.1485	1.8156	117.89
cc-pCVTZ-DK	1.1366	1.8388	117.55
cc-pCVQZ-DK	1.1337	1.8454	117.34
cc-pCV5Z-DK	1.1330	1.8467	117.20
MRCI+Q/cc-pVQZ[a]	1.1366	1.8610	117.21
MRCI+Q/cc-pVQZ[b]	1.137	1.847	117.1
MRCI+Q/cc-pVQZ[c]	1.137	1.870	117.0
SDCI+Q/DZP[d]	1.160	1.816	119.0

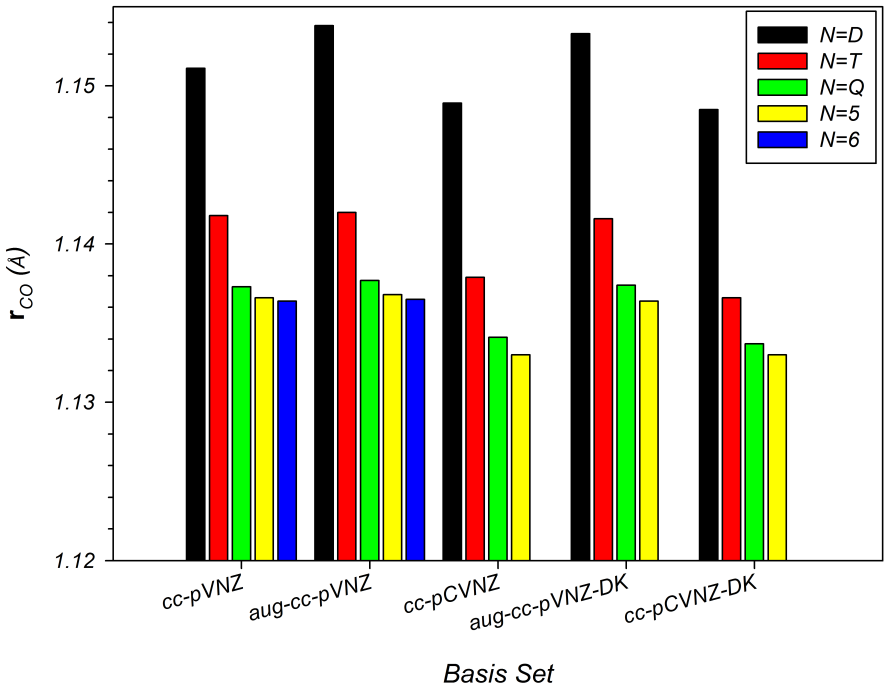

Figure 17: Chart showing the variation in the CO bond length within the TS to the formation of HCO with respect to the basis set.

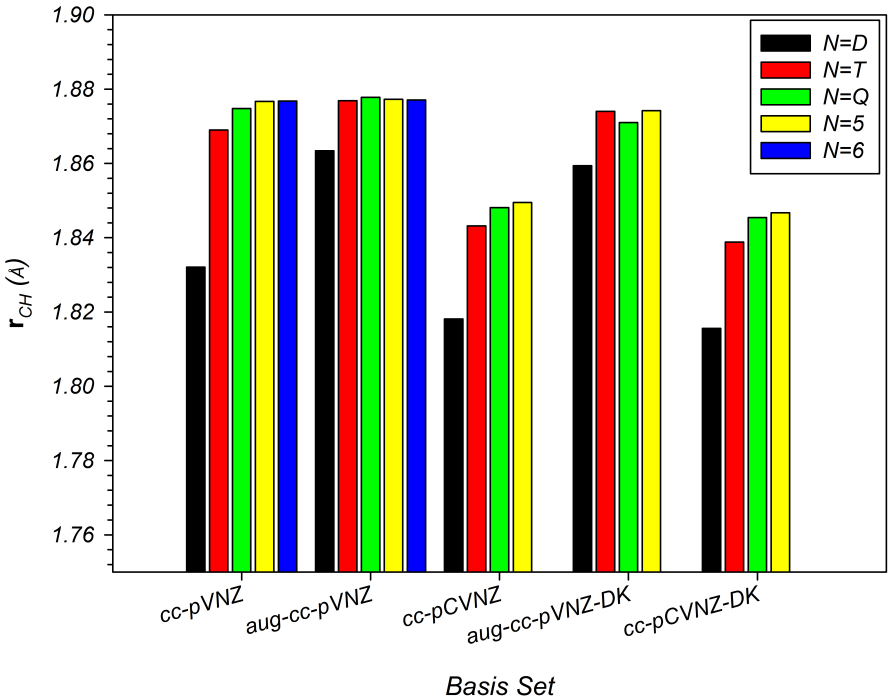

Figure 18: Chart showing the variation in the CH bond length within the TS to the formation of HCO with respect to the basis set.

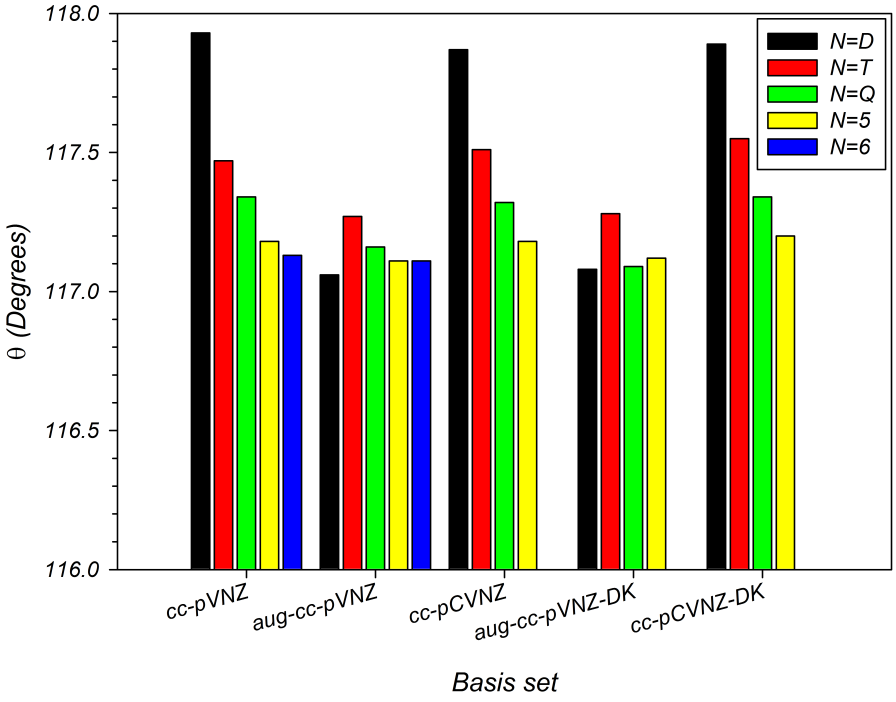

Figure 19: Chart showing the variation in the HCO bond angle, Θ, within the TS to the formation HCO with respect to the basis set.

anharmonic correction to the ZPE with the correction, where there is any, from the other basis set effects. All of the ZPEs are presented in table 13. Let us first address the size of the anharmonic correction for HCO and DCO. We see that for the minima it is ~ 0.1 kcal.mol^{-1}, with the correction being greater for HCO than DCO. For CO, the anharmonic correction is considerably smaller, of the order of 0.01 kcal.mol^{-1}. We also see that the size of the anharmonic correction is independent of the basis set employed.

By comparison, the correction by adding diffuse function is considerably smaller than this for all species. However, core valence effects, for all species apart from CO, are roughly the same size as the anharmonic correction. We note however that they tend to increase the ZPE whereas the anharmonic correction lowers it. Therefore by correcting for core valence effects and anharmonicity one obtains the same ZPE as without either correction. In the case of CO, there is no effect on the ZPE by adding in the core valence effects. As we saw with the geometries, the relativistic corrections are small and the aug-cc-pVNZ-DK and cc-pCVNZ-DK basis sets agree with their non-reletavistic counterparts. To conclude, we should say that it appears including core valence effects and anharmonic corrections leads to the same ZPE as using a standard basis set and the harmonic approximation. In addition, all of the corrections considered have a negligible effect on the ZPE of CO.

We now consider how the barrier height and the reaction ergicity are affected by these effects, table 14 and figures 20 and 21. For the activation energy, we see that both the addition of diffuse functions and inclusion of relativistic effects are negligible. In contrast, core valence effect raise the barrier by 0.5 kcal.mol^{-1}.

With respect to the ergicities, we see inclusion of an anharmonic correction increases the exothermicity by 0.1 kcal.mol^{-1}, in accord with the effect on ZPE we see in table 13. The effect of adding diffuse functions seems to be basis set size dependent: for the DZ basis sets

Table 13: Calculated zero point vibrational energies (kcal.mol^{-1}). [a] Anharmonic values.

	HCO	HCO[a]	DCO	DCO[a]	TS-HCO	TS-DCO	CO	CO[a]
cc-pVDZ	8.01	7.88	6.65	6.56	3.55	3.44	3.03	3.03
cc-pVTZ	8.01	7.90	6.64	6.56	3.54	3.43	3.10	2.09
cc-pVQZ	8.02	7.92	6.66	6.58	3.55	3.44	3.08	3.07
cc-pV5Z	8.03	7.92	6.66	6.58	3.55	3.45	3.08	3.07
cc-pV6Z	8.03	7.93	6.66	6.58	3.54	3.43	3.08	3.07
aug-cc-pVDZ	7.90	7.79	6.55	6.47	3.55	3.44	2.98	2.97
aug-cc-pVTZ	7.98	7.88	6.62	6.54	3.51	3.41	3.08	3.08
aug-cc-pVQZ	8.02	7.91	6.65	6.57	3.54	3.44	3.07	3.06
aug-cc-pV5Z	8.03	7.92	6.66	6.58	3.54	3.44	3.07	3.06
aug-cc-pV6Z	8.03	7.92	6.66	6.58	3.54	3.43	3.08	3.07
cc-pCVDZ	8.01	7.89	6.65	6.55	3.56	3.44	3.06	3.05
cc-pCVTZ	8.14	8.01	6.74	6.65	3.56	3.45	3.08	3.08
cc-pCVQZ	8.19	8.06	6.78	6.69	3.57	3.46	3.10	3.09
cc-pCV5Z	8.20	8.07	6.79	6.70	3.57	3.46	3.10	3.09
aug-cc-pVDZ-DK	7.89	7.78	6.54	6.46	3.45	3.34	2.98	2.97
aug-cc-pVTZ-DK	7.97	7.86	6.61	6.53	3.50	3.42	3.08	3.07
aug-cc-pVQZ-DK	8.00	7.90	6.64	6.56	3.53	3.42	3.07	3.06
aug-cc-pV5Z-DK	8.01	7.91	6.65	6.57	3.53	3.43	3.07	3.06
cc-pCVDZ-DK	8.00	7.87	6.64	6.54	3.55	3.44	3.06	3.05
cc-pCVTZ-DK	8.14	8.00	6.74	6.65	3.56	3.45	3.08	3.07
cc-pCVQZ-DK	8.17	8.04	6.77	6.68	3.57	3.46	3.10	3.09
cc-pCV5Z-DK	8.18	8.05	6.78	6.69	3.57	3.46	3.11	3.10

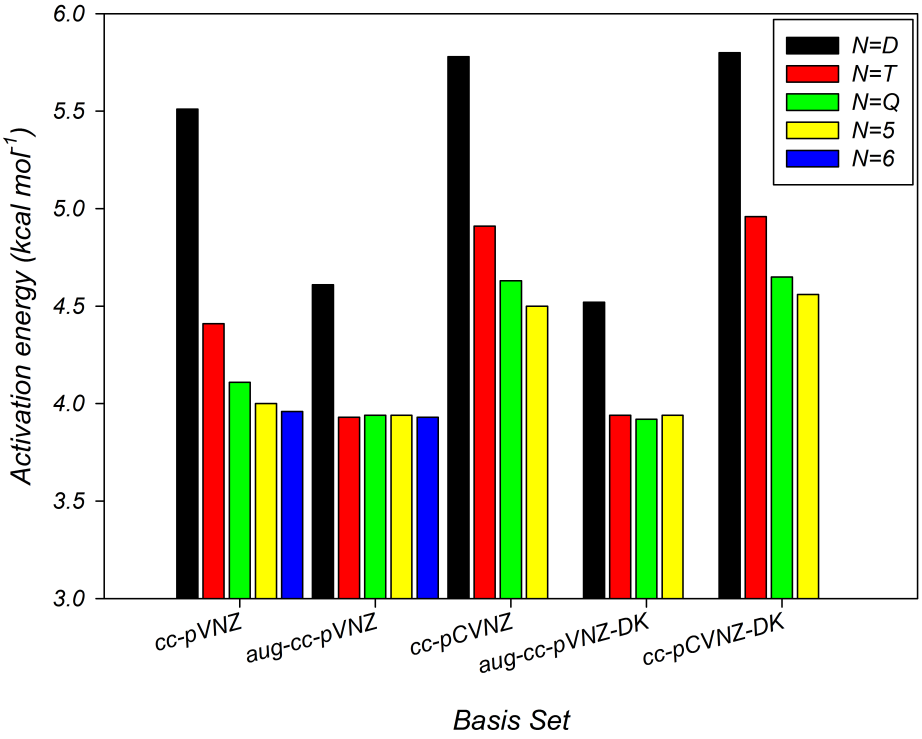

Figure 20: Chart showing the variation in the activation energy for the formation HCO with respect to the basis set.

there is an increase of 2 kcal.mol^{-1} in the exothermicity, but for the 6Z basis sets this change is only 0.1 kcal.mol^{-1}. This suggests that having a larger basis set is of more importance than the addition of diffuse functions alone. With respect to core valence effects, we see they tend to decrease the exothermicity by $\sim$ 0.2 kcal.mol^{-1}, except for the TZ basis sets where the change is $\sim$ 0.5 kcal.mol^{-1}. For the inclusion of relativistic effects only, we see a decrease of $\sim$ 0.5 kcal.mol^{-1} in the exothermicty, except for the TZ basis sets which again show a larger change of $\sim$ 0.8 kcal.mol^{-1}, figures 22 and 23. Inclusion of both core valence correlation and relativistic effects shows the same trend as just inclusion of the reletavistic effects alone. Finally, in comparing the results with the experimental values of the reaction ergicity given in table 14, the best results are obtained using the aug-cc-pVNZ basis sets. Even without the anharmonic correction these results offer the best agreement. However, all of the basis sets provide activation energies which are twice as large as the experimental value.

We shall now extrapolate all of the reaction ergicities, for both HCO and DCO to the complete basis set limit (CBS). We shall also extrapolate all of the basis set results for the activation energy, since none of them show any consensus with the experimental value. For both of these quantities we shall perform the analysis with harmonic ZPE. The reason for this is that the difference between the harmonic and anharmonic zero point energies is always $\sim$ 0.1 kcal.mol^{-1} regardless of the basis set used.

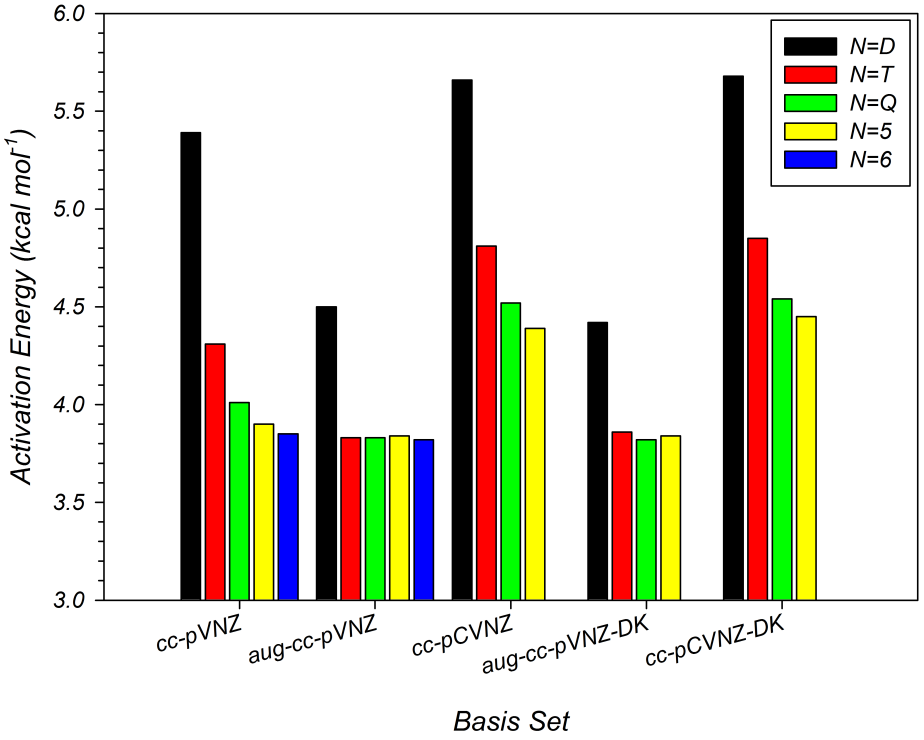

Figure 21: Chart showing the variation in the activation energy for the formation DCO with respect to the basis set.

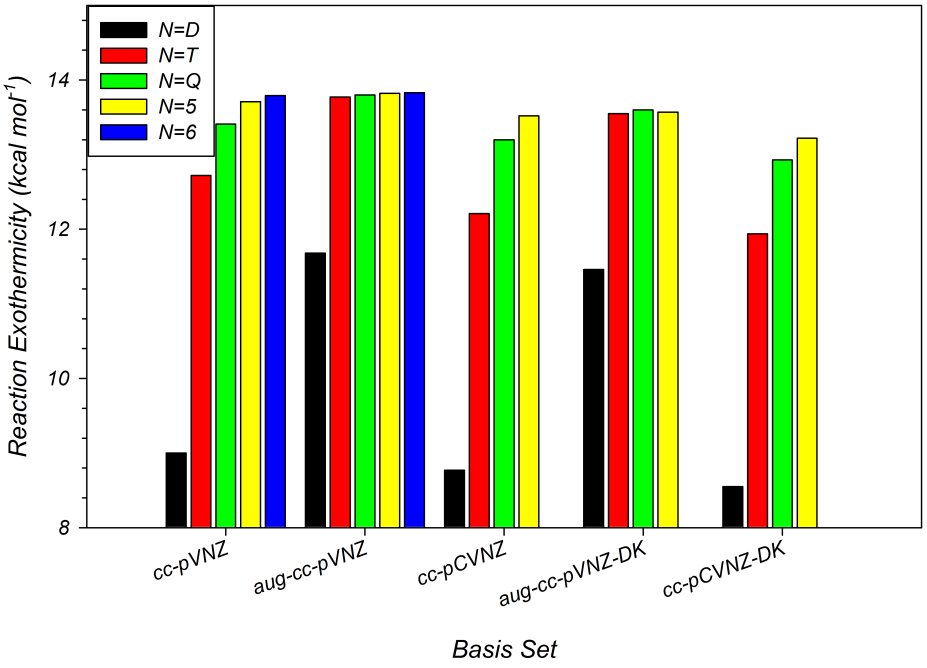

Figure 22: Chart showing the variation in the exothermicity for the formation HCO with respect to the basis set.

Table 14: Barrier heights and reaction ergicities for the formation of HCO and DCO. Energies are shown in kcal mol^{-1}. [a]Without ZPE, [b] Harmonic ZPE, [c]Anharmonic ZPE [d]Ref.[55], [e]Ref.[56], [f]Ref.[52], [g]Ref. [168], [h]Ref.[162], [i]Ref.[185], [j]Ref.[186], [k]Ref.[57]

Basis set	Barrier Height			Ergicity				
	ΔE_e^a	ΔE_a^b HCO	ΔE_a^b DCO	ΔE_e^a	ΔE_r^b HCO	ΔE_r^b DCO	ΔE_r^c HCO	ΔE_r^c DCO
cc-pVDZ	4.99	5.51	5.39	-13.98	-9.00	-10.37	-9.12	-10.45
cc-pVTZ	3.98	4.41	4.31	-17.63	-12.72	-14.09	-12.82	-14.16
cc-pVQZ	3.64	4.11	4.01	-18.36	-13.41	-14.78	-13.51	-14.85
cc-pV5Z	3.53	4.00	3.90	-18.66	-13.71	-15.08	-13.81	-15.15
cc-pV6Z	3.50	3.96	3.85	-18.74	-13.79	-15.16	-13.92	-15.23
aug-cc-pVDZ	4.04	4.61	4.50	-16.60	-11.68	-13.03	-11.78	-13.11
aug-cc-pVTZ	3.50	3.93	3.83	-18.67	-13.77	-15.14	-13.87	-15.21
aug-cc-pVQZ	3.47	3.94	3.83	-18.75	-13.80	-15.17	-13.90	-15.24
aug-cc-pV5Z	3.46	3.94	3.84	-18.78	-13.82	-15.19	-13.92	-15.26
aug-cc-pV6Z	3.46	3.93	3.82	18.79	-13.83	-15.20	-13.93	-15.28
cc-pCVDZ	5.28	5.78	5.66	-13.72	-8.77	-10.13	-8.89	-10.22
cc-pCVTZ	4.44	4.91	4.81	-17.26	-12.21	-13.61	-12.33	-13.69
cc-pCVQZ	4.15	4.63	4.52	-18.28	-13.20	-14.60	-13.32	-14.68
cc-pCV5Z	4.03	4.50	4.39	-18.62	-13.52	-14.93	-13.64	-15.01
aug-cc-pVDZ-DK	4.05	4.52	4.42	-16.38	-11.46	-12.82	-11.57	-12.89
aug-cc-pVTZ-DK	3.52	3.94	3.86	-18.43	-13.55	-14.91	-13.64	-14.98
aug-cc-pVQZ-DK	3.46	3.92	3.82	-18.53	-13.60	-14.96	-13.69	-15.03
aug-cc-pV5Z-DK	3.48	3.94	3.84	-18.52	-13.57	-14.94	-13.67	-15.01
cc-pCVDZ-DK	5.30	5.80	5.68	-13.50	-8.55	-9.91	-8.67	-10.00
cc-pCVTZ-DK	4.48	4.96	4.85	-16.99	-11.94	-13.33	-12.06	-13.42
cc-pCVQZ-DK	4.18	4.65	4.54	-18.01	-12.93	-14.34	-13.06	-14.42
cc-pCV5Z-DK	4.40	4.56	4.45	-18.30	-13.22	-14.63	-13.34	-14.71
MRCI+Q/cc-pVQZ[d]	3.90			-19.23			-13.14	
MRCI+Q/cc-pVQZ [e]	2.89			-18.08				
MRCI+Q/cc-pVQZ [f]	3.73	4.20		-18.38	-13.38			
MRCI+Q/CBS [f]	3.59	4.07		-18.70	-13.70			
RCCSD(T)/cc-pV5Z [f]	3.82	4.32		-18.57	-13.48			
RCCSD(T)/CBS [f]	3.65	4.15		-18.88	-13.79			
R-UCCSD(T)/cc-aug-pV5Z[g]				-19.02	-14.04			
SDCI+Q/DZP [h]	5.8			-18.1				
Exp. [i]							-14.3	
Exp. [j]							-13.9	
Exp. [k]		2.0±0.4						

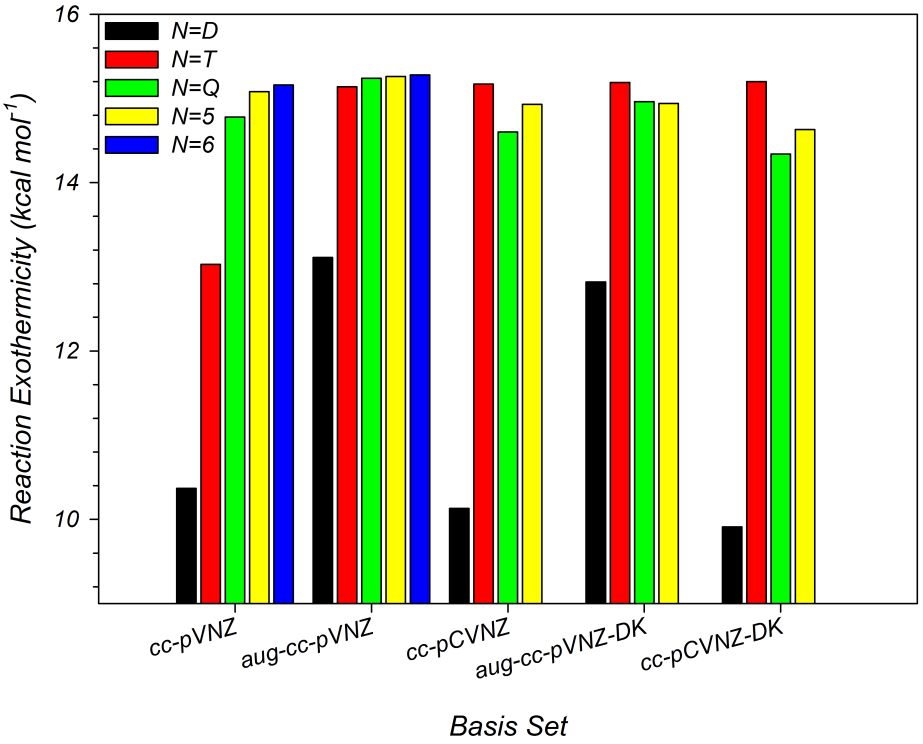

Figure 23: Chart showing the variation in the exothermicity for the formation DCO with respect to the basis set.

3.4.3 *Extrapolation of activation energies and ergicities for HCO and DCO*

We see from figure 24 and table 15 that the cc-pVNZ, aug-cc-pVNZ, and aug-cc-pVNZ-DK basis all predict the same CBS limit of 3.93 kcal.mol^{-1} for the barrier height. Whereas, the cc-pCVNZ, and the cc-pCVNZ-DK basis sets predict the barrier height to be ~4.5 kcal.mol^{-1}. In comparison to the previous values of Woon [52], $E_a = 4.07$ kcal.mol^{-1}, we see that our CBS value with the ordinary basis sets is lower than the value of Woon by 0.1 kcal.mol^{-1} and agrees excellently with the value of 3.9 kcal.mol^{-1} determined by Werner et al [55]. In contrast the barrier height obtained with core valence effects included is higher than both values.

Table 15: Values of the CBS Activation Energy for the basis set families listed. Values are in kcal.mol^{-1}.

	CBS HCO		CBS DCO	
	Activation Energy	Ergicity	Activation Energy	Ergicity
cc-pVNZ	3.94	-13.83	3.83	-15.20
aug-cc-pVNZ	3.94	-13.81	3.84	-15.18
cc-pCVNZ	4.45	-13.73	4.33	-15.13
aug-cc-pVNZ-DK	3.94	-13.55	3.83	-14.92
cc-pCVNZ-DK	4.49	-13.43	4.38	-14.85

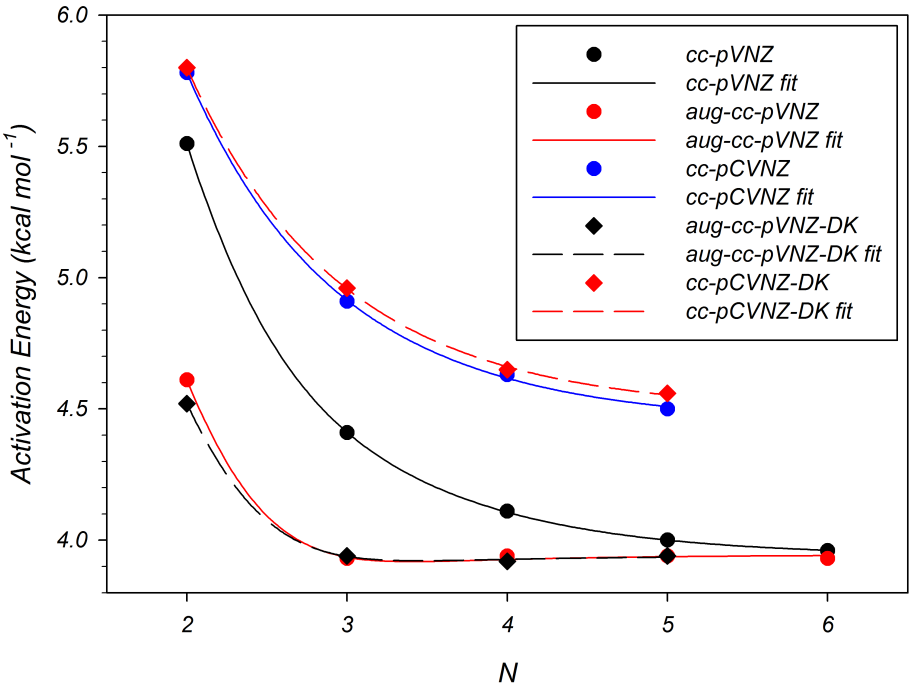

Figure 24: Plot of the activation energy for the formation of HCO as a function of the cardinal number, N, of the basis set. Data fitted with the double exponential function given in equation 137.

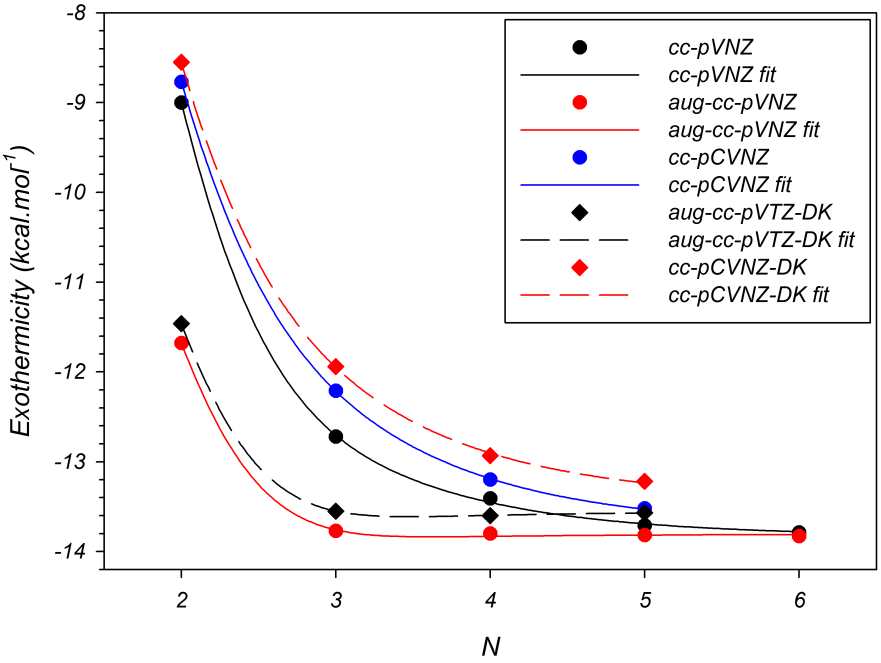

Figure 25: Plot of the reaction ergicity for the formation of HCO as a function of the cardinal number, N, of the basis set. Data fitted with the double exponential function given in equation 137.

If we now consider the ergicity, figure 25 and table 15, the value predicted for the CBS limit with harmonic ZPE with the aug-cc-pVNZ basis sets is -13.81 kcal.mol^{-1} which is in quite good agreement with the -13.9 kcal.mol^{-1} obtained experimentally, and in fact is in almost perfect agreement when we include the lowering of 0.1 kcal.mol^{-1} due to the anharmonic correction. Indeed the CBS limit values for the cc-pVNZ, and cc-pCVNZ basis sets are also in reasonable agreement with the experimental value. However, inclusion of scalar relativistic effects leads to an under prediction of the reaction ergicity for the formation of HCO by 0.5 kcal.mol^{-1}.

If we consider the formation of DCO we see that at the CBS limit that all of the basis sets predict it to have an activation energy which is lower by ~ 0.1 kcal.mol^{-1} compared to HCO, table 15. Likewise, with respect to the reaction ergicity, we see that for DCO the limit for all of the sets if predicted to be ~ 1.4 kcal.mol^{-1} greater than for HCO.

Since after inclusion of all of the basis set effects and extrapolation to the CBS limit, the activation energy remains higher than the experimental observation of Wang et al [57], we must move to consider thermochemical corrections to the energy. This will be done by considering the free energy changes of activation, $\Delta G^{\ddagger}$, and of reaction, ΔG_r. As computation of these quantities has a dependence on the entropy change, we should first look more closely at the VDW complex, as the entropy change from the complex compared to H and CO at infinite separation will be different. However, we shall first discuss the DFT benchmark results.

3.4.4 *DFT Benchmark tests*

For the DFT benchmark, we have used a variety of functionals in combination with the aug-cc-pVTZ basis set. Here, the aug-cc-pVTZ basis set has been used as it will offer the best compromise between accuracy and computational cost for cluster calculations. Table 16 shows the values obtained from the various functionals. We see that the DFT results span a broad range from -1.86 to 3.50 kcal.mol^{-}1 with BHLYP providing the closest estimate in comparison to the experimental value, and B971 and B97D providing the best comparison with the MRCI+Q value. With this in mind, we should consider using both BHLYP and either B971 or B97D for the following cluster calculations. The key difference between these functions is that B97D includes an empirical correction for long range interactions, which may be important for describing the weak interactions within the CO clusters.

3.4.5 *HCO Van der Waals complex in the formation of HCO*

In considering the interaction of H with CO for distances beyond the CH bond length of the TS, we find a VDW complex. This complex has a CH bond length of ~ 3.6 Å. It is predicted to be stable by 0.09 kcal.mol^{-1}. This is in reasonable agreement with the recent work by Andersson et. al [53], who predict this complex to have a CH bond length of 3.8 Å and be 0.08 kcal.mol^{-1} more stable than the dissociated reactants. Better agreement is obtained by comparison to the recent work of Salazar [163], which has been conducted at the RCCSD(T) level in conjuction with a basis set which includes mid-bond functions. In this study the complex is predicted to have a CH bond length of 3.65 Å and a stability of 0.1 kcal.mol^{-1}. We note however, that the older MRCI+Q global PES of Werner [55, 56] does not contain this complex. In addition to this, a more recent review of low temperature scattering experiments on this reaction and of the theoretical works used to model these experiments [187] does not discuss the presence, detection or need for such a complex. Therefore, it might be interesting

Table 16: Barrier heights estimated with the functionals listed in conjuction with the aug-cc-pVTZ basis set. The MRCI+Q value with the same basis set and the experimental value are also provided as references. Values in kcal.mol^{-}1. [a] The KMLYP-mod functional has a reduced amount of correllation from the VWN functional compared to KMLYP.

Functional	Barrier Height	Ref.
B3LYP	0.71	[137]
B971	3.85	[173]
KMLYP	0.39	[174]
PBEPBE1	1.24	[175]
BHLYP	1.74	[176]
KMLYP-mod[a]	2.43	[177]
TPSSH	-1.86	[178]
B97D	3.86	[142]
EXP	2.00	[57]
MRCI+Q	3.50	This work

to look more closely at this complex to ascertain if it could indeed be detected experimentally or not.

Figure 26 shows a scan of the CH bond length of HCO and the resulting energy profile. The zoomed in region shows a shallow well at ~ 3.6 Å corresponding to the VDW complex. We note that during this scan the HĈO angle and the CO bond length were allowed to relax. This provides an optimised geometry for the VDW complex of $r_{CH} = 3.6$ Å, $r_{CO} = 1.2$ Å, and HĈO $= 100°$. In the recent work by Andersson [53], the authors report that the VDW complex has $r_{CH} = 3.8$ Å and HĈO $= 72°$. To better understand this discrepancy, we have investigated how the energy varies as a function of the HĈO angle, θ, and r_{CH}, figure 27. As can be seen from figure 27, the energy difference between our structure and the Andersson one is 0.008 kcal.mol^{-1} with our complex being 0.088 kcal.mol^{-1} more stable than the dissociated reactants.

Due to this very small energy difference, we may for practical purposes consider them as the same complex. In addition, we see from figure 27 that for distances greater than 3.4 Å there is not a strong angular dependence. This is of particular importance if we consider this as a model of a physisorbed state on a surface: on a surface of pure CO, the nearest CO neighbour would be ~ 5.5 Å away. Thus, if there were a strong angular dependence at this distance, the physisorbed state would be destabilised. We have also performed an extrapolation of the the stabilisation energy of the VDW complex to the CBS limit using equation 137. We find that the stability is predicted to be lower at the CBS limit, and is in fact only stable by 0.04 kcal.mol^{-1}. Due to this low stability without ZPE, we conclude that it would be incredibly difficult to detect experimentally. Nevertheless, we now consider the thermochemistry for the formation of HCO and we shall perform this analysis with and without the VDW complex. The thermochemical anlysis will be carried out under interstellar conditions with the temperature ranging from 10 to 20 K and a pressure between 1x10^{-16} and 1x10^{-14} atm.

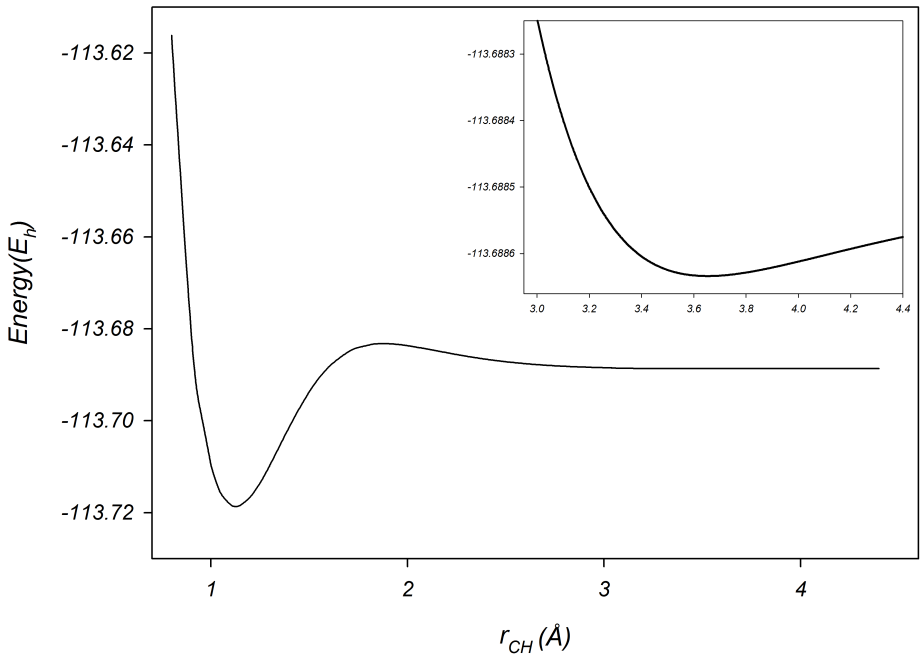

Figure 26: Scan of the CH bond length in HCO. The upper right panel is a zoom of the region between 3.0 and 4.4 Å showing the Van der Waals complex. Computed at the MRCI+Q/aug-cc-pVQZ level.

3.4.6 *Gas Phase Thermochemistry*

We commence our thermochemical analysis by considering $\Delta G^{\ddagger}$ for HCO and as said previously, we will initially consider the reactants to be H and CO at the dissociation limit, table 17, and we will then perform the same analysis from the VDW complex, table 18. From table 17, only the translation entropy makes any significant contribution to the free energy. This is not surprising since it is the only contribution which depends on the pressure and not just the temperature. The change in translational entropy is negative, which again is to be expected since we are looking at a reaction in which we go from two gas phase species to just one. As a consequence, of this loss of translational entropy we see that $\Delta G^{\ddagger}$ is larger than both the electronic barrier and the enthalpy of activation alone by at least 1 kcal.mol^{-1}. Since this analysis has only been performed with diffuse functions in the basis set, we can also conclude that if core valence effects were considered as well the final result would be at least 1.5 kcal.mol^{-1} greater, than the electronic barrier.

Now if we consider the same from the VDW complex, table 18, the only non-zero contribution to the entropy is from rotation. Whilst it is negative, it is also small since it depends upon temperature alone. As such, $\Delta G^{\ddagger}$ from the VDW complex is only slightly different from the enthalpy.

We now move to consider the free energy of reaction. Tables 19 and 20 show the analysis of the entropy contributions when the reactants are considered as the dissociated reactants and the VDW complex respectively. As with the $\Delta G^{\ddagger}$, if we consider the dissociated reactants, the entropic contribution is dominated by the loss of translational entropy and a decrease in the free energy of reaction. Consideration of the same quantity from the VDW complex provides

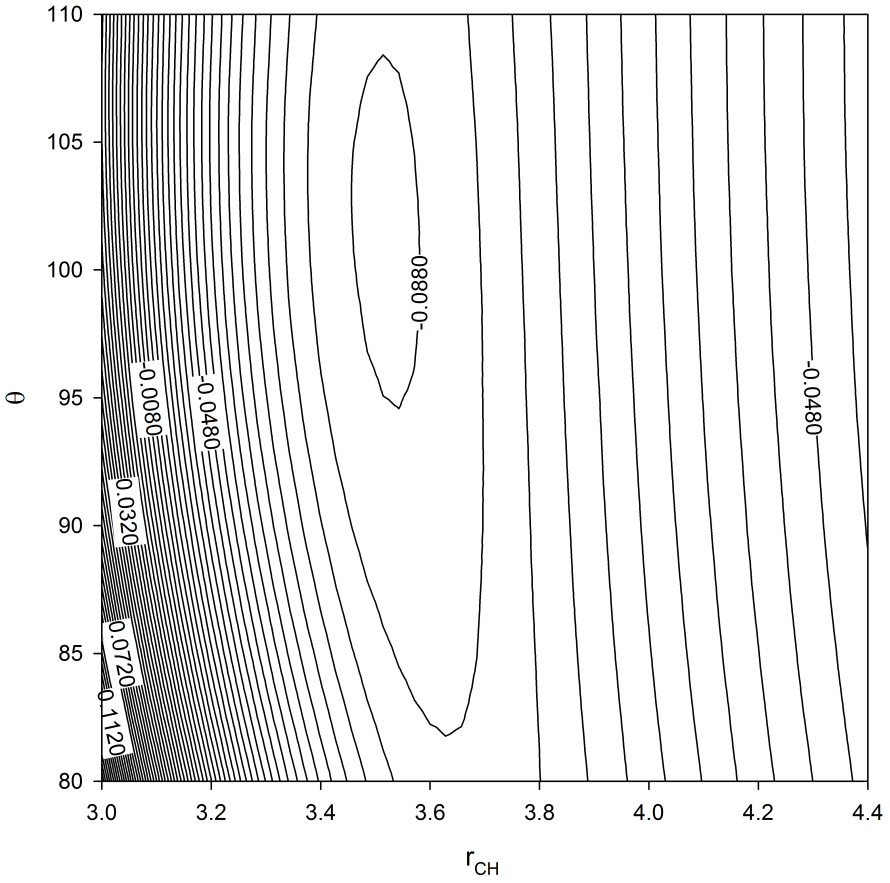

Figure 27: Contour plot of the energy of the Van der Waals complex as a function of the HĈO angle, θ, and the CH distance, r_{CH}. Contours are separated by 0.004 kcal mol^{-1}, θ is given in degrees and r_{CH} is in Å. Computed at the MRCI+Q/aug-cc-pVQZ level.

Table 17: $\Delta G^{\ddagger}$ for HCO considering the reactants as H and CO at infinite separation.

Particle density	Pressure	Temp	ΔS_{trans}	ΔS_{rot}	ΔS_e	ΔS_{vib}	$\Delta H^{\ddagger}$	$\Delta G^{\ddagger}$
n cm^{-3}	atm	K	cal mol^{-1} K^{-1}				kcal mol^{-1}	
10^7	$1.00E^{-14}$	10.00	-73.10	2.69	0.00	0.00	3.78	4.48
		15.00	-75.12	3.09	0.00	0.00	3.76	4.84
		20.00	-81.12	3.38	0.00	0.00	3.74	5.29
10^6	$1.00E^{-15}$	10.00	-77.68	2.69	0.00	0.00	3.78	4.53
		15.00	-79.69	3.09	0.00	0.00	3.76	4.91
		20.00	-84.27	3.38	0.00	0.00	3.74	5.36
10^5	$1.00E^{-16}$	10.00	-82.25	2.69	0.00	0.00	3.78	4.57
		15.00	-84.27	3.09	0.00	0.00	3.76	4.98
		20.00	-85.70	3.38	0.00	0.00	3.74	5.38

Table 18: $\Delta G^{\ddagger}$ for the formation of HCO condisering the reactants to be the VDW complex.

Particle density	Pressure	Temp	ΔS_{trans}	ΔS_{rot}	ΔS_e	ΔS_{vib}	$\Delta H^{\ddagger}$	$\Delta G^{\ddagger}$
n cm^{-3}	atm	K		cal mol^{-1} K^{-1}			kcal mol^{-1}	
10^7	$1.00E^{-14}$	10.00	0.00	-2.12	0.00	0.00	3.90	3.92
		15.00	0.00	-2.12	0.00	0.00	3.90	3.94
		20.00	0.00	-2.12	0.00	0.00	3.90	3.95
10^6	$1.00E^{-15}$	10.00	0.00	-2.12	0.00	0.00	3.90	3.92
		15.00	0.00	-2.12	0.00	0.00	3.90	3.94
		20.00	0.00	-2.12	0.00	0.00	3.90	3.95
10^5	$1.00E^{-16}$	10.00	0.00	-2.12	0.00	0.00	3.90	3.92
		15.00	0.00	-2.12	0.00	0.00	3.90	3.94
		20.00	0.00	-2.12	0.00	0.00	3.90	3.95

Table 19: ΔG_r for the formation of HCO considering the reactants to be H and CO at infinite separation.

Particle density	Pressure	Temp	ΔS_{trans}	ΔS_{rot}	ΔS_e	ΔS_{vib}	ΔH_r	ΔG_r
n cm^{-3}	atm	K		cal mol^{-1} K^{-1}			kcal mol^{-1}	
10^7	$1.00E^{-14}$	10.00	-73.10	1.47	0.00	0.00	-13.93	-13.21
		15.00	-75.12	1.87	0.00	0.00	-13.95	-12.85
		20.00	-81.12	2.16	0.00	0.00	-13.97	-12.39
10^6	$1.00E^{-15}$	10.00	-77.68	1.47	0.00	0.00	-13.93	-13.17
		15.00	-79.69	1.87	0.00	0.00	-13.95	-12.78
		20.00	-84.27	2.16	0.00	0.00	-13.97	-12.33
10^5	$1.00E^{-16}$	10.00	-82.25	1.47	0.00	0.00	-13.93	-13.12
		15.00	-84.27	1.87	0.00	0.00	-13.95	-12.71
		20.00	-85.70	2.16	0.00	0.00	-13.97	-12.30

only a small loss of rotational entropy and consequently the change in the free energy is negligible.

We are therefore led to the conclusion that the VDW complex would assist the reaction by essentially removing any dependence on the translational entropy once the complex is formed. As such, we must now consider the implications of the loss of translational entropy on the stability of the VDW complex. Table 21 shows the analysis of the entropy contributions to ΔG_r for the formation of the VDW complex. Here the translational entropy contribution is of the same order of magnitude as the enthalpy, consequently the free energy is now positive. With this in mind, we are forced to conclude that under these conditions, the VDW complex would not be formed and therefore would not be detected experimentally. This observation is supported by the fact that it has never been detected.

Table 20: ΔG_r for the formation of HCO considering the reactants to be the Van der Waals complex.

Particle density n cm^{-3}	Pressure atm	Temp K	ΔS_{trans}	ΔS_{rot}	ΔS_e	ΔS_{vib}	ΔH_r	ΔG_r
				cal mol^{-1} K^{-1}			kcal mol^{-1}	
10^7	$1.00E^{-14}$	10.00	0.00	-3.35	0.00	0.00	-13.80	-13.77
		15.00	0.00	-3.35	0.00	0.00	-13.80	-13.75
		20.00	0.00	-3.35	0.00	0.00	-13.80	-13.74
10^6	$1.00E^{-15}$	10.00	0.00	-3.35	0.00	0.00	-13.80	-13.77
		15.00	0.00	-3.35	0.00	0.00	-13.80	-13.75
		20.00	0.00	-3.35	0.00	0.00	-13.80	-13.74
10^5	$1.00E^{-16}$	10.00	0.00	-3.35	0.00	0.00	-13.80	-13.77
		15.00	0.00	-3.35	0.00	0.00	-13.80	-13.75
		20.00	0.00	-3.35	0.00	0.00	-13.80	-13.74

Table 21: ΔG_r for the formation of the VDW complex considering the reactants to be H and CO at infinite separation.

Particle density n cm^{-3}	Pressure atm	Temp K	ΔS_{trans}	ΔS_{rot}	ΔS_e	ΔS_{vib}	ΔH_r	ΔG_r
				cal mol^{-1} K^{-1}			kcal mol^{-1}	
10^7	$1.00E^{-14}$	10.00	-73.10	4.81	0.00	0.00	-0.13	0.56
		15.00	-75.12	5.22	0.00	0.00	-0.61	0.90
		20.00	-81.12	5.50	0.00	0.00	-0.17	1.35
10^6	$1.00E^{-15}$	10.00	-77.68	4.81	0.00	0.00	-0.13	0.60
		15.00	-79.69	5.22	0.00	0.00	-0.15	0.97
		20.00	-84.27	5.50	0.00	0.00	-0.17	1.41
10^5	$1.00E^{-16}$	10.00	-82.25	4.81	0.00	0.00	-0.13	0.65
		15.00	-84.27	5.22	0.00	0.00	-0.15	1.04
		20.00	-85.70	5.50	0.00	0.00	-0.17	1.44

Table 22: $\Delta G^{\ddagger}$ for the formation of HCO considering the reactants as H and CO at infinte separation.

Pressure	Temp	ΔS_{trans}	ΔS_{rot}	ΔS_e	ΔS_{vib}	$\Delta H^{\ddagger}$	$\Delta G^{\ddagger}$
atm	K		cal mol^{-1} K^{-1}			kcal mol^{-1}	
1	10.00	-9.02	2.69	0.00	0.00	3.78	3.84
	100	-20.46	4.98	0.00	0.06	3.42	4.96
	300	-25.94	6.07	0.00	1.094	2.84	8.47

Our final undertaking is now to consider the free energy of reaction under standard conditions, 298.15 K [1] and 1 atm pressure, to see if we can reproduce the barrier obtained in the experiment by Wang et al [57] of 2.0 ± 0.4 kcal.mol^{-1}. Table 22 shows the entropic contributions under these conditions and also the same quantities at interstellar temperatures but 1 atmosphere pressure. From table 22, if the reaction were carried out at 1 atmosphere and 10 K, then the entropy change is greatly reduced compared to interstellar pressures. We also note that the enthalpy at 300 K approaches the experimental activation energy but upon inclusion of the entropy, it increases considerably. We therefore are left with two possibilities with regard to the experiment: either our model is lacking some effect that is present in the experiment or the experimental value of Wang et al [57] is incorrect. If we explore the first of these possibilities, we can consider the following possible sources of error: the pressure is greater than 1 atmosphere, the third body required experimentally plays some role in the mechanism other than just as an energy sink. Indeed, within the experiment the reaction proceeds via the equilibrium $H + CO + M \rightleftharpoons HCO + M^*$. In this case, if M is atomic, the only contribution which could be made is through increased translational energy. This would then lead to a change in ΔH for the reaction, but the entropy would not be affected. If M is a molecule, its exact contribution would depend on the exact overlap of the vibrational and rotational energy levels of HCO and M. If we consider the experimental set-up, it seems the third body is at a pressure of 1600 torr (~ 2 atm), CO is added at a pressure of 3 torr, and H is added to the combined system at a pressure of 2 torr. It is unclear if the uncharged vessel is at ambient pressure or not. Consequently, the vessel may be at a total pressure of between 2.1 and 3 atm. Since this clearly represents a significant discrepancy the analysis should perhaps be re-performed at 2 and 3 atm.

3.5 SUMMARY

After consideration of all effects, we see that the formation of both COH and HCO in the gas phase will be difficult, since the formation of COH is endothermic by ~ 20 kcal.mol^{-1} and the activation energy for the formation of HCO is at best, 3.8 kcal.mol^{-1}. In addition, inclusion of thermochemical effects provides a free energy of activation which is greater than this by at least 0.5 kcal.mol^{-1}, due to the loss of translational entropy. However, this same process, which will hinder addition reactions with a barrier, will assist those without, as they would now need to lose less energy to form a stable product.

We also see from the DFT benchmark tests that using a variety of different functionals we can get a range of values from -1.86 kcal.mol^{-1} to 3.50 kcal.mol^{-1}. With this in mind, we will use both the BHLYP and B97D functionals for the cluster computations. The reasoning

1 We shall in fact consider the temperature as 300 K since this is the lowest reported value of the experiment

behind using the two functionals is that BHLYP gives an estimate for the gas phase addition to HCO which is in reasonable agreement with the experimental one and B97D provides a result which is in good agreement with the MRCI+Q value (3.86 vs 3.94 kcal.mol^{-1}).

However, we note that we are unable to reconcile the value of Wang et al [57], 2.0 ± 0.4 kcal.mol^{-1}. Though, it should be said the more recent experimental papers in combustion chemistry [58, 59, 160] have called this value into question and now propose a range for the activation energy, including experimental errors, between 2.0 and 6.0 kcal.mol^{-1}. If we consider our best estimate for the elctronic barrier, ignoring thermochemical effects, then we have a value of 3.94 kcal.mol^{-1} without core-valence effects and 4.49 kcal.mol^{-1} with. We see that both values fall within the experimental range without inclusion of thermochemistry, which we note is complicated by the nature of the third body.

Chapter IV

REACTION OF HYDROGEN ATOMS WITH CO IN MOLECULAR CLUSTERS

4

REACTION OF HYDROGEN ATOMS WITH CO IN MOLECULAR CLUSTERS

In this chapter, we investigate the effects of cluster size and composition on the formation of HCO and COH. We commence our discussion by considering these processes in clusters of several CO molecules, this will then be followed by a discussion of the same processes in clusters of several water molecules. Indeed, experiments conducted by several groups [41–44] have considered the hydrogen atom bombardment of both pure CO and CO/H_2O mixed surfaces.

For computational reasons the two sets of clusters have been treated using different methods. As such the methods employed and the reasoning behind the choice of method will be discussed in each section.

4.1 CLUSTERS OF CO

We have considered two different clusters sizes. The first is a cluster consisting of 4 CO and the second of 6 CO. The 4 CO cluster has been built from the experimentally determined unit cell of α CO [188], figure 28(a). The structure was then reoptimised at the RI-MP2/aug-cc-pVTZ level using Turbomole [149]. The choice of MP2 was taken as tests with BHLYP and B97D [142, 176] were unable to correctly describe the VDW forces which hold the cluster together.

The 6 CO cluster was built by initially constructing a (211) supercell, figure 28(b), of the α CO unit cell from which two CO molecules were then removed. The structure was optimised at the RI-MP2/aug-cc-pVTZ level. In order to speed up the computation, the RI [150] approximation was employed with Turbomole. We note however, that it was not possible to obtain the TS structures for the complexes as an HF initial hessian was not sufficient for this kind of VDW complex. Moreover, Turbomole will not compute a numerical hessian unless the gradient is already zero. Further to this, the use of MP2 with Gaussian was not possible as the computational cost was too great. The resulting structures of the clusters are shown in figure 29.

The cluster of 4 CO, figure 29(a), retains a similar geometry to the unit cell, figure 28(a). However, the cluster of 6 CO, figure 29(b), shows a strange octahedral like structure. Whilst we cannot say that this structure is the global minimum for the cluster, an analysis of the normal modes shows that it is at least a local minimum. Given the geometries of the pure clusters, we now move to consider the energetics and changes brought about by the addition of hydrogen to these clusters.

4.2 HYDROGENATION OF CO CLUSTERS

With regard to the addition of a hydrogen atom to the clusters, we shall consider both the formation of HCO and COH. Table 23 presents the energetics associated with these processes within the two clusters. We will treat the reactions withing the 4 CO and 6 CO clusters separately.

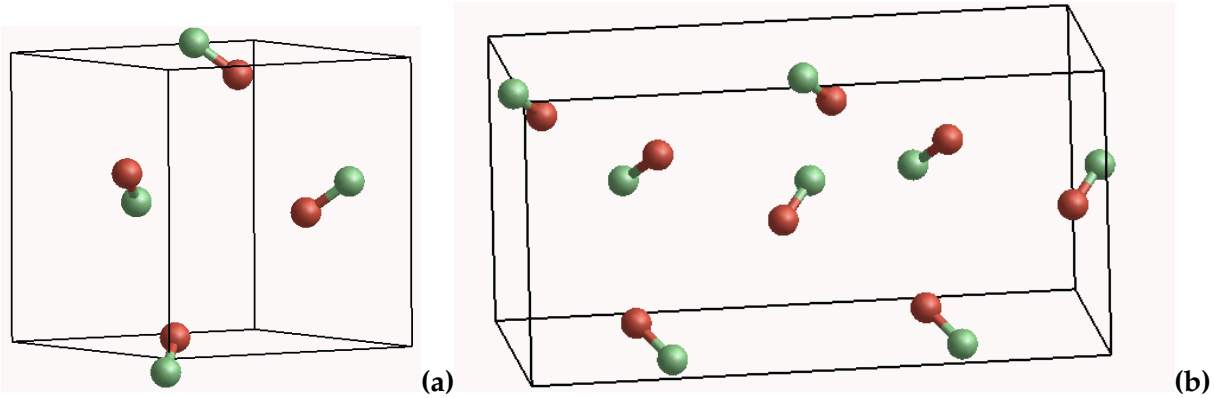

Figure 28: Images of the α—CO phase of solid CO, (a) the unit cell, (b) the (211) supercell used to build the 6 CO cluster.Carbon atoms are shown in green whilst oxygen atoms are shown in red

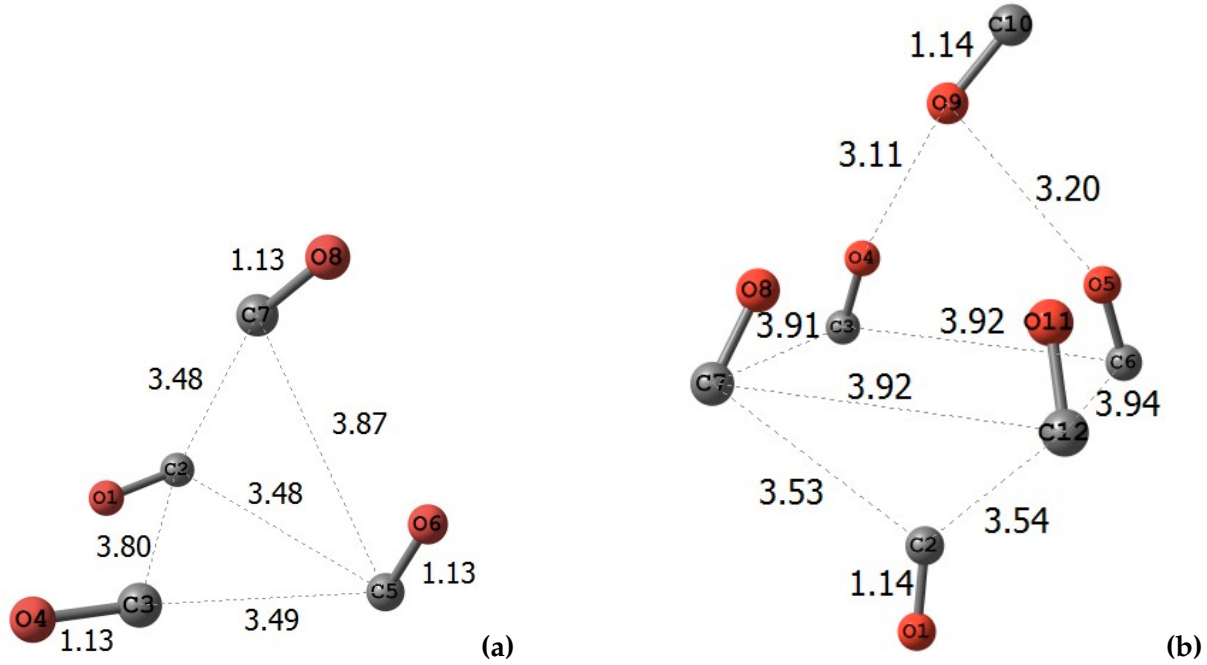

Figure 29: Pure (CO)n clusters (a) with $n = 4$, (b) $n = 6$. Distances are given in Å and angles in degrees

Table 23: Activation energies, E_a, and energies of reaction, E_r, for the reaction of H with CO in the presence of 3 CO, 5 CO, and in the gas phase for reference. Energies have been computed at the RI-MP2/aug-cc-pVTZ level, values given in kcal mol^{-1}.

Reaction	E_a	E_r
$H + 4\,CO \rightarrow HCO \cdot (CO)_3$	-	-19.40
$H + 4\,CO \rightarrow COH \cdot (CO)_3$	-	+22.20
$H + 6\,CO \rightarrow HCO \cdot (CO)_5$	-	-17.44
$H + 6\,CO \rightarrow COH \cdot (CO)_5$	-	+23.93
$H + CO \rightarrow HCO$	5.20	-17.37
$H + CO \rightarrow COH$	41.45	+27.82

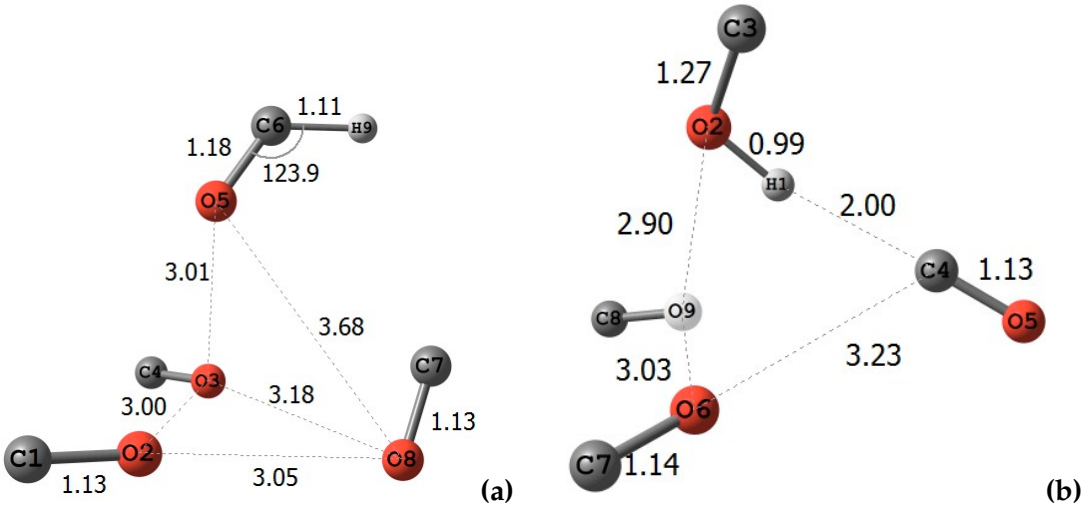

Figure 30: HCO and COH within clusters of CO (a) $HCO \cdot (CO)_3$, (b) $COH \cdot (CO)_3$. Distances are given in Å and angles in degrees

4.2.1 *Addition of H to the 4 CO cluster*

If we consider first the formation of HCO we see, from table 23, an increase in the reaction exothermicity by ~ 2 kcal.mol^{-1}. We also see that during the optimisation process, some of the CO molecules, figure 30, have rotated compared to the pure CO clusters. If this process were to take place on an actual surface, this could not happen. However, within α CO, the relative head to tail orientations of the CO molecules are not fixed and this gives rise to a residual entropy at 0 K [189]. As such, we consider that it is of no great importance.

For COH, we also see an increase in its stability within the cluster, compared to the gas phase: it is less endothermic by ~ 5 kcal.mol^{-1}. However, the process remains endothermic and as such, it is unlikely that we would form any COH at 10 K.

Using an unrelaxed scan of the CH bond in HCO, the TS is estimated to have a CH bond length of 1.8 Å and the activation energy is ~ 6 kcal.mol^{-1}. Thus, this estimated structure lies slightly above the gas phase result. However, since this is not a fully optimised structure, we conclude that the cluster has little effect on the activation energy for the formation of HCO.

4.2.2 *Addition of H to the 6 CO cluster*

For the formation of COH in this cluster, much like the 4 CO, we see a stabilisation by ~ 4 kcal.mol^{-1}, table 23. Whilst this means the process is less endothermic than the gas phase, it still remains considerably endothermic. As such, we do not expect that COH could participate in any further reactions, since it is unlikely ever to be formed.

For HCO, on the other hand, we see little change compared to the gas phase. Since we see little difference between the 6 CO and the 4 CO cluster with regard to the exothermicity of this reaction, we suspect the activation energy will likewise be much the same. Consequently we suspect that the process is changed very little in clusters of CO compared to the gas phase.

As with the 4 CO, figure 31 shows some changes in the relative head to tail orientations of the CO molecules.

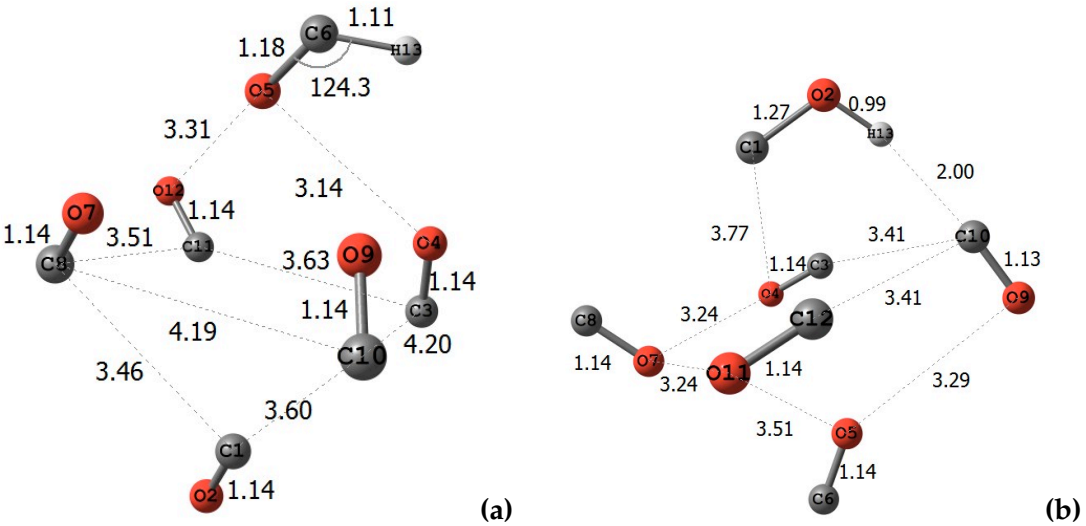

Figure 31: HCO and COH within clusters of CO (a) $HCO \cdot (CO)_5$, (b) $COH \cdot (CO)_5$. Distances given are in Å and angles are in degrees

4.3 AIM ANALYSIS OF CO CLUSTERS

4.3.1 *AIM analysis of the 4 CO, $HCO \cdot (CO)_3$, and $COH \cdot (CO)_3$ clusters*

Since the energetics for the two reactions within the clusters change little from the gas phase, we can conclude that the interactions within the clusters must be weak. We shall therefore discuss the AIM analysis of 4 CO, $HCO \cdot (CO)_3$, and $COH \cdot (CO)_3$ clusters together. The results of the AIM analysis for the three species are presented in tables 24, 25, and 26.

If we consider the 4 CO cluster, the four molecules interact very weakly with each other since the value of ρ at each of the BCPs between the molecules is very small, and the value of L indicates the charge is being built up away from these points, suggesting a weak ionic nature. From table 24, we do not see four identical CO molecules but rather two pairs. This is clearly a result of the geometry which brings two of the CO molecules slightly closer together. Since this geometry encloses a volume of space we see a CCP. Moreover, the values of ρ and L at one of the BCPs between a carbon and oxygen which form a CO molecule, ρ is large, suggesting that there is a significant amount of density being shared by the nuclei. However, L is positive, indicating charge is being accumulated outside of the bonding region. This is a well known phenomenon [151], caused by the electronegativity difference between C and O, and not an indication that our wavefunction is describing the interaction as ionic.

Upon addition of the hydrogen to form HCO, we see the formation of an additional weak interaction between H_1 and C_4. This is also accompanied by the formation of the covalent CH bond between H_1 and C_1, table 25. Other than these two additional interactions, the cluster is relatively unperturbed by the radical. This explains, to a certain extent, the small difference in the energetics. The increase in exothermicity is evidently due to the additional interactions providing extra density to the radical.

In contrast, the formation of COH seems to perturb the cluster to a greater extent, table 26. This is evidenced by the loss of one of the RCPs and of the CCP. This is evidently caused by the weakening of the interaction between C_2 and O_3. We also see the interaction between H_1 and C_2 is stronger than the interaction between H_1 and C_4 in the $HCO \cdot (CO)_3$ cluster. It is

Table 24: Values of the electron density, ρ. the laplacian, L, at the critical point between the nuclear centres (left) Molecular graph of the 4 CO cluster. Bond critical points are shown in red ring critical points are shown in yellow and cage critical points in green.(right)

Type of Critical Point	Nuclei involved	ρ	L (a.u)
BCP	O_1C_1	0.496	0.637
BCP	O_1C_2	0.004	0.016
BCP	C_2O_2	0.497	0.645
BCP	C_1C_3	0.004	0.014
BCP	C_2C_3	0.003	0.012
BCP	C_3O_3	0.497	0.645
BCP	C_2C_4	0.004	0.013
BCP	C_3O_4	0.004	0.016
BCP	C_1C_4	0.003	0.011
BCP	C_4O_4	0.496	0.637
RCP	$C_1O_1C_2C_3$	0.002	0.006
RCP	$C_1O_1C_2C_4$	0.001	0.005
RCP	$C_1C_3O_4C_4$	0.002	0.005
RCP	$C_2C_3O_4C_4$	0.002	0.006
CCP	C_1, O_1, C_2, C_3, O_4, C_4	0.001	0.004

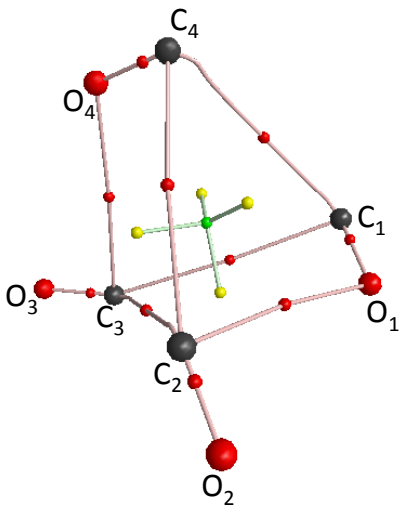

Table 25: Values of the electron density, ρ. the laplacian, L, at the critical point between the nuclear centres (left) Molecular graph of the $HCO \cdot (CO)_3$ cluster. Bond critical points are shown in red ring critical points are shown in yellow and cage critical points in green.(right)

Type of Critical Point	Nuclei involved	ρ	L (a.u)
BCP	O_3C_3	0.496	0.654
BCP	O_2O_3	0.005	0.026
BCP	O_2C_2	0.496	0.650
BCP	O_3O_1	0.005	0.026
BCP	O_2O_1	0.005	0.026
BCP	O_1C_1	0.441	0.473
BCP	O_3O_4	0.005	0.023
BCP	O_2O_4	0.004	0.019
BCP	O_1C_4	0.005	0.022
BCP	C_4O_4	0.497	0.659
BCP	H_1C_4	0.005	0.020
BCP	H_1C_1	0.282	-1.148
RCP	$H_1C_1O_1C_4$	0.005	0.022
RCP	$O_1O_3O_4C_4$	0.002	0.009
RCP	$O_1O_2O_3$	0.003	0.012
RCP	$O_2O_3O_4$	0.002	0.010
RCP	$O_1O_2O_4C_4$	0.002	0.010
CCP	O_1, O_2, O_3, O_4, C_4	0.002	0.008

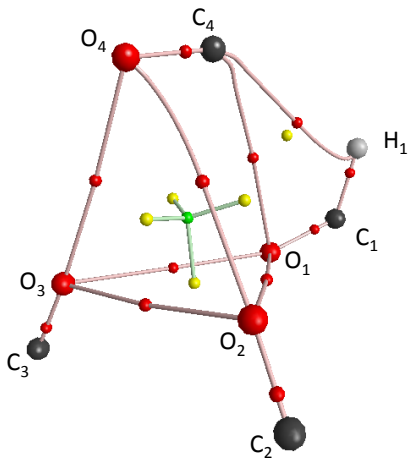

Table 26: Values of the electron density, ρ. the laplacian, L, at the critical point between the nuclear centres (left) Molecular graph of the $COH \cdot (CO)_3$ cluster. Bond critical points are shown in red ring critical points are shown in yellow and cage critical points in green.(right)

Type of Critical Point	Nuclei involved	ρ	L (a.u)
BCP	C_1O_1	0.346	0.272
BCP	O_1O_3	0.007	0.037
BCP	O_3C_3	0.495	0.643
BCP	H_1C_2	0.028	0.062
BCP	C_2O_2	0.502	0.669
BCP	O_1O_4	0.006	0.028
BCP	O_3O_4	0.005	0.024
BCP	C_2O_4	0.004	0.019
BCP	O_4C_4	0.495	0.643
BCP	H_1C_1	0.343	-2.694
BCP	C_2O_3	0.004	0.017
RCP	$O_1H_1C_2O_4$	0.004	0.018
RCP	O_1, O_3, O_4	0.003	0.015

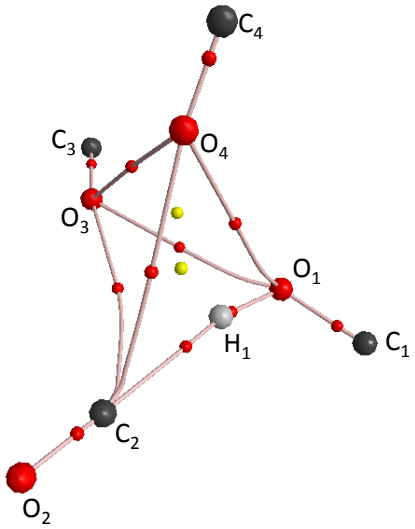

perhaps the benefit of this interaction, and the additional shared density it brings, that gives rise to the additional stability of COH in the cluster, compared to the gas phase, and also why it experiences a greater change in its reaction ergicity than HCO.

4.3.2 *AIM analysis of the 6 CO, $HCO \cdot (CO)_5$, and $COH \cdot (CO)_5$ clusters*

By comparison with the $(CO)_4$ cluster, the $(CO)_6$ cluster shows that two of the CO molecules are in slightly different environments to the other four, table 27. This is due to the geometry of the cluster as the four COs which sit in the "square" arrangement in the centre of the cluster are closer to one another than the two which are above and below. Again, the cluster is held together by very weak interactions which are all approximatly the same.

Upon the formation of HCO, as with the smaller cluster, there is not a great perturbation of the cluster by the presence of the radical, table 28. We also see again that some of the relative head tail orientations of the other CO molecules have changed, though this has made little difference to the interactions between the molecules. This clearly supports the fact that the CO molecules are insensitive to each others orientation.

The presence of COH in the cluster shows little difference, like HCO, between the two cluster sizes, table 29. Indeed the interaction of H_1 and C_2 is almost identical between the two clusters. However, a difference arises between the other interactions within the cluster: in so much as in the smaller cluster, it is through O_1 and in the larger it is through C_1. This change results in a slightly weaker interaction and consequently the stabilisation of COH is slightly less.

This small difference suggests that COH may be influenced by its environment. As such, we may reasonably expect that the stability of COH may be greatly influenced by the presence of

Table 27: Values of the electron density, ρ. the laplacian, L, at the critical point between the nuclear centres (left) Molecular graph of the $(CO)_6$ cluster. Bond critical points are shown in red ring critical points are shown in yellow and cage critical points in green.(right)

Type of Critical Point	Nuclei involved	ρ	L (a.u)
BCP	O_1C_1	0.495	0.646
BCP	C_1C_3	0.003	0.011
BCP	C_3O_3	0.494	0.635
BCP	O_3O_4	0.004	0.020
BCP	O_4C_4	0.495	0.641
BCP	C_1C_2	0.003	0.011
BCP	O_2O_3	0.003	0.014
BCP	O_2O_4	0.004	0.019
BCP	C_2O_2	0.494	0.635
BCP	C_1C_5	0.003	0.011
BCP	O_5O_3	0.003	0.014
BCP	O_5O_4	0.004	0.017
BCP	C_5O_5	0.494	0.635
BCP	C_1C_6	0.003	0.011
BCP	O_6O_4	0.003	0.016
BCP	O_2O_6	0.003	0.014
BCP	O_5O_6	0.003	0.014
BCP	C_6O_6	0.494	0.634
RCP	$C_1C_2O_2O_3C_3$	0.001	0.004
RCP	$O_2O_3O_4$	0.002	0.008
RCP	$O_2O_4O_6$	0.002	0.008
RCP	$C_1C_3O_3O_5C_5$	0.001	0.004
RCP	$O_3O_4O_5$	0.002	0.008
RCP	$C_1C_2O_2O_6C_6$	0.001	0.004
RCP	$O_4O_5O_6$	0.002	0.008
CCP	C_1-C_3, O_2-O_6, C_5, C_6	0.0002	0.002

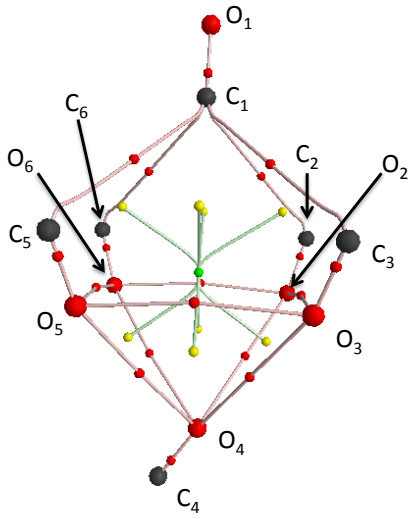

Table 28: Values of the electron density, ρ. the laplacian, L, at the critical point between the nuclear centres (left) Molecular graph of the $HCO \cdot (CO)_5$ cluster. Bond critical points are shown in red ring critical points are shown in yellow and cage critical points in green.(right)

Type of Critical Point	Nuclei involved	ρ	L (a.u)
BCP	O_4C_4	0.495	0.641
BCP	O_4C_2	0.003	0.013
BCP	C_2O_2	0.494	0.631
BCP	O_2O_1	0.004	0.020
BCP	O_1C_1	0.440	0.462
BCP	C_4C_5	0.003	0.012
BCP	O_5O_1	0.004	0.018
BCP	C_5O_5	0.005	0.640
BCP	C_4C_3	0.002	0.011
BCP	O_2O_3	0.003	0.015
BCP	O_3C_1	0.004	0.019
BCP	O_3O_5	0.004	0.015
BCP	C_3O_3	0.494	0.629
BCP	C_4C_6	0.003	0.011
BCP	C_2C_6	0.002	0.010
BCP	O_6O_1	0.004	0.017
BCP	C_5C_6	0.003	0.011
BCP	C_6O_6	0.495	0.640
BCP	H_1C_1	0.283	-1.164
RCP	$O_1C_1O_3O_5$	0.002	0.008
RCP	$C_2O_2O_1O_6C_6$	0.001	0.006
RCP	$O_1O_6C_6C_5O_5$	0.001	0.006
RCP	$O_3O_5C_3C_5C_4$	0.001	0.004
RCP	$C_4C_5C_6$	0.001	0.005
RCP	$O_3C_3O_2C_2C_4$	0.001	0.004
RCP	$C_1O_1O_3O_2$	0.002	0.009
RCP	$C_6C_2C_4$	0.001	0.005
CCP	C_1-C_6, O_1-O_6	0.0002	0.002

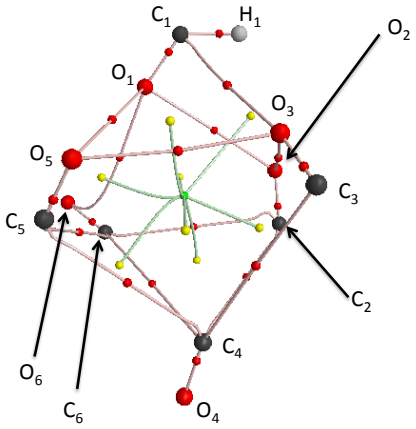

Table 29: Values of the electron density, ρ. the laplacian, L, at the critical point between the nuclear centres (left) Molecular graph of the $COH \cdot (CO)_5$ cluster. Bond critical points are shown in red ring critical points are shown in yellow and cage critical points in green.(right)

Type of Critical Point	Nuclei involved	ρ	L (a.u)
BCP	C_1O_1	0.346	0.242
BCP	H_1C_2	0.028	0.062
BCP	C_2O_2	0.499	0.670
BCP	O_2O_4	0.003	0.013
BCP	C_4O_4	0.494	0.627
BCP	C_1O_5	0.003	0.011
BCP	O_4O_5	0.003	0.015
BCP	C_5O_5	0.494	0.627
BCP	C_1C_3	0.005	0.017
BCP	C_2C_3	0.004	0.015
BCP	O_4O_3	0.003	0.012
BCP	O_3O_5	0.003	0.014
BCP	C_3O_3	0.495	0.642
BCP	C_6C_1	0.005	0.017
BCP	C_2C_6	0.004	0.015
BCP	O_4O_6	0.003	0.012
BCP	O_5O_6	0.003	0.014
BCP	O_6C_6	0.495	0.642
BCP	H_1O_1	0.342	-2.663
RCP	$C_6O_6O_4C_2O_2$	0.001	0.006
RCP	$C_1O_1H_1C_2C_3$	0.003	0.010
RCP	$C_3O_3O_5C_1$	0.001	0.006
RCP	$O_3O_4O_5$	0.001	0.006
RCP	$C_3O_3C_2O_2O_4$	0.001	0.006
RCP	$C_1O_1H_1C_2C_6$	0.003	0.010
RCP	$C_6O_6O_5C_1$	0.001	0.005
RCP	$O_6O_5O_4$	0.001	0.006
CCP	C_1, C_3, C_4, C_6, O_3, O_5, O_6	0.0005	0.002

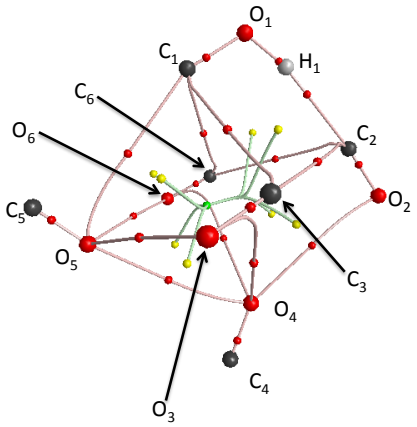

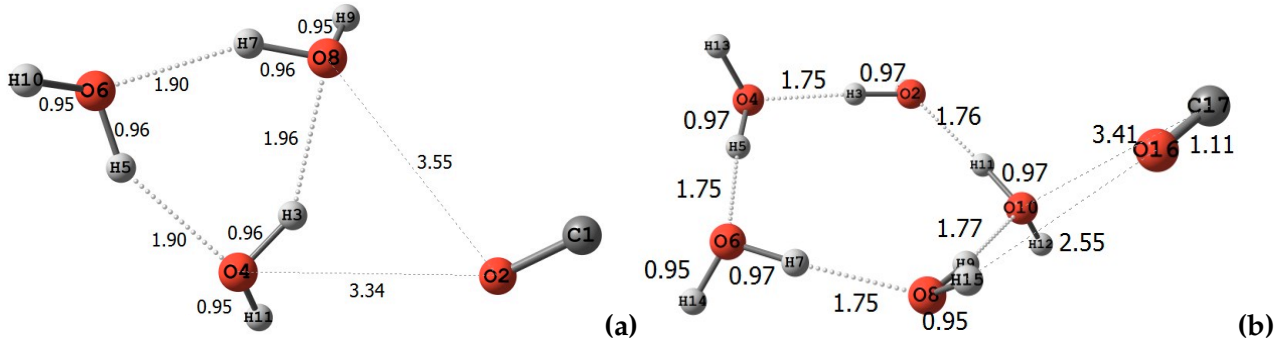

Figure 32: Mixed CO-H_2O clusters (a) CO and 3 H_2O, (b) CO and 5 H_2O. Distances are given in Å and angles in degrees

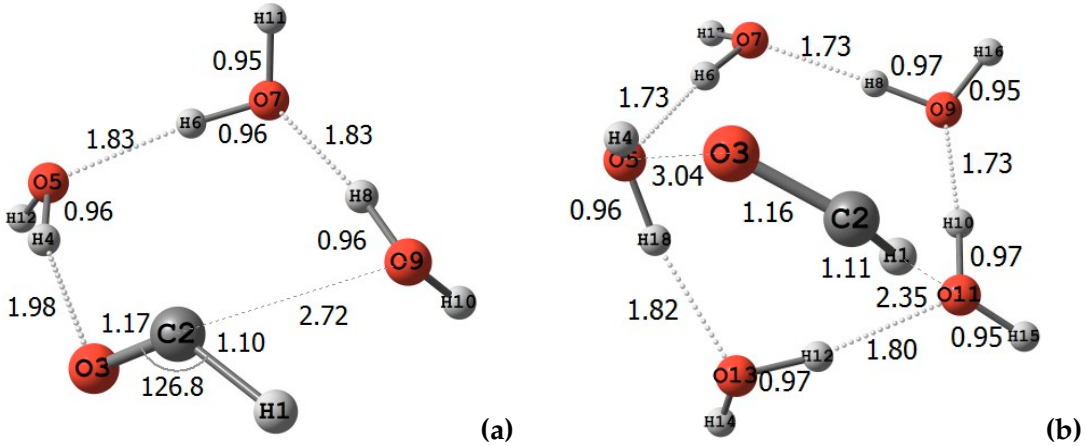

Figure 33: Mixed HCO-H_2O clusters (a) HCO · $(H_2O)_3$ and (b) HCO · $(H_2O)_5$. Distances given are in Å and angles in degrees

molecules which can participate in hydrogen bonding. We shall therefore proceed to consider the formation of HCO and COH in clusters of three and five water molecules.

4.4 FORMATION OF HCO AND COH IN CO · $(H_2O)_n$ CLUSTERS

4.4.1 *Energetics*

For these clusters the geometries have been optimised with the BHLYP and B97D functionals combined with the aug-cc-pVTZ basis set. The calculations were performed using DFT due to the difficulties obtaining TS structures with Turbomole. As such we switched to Gaussian and the MP2 optimisation became too computationally intensive.

Figures 32 to 35 show the geometries of CO, HCO, COH, and the transition states for the formation of HCO with 3 and 5 water molecules. Figure 36 shows the TS for the formation of COH with 3 water molecules.

From figure 32, in both cases, the CO sits quite far from the water cluster, but upon addition of hydrogen, it moves closer. This is due to the much weaker CO-H_2O interaction, with respect to the H_2O-H_2O interaction. Ultimately, the final proximity of HCO or COH to the cluster is determined by the strength of the hydrogen bond it can form with the cluster.

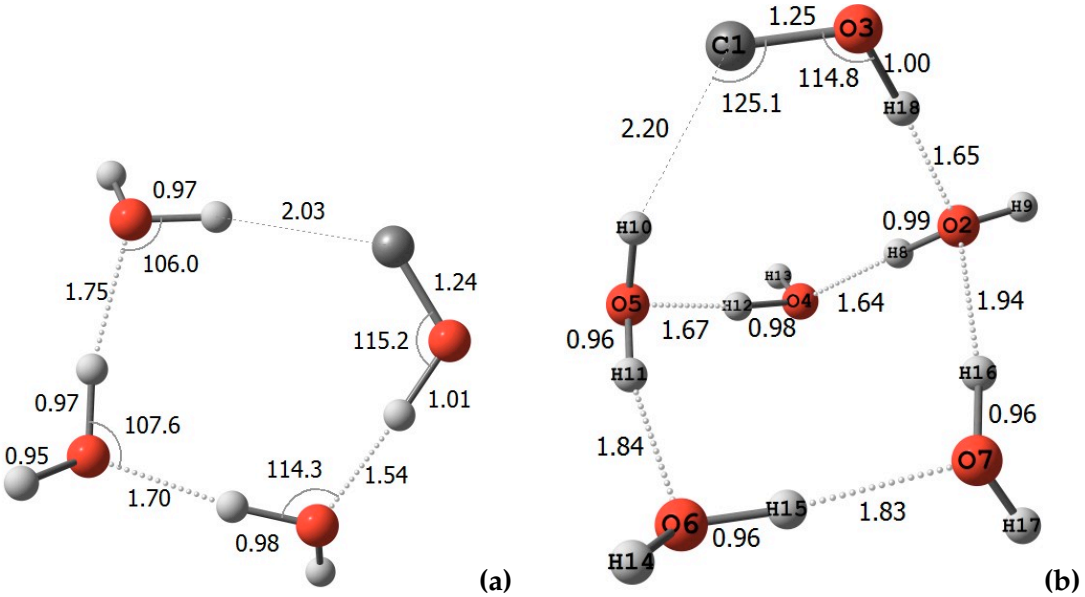

Figure 34: Mixed COH-H_2O clusters (a) $COH \cdot (H_2O)_3$ and (b) $COH \cdot (H_2O)_5$. Distances are given in Å and angles in degrees

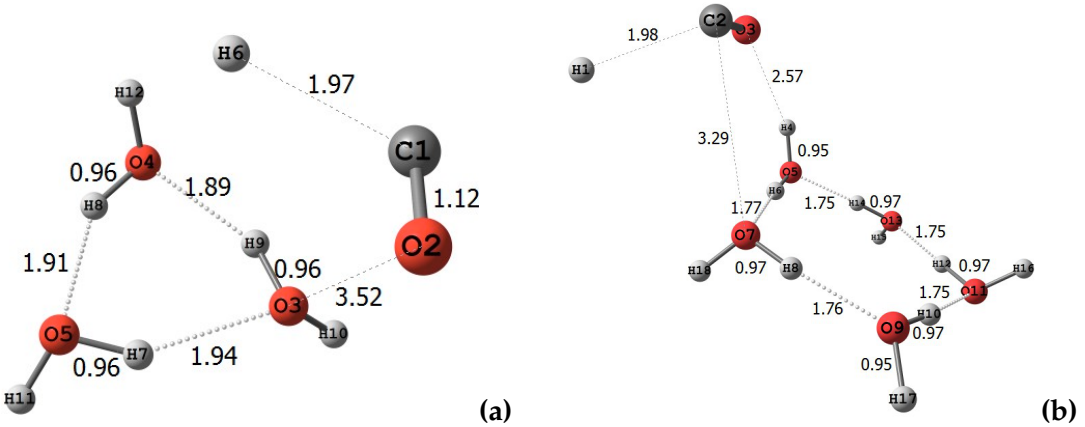

Figure 35: Mixed HCO H_2O clusters (a) TS in formation of HCO with $3\,H_2O$, (b) TS in formation of HCO with $5\,H_2O$. Distances are given in Å and angles in degrees

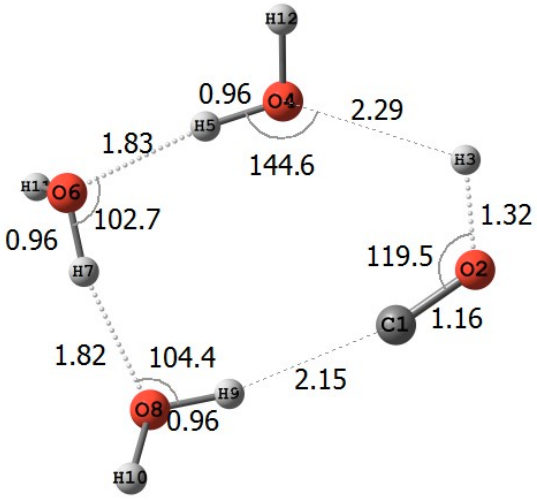

Figure 36: TS in formation the of COH with 3 H_2O. Distances are given in Å and angles in degrees

As a result, we see that in the case of the $COH \cdot (H_2O)_3$ cluster, the COH radical becomes integrated within the ring structure of the water molecules, figure 34. This seems to be accompanied by a substantial increase in the stability of COH, table 30. Indeed, irrespective of the functional employed, COH goes from being endothermic in formation in the gas phase to being weakly exothermic within the cluster. There is also enhancement in the stability of HCO but by comparison, it is much less significant. We can also reason that since HCO does not become incorporated within the ring, the HCO-H_2O interaction is weaker than the H_2O-H_2O interaction. This is not surprising since CHO hydrogen bonds are weaker than OHO hydrogen bonds.

From table 30, it also appears that the barrier to the COH formation is lowered by more than 6 kcal.mol^{-1}, though it still remains considerably larger than the barrier to the formation of HCO. In contrast, the barrier to HCO formation is relatively unchanged compared to the gas phase values: with BHLYP there is a decrease of 0.2 kcal.mol^{-1} and for B97D it increases by 0.07 kcal.mol^{-1}. This agrees well with the results previously reported by Woon, at the MP2, level where he observes a 0.2 kcal.mol^{-1} increase in the barrier height [190]. We also see, that within the 5 H_2O cluster, HCO is relatively unchanged, both in terms of stability and the barrier to its formation.

In contrast, COH is once again changed considerably within the 5 H_2O cluster. From table 30, the reaction becomes slightly endothermic once again. This suggests that the formation of COH is very much dependent upon the structure of the ice. It is clear that these shifts in stability of COH are due to the relative strengths of the hydrogen bonds it can form with the cluster. As such, we now proceed to analyse the interaction each species has with the clusters using AIM analysis.

4.5 AIM ANALYSIS OF MIXED CLUSTERS

4.5.1 *AIM analysis of CO, HCO, and COH with 3H_2O*

If we consider the BCPs and RCPs present in the $CO \cdot (H_2O)_3$ cluster, table 31, at first glance, there are two subsets of ρ: one set where ρ is quite large and the other set where it is considerably lower. We shall first consider the high values of ρ. On closer inspection, three distinct

Table 30: Activation energies, E_a, and energies of reaction, E_r, for the reaction of H with CO in the presence of 3 H_2O, 5 H_2O, and in the gas phase for reference. Energies have been computed using the aug-cc-pVTZ basis set and the functional listed, values given in kcal mol^{-1}. [a] Ref. [190]

Functional	Reaction	E_a	E_r
BHLYP	$H + CO \cdot (H_2O)_3 \rightarrow HCO \cdot (H_2O)_3$	1.54	-26.61
B97D	$H + CO \cdot (H_2O)_3 \rightarrow HCO \cdot (H_2O)_3$	3.93	-26.76
BHLYP	$H + CO \cdot (H_2O)_3 \rightarrow COH \cdot (H_2O)_3$	25.54	-2.20
B97D	$H + CO \cdot (H_2O)_3 \rightarrow COH \cdot (H_2O)_3$	16.60	-2.25
BHLYP	$H + CO \cdot (H_2O)_5 \rightarrow HCO \cdot (H_2O)_5$	1.62	-26.36
B97D	$H + CO \cdot (H_2O)_5 \rightarrow HCO \cdot (H_2O)_5$	3.73	-26.68
BHLYP	$H + CO \cdot (H_2O)_5 \rightarrow COH \cdot (H_2O)_5$	-	4.32
B97D	$H + CO \cdot (H_2O)_5 \rightarrow COH \cdot (H_2O)_5$	22.81	2.65
BHLYP	$H + CO \rightarrow HCO$	1.74	-18.35
B97D	$H + CO \rightarrow HCO$	3.86	-25.69
BHLYP	$H + CO \rightarrow COH$	33.62	+20.42
B97D	$H + CO \rightarrow COH$	22.81	+16.26
UMP2[a]	$H + CO \cdot (H_2O)_3 \rightarrow HCO \cdot (H_2O)_3$	7.51	-15.96
PMP2[a]	$H + CO \cdot (H_2O)_3 \rightarrow HCO \cdot (H_2O)_3$	4.75	-17.47
QCISD//UMP2[a]	$H + CO \cdot (H_2O)_3 \rightarrow HCO \cdot (H_2O)_3$	4.77	-18.65

Table 31: Values of the electron density, ρ. the laplacian, L, at the critical point between the nuclear centres (left) Molecular graph of the $CO \cdot (H_2O)_3$ cluster. Bond critical points are shown in red, and ring critical points are shown in yellow.(right)

Type of Critical Point	Nuclei involved	ρ	L (a.u)
BCP	C_1O_1	0.522	0.691
BCP	O_1H_{w1}	0.004	0.016
BCP	$H_{w2}O_{w2}$	0.024	0.086
BCP	$O_{w1}H_{w6}$	0.027	0.094
BCP	O_1O_{w2}	0.024	0.094
BCP	$H_{w4}O_{w3}$	0.028	0.092
BCP	$H_{w2}O_{w1}$	0.367	-2.829
BCP	$H_{w6}O_{w3}$	0.365	-2.818
BCP	$H_{w4}O_{w2}$	0.364	-2.806
BCP	$H_{w3}O_{w2}$	0.382	-2.879
BCP	$H_{w5}O_{w3}$	0.383	-2.882
BCP	$H_{w1}O_{w1}$	0.383	-2.892
RCP	$H_{w2}O_{w2}O_{w1}$ $H_{w4}O_{w3}H_{w6}$	0.008	0.036
RCP	O_1, O_{w1}, H_{w2}, O_{w2}	0.002	0.009

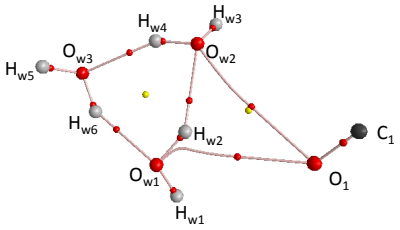

types of critical points are identifiable: one for the C_1O_1 interaction, one for OH groups involved in hydrogen bonding, and a final set for the OH groups which are not involved in hydrogen bonding.

The C_1O_1 interaction shows the same large value of ρ and positive value of L that we saw in the CO clusters. The two sets corresponding to the OH groups are all covalent with those OH groups participating in hydrogen bonding, showing a slightly lower density and slightly more positive laplacian than those which are not.

If we now consider the interactions between the molecules, all of the hydrogen bonds within the water cluster are more or less the same, with the bond between H_{w2} and O_{w2} being slightly perturbed by the CO. The one interaction between the CO is clearly stronger than the other, which is evidenced by the relative proximity of the CO to one of the water molecules and also by the location of the RCP. The RCP enclosed by $H_{w2}O_{w2}O_{w1}$ $H_{w4}O_{w3}H_{w6}$ is very close to the BCP between O_1O_{w2}, indicating a movement of O_1 away from the cluster, by only a small amount, would result in the loss of both of these critical points. In contrast, due to the relative strength and similarity of the interactions within the water cluster, the RCP is quite centrally positioned.

If we now consider the $HCO \cdot (H_2O)_3$ cluster, the CO bond once again shows its classic large value of ρ and positive Laplacian, table 25. As with the $CO \cdot (H_2O)_3$ cluster, there is a distinct difference between the OH groups which are involved in hydrogen bonding compared to those which are not. The interaction between O_1H_{w2} is clearly stronger than the interaction between C_1O_{w2}, evidenced by the difference in the values of ρ and L of the two interactions

Table 32: Values of the electron density, ρ. the laplacian, L, at the critical point between the nuclear centres (left) Molecular graph of the $HCO \cdot (H_2O)_3$ cluster. Bond critical points are shown in red, and ring critical points are shown in yellow.(right)

Type of Critical Point	Nuclei involved	ρ	L (a.u)
BCP	C_1O_1	0.453	0.409
BCP	C_1O_{w2}	0.013	0.052
BCP	$H_{w4}O_{w3}$	0.032	0.095
BCP	O_1H_{w2}	0.021	0.077
BCP	$O_{w1}H_{w6}$	0.032	0.096
BCP	H_1C_1	0.284	-1.147
BCP	$H_{w2}O_{w1}$	0.371	-2.861
BCP	$H_{w6}O_{w3}$	0.362	-2.798
BCP	$H_{w4}O_{w2}$	0.362	-2.791
BCP	$H_{w3}O_{w2}$	0.384	-2.863
BCP	$H_{w5}O_{w3}$	0.383	-2.878
BCP	$H_{w1}O_{w1}$	0.382	-2.887
RCP	C_1, O_1, O_{w1}-O_{w3}, H_{w2}, H_{w4}, H_{w6}	0.148	0.007

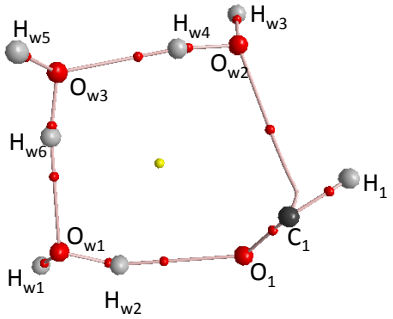

as well as the bent bond path between C_1O_{w2}. In addition, there is no interaction between H_1 and the cluster.

Finally, we note that given the geometry of the system, it is not immediately obvious how one could go about directly forming formaldehyde without encountering significant steric effects, figure 37(a). As can be seen from figure 37(a), if the cluster is part of a surface, then the initial hydrogen will have been added from above the surface. Consequently, any approach to the carbon atom encounters the first hydrogen atom. However, the approach to the oxygen atom is open, in terms of steric effects, though this would lead to the formation of *cis*-HCOH.

In contrast with the $CO \cdot (H_2O)_3$ and $HCO \cdot (H_2O)_3$ the COH becomes fully integrated within the ring of water molecules by forming two hydrogen bonds. From table 33, within this cluster, the interaction of the carbon atom and the water cluster is much stronger than in the other two clusters. Indeed the value of ρ at the BCP between $H_{w2}C_1$ here is almost twice that of the same BCP in the $HCO \cdot (H_2O)_3$ cluster.

The interaction between H_1O_{w2} is also comparable to the interactions between the other water molecules. Evidently, it is a combination of these two interactions which leads to the greatly enhanced stability of COH within the $COH \cdot (H_2O)_3$ cluster, compared to the gas phase. From the geometry, it is clear that the carbon is relatively open for attack of the next hydrogen, figure 37(b), though this would lead to the formation of *trans*-HCOH and not H_2CO.

Table 33: Values of the electron density, ρ. the laplacian, L, at the critical point between the nuclear centres (left) Molecular graph of the $COH \cdot (H_2O)_3$ cluster. Bond critical points are shown in red, and ring critical points are shown in yellow.(right)

Type of Critical Point	Nuclei involved	ρ	L (a.u)
BCP	$H_{w2}O_{w1}$	0.354	-2.805
BCP	$O_{w1}H_{w6}$	0.037	0.114
BCP	$H_{w6}O_{w3}$	0.352	-2.837
BCP	$O_{w3}H_{w4}$	0.043	0.119
BCP	$O_{w2}H_{w4}$	0.343	-2.778
BCP	H_1O_{w2}	0.064	0.130
BCP	H_1O_1	0.304	-2.393
BCP	$H_{w2}C_1$	0.028	0.055
BCP	C_1O_1	0.370	0.344
BCP	$H_{w3}O_{w2}$	0.381	-2.957
BCP	$H_{w1}O_{w1}$	0.382	-2.950
BCP	$H_{w5}O_{w3}$	0.382	-2.952
RCP	H_1, O_1, C_1, H_{w2}, O_{w1}, H_{w6}, O_{w3}, H_{w4}, O_{w2}	0.002	0.007

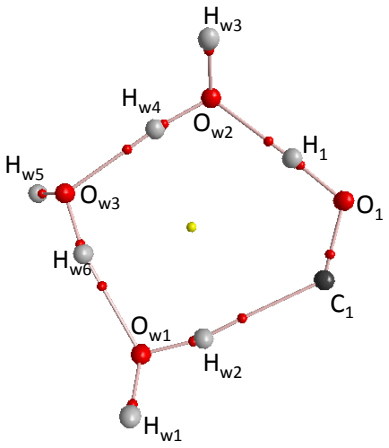

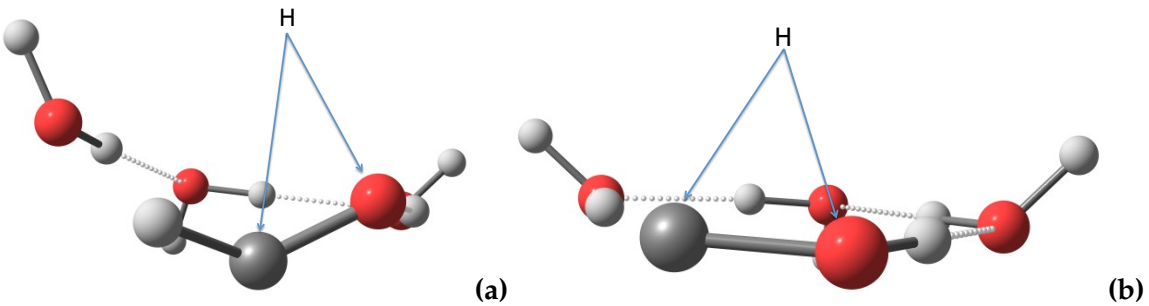

Figure 37: Figures showing the approach of a second hydrogen atom to (a)the $HCO \cdot (H_2O)_3$ cluster and (b) the $COH \cdot (H_2O)_3$ cluster. The approaches shown consider that the cluster is part of a surface.

Table 34: Values of the electron density, ρ. the laplacian, L, at the critical point between the nuclear centres (left) Molecular graph of the $CO \cdot (H_2O)_5$ cluster. Bond critical points are shown in red, and ring critical points are shown in yellow.(right)

Type of Critical Point	Nuclei involved	ρ	L (a.u)
BCP	$H_{w5}O_{w3}$	0.383	-2.877
BCP	$H_{w7}O_{w4}$	0.353	-2.737
BCP	$H_{w7}O_{w3}$	0.396	0.103
BCP	$H_{w5}O_{w3}$	0.353	-1.370
BCP	$H_{w5}O_{w2}$	0.395	0.104
BCP	$H_{w3}O_{w2}$	0.353	-2.737
BCP	$H_{w3}O_{w1}$	0.399	0.104
BCP	$H_{w2}O_{w1}$	0.356	-2.758
BCP	$H_{w9}O_{w4}$	0.378	0.103
BCP	$H_{w2}O_{w5}$	0.377	0.101
BCP	$H_{w9}O_{w5}$	0.354	-2.750
BCP	$H_{w10}O_{w5}$	0.383	-2.875
BCP	$H_{w6}O_{w3}$	0.383	-2.875
BCP	$H_{w4}O_{w2}$	0.383	-2.878
BCP	$H_{w1}O_{w1}$	0.382	-2.882
BCP	O_1O_{w5}	0.355	0.013
BCP	$H_{w1}O_1$	0.006	0.024
BCP	C_1O_1	0.521	0.677
RCP	O_1, O_{w5}, H_{w2}, O_{w1}	0.003	0.011
RCP	O_{w1}-O_{w5}, H_{w2}, H_{w3}, H_{w5}, H_{w7}, H_{w9}	0.001	0.003

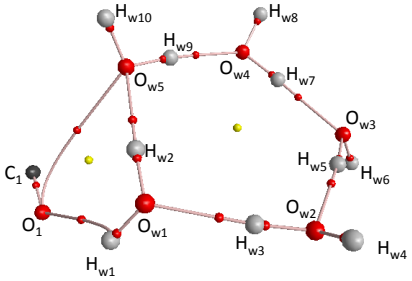

4.5.2 *AIM analysis of CO, HCO, and COH with $5H_2O$*

With regard to the $CO \cdot (H_2O)_5$ cluster, there is little difference compared to the $CO \cdot (H_2O)_3$ cluster, table 34. The CO forms two relatively weak interactions with the cluster through O_1. We once again see the difference between the OH groups involved in hydrogen bonding and those which are not.

Likewise, for the $HCO \cdot (H_2O)_5$ cluster, table 35, the only notable difference from the $HCO \cdot (H_2O)_3$ cluster is the interaction of H_1 with the cluster. The interaction, whilst weak, is important, since it provides easy access to the carbon atom for further reactions, figure 38(a). In considering figure 38, in both cases, the carbon atom is accessible for onward reaction. This would mean that in the $(H_2O)_5$ cluster, one could conceivably form formaldehyde directly, unlike the $(H_2O)_3$ cluster.

Furthermore, the stability of HCO increases slightly compared to the gas phase: the exothermicity of the reaction is ~ 26 kcal.mol^{-1} vs. ~ 18 kcal.mol^{-1} with BHLYP; there is little

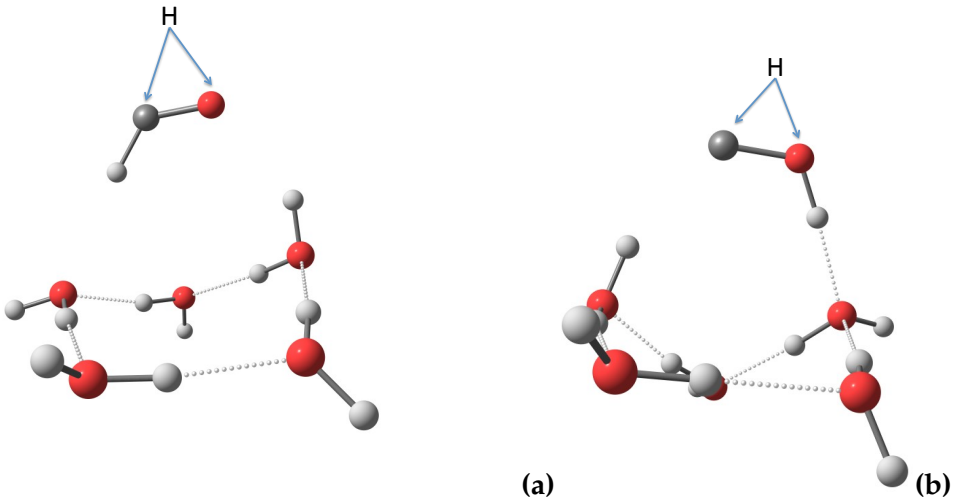

Figure 38: Figures showing the approach of a second hydrogen atom to (a)the $HCO \cdot (H_2O)_5$ cluster and (b) the $COH \cdot (H_2O)_3$ cluster. The approaches shown consider that the cluster is part of a surface.

difference with B97D with only ~ 1 kcal.mol^{-1} difference between the cluster and the gas phase.

Once again, the $COH \cdot (H_2O)_5$ shows a greater change in comparison, table 36. The two hydrogen bonds which provided the aditional stability in the $COH \cdot (H_2O)_3$ cluster have both been weakened. This therefore explains why the reaction ergicity undergoes the change it does, namely to become positive.

It seems therefore that the number of hydrogen bonds that COH can form with the water cluster, or indeed with an ice surface, and their relative strengths play a crucial role in the stability and thus the ergicity of the formation of COH.

4.6 SUMMARY

In this chapter we have considered how cluster size and composition affect the formation of HCO and COH. The formation of HCO is relatively unaffected by either the cluster size or its composition. With this in mind, we consider that the gas phase formation of HCO is unchanged by the surface. Therefore any catalytic effect observed in the rate of formation HCO is brought about by the fact the surface increases the contact time between the hydrogen atom and the CO molecule.

In comparing the $HCO \cdot (H_2O)_3$ cluster results with the previous work of Woon [190], we see that both BHLYP and B97D predict lower activation energies than the values of Woon (UMP2 7.51, PMP2 4.75, QCISD//UMP2 4.77 kcal.mol^{-1}). In addition both functionals predict greater exothermicities for the reactions by at least 8 kcal.mol^{-1}. With respect to the barrier heights, we recall that these functionals were chosen because the barrier height they gave for the gas phase reaction was either in good agreement with the Wang et al [57] experimental value, BHLYP, or the MRCI+Q value, B97D. Since in both cases only small shifts in the barrier heights occur, we can expect they are performing reasonably well. The difference therefore between the MP2 results of Woon and the functionals is then likely due to the spin contaminant being considerably different between the two calculations. Indeed, since the UMP2 activation energy Woon provides for the gas phase is almost twice the value we

Table 35: Values of the electron density, ρ. the laplacian, L, at the critical point between the nuclear centres (left) Molecular graph of the $HCO \cdot (H_2O)_5$ cluster. Bond critical points are shown in red, and ring critical points are shown in yellow.(right)

Type of Critical Point	Nuclei involved	ρ	L (a.u)
BCP	C_1O_1	0.455	0.457
BCP	$H_{w6}O_1$	0.013	0.054
BCP	$H_{w4}O_{w3}$	0.042	0.104
BCP	$H_{w2}O_{w2}$	0.041	0.107
BCP	H_1O_{w5}	0.011	0.040
BCP	$H_{w10}O_{w1}$	0.042	0.105
BCP	$H_{w5}O_{w4}$	0.033	0.097
BCP	$H_{w8}O_{w5}$	0.035	0.099
BCP	H_1C_1	0.280	-1.121
BCP	$H_{w6}O_{w3}$	0.377	-2.873
BCP	$H_{w4}O_{w2}$	0.350	-2.711
BCP	$H_{w2}O_{w1}$	0.351	-2.724
BCP	$H_{w10}O_{w5}$	0.349	-2.708
BCP	$H_{w8}O_{w4}$	0.360	-2.785
BCP	$H_{w7}O_{w4}$	0.383	-2.884
BCP	$H_{w9}O_{w5}$	0.382	-2.880
BCP	$H_{w1}O_{w1}$	0.383	-2.875
BCP	$H_{w3}O_{w2}$	0.383	-2.881
BCP	$H_{w5}O_{w3}$	0.361	-2.793
RCP	H_1, C_1, O_1, O_{w5}, H_{w8}, O_{w4}, H_{w5}, O_{w3}, H_{w6}	0.003	0.011
RCP	O_{w1}-O_{w5}, H_{w2}, H_{w4}, H_{w5}, H_{w8}, H_{w10}	0.001	0.003

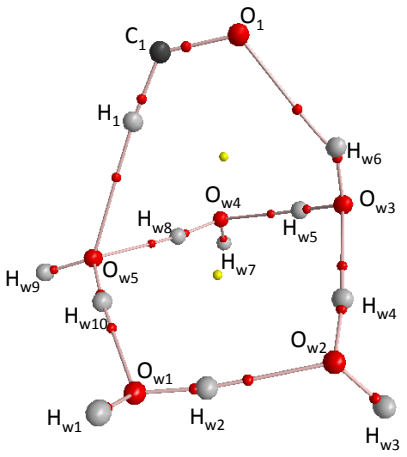

Table 36: Values of the electron density, ρ. the laplacian, L, at the critical point between the nuclear centres (left) Molecular graph of the $COH \cdot (H_2O)_5$ cluster. Bond critical points are shown in red, and ring critical points are shown in yellow.(right)

Type of Critical Point	Nuclei involved	ρ	L (a.u)
BCP	C_1O_1	0.363	0.135
BCP	H_1O_1w3	0.052	0.104
BCP	$H_{w5}O_{w4}$	0.053	0.114
BCP	$H_{w10}C_1$	0.020	0.045
BCP	$H_{w7}O_{w5}$	0.049	0.109
BCP	$H_{w9}O_{w1}$	0.321	0.096
BCP	$H_{w4}O_{w3}$	0.025	0.081
BCP	$H_{w2}O_{w2}$	0.032	0.095
BCP	$H_{w5}O_{w3}$	0.333	-2.575
BCP	$H_{w6}O_{w3}$	0.380	-2.887
BCP	$H_{w10}O_{w5}$	0.367	-2.793
BCP	$H_{w9}O_{w5}$	0.361	-2.789
BCP	$H_{w7}O_{w4}$	0.339	-2.610
BCP	$H_{w8}O_{w4}$	0.382	-2.884
BCP	$H_{w1}O_{w1}$	0.383	-2.878
BCP	$H_{w2}O_{w1}$	0.362	-2.797
BCP	$H_{w4}O_{w2}$	0.368	-2.836
BCP	$H_{w3}O_{w2}$	0.382	-2.878
BCP	H_1O_1	0.326	-2.502
RCP	H_1, C_1, O_1, O_{w5}, H_{w7}, O_{w4}, H_{w5}, O_{w3}, H_{w10}	0.002	0.008
RCP	O_{w1}-O_{w5}, H_{w2}, H_{w4}, H_{w5}, H_{w7}, H_{w9}	0.001	0.004

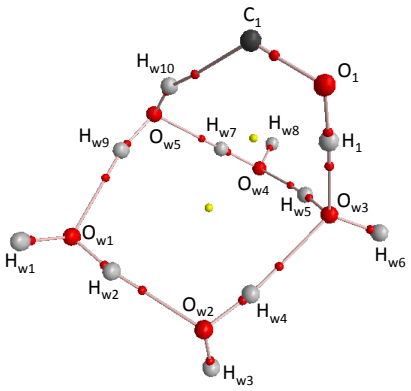

have at the MRCI+Q level, the spin contaminant is likely quite different from the 0.75 value it should have. This is indeed, made quite clear by the fact that the PMP2 value he provides for the same process is only ~ 0.5 kcal.mol^{-1} higher than the value we obtain at the MRCI+Q level. Here, PMP2 projects out the spin and so resolves to a certain degree the contamination of the wavefunction.

With regard to the reaction exothermicity, both functionals over predict this value in the gas phase as well. So whilst we cannot use the results in a quantitative manner, they should at least provide a reasonable qualitative picture. This therefore supports the claim that the formation of HCO is in fact changed very little by the presence of the cluster.

In contrast, the formation of COH is strongly affected by the size and composition of the cluster. In the CO clusters, the formation is relatively unchanged but within water clusters, things are very different. Indeed, in the presence of only a few water molecules the reaction becomes slightly exothermic. On increasing the size of the cluster, the reaction becomes slightly endothermic due to a decrease in the relative strength of the hydrogen bonds with the cluster.

In considering the subsequent hydrogenations, for the water clusters, there is a size effect. Due to the hydrogen bonding in the $(H_2O)_5$ cluster, addition to the carbon atoms is always possible. As such, it is possible to form H_2CO directly from HCO. However, in the $(H_2O)_3$ clusters, for steric reasons attack at the carbon of HCO is no longer possible and as such from both the $HCO \cdot (H_2O)_3$ and the $COH \cdot (H_2O)_3$ clusters, we can only directly form HCOH. This is of significance for the astrophysical models since they currently only consider that H_2CO can be formed and not HCOH. Furthermore, they do not consider that the local structure could have such a large influence on the chemistry that could occur.

Finally, we note that within the CO clusters, upon addition of the hydrogen, the relative orientations of the CO units change. Whilst this is representative of the fact that the relative positions are not determined by the space group of α-CO, once the solid is formed, they are fixed. Consequently, if it were possible to model an actual CO surface this would not occur, and the fact that we see it here represents a deficiency of the cluster approach.

We therefore conclude that the formation of COH is strongly dependent upon the surface structure. In the following chapter, we shall consider the formation of HCOH and H_2CO from both HCO and COH in the gas phase. We shall also consider the effect water has on the isomerisation of *trans*-HCOH to H_2CO.

Chapter V

REACTION OF HYDROGEN ATOMS WITH HCO AND COH

5

REACTION OF HYDROGEN ATOMS WITH HCO AND COH

5.1 INTRODUCTION

Typically for the second hydrogenation step, only the addition of hydrogen to HCO to form H_2CO is considered. This is due to the fact that it is assumed to be barrierless. Here, we have considered that one may also form *cis* and *trans*-HCOH from HCO. Indeed, from some of the structures obtained within chapter 4 the formation of these two isomers of H_2CO my be more favoured for steric reasons. The formation of all three species have been considered in the gas phase, and in addition the isomerisation of *trans*-HCOH to H_2CO has been considered in clusters of water.

5.2 COMPUTATIONAL METHODS

For the second hydrogenation we have benchmarked the gas phase process at the MRCI+Q level with the aug-cc-pVTZ basis set. This has been conducted using a (16 e^{-1}, 12 MO's) active space for the CASSCF procedure. Whilst for the CASSCF the 1s orbitals were used these core orbitals were kept inactive in the MRCI+Q calculation. The inclusion of the 1s orbitals in the CASSCF was necessary due to the population of the 3rd orbital being almost 2 and consequently the Oxygen 1s and orbital 3 being exchanged by the software for HCOH, (this occurred with Molpro and GAMESS). Consequently for the MRCI calculation this then lead to the correlation energy being underestimated and subsequently making HCOH some 30 kcal.mol^{-1} less stable. This reordering only occurred for HCOH, and not the trasition states or H_2CO, and only in the CASSCF procedure.

5.3 GAS PHASE FORMATION OF *cis*-HCOH, *trans*-HCOH AND H_2CO

As with the first addition, both the addition of a hydrogen atoms to the carbon and oxygen have been considered (see figure 39). In this case, only the ^{1}A' surface has been considered as the singlet-triplet gap is at least 25 kcal.mol^{-1} for all the stationary points [191]. The only exception to this this is the TS in formation of *trans*-HCOH where it is smaller due to the fact the combination of two doublets at long distances can either be calculated as a singlet or triplet, and indeed both state are degenerate at infinite separation. For formaldehyde, it is considerably larger, $\sim$ 70 kcal.mol^{-1} [191, 192].

When adding the hydrogen to the oxygen atom, we find activation energies of 9.05 kcal.mol^{-1}, for the formation of *cis*-HCOH, and 7.63 kcal.mol^{-1}, for the formation of *trans*-HCOH, see figure 39. As can be seen in figure 40, the existence of a saddle point in the formation of *trans*-HCOH may be rationalised by considering the electronic arrangements at long and short internuclear distances. When the hydrogen atom is approaching the oxygen end of the formyl radical in its ground ^{2}A' state , the formation of the OH bond requires the transfer of one electron of the doubly occupied O lone pair to the carbon one. Thus, the presence of the saddle point may be interpreted as the avoided crossing between the first and second ^{1}A' potential energy surfaces of HCOH. It should also be stated that the TS is

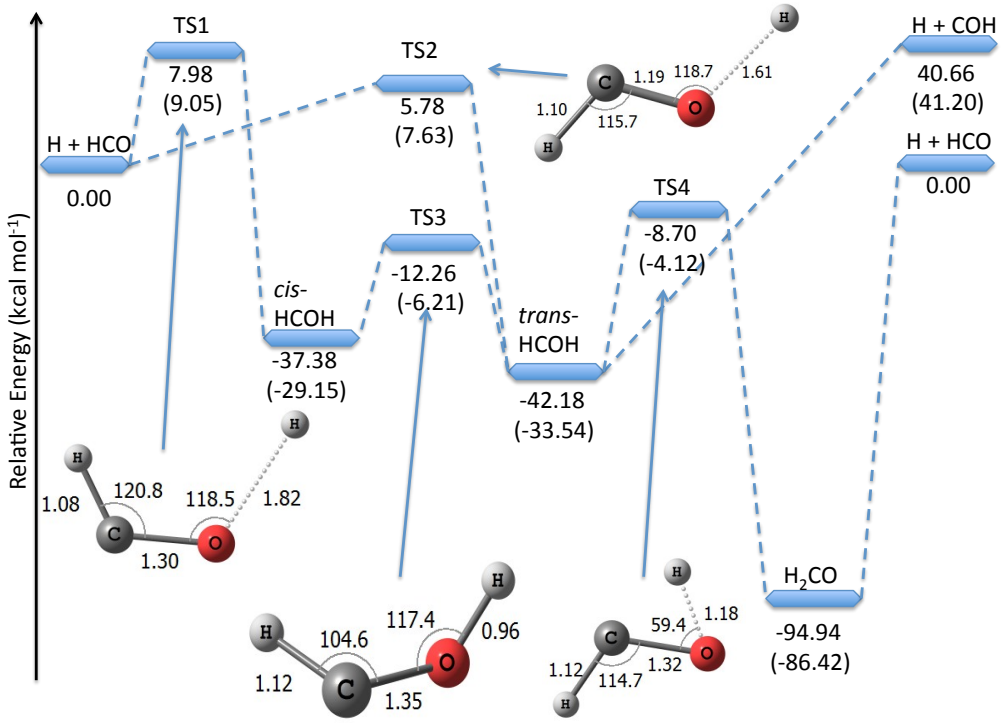

Figure 39: Stationary points in the addition of H to HCO and COH in the gas phase. Energies given were computed at the MRCI+Q/aug-cc-pVTZ level and are given in kcal mol^{-1}. Values in parentheses include the harmonic zero point energy

only found when using CCSD(T) and multi reference methods. B3LYP and the M06 family of functionals fail to find a TS and also predict the wrong dissociation limit. MP2 is able to find a TS, but predicts that the dissociated reactants are more stable than the product.

In contrast if we consider the same process on the first $^3A'$ state, such a rearrangement is not necessary. In this case, we see that the formation of HCOH is barrierless, though the potentail is in fact dissociative.

On the other hand, hydrogen addition to the carbon atom is indeed barrierless, figure 39. However, we see that the reactants are higher in energy than the saddle point for the isomerization between *trans*-HCOH and H_2CO and also the TS for the isomerization between *cis*-HCOH and *trans*-HCOH. This agrees well with the idea of having a roaming hydrogen atom on this PES as proposed by Bowman et al [193–198].

Consequently, the formation of HCOH from this reaction may not be ruled out, but would rather be dependent on the flux of hydrogen atoms and the branching ratios of the reactions. Therefore, when considering the availability of HCOH for further reactions, one must consider : the branching ratios of both direct and indirect formation of the two stereoisomers of HCOH, the isomerisation of between the *cis* and *trans*-HCOH isomers, the isomerisation of HCOH to H_2CO, and the rate of addition of hydrogen to HCOH. With this in mind, in the following section, we look in detail at the isomerisation of *trans*-HCOH to H_2CO in the gas phase and in the presence of a few water molecules.

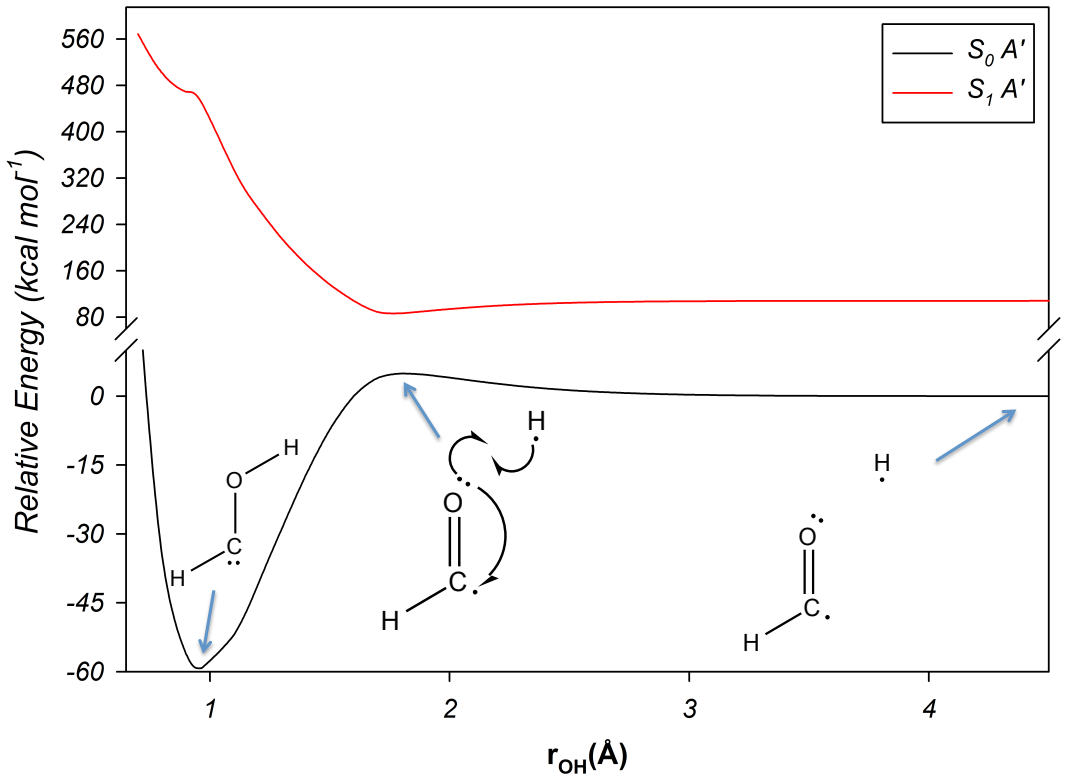

Figure 40: Plot showing the avoided crossing between the ground singlet A′ state potential, S_0, and the 1st excited singlet A′ state, S_1. Geometries shown highlight the structural changes as one proceeds along the potentials. Single headed curly arrows indicate the movement of a single electron.Potentials computed at the CASSCF/aug-cc-pVTZ level.

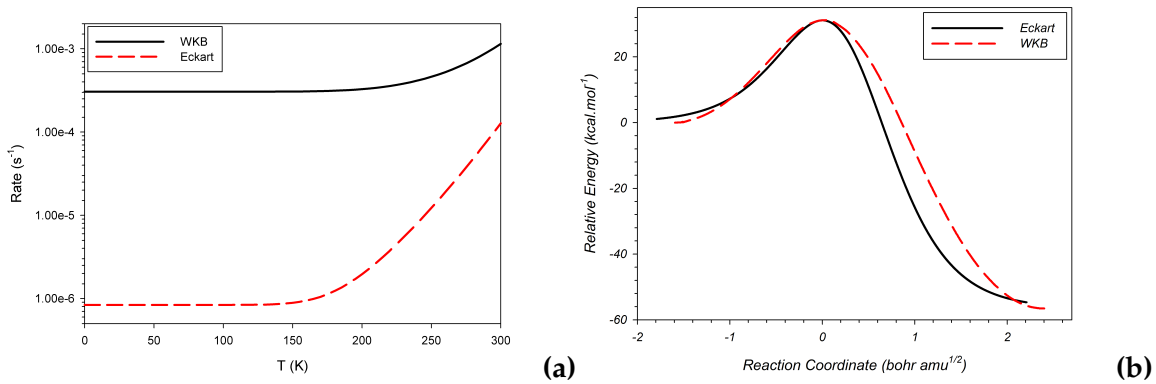

Figure 41: (a)Rate constants for the gas phase isomerisation of HCOH to H_2CO as a function of the temperature, T. Rates computed using the MRMP2/aug-cc-pVTZ energies in combination with the Eckart and WKB methods. (b) the IRC and Eckart potentials used for computing the rate constants.

5.3.1 *Tunnelling rates for the trans-HCOH to H_2CO isomerisation in the gas phase*

In order to compute the rate constants for the gas phase isomerisation using multi-reference methods, it was necessary to switch to the MRMP2 level [125] and the GAMESS package [146, 147]. This necessity arises since Molpro [148] does not compute IRCs, consequently since with GAMESS it is not possible to compute at the MRCI+Q we had to work at the lower level.

In considering figure 41(a), we see that the Eckart method predicts a rate constant for the process which is at least 2 orders of magnitude lower than the WKB result. In addition, in comparison to the rate constant computed by Kiselev [192], $k(0K) = 9.2x10^{-5}$ s^{-1}, and the experimentally determined $t_{\frac{1}{2}}$ value [199], ~ 2 hours, we see that the WKB rate is slightly higher and the Eckart is much too low.

The reason our WKB result is higher than the ones previously computed is that the MRMP2 barrier is lower and as such, the area under the IRC is reduced, leading to a higher transmission probability. Conversely, the Eckart rates agree with the observation made by Kiselev [192], in that the rates are underestimated by the method. The cause of this underestimation lies in the fact that the Eckart potential is wider than the IRC potential, as demonstrated by Kiselev [192] and also shown in figure 41(b).

In spite of this discrepancy, we shall continue to consider the effect that water has on this isomerisation process. This will be done by considering HCOH, H_2CO, and the isomerisation TS within $(H_2O)n$ clusters. We shall consider clusters with n being sequentially increased from 0 to 3.

5.4 REACTIONS IN $(H_2O)N$ CLUSTERS

5.4.1 *Trans-HCOH to H_2CO isomerisation*

In the study of Zhang et al. [200], the isomerization of *trans*-hydroxymethylene to formaldehyde has been considered as part of the photodissociation of formaldehyde producing H_2 and CO. The activation energy computed at CCSD(T) / aug-cc-pVTZ level, is reported to be

equal to 34.75 kcal mol^{-1}. Another computational study [191] considers this isomerization in a series of reactions starting from ground state carbon atoms associated with water at the CCSD(T) / aug-cc-pVTZ level. The zero-point corrected activation energy calculated at the CCSD(T) / cc-pVTZ level, is calculated to be 30.5 $kcal.mol^{-1}$ in their study. Further to these studies, the isomerisation was also considered at the CCSDT(Q)/CBS + ZPE level by Schreiner et al. [199] where the barrier is reported to be 29.7 $kcal.mol^{-1}$.

In the present study, the activation energy varies, dependent on the method employed, within the range 30.46 to 38.88 kcal mol^{-1} and between 26.31 and 34.79kcal mol^{-1} with the ZPE correction. The B3LYP energies, agree very well with the values previously computed at the CCSD(T) / cc-pVTZ level by Schreiner et al. [191], table 37. Whereas the non corrected one is in closer agreement with Zhang et al.. [200]. With respect to the CCSDT(Q) results [199], the CCSD energies calculated with the augmented basis set over-predict the barrier height by almost ~ 4 $kcal.mol^{-1}$, table 37, whereas the MP2 energies underpredict the barrier by almost ~ 3 $kcal.mol^{-1}$. We see that the M06, M06-L and CASSCF/MRCI(+Q) results are in good agreement with the CCSDT(Q) results [199] suggesting that the M06 functional may perform reasonably well. Further to this, given the close agreement between the CCSDT(Q) [199] and the results from multireference methods it would appear that the wavefunction is well described by a single determinant.

However, we also note within the M06 family of functionals, there is a degree of variation, figure 42, with the M06-HF functional performing the worst in comparison with the CCSDT(Q) results [199]. This is significant since in the calculation of reaction rates, a difference of ~ 1 $kcal.mol^{-1}$ in the activation energy can lead to a difference of up to an order of magnitude in the rate. In contrast to the energetics, the geometries do not vary greatly with the method used. Whilst the variation in the angles is much greater than for the bond lengths, the actual arrangement of the atoms does not alter significantly. Additionally, in comparing the MP2/aug-cc-pVTZ geometries with the CCSD(T)/cc-pCVQZ geometries of Schreiner et al [199] we see only minor variations. For illustrative purposes the gas phase transition state (TS) is shown in figure 43(a). For comparison the bond lengths computed by Schreiner et al. [199] are shown in parentheses within the figure.

As evidenced for the HNC/HCN isomerization [201] and for some other reactions, such as the H_2CO + HCN, and the HCN + NH_3 [202–205], that have unfavorably high activation energies in the gas phase, water can play the role of a catalyst. We decided to add one explicit water molecule that can actively participate in the reaction. In the TS structure, shown in figure 43(b), the dissociating hydrogen of HCOH is transferred to the water molecule and one of the hydrogen atoms of the water molecule is subsequently transferred to the carbon atom. Analysis of the normal modes shows that within this TS structure the H atom transfer corresponds to only one imaginary mode, making it consistent with a concerted mechanism. With respect to the different methods, the absolute geometrical parameters show some variations, more especially for the lengths of the two hydrogen bonds present in the TS, whereas the angles and lengths of the covalent bonds have similar values. Consequently, the five membered ring geometry is conserved regardless of the method chosen.

Table 37: Activation Energies E_a with and without the ZPE correction for the case with $N = 0$ and $N = 1$. Energies are given in kcal mol^{-1}. [a] Zhang et al.[200] [b] Schreiner et al. [191] [c] Schreiner et al.[199] [d] Kiselev at al [192]

		N = 0		N = 1	
Method	Basis	E_a	E_a + ZPE	E_a	E_a + ZPE
B3LYP	6-31+G**	34.21	37.06	8.14	4.94
	aug-cc-pVTZ	34.27	30.54	8.93	5.69
M06-HF	6-31+G**	39.24	35.33	6.69	3.76
	aug-cc-pVTZ	38.88	34.79	7.83	5.06
M06	6-31+G**	33.15	29.47	10.15	7.05
	aug-cc-pVTZ	32.84	29.11	10.45	7.34
M06-L	6-31+G**	31.87	28.08	9.89	6.58
	aug-cc-pVTZ	31.29	27.57	10.01	6.46
M06-2X	6-31+G**	35.64	31.84	9.02	5.90
	aug-cc-pVTZ	35.27	31.45	9.84	6.66
MP2	6-31+G**	39.34	35.49	9.48	6.27
	aug-cc-pVTZ	30.46	26.61	6.84	4.47
CCSD	6-31+G**	38.51	34.41	15.30	12.16
	aug-cc-pVTZ	37.39	33.37	13.74	10.62
CCSD(T)	6-31+G**	35.80	31.82	13.17	9.87
	aug-cc-pVTZ	34.31	30.29	11.10	7.93
CASSCF/RS2C	6-31+G**	34.37	30.54	-	-
	aug-cc-pVTZ	30.59	26.31	-	-
CASSCF/MRCI(+Q)	6-31+G**	34.89	30.81	-	-
	aug-cc-pVTZ	33.48	29.42	-	-
CCSD(T)[a]	aug-cc-pVTZ	34.75	-	-	-
CCSD(T)[b]	cc-VTZ	-	30.5	-	-
CCSDT(Q)[c]	CBS limit	-	29.7	-	-
CCSD(T)//QCISD[d]	aug-cc-pVTZ	-	30.3	-	-

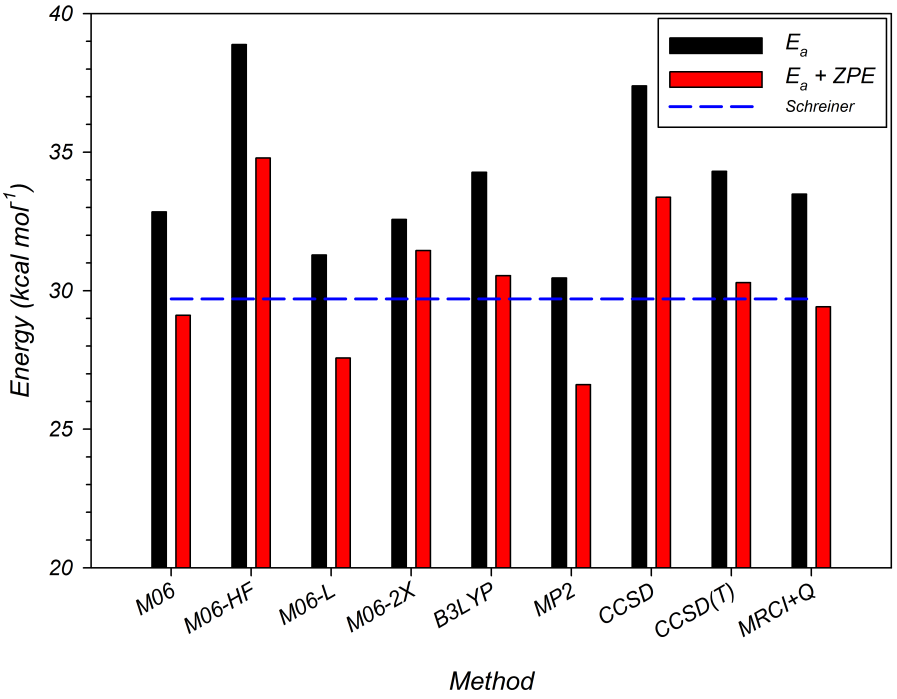

Figure 42: Variation of the activation energy, E_a, and the zero point corrected activation energy, E_a + ZPE for the methods indicated with the aug-cc-pVTZ basis set in the gas phase. The value of Screiner et al [199] is also shown for comparison.

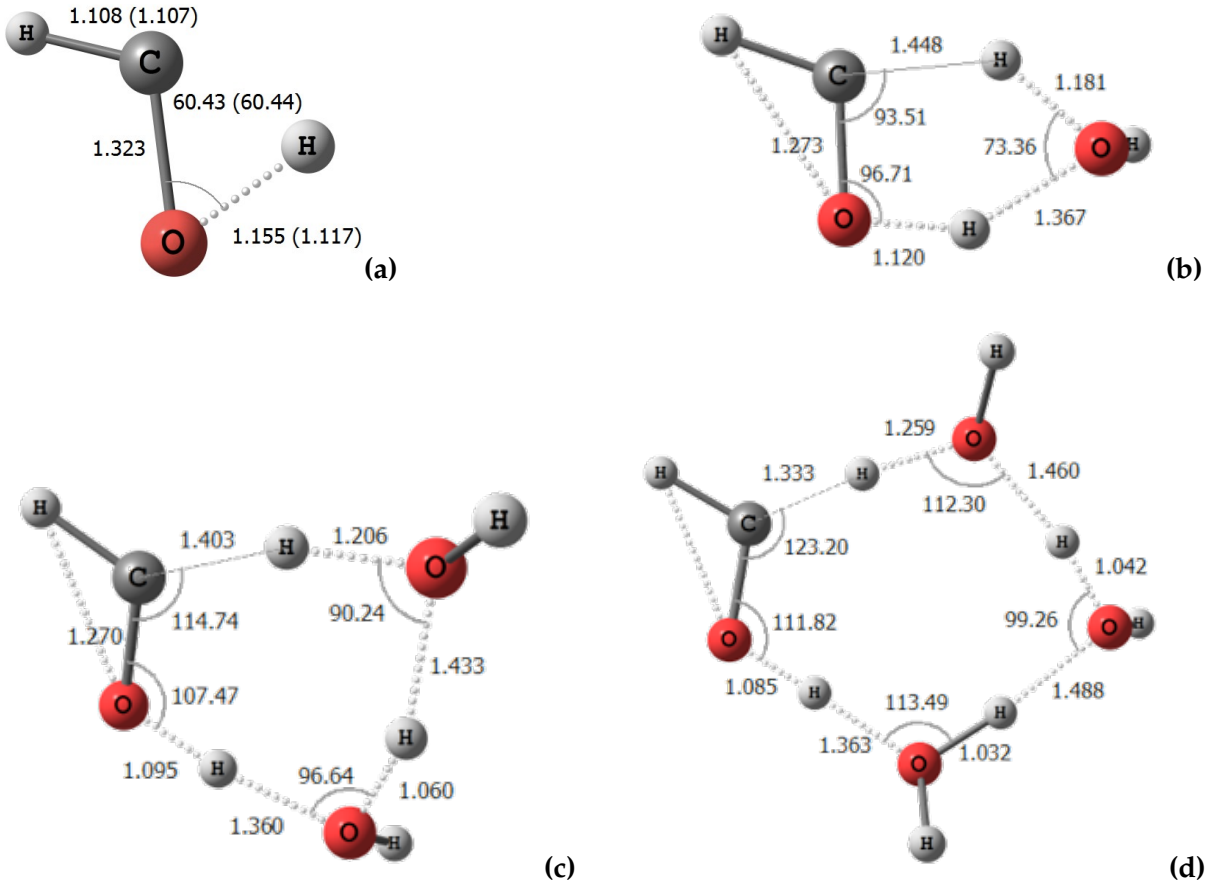

Figure 43: The geometries of the transition states computed at the MP2 / aug-cc-pVTZ with N water molecules for N = 0,1,2,3. Angles are given in degrees and lengths in Angstroms values in parentheses were computed at the CCSDT(Q)/CBS + ZPE level by Schreiner et al.[199].

By contrast with the results for the formation of HCO, chapter 4 and the work of Woon [190], the addition of one water molecule leads to a significant reduction in the activation energy, E_a. With values of E_a now ranging from 6.84 to 13.74 kcal.mol^{-1}, table (37), by comparison with the gas phase values in the range $30.46 < E_a < 38.88$ kcal mol^{-1}. As already observed for the gas phase, the MP2 non-corrected barrier is calculated to be the lowest, but after the zero point energy correction, the MP2 energy differs only by ~ 0.48 kcal mol^{-1} from the B3LYP value. However, the activation energies predicted by both the MP2 and B3LYP methods are about half of the CCSD barrier. This suggests that these methods overestimate the stabilization effect brought about by the interaction with the water molecule in the transition state. Additionally, we find that the M06 functionals give activation energies which are intermediate with respect to those of MP2 and CCSD(T). With the M06 functional reproducing the CCSD(T) energy to within a few tenths of a kcal mol^{-1}, figure 44.

5.4.2 *$(H_2O)_2$ and $(H_2O)_3$ clusters*

When two water molecules are present, the corresponding transition state, where the water molecules may exchange hydrogen atoms, is a seven membered ring structure, as shown in figure 43(c). The concerted transfer of the hydrogen atoms between the water molecules and *trans*-HCOH leads to the formation of formaldehyde complexed with two water mo-

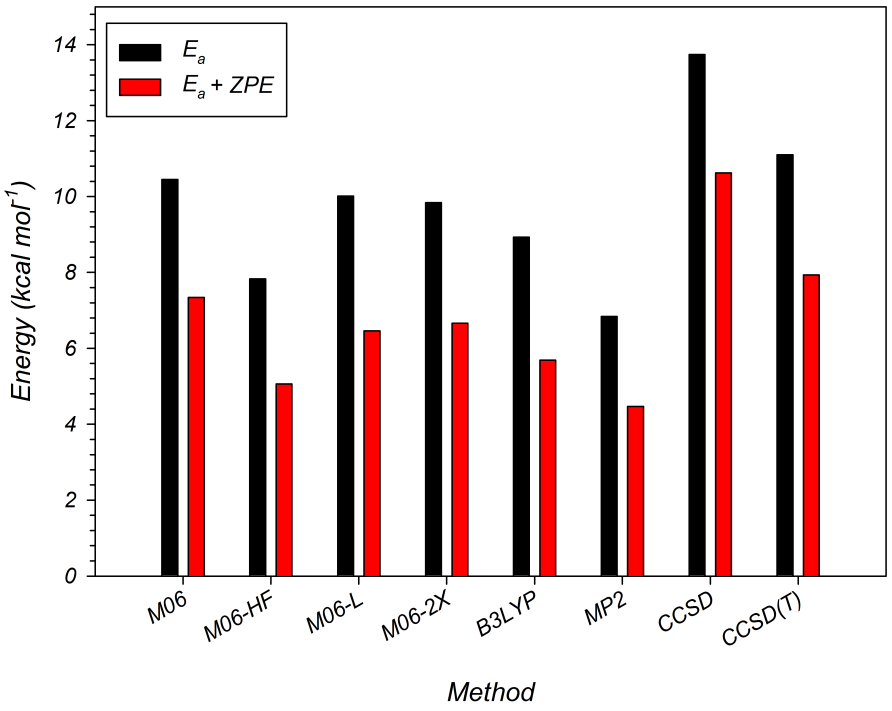

Figure 44: Variation of the activation energy, E_a, and the zero point corrected activation energy, E_a + ZPE for the methods indicated with the aug-cc-pVTZ basis set with one water molecule.

lecules. Considering the TS-2H_2O geometry (figure 43(c)), all of the hydrogen atoms are shared between the molecules rather than belonging to distinct units and as observed with a single water molecule present, all of the hydrogen atoms are transferred in a single step. This feature is also observed for the case with three water molecules, figure 43(d), but in this case the atoms enclose a nine membered ring system that shows greater flexibility.

For the energetics, the overall trend in the presence of water molecules is reported in figure 45 and values for the corresponding activation energies are given in table 38. The major reduction of the activation energy, by a factor of 3.5 to 7 depending on the method, occurs upon addition of the first molecule. The second water molecule tends to stabilize the TS by $3-5$ kcal mol^{-1} depending on the method, giving a ZPE corrected activation energy

Table 38: Activation Energies E_a with and without the ZPE correction for $N = 2$ and $N = 3$. Energies are given in kcal mol^{-1}

	$N = 2$		$N = 3$	
Method	E_a	E_a + ZPE	E_a	E_a + ZPE
B3LYP	5.08	0.93	5.28	0.84
MP2	4.41	0.36	4.80	0.54
CCSD	9.35	5.31	9.87	5.62
CCSD(T)	7.33	3.28	7.87	3.62

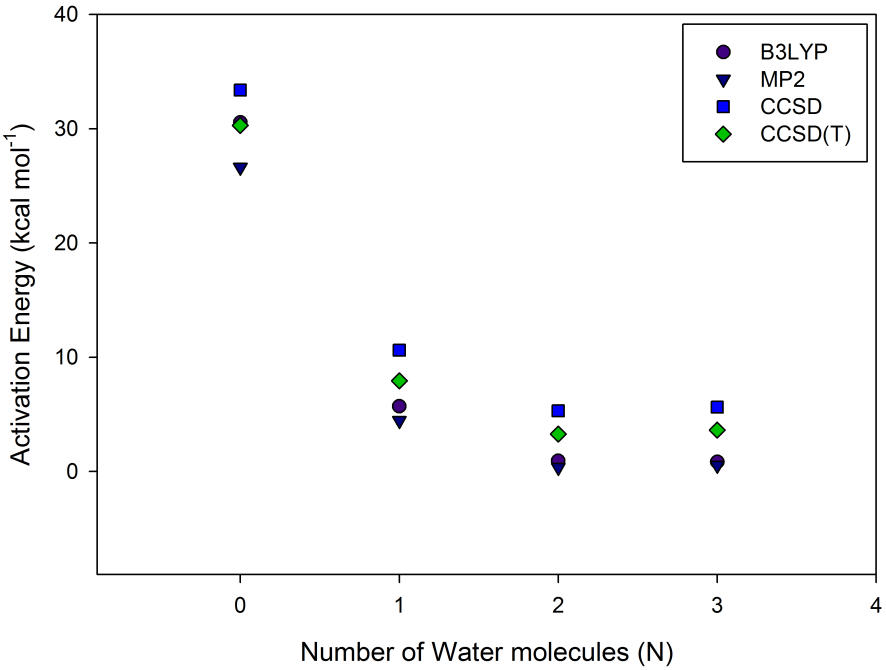

Figure 45: Trend in the Activation Energy,with the zero point energy correction, as a function of the number, N, of water molecules. For all the methods of computation shown the aug-cc-pVTZ basis set was used.

lower than 1 kcal mol^{-1}, for the MP2 and B3LYP results, by comparison with the $30-40$ kcal mol^{-1} barrier calculated in gas phase. This is likely due to a further decrease in the steric strain within the system. The addition of the third water molecule has no significant effect on the barrier, the value of the activation energy varying only by few tenths of a kcal mol^{-1}. This result suggests that the inclusion of two explicit H_2O molecules provides optimal conditions for the concerted hydrogen exchange.

From a quantum chemistry perspective, even if the methods agree fairly well on the global trend, the absolute values of the computed activation energies vary depending on the method used; for some cases, differences of up to 30 % are observed. The B3LYP functional, despite its efficiency, is known to be unsatisfactory in predicting barrier heights and non-covalent interactions, such as H-bonds, which are present in the investigated mechanism. This may in part explain the deviation between the CCSD(T) result and the B3LYP. Moreover, it should be noted that the B3LYP results do not perform with any less efficiency than the MP2 for which no such deficiency in describing hydrogen bonding interactions is known.

For the cases where $n > 1$, no results are reported using the M06 family of functionals, since for the cases with $N = 0$ and $N = 1$, they provide a wide range of values for the activation energy, with only the M06 functional performing considerably better than B3LYP in comparison with the CCSD(T) results. Furthermore, there were numerical difficulties in converging the product geometries with these functionals, which could not be resolved by modifying the convergence criteria or the integration grid.

In the following section, we shall consider how the interactions in the reactants, TS, and products change due to solvation before moving onto an analysis of the effect of solvation on the rate constant.

5.5 AIM ANALYSIS FOR THE GAS PHASE AND $(H_2O)_1$ CLUSTER

Table 39: Values of the electron density, ρ. the laplacian, L, at the critical point between the nuclear centres and the distance between these centres. (left) Contour plot of the electron density and molecular graph for: *trans*-HCOH (Top), the TS, (middle) and H_2CO (bottom), bond critical points are shown in red and the nuclei are shown in black.(right)

Critical Point between	ρ	L (a.u)	Bond Lenth (Å)
C and O_f	0.354	-3.420	1.312
H_1 and C	0.229	-0.764	1.111
O_f and H_2	0.110	-1.264	0.964

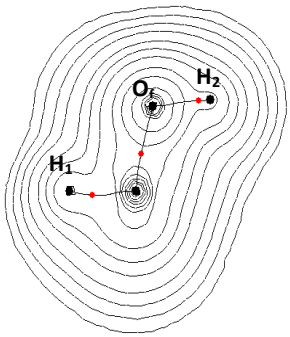

Critical Point between	ρ	L (a.u)	Bond Lenth (Å)
C and O_f	0.327	-0.696	1.299
H_1 and C	0.116	-0.732	1.176
O_f and H_2	0.152	-0.676	0.964

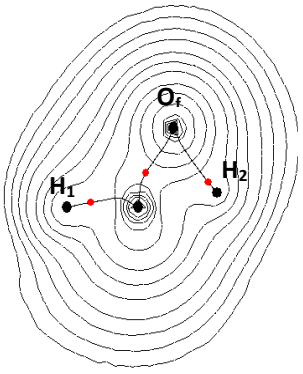

Critical Point between	ρ	L(a.u)	Bond Lenth (Å)
C and O_f	0.424	0.100	1.205
H_1 and C	0.299	-1.270	1.101
H_2 and C	0.299	-1.270	1.101

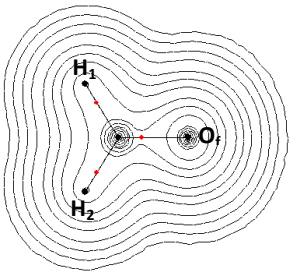

Starting with *trans*-HCOH, table 39 (top), we see here that the value of ρ at all of the critical points is large. This indicates that the electrons are being shared between the centres. This is indicative of a covalent type interaction. This is confirmed by the fact that L is negative, charge is therefore being accumulated in the region of the critical point which we would expect for a covalent interaction.

If we now consider the results for the transition state, table 39 (middle), we also see that the density is high at the critical points and the laplacian is negative. The TS here is very much like HCOH in nature, as all of the interactions are covalent in nature and there is no interaction between the transferring hydrogen and the carbon atom. This is evidenced since

we do not observe a bond critical point between the hydrogen and the carbon atom. This is not surprising since such an interaction would enclose a three membered ring which would be electron deficient, the hydrogen would have two bonds, and the ring would be highly strained.

In the case of H_2CO, we see that the molecular symmetry has an influence of the nature of the critical points. Both of the CH bond critical points are identical not only in the nature of the bonds but also in the values of both ρ and L. This is not surprising since the molecule has C_{2V} symmetry. The CO bond critical point is more interesting, since the value of ρ suggests that the electrons are shared between the two centres. But the Laplacian suggests that we are looking at a closed shell interaction. We would normally expect a covalent type interaction within this system, and the value of the laplacian can be rationalised if we consider that it is telling us that the charge is accumulated away from the critical point [151]. This is not surprising since we expect that the oxygen will want more density that the carbon atom. As such charge will be accumulated away from the bonding region. This also agrees well with the AIM analysis performed on the pure CO clusters in chapter 4.

Table 40: Values of the electron density, ρ. the laplacian, L, at the critical point between the nuclear centres and the distance between these centres. (left) Contour plot of the electron densities and molecular graphs (right) for: *trans*-HCOH (Top), the TS, (middle) and H_2CO (bottom) with one water molecule, bond critical points are shown in red, the nuclei are shown in black, and the ring critical point is shown in yellow.

Critical Point between	ρ	L	Bond Lenth (Å)
C and O_f	0.299	-0.528	1.300
H_1 and C	0.114	-0.064	1.108
H_{W1} and C	0.013	0.044	2.177
O_f and H_2	0.207	-0.608	0.979
O_W and H_{W1}	0.166	-0.132	0.972
O_W and H_{W2}	0.317	-1.916	0.959
H_2 and O_W	0.024	0.108	1.851
ring	0.013	0.044	

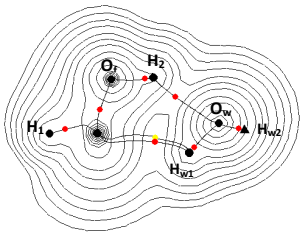

Critical Point between	ρ	L	Bond Lenth (Å)
C and O_f	0.362	0.440	1.265
H_1 and C	0.301	-1.296	1.098
H_{W1} and C	0.132	-0.228	1.404
O_f and H_2	0.222	-1.336	1.121
O_W and H_{W1}	0.174	-0.472	1.215
O_W and H_{W2}	0.373	-2.790	0.959
H_2 and O_W	0.117	-0.004	1.349
ring	0.046	-0.076	

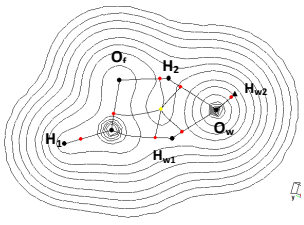

Critical Point between	ρ	L	Bond Lenth (Å)
C and O_f	0.276	0.300	1.209
H_1 and C	0.126	-0.112	1.099
H_{W1} and C	0.255	-0.960	1.098
O_f and H_2	0.022	0.084	2.009
O_W and H_{W2}	0.247	-0.868	0.958
H_2 and O_W	0.321	-2.088	0.964

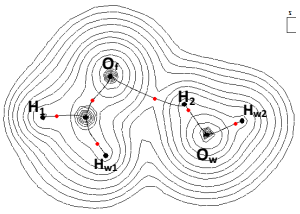

Upon the addition of water to HCOH, table 40 (top), the covalent nature of the bonds within HCOH remains uncahnged. In addition the bonds within water are seen to be covalent in nature. Additionally, we now see two additional interactions between HCOH and water. These can be characterised by the two additional bond critical points and the ring critical point. The density at these bond critical points is low and the laplacian is positive. This indicates that this type of interaction is a hydrogen bond.

Due to these interactions, the bond paths and critical points now enclose a ring. As such we observe that there is now a ring critical point. However, it is close to the critical point between H_{W1} and C, which suggests that the interaction here is very weak and if the centres were further apart, then this interaction would not be observed.

For the TS with water, table 40 (middle), we observe that the water molecule has moved closer to the formyl group backbone, evidenced by the fact that the H_2-O_W and H_{W1}-C bond lengths have both decreased compared to the HCOH + H_2O complex. We also see from the values of ρ and L at the bond critical point between H_{W1} and C that this interaction is now covalent in nature, $(L < 0)$. This suggests as the water has moved closer, density has been pushed into the region between these two nuclei. This is also evidenced by the fact that the value of L between C and O has become positive, suggesting that the electrons have moved from the bond to be accumulated at the atomic centres. Additionally, the interaction between H_2 and O_W has become covalent in nature, so two hydrogen bonds have been changed into two covalent bonds on going from the reactants to the TS.

As such, the geometry of the TS may now be more accurately described as a covalently bound ring of 5 atoms and not two weakly interacting molecules. This is evidenced by the location of the ring critical point, which is now in the centre of the ring and not on the ring edge unlike the HCOH +H_2O complex.

As we move to the product complex, table 40 (bottom), the ring is broken and we are left with only one hydrogen bond interaction between O_f and H_2. Additionally, although both water and formaldehyde have C_{2V} symmetry, when considered in isolation, we see upon forming this complex that the symmetry is lost. Consequently, in both cases the hydrogen atoms in each molecule are no longer equivalent. Since H_2 is hydrogen bonded to O_f, we would reasonably expect that the two hydrogen atoms on water would no longer be the same. However, in the case of H_2CO, since the analysis shows that there is no bonding interaction between H_{W1} and O_W, the difference in the hydrogen atoms on H_2CO can only be due to the proximity of the water molecule to H_{W1}.

From this analysis, it is clear that the water molecule greatly facilitates the formation of a covalent bond between the transferring hydrogen atom and the carbon atom. This is seen by comparing the transition states: in the gas phase, there is no interaction at all between the hydrogen atom being transferred and the carbon atom, in contrast, within the TS with

water present, a covalent bond is formed between the hydrogen atom and the carbon atom. As a result of this bond and a OHO bridge being formed, the TS can now be considered as a covalently bound ring structure.

We therefore postulate that this ring formation has a stabilising effect on the transition state. As such, the activation energy is lowered considerably compared to the isolated case. We could expect that with two water molecules present we would, within the AIM analysis, observe the existence of a covalently bound, 7-membered ring structure for the TS. This would then explain the additional stabilisation that is observed, figure 45. However, this effect is reduced on going from a 5 to a 7 membered ring in comparison to the stabilisation gained in initially forming the 5 membered ring.

Since our analysis postulates the existence of these covalently bound ring states in the TS and the imaginary mode corresponds to the concerted motion of multiple hydrogen atoms within these rings, we might expect to observe a tunnelling mechanism for this reaction. As such, in the following section we consider the impact of this solvation effect upon the rate of reaction.

5.5.1 *Comparison of tunnelling rates for the trans-HCOH to H_2CO isomerisation in the gas phase and in the presence of one water molecule*

Using the tunnelling methods discussed in chapter 2, we have computed the tunnelling rate for this isomerization. Figure 46 shows how the rate varies as a function of temperature and with the number of water molecules present in the reaction complex. With no water present, the timescale of H atom transfer is of the order of a few 1000 hours, according to the Eckart model, in the low temperature regime. In contrast the rate from the WKB model is between 10 and 100 hours.

In comparison with the results of Kiselev et al. [192] these rates are two orders of magnitude lower. This corresponds to the fact that our activation energy at the CCSD(T)/aug-cc-pVTZ level is 2 kcal mol^{-1} higher than their CCSD(T)/aug-cc-pVTZ//QCISD/aug-cc-pVDZ barrier (table 37). We note that the zero temperature limit of the WKB rate computed by Kiselev et al. corresponds to a half life of 2 hours, which is in perfect agreement with the matrix isolation experiments [199].

In contrast, this timescale is significantly reduced to less than a second when one water molecule is added. Upon addition of the second water molecule, we would expect to see an increase in the rate of 2-3 orders of magnitude due to the lower barrier. In fact, when the ZPE is included for the reaction the barrier height is so low that the transmission probability is ~ 1. Interestingly, the results show us that in spite of the considerable activation energy in the gas phase, the reaction may still proceed on a relatively short timescale at low temperatures, where such a barrier might reasonably be expected to be prohibitive.

The difference in the rates obtained by the Eckart and WKB methods can be rationalized in the same manner as discussed in section 5.3.1. In the one water case the Eckart and full IRC potentials are in much better agreement (figure 47), with the Eckart being slightly narrower for the lowest vibrational levels. This then yields a slightly higher rate (figure 46), since these terms dominate the rate expression.

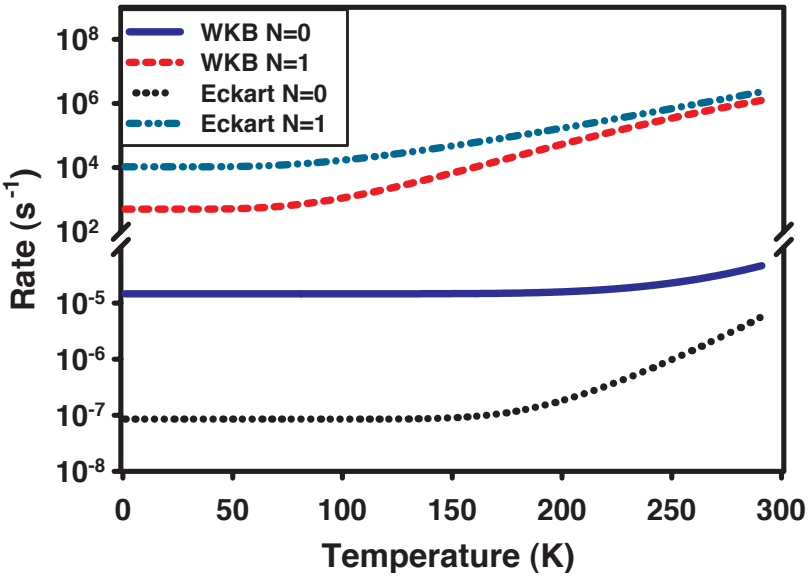

Figure 46: Rate of reaction for the isomerization of *trans*-HCOH to H_2CO plotted as a function of temperature and the number , N, of water molecules. Eckart rates computed using the optimized CCSD(T)/aug-cc-pVTZ geometries and WKB rates determined by the interpolation of the CCSD(T)/aug-cc-pVTZ // MP2/aug-cc-pVTZ IRC.

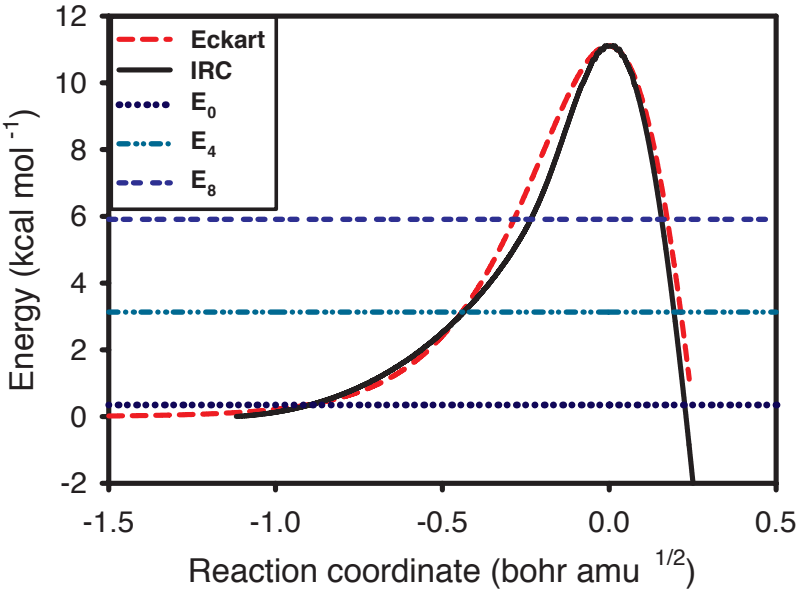

Figure 47: Comparison of the interpolated CCSD(T)/aug-cc-pVTZ//MP2/aug-cc-pVTZ IRC and Eckart potentials in the region of the transition state for the N =1 case. E_0, E_4, and E_8 are the corresponding energy levels of the harmonic oscillator, $E_n = h\nu_0(n+1/2)$, with $n = 0$, 4 and 8.

5.6 SUMMARY

From the gas phase results, it is apparent that the formation of H_2CO from HCO is indeed barrierless. In contrast, the formation of either the *cis* or *trans* isomers of HCOH have activation energies which are slightly higher than the barrier to the formation of HCO. The TS for the formation of HCOH can be rationalised as the energy required for the electronic rearrangement which is needed to remain a singlet, figure 40. Since such a rearrangement is not required for formation of the triplet state or if we are forming HCOH from COH these processes are also barrierless. In addition it should be noted that the triplet stae is in fact dissociative.

In addition the energy of the reactants, in the H + HCO reaction, is also above the barrier to the isomerisation between *trans*-HCOH and H_2CO, as well as the TS for the *cis*/*trans* isomerisation of HCOH. This is further evidence for the existence of a roaming hydrogen atom on the surface as previously reported by Bowman [193–198]. As such, we cannot rule out the formation of HCOH, as it will depend on the branching ratios of the reactions and the flux of hydrogen atoms.

If we now consider the isomerization of *trans*-HCOH to H_2CO in the presence of several water molecules, there is evidence that the hydrogen atoms of water molecules may participate in the reaction in a concerted manner.

As a result, we observe a drastic decrease of the activation energy by at least 80%, thus making the reaction feasible even in the conditions of interstellar molecular clouds. More specifically, this suggests that the addition of H to HCO predominately leads to H_2CO, as the competing isomer HCOH is quickly converted into H_2CO on the grain surfaces, when water molecules are present.

If one considers the experimentally derived rate of Schreiner et al. [199] *trans*-HCOH isomerizes in a few hours. This means in the interstellar medium *trans*-HCOH could play only a limited role in the subsequent hydrogenation steps to methanol: even if one considers a pure solid CO ice, the isomerization occurs on a time scale which is as long or shorter than the accumulation of H atoms on the grain surface, which is typically a few hours at 10 K [206].

Therefore for *trans*-HCOH to participate in the subsequent hydrogenation steps, the addition of a H atom to it would have to have a rate that is much greater than for the isomerization. However, should the flux of H atoms be greater than for the interstellar medium, and the reaction is performed without any water molecules being present, the participation of *trans*-HCOH within subsequent reactions cannot be ruled out as a possibility without further investigation. If we consider the rates derived in the presence of one water molecule, it is clear that should *trans*-HCOH be formed on the grain mantles, where CO and H_2O are in close proximity *trans*-HCOH will be converted to H_2CO on a far shorter timescale than H atom bombardment of the surface.

As it seems, the formation and interconversion of HCOH is highly dependent upon the flux. As such, its subsequent participation in further hydrogenations towards methanol cannot be ruled out. Therefore, in the next chapter, we have considered the addition of hydrogen to both H_2CO and HCOH.

Chapter VI

REACTIONS OF HYDROGEN WITH H_2CO AND LARGER SPECIES

6

REACTIONS OF HYDROGEN WITH H_2CO AND LARGER SPECIES

In this chapter, we discus calculations for processes which involve H_2CO and CH_3OH. In this sense this chapter will differ from the previous chapters as it will not focus on just addition reactions. In addition, due to the fact that each process has been studied using slightly different methodology, we shall discuss the computational details within each section. With regard to the methodology, for the gas phase formation of H_2COH we observe the same switching problem within the CASSCF procedure, as we did for HCOH as such as such a section of this chapter is dedicated to consolidating all of the tests we have performed in order to understand this problem. This discussion will commence by focussing on the addition of hydrogen to H_2CO and HCOH in the gas phase. We then continue to consider the formation of methanol from both H_3CO and H_2COH in the gas phase. This is then followed by a consideration of the formation of H_3CO and H_2COH in $(H_2O)_3$ clusters.

Subsequently, the discussion continues to consider the role of deuterium upon the chemistry by focusing on the abstraction reactions from H_2CO and CH_3OH. Finally, we discuss the potential hydrogen deuterium exchange within ices composed of methanol and water, which we model as a $CH_3OD \cdot (H_2O)_3$ cluster.

6.1 ADDITION OF HYDROGEN TO H_2CO, HCOH, H_3CO, H_2COH

6.1.1 *Formation of H_3CO and H_2COH in the gas phase*

It has been shown that the methoxy radical H_3CO, formed by the addition of a hydrogen atom to formaldehyde undergoes a Jahn-Teller distortion [207–209] : the initial ^2E ground state splits into two quasi-degenerate A′ and A" components. The A′-A" energy difference is predicted to be 37 cm^{-1} [207] or 49 cm^{-1} [209]. In the present work, only the lowest $^2A'$ was considered. As a consequence, it was not possible to calculate the frequencies and ZPE for H_3CO. Indeed, at the CASSCF level, the hessian evaluation in Molpro is done numerically and the symmetry is removed. When the molecule is distorted from equilibrium, the crossing between the two states leads to spurious frequency values.

Initially, for this third hydrogenation, a (17 e^{-1}, 13 MO's) active space, i.e. setting the 1s MO's as active, was used to obtain the geometry of the stationary points. Then, a single point energy evaluation at the MRCI+Q level was performed at the resulting CASSCF geometry. However, in this case, the H_2CO-H_3CO isomerisation saddle point is predicted to have a C−H bond length which is shorter (1.585 Å) than the length predicted by an MRCI+Q energy correction of the CASSCF geometries, see table 42. This seems to indicate a huge influence of dynamical correlation on this saddle point geometry. As the MRCI optimization would be much too costly, all structures were then re-optimized using a (13 e^{-1}, 11 MO's) active space, i.e. without the 1s MO's. The resulting wave function was then used to carry out a geometry optimization at the RS2C level [124], using the IPEA shift option [210]. This resulted in a bond length of 1.779 Å. In order to further investigate this question, the geometry of this transition state has been re-optimised using various methods, as shown in table 42. Mono-reference calculations were made using the Gaussian 09 package [145]. From table 42,

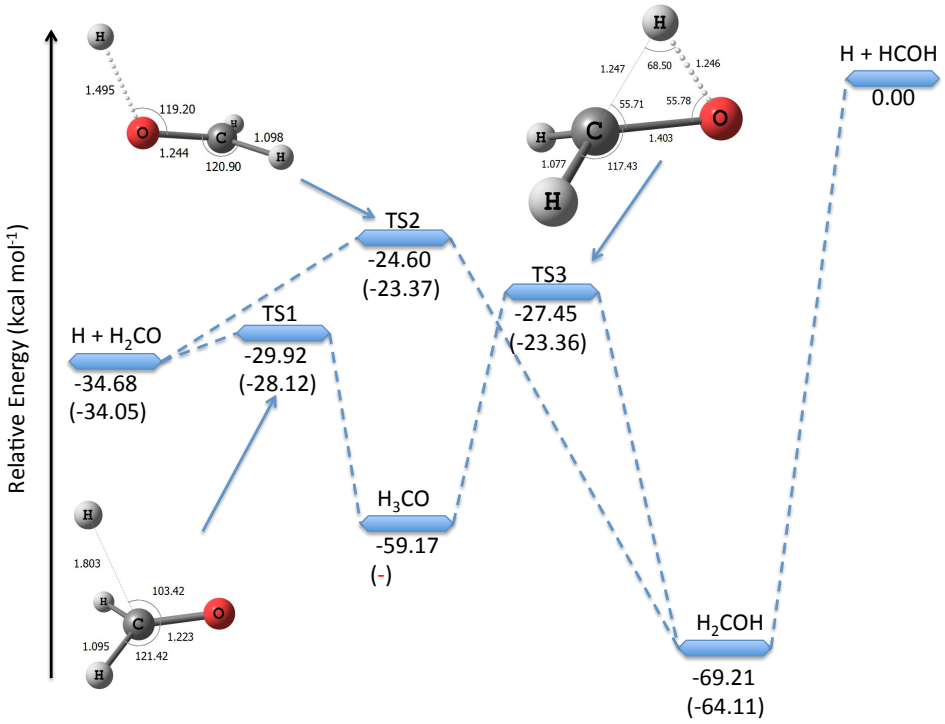

Figure 48: Calculated RS2C/aug-cc-pVTZ relative energies (kcal.mol^{-1}) of H_2COH, H_3CO and transition states associated with their formation or interconversion in the H + HCOH reaction and the H + H_2CO reaction. Energies are given relative to H and HCOH at infinite separation. Values in parentheses include the harmonic ZPE's. Bond lengths are in Å and angles in degrees.

it appears that this bond length is extremely dependent on the method employed and varies between 1.5 and 1.9 Å.

Addition of hydrogen to HCOH is barrierless leading to H_2COH, although, as noticed previously, the energy of the reactants is above the energy of the other transition states. This may also give rise to a roaming hydrogen atom, making the dynamics of this process rather complex [193–198]. We confirm that it is considerably easier to form H_3CO from H_2CO rather than forming H_2COH. Indeed, as shown in table 41, the barrier to H_3CO formation is approximately half that of H_2COH (5.93 and 10.65 kcal.mol^{-1}, respectively). This suggests that the formation of methanol from formaldehyde must proceed through H_3CO in the gas phase. Nevertheless, the formation of H_3CO will still require hydrogen atom tunnelling. For both H_3CO and H_2COH, we have only considered the doublet states as the doublet-quartet gap for H_3CO is ~90 kcal.mol^{-1} and for H_2COH ~220 kcal.mol^{-1} [211–213]. In this case with the RS2C optimizations we were able to prevent the switching by using a special convergence threshold which is present within Molpro. For the isomerization this was not possible as GAMESS does not contain the same options for the CASSCF procedure as Molpro. However, Molpro is unable to compute IRCs, so at least to compute the rate constants for isomerization we have to put the 1s orbitals within the active space.

Table 41: Activation Energies E_A (kcal.mol^{-1}) with and without ZPE for the formation of H_3CO and H_2COH.[a] Extrapolated energies of MP2/aug-cc-pVTZ geometries.

Reaction	Method	Basis	E_a	E_a + ZPE	Ref.
$H + H_2CO \rightarrow H_3CO$	RS2C	aug-cc-pVTZ	4.76	-	This work
	QCISD	aug-cc-pVDZ	4.94	6.64	[190]
	BB1K	6-311+G**	3.61	4.64	[54]
	RCCSD(T)	CBS	-	5.42	[214]
	MRCI + Q	TZP	3.91	5.59	[215]
	MCSCF	3-21G	5.61	6.51	[216]
$H_3CO \rightarrow CH_2OH$	MRMP2	aug-cc-pVTZ	28.9	25.9	This work
	B97D	aug-cc-pVTZ	30.11	28.10	This work
	RS2C	aug-cc-pVTZ	31.72		This work
	CASSCF	STO-3G	41.00		[217]
	AE-CCSD(T)[a]	CBS[a]	29.88		[218]
$H + H_2CO \rightarrow H_2COH$	RS2C	aug-cc-pVTZ	10.08	10.68	This work
	RCCSD(T)	CBS	-	11.26	[214]
	MCSCF	3-21G	14.04	14.74	[216]

Table 42: Predicted CH distance (aug-cc-pVTZ basis set), in Å, for the incoming hydrogen of the TS in the formation of the methoxy radical

Method	distance
ROHF	1.536
UHF	1.815
UMP2	1.651
UB3LYP	1.474
UBB1K	1.906
UCCSD	1.7
Full-CASSCF	1.585
MRCI+Q//Full-CASSCF	1.65
RS2C	1.779

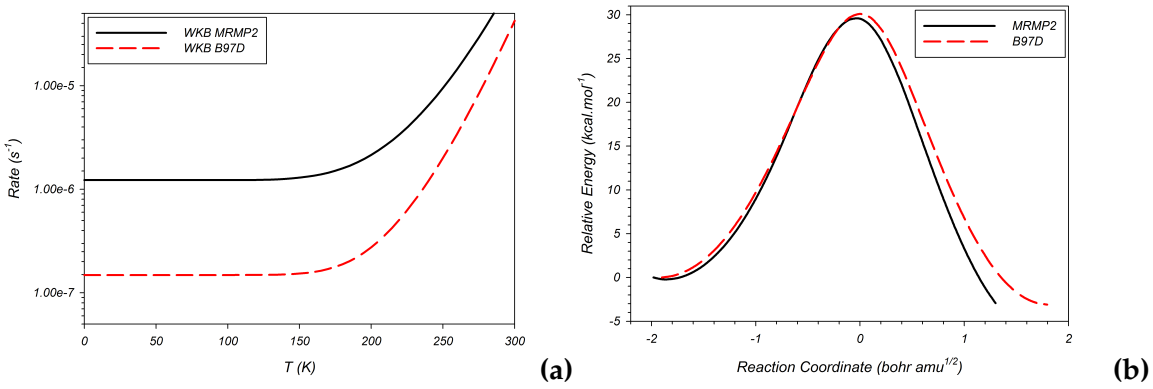

Figure 49: (a)Rate constants for the gas phase isomerisation of H_3CO to H_2COH as a function of the temperature, T.(b) IRC for the isomerisation using MRMP2 and B97D.

6.1.2 *Isomerisation of H_3CO to H_2COH*

In order to consider the isomerisation in the gas phase, it was necessary to use the MRMP2 method in the GAMESS package. Due to the fact the basis set contraction scheme, and the fact that MRMP2 is not exactly the same as RS2C the energies we obtain are slightly different, table 41. The rate constant for the isomerisation has been computed for both the MRMP2 and B97D IRCs and the results with the WKB method are presented in figure 49.

From figure 49, the MRMP2 results yield higher rate constants than their B97D equivalents by an order of magnitude. This is related to the lower activation energy for the process obtained by MRMP2. In fact, there is better agreement between the energies obtained with B97D and the RS2C values. In addition, the B97D results also show an excellent agreement with the AE-CCSD(T)/CBS//AE-MP2/aug-cc-pVTZ results of Wang et al [218] who obtain a barrier height 29.88 kcal.mol^{-1} and predict a rate constant of 4.44x10^{-8} s^{-1} at 50 K. Indeed both their results and ours would suggest the gas phase isomerisation happens much too slowly for H_3CO to be converted to CH_2OH before being hydrogenated to methanol.

6.1.3 *Inclusion of the 1s orbitals explained*

For HCOH and for H_2COH it was necessary to include the 1s core orbitals in the valence active space: during the CAS procedure, with Molpro [148], Gamess [146, 147], and Gaussian [145], the oxygen 1s would be brought into the active space whilst the CH hybrid orbital was added to the core. Subsequently, this then meant any following correction for correlation effects, be that MRCI+Q or some form of MRMP2, would be underestimated leading to a decrease in the stability of HCOH by $\sim$30 kcal.mol^{-1}. In order to understand this phenomenon, we have performed several tests. Initially, these tests focused on using the cc-pVNZ vs the aug-cc-pVNZ basis sets. Throughout these tests, the use of the augmented basis sets leads to switching. Another set of tests were conducted by removing selected diffuse functions from the hydrogen atoms of HCOH, the results of these tests are reported in table 43. We note that whilst these tests have been performed for HCOH derivatives the same problem occurrs in the same fashion for H_2COH and as such are applicable there as well. Indeed, these tests were performed on HCOH in order to minimise the computational cost.

Table 43: Table showing the diffuse functions present upon the hydrogen atoms within HCOH and the corresponding result regarding the 1s switching problem. H_1 is the hydrogen attached to the carbon and H_2 is the hydrogen attached to oxygen.

Atom with diffuse functions	Diffuse functions added	Does switching of the 1s occur?
H_1 and H_2	spd	✓
H_1 and H_2	s	✓
H_1 and H_2	p	✓
H_1 and H_2	d	×
H_1	s	✓
H_2	s	✓
H_1	pd	×
H_2	pd	✓
H_1	p	×
H_2	p	✓
H_1	d	×
H_2	d	×
H_1 and H_2		×

As can be seen from table 43, whilst we can obtain a clear idea of which functions are involved, in this switching problem, it is unclear exactly how they bring it about. This problem is further complicated by the fact that if one changes from the default CASSCF procedures in Molpro and GAMESS, to the first order algorithm in GAMESS the switching does not occur, though convergence is considerably slower. Additionally, if one considers HCSH instead of HCOH then the carbon 1s is switched into the CAS, presumably because the sulfur 1s is much lower in energy. One may then rationally think that making the energy difference between the two 1s orbitals smaller, that the problem would become worse, but in fact switching does not occur for either HCCH or HCNH.

At this time we have no physical explanation for the cause of the switching. It appears that it is in some way related to the diffuse s and p functions of hydrogen and the nature of the CASSCF algorithms. In addition, our tests suggest it is not limited to HCOH, but rather that switching also occurs for HCSH and H_2COH as well but does not occur for their isomers or TS in formation or isomerisation.

6.1.4 *Formation of H_3COH*

The formation of methanol is indeed barrierless from both H_2COH and H_3CO. Indeed, the relative difference between the two is purely the difference in energy to dissociate a CH, or and OH bond. These quantities are predicted to be 100 and 110 kcal.mol^{-1} at the RS2C/aug-cc-pVTZ level.

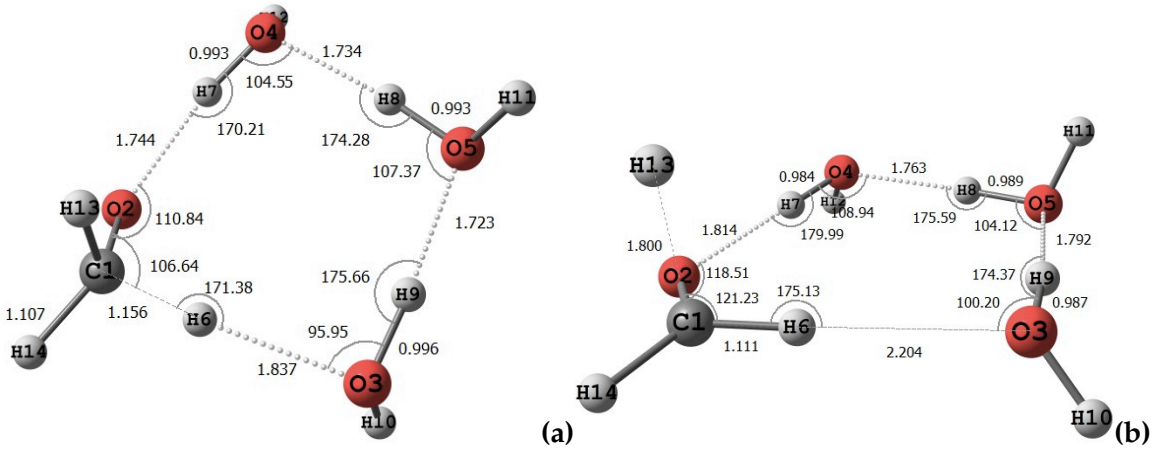

Figure 50: $H_3CO \cdot (H_2O)_3$ clusters (a) minima, and (b) the TS in formation. Distances are given in Å and angles in degrees.

6.2 FORMATION OF H_3CO AND H_2COH IN $(H_2O)_3$ CLUSTERS

We have considered the formation of H_3CO and H_2COH within clusters of 3 water molecules. In addition, the isomerisation of H_3CO to H_2COH has also been considered within these clusters. These calculations have been computed using the B97D functional with the aug-cc-pVTZ basis set.

The geometries for the clusters are given in figures 50 to 52. In considering the H_3CO minima and TS, figure 50, we see that two hydrogen bonds are formed. The first between the oxygen of H_3CO and the OH of the nearest water molecule, the second being a CHO hydrogen bond. Normally, this second interaction would be considered the weaker of the two, but we note that the presence of the CHO interaction has significantly weakened the CH bond. This is indicated by the bond length being 0.05 Å longer than in the gas phase.

Turning now to the H_2COH clusters, in the minima, figure 51(a), we see two hydrogen bonds, as we might expect: one through the OH of H_2COH and the second through a CH. In general the minima presents nothing remarkable, however the TS to formation does: in figure 51(b), we see that the incoming hydrogen approaches, and is transferred, through one of the water molecules.

Such a geometry is of interest as it potentially represents the addition of a hydrogen through the surface. In this case, we would suppose that the hydrogen atom has landed in some other part of the surface and has subsequently arrived at the reaction site via an exchange through the surface.

The TS for the isomerisation shows a geometry which is not entirely disimilar to the geometries found for the HCOH to H_2CO isomerisation, Chapter 5.

As such, we have considered the effect of the water molecules on the energetics of these processes, table 44. For H_2COH, the activation energy in fact increases by ~ 2 kcal.mol^{-1} in comparison to the gas phase. In contrast, both the formation and isomerisation barriers are lowered by ~ 3 and ~ 20 kcal.mol^{-1} respectively.

The lowering of the barrier to formation of H_3CO confirms the result of Woon [190]. Who also observed a lowering of the barrier within a cluster of 3 water molecules. However, his results suggest that the amount the barrier decreases is method dependent: he reports a

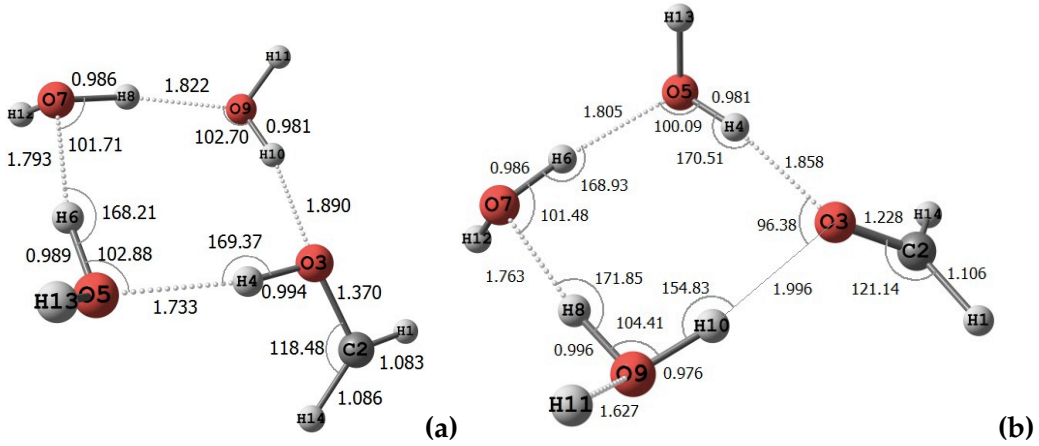

Figure 51: $H_2COH \cdot (H_2O)_3$ clusters (a) minima, and (b) the TS in formation. Distances are given in Å and angles in degrees.

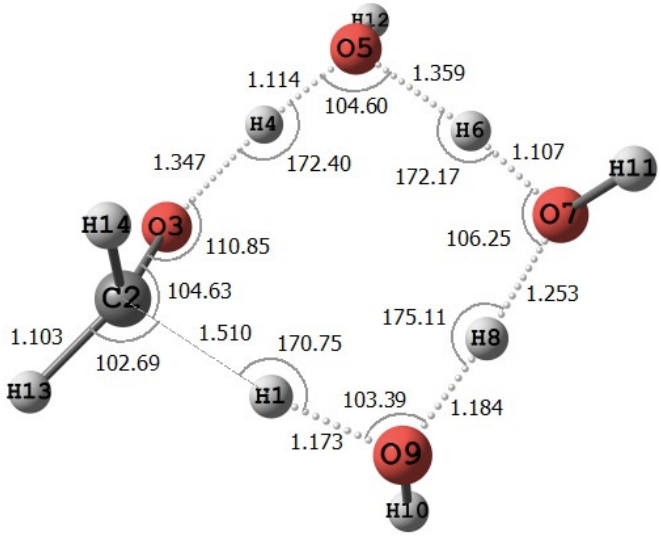

Figure 52: TS for the isomerisation of the $H_3CO \cdot (H_2O)_3$ to the $H_2COH \cdot (H_2O)_3$ cluster. Distances are given in Å and angles in degrees.

Table 44: Energetics of the formation and isomerisation of H_3CO and H_2COH in the gas phase, $n = 0$, and $(H_2O)_3$ clusters. Values given in kcal.mol^{-1} and computed using B97D/aug-cc-pVTZ

Reaction			Activation Energy	Reaction Energy
$H + H_2CO$	$\rightarrow$	H_3CO	4.03	−28.28
$H + H_2CO$	$\rightarrow$	H_2COH	7.36	−36.39
H_3CO	$\rightarrow$	H_2COH	30.11	−8.11
$H + H_2CO \cdot (H_2O)_3$	$\rightarrow$	$H_3CO \cdot (H_2O)_3$	1.29	−22.20
$H + H_2CO \cdot (H_2O)_3$	$\rightarrow$	$H_2COH \cdot (H_2O)_3$	9.53	−36.34
$H_3CO \cdot (H_2O)_3$	$\rightarrow$	$H_2COH \cdot (H_2O)_3$	9.82	−14.14

decrease in the barrier height of 3 kcal.mol^{-1} at the MP2 level but only 0.5 kcal.mol^{-1} at the QCISD level.

However, clearly the strongest effect is for the isomerisation with a decrease of ~ 20 kcal.mol^{-1}. Even if this quantity is also strongly method dependent, it is clear that a significant decrease is likely to be found with all methods. We now proceed to consider the effect this change has on the isomerisation rate. However, since the potential has changed so much we can expect a significant difference between the gas phase and cluster isomerisation rate constants, as such this process has significant implications for astrophysical models.

For evaluation of the rate constants, we have currently only employed the WKB approach. As expected, figure 53 confirms that there is a significant change in the rate constant from the gas phase. We see that the rate constant has increased by almost 4 orders of magnitude. Given this huge difference, we note that the timescale for the isomerisation is now likely faster than the arrival time for the next hydrogen. This implies that methanol must be formed from CH_2OH primarily. This is in clear contrast to the current route considered within the astrophysical models where has methanol is formed from H_3CO.

6.3 HYDROGEN ABSTRACTIONS FROM H_2CO

For the abstractions of hydrogen from H_2CO, the Gaussian 4 [143] composite method was used. The choice of the method came as a result of an initial test conducted on the $H + H_2CO \rightarrow HCO + H_2$ reaction, where it estimated the activation energy of the process to within 0.09 kcal.mol^{-1} of the experimental value of Oehelers et al [219]. This rather small error is additionally within the experimental error of ± 0.17 kcal.mol^{-1}. However, for the reaction between deuterium and H_2CO, the G4 method underpredicts the barrier by 0.31 kcal.mol^{-1}, which lies below the experimental error margin by 0.12 kcal.mol^{-1}. However, it should be stated that the method was designed to provide energies with an accuracy of ± 2 kcalmol^{-1} with respect to experiment, and here it is performing considerably better. As such, the decision was then taken to use the method for all of the abstraction reactions. Figure 54 shows the TS for the reaction and table 45 gives the values for all of the abstraction reactions.

In comparison with the values of Goumans [54] our G4 results provide better agreement with the experiment for the $H + H_2CO$ channel than the BB1K/6 − 311+G** value. However, for the $D + H_2CO$ the BB1K/6 − 311+G** is in better agreement with the experimental one. However, overall, the performance of G4 for both reactions is better since for the $D + H_2CO$, channel it is outside the experimental error for the barrier by 0.09 kcal.mol^{-1} whereas the

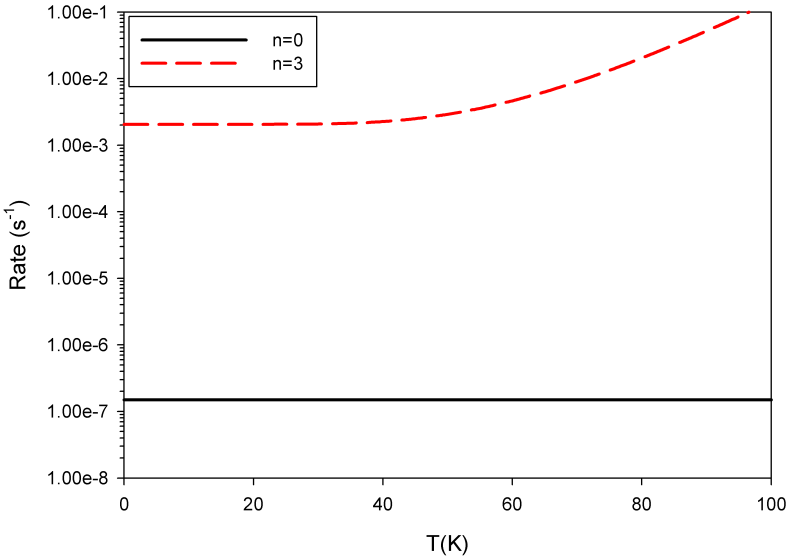

Figure 53: WKB rate constants for the isomerisation of H_3CO to H_2COH in $(H_2O)n$ clusters as a function of the temperature T.

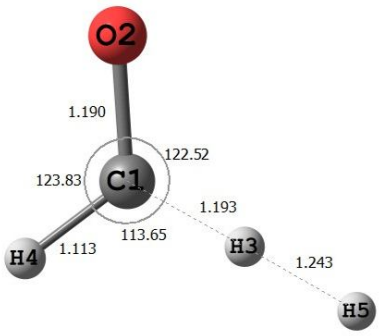

Figure 54: TS for the hydrogen abstraction from H_2CO. Distances are given in Å and angles in degrees.

Table 45: Table of activation energies and exothermicities for the abstraction reaction of H_2CO. Energies are given in kcal.mol^{-1}. [a]Computed using BB1K/6-311+G**[54], [b] Experimental value [219].

Reaction			Activation Energy	Exothermicity
$H + H_2CO$	$\rightarrow$	$H_2 + HCO$	3.55	22.43
$H + H_2CO$	$\rightarrow$	$H_2 + HCO^a$	4.47	...
$H + H_2CO$	$\rightarrow$	$H_2 + HCO^b$	3.46 ± 0.16	...
$H + HDCO$	$\rightarrow$	$HD + HCO$	4.06	21.53
$H + HDCO$	$\rightarrow$	$H_2 + DCO$	4.06	22.06
$H + D_2CO$	$\rightarrow$	$HD + DCO$	4.06	21.10
$H + D_2CO$	$\rightarrow$	$HD + DCO^a$	5.00	...
$D + H_2CO$	$\rightarrow$	$HD + HCO$	3.45	23.27
$D + H_2CO$	$\rightarrow$	$HD + HCO^a$	3.87	...
$D + H_2CO$	$\rightarrow$	$HD + HCO^b$	3.77 ± 0.19	...
$D + HDCO$	$\rightarrow$	$HD + DCO$	3.77	22.90
$D + HDCO$	$\rightarrow$	$D_2 + HCO$	3.77	22.53
$D + D_2CO$	$\rightarrow$	$D_2 + DCO$	3.84	22.09

$BB1K/6-311+G^{**}$ result for the $H + H_2CO$ channel falls outside the experimental range by 0.84 kcal.mol^{-1}.

6.4 HYDROGEN ABSTRACTIONS FROM H_3COH

For the abstraction reactions from CH_3OH the structures have been optimised at the AE-MP2/cc-pVTZ level followed by a single point correction at the AE-CCSD(T)/cc-pVTZ level. This approach was taken to complete the set of reactions within the work of Clary et al [220]. Within their work, they gave values for the $H + CH_3OH$ and $H + CD_3OD$ reactions with hydrogen and deuterium being added. In addition from their dynamics studies, they obtain rate constants which are in good agreement with the experiments of Hoyermann et al [221]. We can therefore be reasonably sure these calculations should provide rate constants which are qualitatively accurate.

The geometry of the transition state is shown in figure 55 and our values for the activation energy and reaction energies for the abstraction channels of methanol are given in table 46. In considering all of the reactions, we see it is always harder to remove deuterium than hydrogen. This is related to the fact that bonds with deuterium have lower zero point energies and thus greater dissociation energies than the corresponding bond to hydrogen.

In comparison to the more recent work of Goumans [222], our activation energy for the $H + CH_3OH \rightarrow H_2 + H_2COH$ reaction is 1.34 kcal.mol^{-1} larger, table 46. This discrepancy then explains the larger rate constants which they report in comparison to Clary et al, figure 56. In addition for the $D + CH_3OH \rightarrow HD + H_2COH$ reaction Goumans reports a value which is lower than ours by 1.26 kcal.mol^{-1} and for the $H + CHDOD \rightarrow HD + D_2COD$ it is lower by 0.49 kcal.mol^{-1}, table 46. This leads to the rate constants computed by Goumans being greater than the rates of Clary. From figure 56,we see that the rates obtained by Gou-

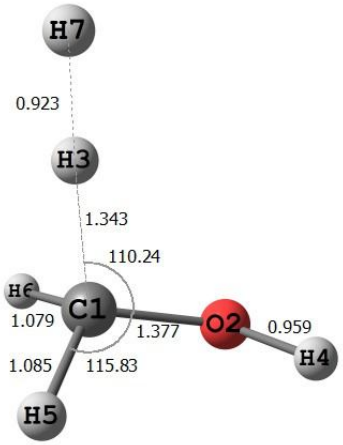

Figure 55: TS for the hydrogen abstraction from H_3COH. Distances are given in Å and angles in degrees.

mans are in better agreement with the experiments of Meagher et al [223]. However, Baulch et al [160] recommend that the best fit of all of the experimental data is produced by fitting to the Hoyermann and not the Meagher values, figure 57. Moreover, in the Baulch paper the Meagher rates are in fact lower than the Hoyermann rates, figure 57. We therefore conclude that the rate constants estimated with HQTST and lower activation energies are clearly underestimated. In contrast the full quantum method, with a higher barrier, leads to rate constants which agree with the best fit of all the experimental data.

6.5 HYDROGEN DEUTERIUM EXCHANGE IN METHANOL WATER CLUSTERS

During this work, we have collaborated with an experimental group within the Institute of Planetology and Astrophysics Grenoble (IPAG) in an attempt to model their experiments [224]. During these experiments, CD_3OD is mixed with H_2O before being deposited on a cold substrate. The mixture is injected and deposited at temperatures in the range 120 to 140 K. By monitoring the infra-red (IR) spectrum of the ice which forms overtime, subsequently they observe that some HDO is formed.

Since the only source of deuterium is from CD_3OD, they postulate that an exchange takes place between CD_3OD and H_2O. Further to this, they suspect that the exchange takes place between the OD group and H_2O. This is due to the fact, as they argue, that the OD group will interact more strongly with the surrounding water than the CD groups.

To test this hypothesis, we conducted a series of calculations on a $CH_3OD \cdot (H_2O)_n$ clusters at the MP2/aug-cc-pVTZ level. The initial cluster and the exchange TS are shown in figure 58. We see that indeed, within our model, the OD group interacts with the water cluster, whilst the CH_3 group does not.

In comparing the experimental data to the calculations, tables 47 and 48, we see that the computed activation energy lies ~ 7 kcal.mol^{-1} above the experimental value. Consequently, the rate constants obtained from the $CH_3OD \cdot (H_2O)_n$ cluster lie at least 7 orders of magnitude below the experimental rate constants. Despite the fact that the experiments use CD_3OD and not CH_3OD, this cannot explain the larger activation energy obtained by the calulations, since CD_3OD has a lower zero point energy than CH_3OD, which would lead to a higher barrier.

Table 46: Table of activation energies and exothermicities for the abstraction reaction of H_3COH. Energies are given in kcal.mol^{-1} [a] Ref. [222]

Reaction			Activation Energy	Reaction Exothermicity
H + H_3COH	→	H_2 + CH_2OH	8.55	7.87
H + H_3COH	→	H_2 + CH_2OH[a]	7.22	-
D + H_3COH	→	HD + CH_2OH	7.71	8.74
D + H_3COH	→	HD + CH_2OH[a]	6.45	-
H + H_2DCOH	→	H_2 + CHDOH	8.60	7.70
H + H_2DCOH	→	HD + CH_2OH	9.72	6.69
D + H_2DCOH	→	HD + CHDOH	7.76	8.56
D + H_2DCOH	→	D_2 + CH_2OH	8.85	7.71
H + H_3COD	→	H_2 + CH_2OD	8.53	7.89
D + H_3COD	→	HD + CH_2OD	7.68	8.75
H + HCD_2OH	→	H_2 + CD_2OH	9.76	6.51
H + HCD_2OH	→	HD + CHDOH	8.60	7.50
D + HCD_2OH	→	HD + CD_2OH	7.75	8.36
D + H_3COH	→	D_2 + CHDOH	8.89	7.54
H + H_2CDOD	→	H_2 + CHDOD	8.58	7.72
H + H_2CDOD	→	HD + CH_2OD	9.69	6.70
D + H_2CDOD	→	HD + CHDOD	7.73	8.58
D + H_2CDOD	→	D_2 + CH_2OD	8.83	7.72
H + D_3COH	→	HD + CD_2OH	9.77	6.29
D + D_3COH	→	D_2 + CD_2OH	8.90	7.32
H + HCD_2OD	→	H_2 + CD_2OD	10.69	7.52
H + HCD_2OD	→	HD + CHDOD	9.73	6.53
D + HCD_2OD	→	HD + CD_2OD	7.72	8.39
D + HCD_2OD	→	D_2 + CHDOD	7.69	7.56
H + D_3COD	→	HD + CD_2OD	9.75	6.31
H + D_3COD	→	HD + CD_2OD[a]	8.39	-
D + D_3COD	→	D_2 + CD_2OD	8.88	7.34

Table 47: Activation energies for the H/D exchange in $CH_3OD \cdot (H_2O)$n clusters. Values are given in kcal.mol^{-1}.

Cluster	Activation Energy
$CH_3OD \cdot (H_2O)_2$	24.57
$CH_3OD \cdot (H_2O)_3$	21.22
Exp.	13.49

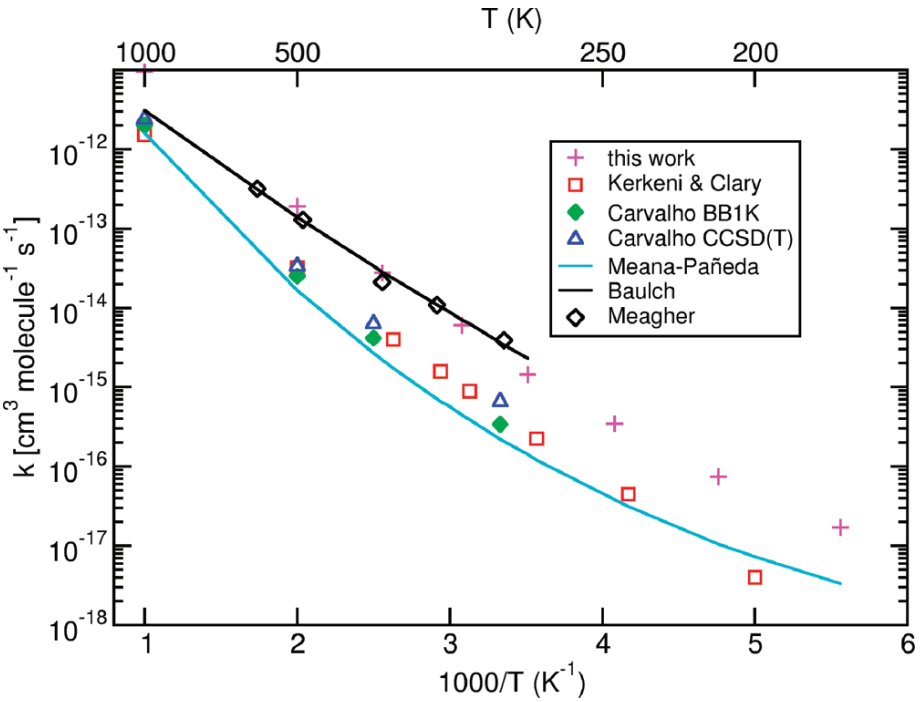

Figure 56: Comparison of the HQTST rate constants of Goumans [222] compared to the experimental data and the recommended fit of Baulch et al [160]. Figure taken from the paper by Goumans [222].

Table 48: Comparison of the WKB rate constants in the $CH_3OD \cdot (H_2O)_n$ clusters with the experiment. Values are given in s^{-1}.

	Rate		
Temperature	$CH_3OD \cdot (H_2O)_2$	$CH_3OD \cdot (H_2O)_3$	Exp.
120	$9.92x10^{-17}$	$1.95x10^{-14}$	$< 6.45x10^{-7}$
130	$1.37x10^{-16}$	$2.58x10^{-13}$	$(3.94 \pm 0.40)x10^{-6}$
135	$4.81x10^{-16}$	$8.72x10^{-13}$	$(2.35 \pm 0.25)x10^{-5}$
140	$1.62x10^{-14}$	$2.81x10^{-12}$	$(1.88 \pm 0.40)x10^{-4}$

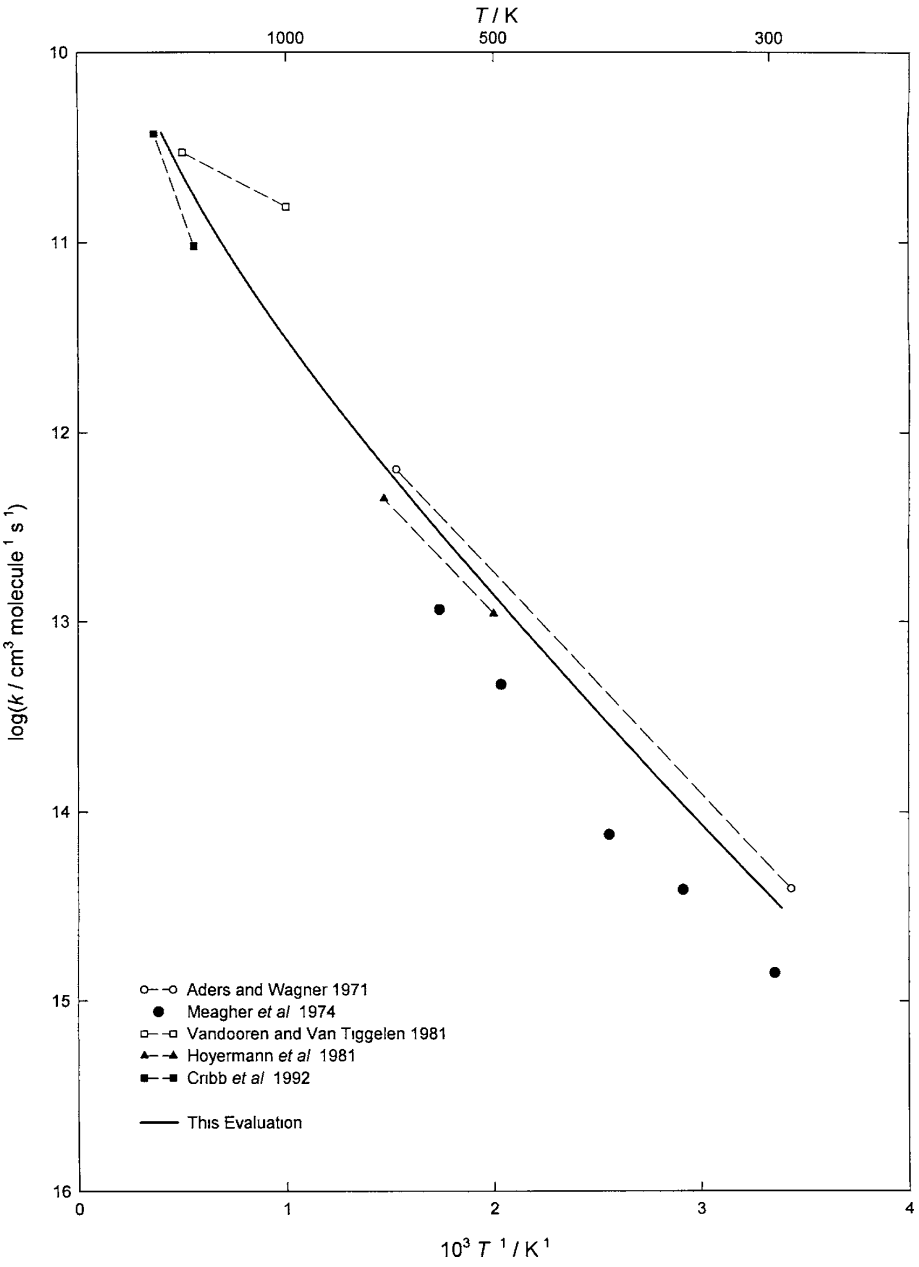

Figure 57: Recommended fit of the experimental rates for the abstraction of hydrogen from methanol by a hydrogen atom. Figure taken from the work of Baulch et al [160]

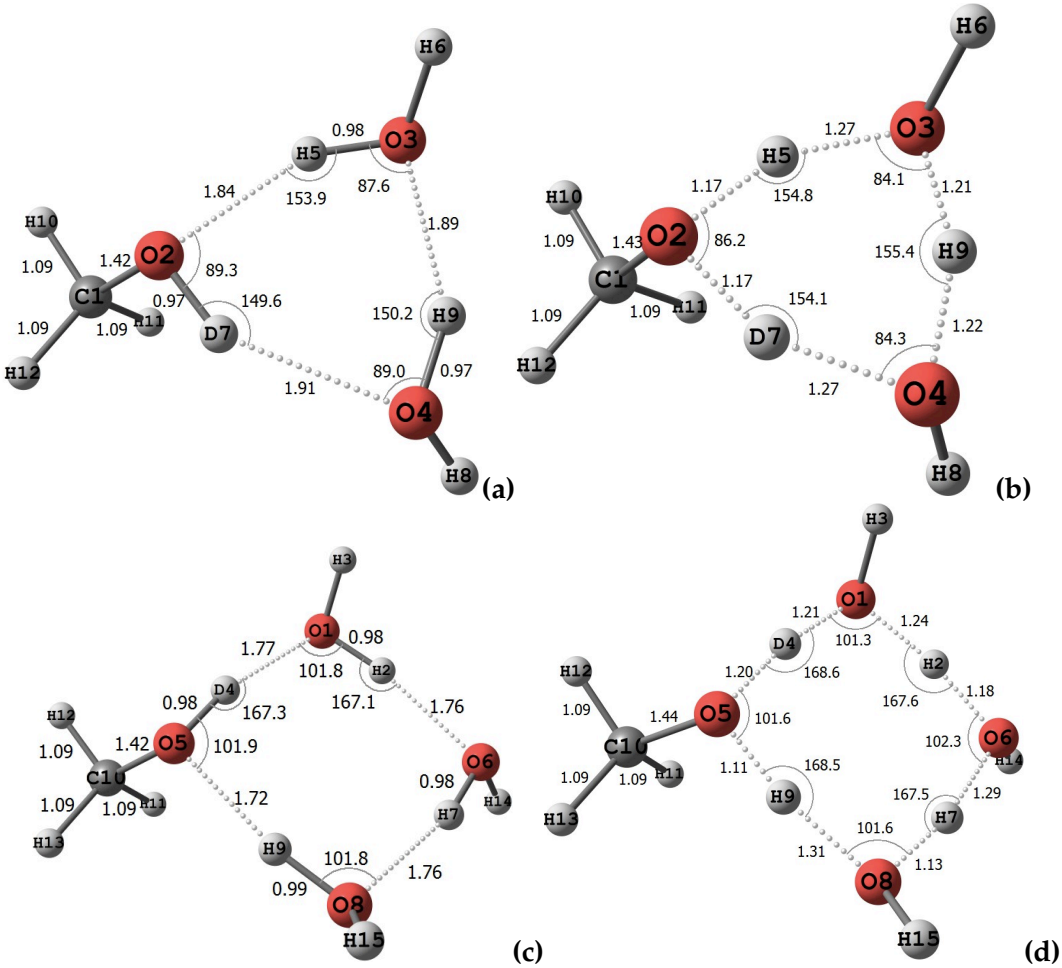

Figure 58: $CH_3OD \cdot (H_2O)n$ clusters (a) $CH_3OD \cdot (H_2O)_2$ minima, (b) $CH_3OD \cdot (H_2O)_2$ TS, (c) $CH_3OD \cdot (H_2O)_3$ minima, and (d) $CH_3OD \cdot (H_2O)_3$ TS. Distance are given in Å and angles in degrees.

We must therefore consider alternative explanations for the discrepancy. One alternative explanation, is that the IRC used for computing the rate constants in both cases contains a significant amount of relaxation of the methyl group moving away from the water cluster. This process is not available within the solid state and certainly will not be observed within the experiment. As such, we can conclude that this causes significant error in the calculations. A way to address this issue would be to freeze the coordinates of the methyl group. The problem here would then be the reaction coordinate would no longer be a minimum energy path. An alternative way to address this problem would be to use a larger cluster.

Such an appoach, would then allow us to test the exchange process, which could potentially exist, between the CD bonds and the water cluster. Such a test could also conclusively say whether or not the experimental rate constants are for OD or CD exchange.

In addition to the obvious problems with the theory, there are some probems with the experiment. Firstly, the experimental fit leads to an unphysical pre-exponential factor. This is most likely due to a lack of data: the value at 120 K given in table 48 is only an upper limit and as such is not included within the fit. In addition, since the pre-exponential factor produced by fitting the remaining 3 values is unphysical, it would suggest that one of the other rate constants is overestimated. This is likely the rate constant at 140 K, since the exchange and the ice crystallisation processes cannot be considered to be truly independent at this temperature, as they occur simultaneously.

Therefore, for the exchange process, it is clear that additional theoretical and experimental work is required to fully understand the mechanism. Indeed, an alternative mechanism has been suggested whereby the methanol is protonated prior to the dissosiation of HDO and attack of OH^-. Consideration of this mechanism may seem like an obvious next step. However, it should be noted that the pK_a values of methanol and water would suggest that in fact methanol would protonate water. At this time it is unclear the exact effect of substituting CH_3OH by either CH_3OD or CD_3OD would have on the pK_a value for methanol compared to water. This is important since an increase in the pK_a value of the isotopologue of methanol could lead to the protonation being favoured in the other direction. This area then also clearly merits further work.

6.6 SUMMARY

In considering the formation of H_3CO and CH_2OH from H_2CO and HCOH, we see that the formation of H_2COH from HCOH is barrierless. In contrast, the formation of both radicals from H_2CO involves a barrier. However, the barrier to the formation of H_3CO is lower, in both the gas phase and within water clusters. We note that within the water cluster the rate of reaction for the isomerisation process is increased by 4 orders of magnitude. This suggests that when water is present, methanol is predominately formed from H_2COH and not H_3CO. From our work on the final hydrogenation, we note that the formation of methanol from either species is barrierless.

In considering all of the results we can see that the route to methanol in the gas phase and within water clusters is ultimately different. This provides a gas phase route which proceeds via:

$$H + CO \rightarrow HCO \xrightarrow{+H} H_2CO \xrightarrow{+H} H_3CO \xrightarrow{+H} H_3COH$$

With the possibility that some HCOH may be formed and destroyed by either isomerising to H_2CO or onward reaction to H_2COH. Within the water clusters, the story is considerably

more complex. Certainly, for the first hydrogenation step, the reaction most likely proceeds to the formation of HCO, but the formation of COH cannot be ruled out since it is strongly dependent upon its local environment and its formation will ultimately be decided by the width of the barrier and not its height.

The story is further complicated in the second step by the fact that, in certain environments, the formation of *cis*-HCOH may be favoured over H_2CO. On the other hand, *trans*-HCOH will readily be converted to H_2CO in these environments. In considering onward reactions, there are two distinct routes:

$$H_2CO + H \rightarrow H_3CO \rightarrow H_2COH \xrightarrow{+H} H_3COH$$

and

$$\textit{cis}\text{-HCOH} + H \rightarrow CH_2OH \xrightarrow{+H} CH_3OH$$

This is important since currently neither route is included within astrophysical models. As such the abundance of methanol computed by these models compute may be underestimated compared to the abundance of H_2CO.

In considering the abstraction reactions from H_2CO and H_3COH, our results agree well with the experiments of Oehelers [219], Hoyermann and Baulch [160, 221]. Indeed, the agreement between the G4 results and the Oehlers [219] experiments for the abstractions from H_2CO is considerably better than the 2 kcal.mol^{-1} accuracy the method is parametrised for, and ultimately provides better estimates for the barrier than the work of Goumans [54]. The agreement for the methanol abstractions and the Hoyermann [221] experiments is of no surprise since the methodology is based upon the work of Clary [220], in which they had already shown an almost perfect agreement of their rate constants with the experimental ones. In addition, the rate constants obtained by Goumans [222] seem to agree better with the experimental results of Meagher [223] which are in fact lower than the results of Hoyermann.

Finally, with respect to modelling of the hydrogen deuterium exchange experiments, we see a relatively poor agreement between theory and experiment. However, we note that the experimental results are in fact poorly constrained, and clearly need to be expanded upon. In addition, the theory also needs to be expanded upon to consider larger cluster sizes, and the possibility that the exchange being observed may be from CD groups and not the OD group.

Chapter VII

ASTROPHYSICAL IMPLICATIONS

7

ASTROPHYSICAL IMPLICATIONS

In this chapter we discuss the implications of our results for astrophysics. This shall be done by considering the potential impact of these results on the astrophysical models, specifically considering how they will impact the GRAINOBLE model [60] where they are to be incorporated within it.

As such we briefly recall how the model works, and how our data can be used. The model commences by first accreating species into various sites. By making use of various chemical networks, it then assesses whether the species can diffuse or react in the current site. Using a series of rate equations, accreation, diffusion, and reaction over a layer continues until all of the surface sites are occupied. Once this happens, a new layer is added and the one below is considered inert. Figure 59 illustrates the genral processes considered within the model.

Since we have worked within the gas phase and small custers, we will not be able to analyse the diffusion processes. Therefore, we shall consider how our results impact upon the chemical network the model considers. We commence then with consideration of the current network for the formation of H_2CO and H_3COH. Initially, this was considered as:

$$H + CO \rightarrow HCO \xrightarrow{+H} H_2CO \xrightarrow{+H} H_3CO \xrightarrow{+H} H_3COH \tag{138}$$

With the activation energy for the formation of HCO being treated as a free parameter and ranging from $0.8 - 5$ kcal.mol^{-1}. In addition, the activation energy for the formation of H_3CO was also varied accross this range.

This was then expanded to consider the relative rates of other processes present in the experiments of Watanabe et al [41] and it subsequently uses the relative rates determined by these experiments for each of the processes, as shown in figure 60.

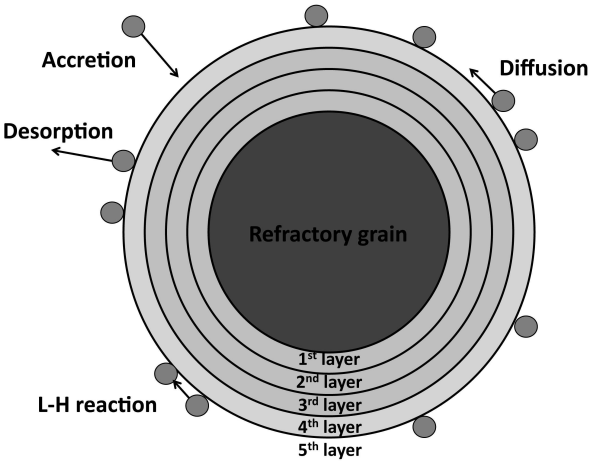

Figure 59: Schematic of the various processes within the multiayer Grainoble model.

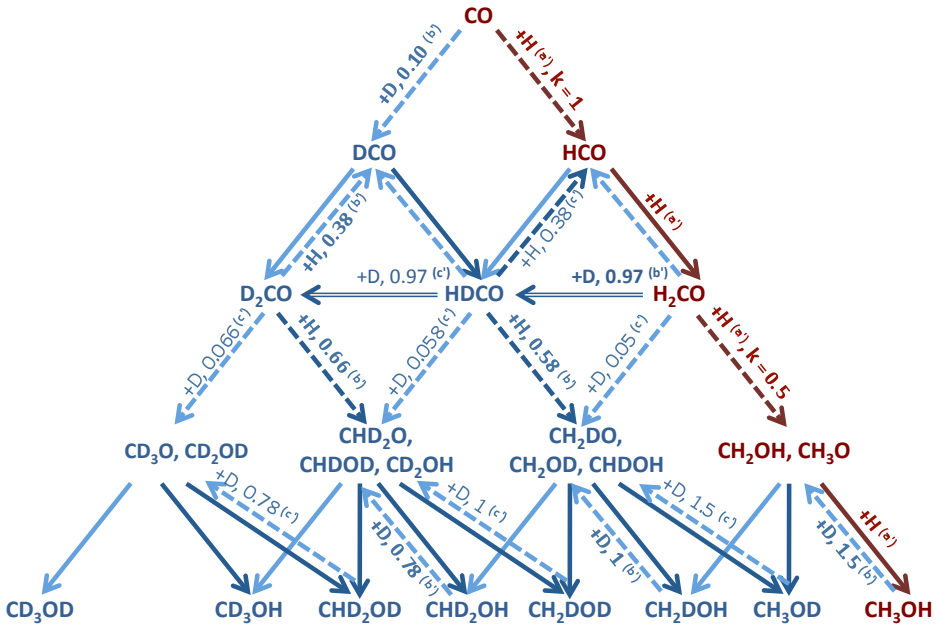

Figure 60: Schematic of the chemical networks used within the model for the formation of CH_3OH. The red marks the initial network and the blue the expanded network. Dark arrows are for hydrogen and light arrows for deuterium. Solid arrows indicate barrierless processes whereas dashed arrows represent those with a barrier. Values over arrows indicate the rates relative to the formation of HCO. a': $E_a = 0.8 - 5$ kcal.mol^{-1} for reactions with a barrier and 0 for those without [45–47, 51, 53, 190] prior to this work; b': Rates deduced from refs. [48, 50] c': abstraction values taken from this work.

Following this work the value for a' in figure 60 is now kept fixed for all of the reactions and for the formation of HCO, it is taken as 3.94 kcal.mol^{-1} This is done in spite of the disagreement with the experimental value of Wang et al of 2.0 ± 0.4 kcal.mol^{-1} [57], primarily as the value of Wang et al has been brought into question [58, 59], and the fact that our value lies in the middle of the experimental range, 2.0 to 6.0 kcal.mol^{-1}, for the activation energy as determined by the fit of all experimental data by Li et al [59].

As such, the model does not include the likely overestimated rate constants of Andersson [53], where the use of the Werner surface [55, 56] means that the rate constants have been computed using an activation energy which has been scaled to fit the experimental value of Wang et al [57]. In addition, the model does not currently include the VDW complex that has been found by Salazar [163], Andersson [53] and now by this work. However, our work suggests that this complex likely cannot be identified experimentally, and as such its existence cannot be confirmed. Nevertheless, it is likely that on a real surface there will be a physisorbed state, which is similar in structure to this VDW complex. However, at present, the stability of this state is unknown and as such, we caution against its inclusion within the model, and question any rate constants computed from it.

Currently, the model does not include any chemistry for COH. This is primarily due to the use of the gas phase mechanism, which indeed would mean COH cannot be formed. However, this work suggests that its formation is very much dependent upon its local environment. Consequently, we feel it should be included within the model and tests be performed to determine if, and exactly what impact COH may have.

Table 49: Eckart and square barrier transmission probabilities, P_{eck} and P_{sq} respectivly, for some of the hydrogenation reactions.

Reaction	P_{eck}	P_{sq}
$H + CO \rightarrow HCO$	$1.92x10^{-7}$	$1.83x10^{-8}$
$D + CO \rightarrow DCO$	$1.92x10^{-8}$	$1.83x10^{-9}$
$H + H_2CO \rightarrow H_3CO$	$9.60x10^{-8}$	$9.15x10^{-9}$
$D + H_2CO \rightarrow H_2DCO$	$9.60x10^{-9}$	$9.15x10^{-10}$
$D + H_2CO \rightarrow HCO + HD$	$9.31x10^{-8}$	$8.88x10^{-9}$

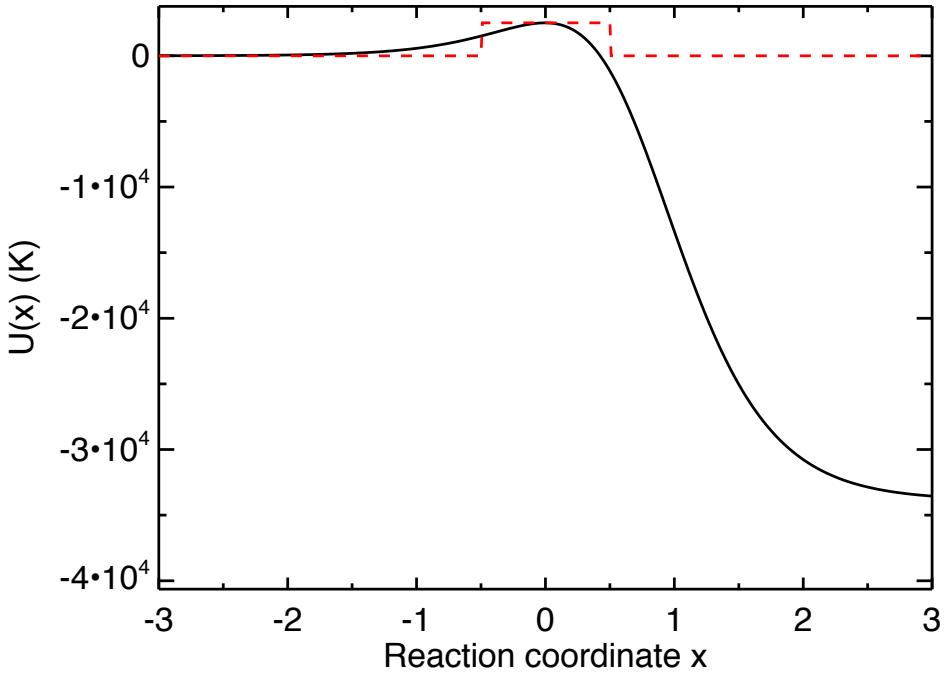

Figure 61: Illustration of the difference between the square barrier (red dashed line) as previously employed and an asymmetric Eckart potential (solid black line). Figure taken from ref. [226]

However, we note that such a test will likely be dependent upon the method used to compute the tunnelling probabilities. Previously, the model used the one dimensional square barrier, like other astrophysical models. The reason for this is that it is simple to implement and analytical. Following many discussions, our recommendation was to use the analytical Eckart [155, 225] model instead, since the square barrier likely underestimates the reaction probabilities, table 49. In addition, previously the width of all potential barriers was arbitrarily set to 1 Å. In contrast, the width of the Eckart barrier is determined from the imaginary mode of the reaction TS, which allows it to be parametrised for each reaction. Figure 61 shows an arbitary square barrier and an Eckart potential. This has now been implemented within the model and is presented in a forthcoming paper in collaboration with the astrophysicists [226].

Moving now to consider the reaction H with HCO or COH in the gas phase we see that formation of HCOH by direct attack at the oxygen has a barrier, whereas formation of H_2CO is barrierless. Interestingly, we observe that the reactants lie above the isomerisation TSs.

This supports the earlier observations of Bowman [200] that this surface exhibits a roaming hydrogen atom. Such a mechanism could lead to the formation of *cis*-HCOH, *trans*-HCOH, and H_2CO, with the final product distribution being decided by the timescale of roaming vs vibrational energy loss. Currently, this is not included within the model and exactly how this can be done is not obvious. However, an attempt should be made to include it as it is possible to form CH_3OH without facing another barrier if any HCOH is present.

If we now consider the results from the cluster calculations, we also see that the onward hydrogenation of HCO to H_2CO appears to be somewhat hindered. This hindrance is a local structural effect that would likely reduce the rate constant for the formation of H_2CO and increase the rate of formation of *cis*-HCOH. Currently, this effect is not included within the model, but it may be significant since it offers an alternative pathway to methanol, namely:

$$\textit{cis}\text{-HCOH} + H \rightarrow H_2COH \xrightarrow{+H} H_3COH$$

instead of

$$H_2CO + H \rightarrow H_3CO \xrightarrow{+H} H_3COH$$

If indeed, this pathway is present, it may help resolve, to a certain extent, the problem of forming more H_2CO then H_3COH, which is contrary to observations as outlined in Chapter 1. In addition, in considering the clusters, we must also note that, whilst addition of hydrogen to formaldehyde leads in the first instance to H_3CO, our results suggest this is quickly converted to CH_2OH. The impact here is that methanol is not formed through the direct route outlined above, but instead through the more convoluted route:

$$H_2CO + H \rightarrow H_3CO \rightarrow H_2COH \xrightarrow{+H} CH_3OH$$

It is immediately apparent that this has only a minor impact on the formation of methanol. The reason for this is that, since the formation of methanol from H_3CO or H_2COH is barrierless, then irrespective of the timescale for the isomerisation, the addition will proceed.

In fact, the greater impact here is for the formation of methylformate which is considered through the reaction of H_3CO with HCO during the warm up phase. This requires that both radicals become initially trapped in the bulk of the mantle, and for them to subsequently not react with incoming hydrogen until then. Indeed, due to the multilayer approach within the model, this is possible. However, the high rate for the isomerisation in water would suggest that the availability of H_3CO may be much lower than currently estimated. In addition, consideration of the reaction between HCO and H_2COH leads to the formation of glycoaldehyde and not methylformate. This causes some problems since generally methylformate is found in greater abundance than glycoaldehyde. As such, future work should consider how glycoaldehyde may be converted to methyformate, or an alternative route to the formation of methylformate should be considered.

For the time being, the activation energy for the formation of H_3CO is taken from the experiments. However we would recommend the use of the lower barrier height from our cluster calculations as this may lead to the formation of more methanol.

Since the abstraction reactions agree quite well with those previously reported, there is little to say. The only addition we have made here is that now the values for the activation energy are available for all the singly, and doubly deuterated species as well as the all hydrogen and all deuterium cases, which were already reported [54, 160, 219–222], and as shown in figure 60 these values have already been incorporated within the model.

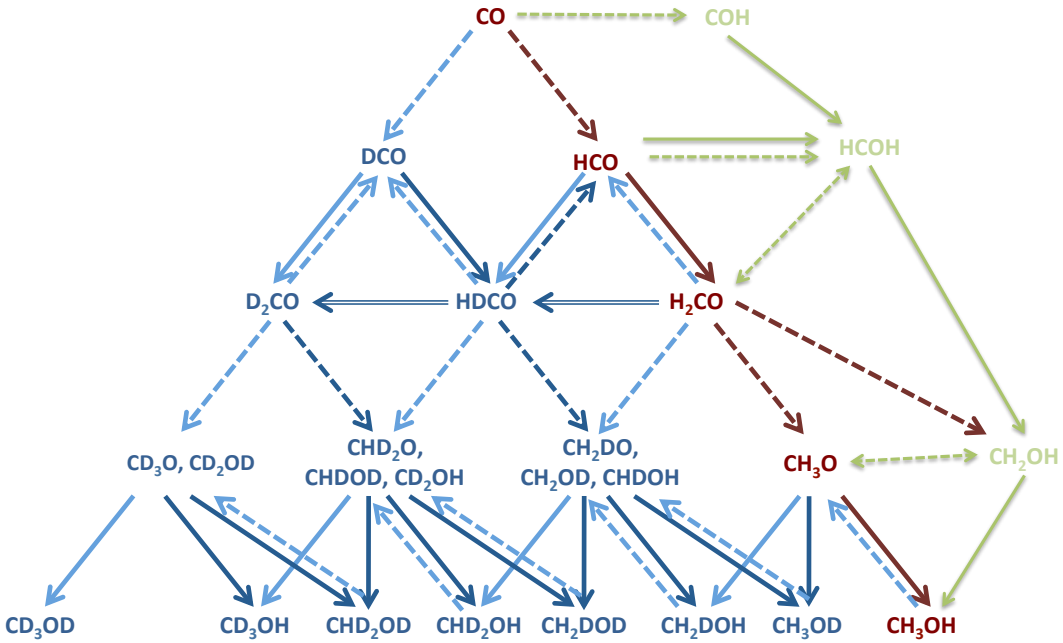

Figure 62: Updated chemical network to incorporate our latest results. Reactions in red indicate the original network, reactions in blue indicate the update to include deuterium additions and abstraction, reactions in green are our suggested additions. Solid arrows represent barrierless processes whilst dashed arrows indicate the presence of a barrier. Double headed arrows represent the isomerisation processes.

Finally, we note that all our values are being incorporated within the model. This will then be used to attempt to model the experiments conducted by Watanbe [41]. This will be done by inclusion of all the hydrogenation reactions and the abstractions. The model will then run through a set of physical conditions using the experimental hydrogen flux to obtain a best fit of these parameters to the experimental data. Following this parametrisation, the physical constants will be kept fixed and the flux lowered to be more typical of the interstellar medium. The idea here is to see how dependent the mechanism is on the flux of hydrogen. Such a determination will allow us to consider, at least to a certain extent, the effect the roaming hydrogen ultimately has upon the abundance of H_2CO and CH_3OH. Figure 62 shows our suggested additions to the chemical network based upon our current results.

Chapter VIII

CONCLUSIONS AND PERSPECTIVES

8

CONCLUSIONS AND PERSPECTIVES

Throughout this work we have used high level quantum chemistry methods to investigate processes which occur on interstellar grains involving: H, D, CO, and H_2O. During this work we had two clear aims at the outset, these were:

1. to investigate all of the possible gas phase routes in the addition of hydrogen to carbon monoxide
2. to investigate the role that the surface of the grain, including H_2O and COMs, may play in altering this chemistry

The chemistry considered has expanded from the hydrogenation to include the abstraction reactions from H_2CO and CH_3OH as well as the potential for hydrogen deuterium exchange in $CH_3OD \cdot (H_2O)n$ clusters.

Whilst a lot has been achieved, it has not been without technical problems along the way. The most obvious of which is the strange problem of the 1s orbital of oxygen being switched into the CAS during the CASSCF procedures for the multi-reference calculations in the gas phase. In addition, problems also arose in trying to build a solid surface model of α CO. In this case, it was not possible to find a way to work around the fact that the CRYSTAL [227] package build plains of atoms and not molecules from the unit cell. This ultimately led to work in the solid state being stopped and our focus shifting back to the cluster chemistry. Though even with these deficiencies we were able to study all of the hydrogenation in the gas phase with multi-reference methods, for the first time all of the processes have been treated together, and we were able to consider the role of water or CO on some of these reactions. Unfortunately, due to time constraints we were not able to compute all of the reactions with water. This limitation was partly due to the high computational cost associated with treating some of the reactions to a reasonable degree of precision. In addition, with specific regard to the formation of HCOH at this time, the TS has only been found using CCSD(T) or MRCI+Q, both of which are much too computational costly for the treatment of clusters, compared to the gas phase calculations.

Within the formation of HCO and COH we see that after consideration of all effects formation of both species in the gas phase will be difficult. The formation of COH is in fact most likely impossible due to its endothermicity. In contrast the formation of HCO is made difficult not just by the presence of an activation barrier but also by the fact that the process is dominated under interstellar conditions by a loss of translational entropy which leads to an increase in the size of the barrier when one considers the free energy of activation. We note however that this same process, which will hinder addition reactions with a barrier, will assist those without as they would now need to lose less energy to form a stable product.

During this work, we have also provided an updated benchmark for the formation of HCO. The last benchmark at the MRCI+Q level performed for this reaction was by Woon in 1996 [52]. Due to the computational cost at that time, it was necessary to add the oxygen 2s orbital to the core orbitals and the largest basis set that could be considered was the aug-cc-pVQZ basis set. Now we have been able to include the 2s orbital within the CAS and go up to the

aug-cc-pV6Z basis set. In addition, we have also been able to assess the effects of core valence correlation and scalar relativity. Such a benchmark is important as this reaction is part of the tests sets used to benchmark new DFT methods. Indeed, we have already used these results in such a fashion ourselves.

From the DFT benchmark tests we have conducted with a variety of different functionals, we can get a range of values from -1.86 kcal.mol^{-1} to 3.50 kcal.mol^{-1}. Both the BHLYP and B97D functionals have been used for the cluster computations. BHLYP has been used since it reproduces the experimental barrier height of Wang [57], though we note that the recent works of Friedrichs [58] and Li [59] call this value into question. In the case of B97D, we see that it provides excellent agreement with the MRCI+Q results. This is significant, since it has a much lower computational cost than MRCI+Q. As such B97D has enabled us to consider these to formation channels within clusters of $(CO)_4$, $(CO)_5$, $(H_2O)_3$, and $(H_2O)_5$.

With regard to the reaction exothermicity we note both functionals over predict this value in the gas phase as well. So whilst we cannot use the results in a quantitative manner for this quantity, they should at least provide a reasonable qualitative picture. This therefore supports the claim that the formation of HCO is in fact changed very little by the presence of the cluster.

In comparing the $HCO \cdot (H_2O)_3$ cluster results with the previous work of Woon [190], we see that both BHLYP and B97D predict lower activation energies than the values of Woon. In addition, both functionals predict greater exothermicities for the reactions. The difference between the MP2 results of Woon and the DFT is likely due to the spin contaminant being considerably different between the two calculations.

In contrast, the formation of COH is strongly affected by the size and composition of the cluster. In the CO clusters, the formation is relatively unchanged but within water clusters, things are very different. Indeed, in the presence of only a few water molecules the reaction becomes slightly exothermic. On increasing the size of the cluster, the reaction becomes slightly endothermic due to a decrease in the relative strength of the hydrogen bonds it is able to make with the cluster.

In considering the subsequent hydrogenations within the water clusters, there is evidence of a size effect. Due to the hydrogen bonding in the $CO \cdot (H_2O)_5$ cluster, addition to the carbon atoms is always possible. As such, it is possible to form H_2CO directly from HCO. However, in the $(H_2O)_3$ clusters, for steric reasons, attack at the carbon of HCO is no longer possible. consequently from both the $HCO \cdot (H_2O)_3$ and the $COH \cdot (H_2O)_3$ clusters we can only directly form HCOH. This is of significance for the astrophysical models since they currently only consider that H_2CO can be formed and not HCOH. Furthermore, they do not consider that the local structure could have such a large influence on the chemistry.

Finally, we note that within the CO clusters, the addition of the hydrogen changes the relative orientations of the CO units. If it were possible to model an actual α—CO surface, this would not occur and the fact that we see it here is a deficiency of the cluster approach. We therefore conclude that the formation of COH is strongly dependent upon the surface structure.

In considering the gas phase results for the formation of H_2CO from HCO, we confirm that it is indeed barrierless. In contrast the formations of either the *cis* or *trans* isomers of HCOH have activation energies which are slightly higher than the barrier to the formation of HCO. The activation energy for the formation of HCOH can be viewed as the energy required for the electronic rearrangement. Such a rearrangement is needed within the singlet state as the unpaired electron of HCO is located on the carbon atom and as such addition

of the hydrogen to the oxygen would initially lead to an additional unpaired electron on the oxygen atom. Since such a rearrangement is not required for formation of the triplet state or if we are forming HCOH from COH, these processes are also barrierless. Though we also note that the triplet A' potential is also entirely repulsive.

We also see that the energy of the reactants, HCO + H, is above the barrier to the isomerisation between *trans*-HCOH and H_2CO as well as the TS for the *cis*/*trans* isomerisation of HCOH. This is further evidence for the existence of a roaming hydrogen atom on the surface as previously reported by Bowman [193–198]. As such, we cannot rule out the formation of HCOH, as it will depend on the branching ratios of the reactions and the flux of hydrogen atoms.

If we now consider the isomerization of *trans*-HCOH to H_2CO in the presence of several water molecules, we see evidence for the hydrogen atoms of water molecules participating in the reaction in a concerted manner. As a result, we observe a drastic decrease of the activation energy by at least 80%, thus making the reaction feasible even in the conditions of interstellar molecular clouds. More specifically, this suggests that the addition of H to HCO ultimately leads to H_2CO, as the competing isomer HCOH is quickly converted into H_2CO on the grain surfaces, when water molecules are present.

If one considers the experimentally derived rate of Schreiner et al. [199] *trans*-HCOH isomerizes in a few hours. This means in the interstellar medium, *trans*-HCOH could play only a limited role in the subsequent hydrogenation steps to methanol, since even if one considers a pure solid CO ice, the isomerization occurs on a time scale which is as long or shorter than the accumulation of H atoms on the grain surface, typically a few hours at 10 K [206].

Therefore, for *trans*-HCOH to participate in the subsequent hydrogenation steps, the addition of a H atom to HCOH should occur with a rate that is much greater than the rate for the isomerization. However, should the flux of H atoms be greater than for the interstellar medium and the reaction is performed without any water molecules being present within the mixture, the participation of *trans*-HCOH within subsequent reactions can not be ruled out as a possibility without further investigation. This does not mean that *cis*-HCOH is not available for further reactions, since it too may also be formed through the roaming hydrogen atom mechanism.

The formation of H_2COH from HCOH is barrierless, whereas the formation of both radicals from H_2CO involves a barrier. Within the water clusters, the rate of reaction for the isomerisation process is increased by 4 orders of magnitude. This suggests that when water is present, methanol is predominately formed from H_2COH and not H_3CO. Though, from our work on the final hydrogenation, we note that the formation of methanol from either species is barrierless.

In considering all of the results we can see that the route to methanol in the gas phase and within water clusters is ultimately different. This provides a gas phase route which proceeds via:

$$H + CO \rightarrow HCO \xrightarrow{+H} H_2CO \xrightarrow{+H} H_3CO \xrightarrow{+H} H_3COH$$

With the possibility that some HCOH may be formed and destroyed by either isomerising to H_2CO or onward reaction to H_2COH. Within water clusters, the story is considerably more complex. Certainly, for the first hydrogenation step the reaction most likely proceeds to the formation of HCO, but the formation of COH cannot be ruled out since it is strongly dependent upon its local environment and its formation will ultimately be decided by the width of the barrier and not its height.

The story is further complicated in the second step by the fact that, in certain environments the formation of *cis*-HCOH may be favoured over H_2CO. Though we note that *trans*-HCOH will readily be converted to H_2CO. In considering onward reactions, there are two distinct routes:

$$H_2CO + H \rightarrow H_3CO \rightarrow H_2COH \xrightarrow{+H} H_3COH$$

and

$$\textit{cis}\text{-HCOH} + H \rightarrow CH_2OH \xrightarrow{+H} CH_3OH$$

This is important since currently neither route is included within astrophysical models. As such the abundance of methanol that they compute may be underestimated compared to the abundance of H_2CO.

In considering the abstraction reactions from H_2CO and H_3COH, our results agree well with the experiments of Oehelers [219] and [160, 221]. Indeed, the agreement between the G4 results and the Oehlers [219] experiments for the abstractions from H_2CO is considerably better than the 2 kcal.mol^{-1} accuracy the method is parametrised for, and ultimately provides better estimates for the barrier than the work of Goumans [54]. The agreement for the methanol abstractions and the Hoyermann [221] is of no surprise since the methodology is based upon the work of Clary [220], in which they had already shown an almost perfect agreement of their rate constants with the experimental ones. In addition, we note that the rate constants obtained by Goumans [222] seem to be agree better with the experimental results of Meagher [223] which are in fact lower than the results of Hoyermann.

Finally, with respect to modelling of the hydrogen deuterium exchange experiments we see a relatively poor agreement between theory and experiment. However, we note that the experimental results are in fact poorly constrained, and clearly need to be expanded upon. In addition, the theory also needs to be expanded upon to consider larger cluster sizes, and the possibility that the exchange being observed may be from CD groups and not the OD group.

Whilst we have answered some questions, many remain unanswered and any future work should therefore expand upon these results. One key question still remains from this work, and that is does HCOH have a role? It is clear that our results show the *trans* isomer can readily be destroyed, but we have no idea with regard to the *cis*. In addition, we are at present unable to ascertain if it can be formed at, though the collaborative work with the astrophysicists should help to clarify this picture. Indeed, if the model shows that in can be formed we should also consider the abstraction reactions in the same manner as for formaldehyde. Furthermore, the abstraction reactions from the radical intermiediates should also be considered, as this may also shed some light on the missing OD group.

In addition, any future work should involve consideration of large cluster sizes and how such cluster may be embedded via a QM/MM type approach or WFT/DFT approach to better model the steric effects of the grain surface.

Furthermore, a key limitation of all of the previous quantum chemistry results is that they do not include an analysis of hydrogen diffusion accross a surface. This is an important quantity for the astrophysical models, which is difficult to constrain experientally. Though, we note it is also a difficult quantity to determine theoretically. The difficulty arises theoretically due to the fact we know little about the surface structure of the grains. As such, in order to investigate this process, a combined approach between quantum chemistry and molecular dynamics would have to be used in conjunction with each other. This can be done by initially

modelling a crystaline surface using DFT followed by a molecular dynamics simmulation at a higher temperature before refreezing the surface. This process would then have to be repeated many times to get an idea of the different types of surface structure one may obtain. From here, one may have several different ways to proceed using either molecular dynamics or quantum chemistry and these should be investigated in details.

In addition the formation and destruction of COH and *cis*-HCOH within clusters need to be investigated further. Finally, the formation of larger molecules than CH_3OH should be considered in the same manner. Ultimately, any future work should converge to considering these processes in the solid state and perhaps at some point lead to the modelling of a quantum mechanical grain.

Chapter IX

CONCLUSIONS ET PERSPECTIVES

9

CONCLUSIONS ET PERSPECTIVES

Au cours de ce travail de thèse, des methodes de chimie quantique de haut niveau ont été utilisées pour caractériser les processus réactionnels impliquant H, D, CO et H_2O à la surface des grains interstellaires. Les objectifs de ce travail étaient les suivants:

1. étudier toutes les voies possibles en phase gazeuse concernant l'hydrogénation de CO
2. mettre en évidence le rôle éventuel joué par la surface du grain dans l'activation de certains processus réactionnels

Les mécanismes considérés n'ont pas été limités à l'hydrogénation seule mais aussi en incluant les réactions d'abstraction de H_2CO et CH_3OH ainsi que les échanges isotopiques dans des agrégats $CH_3OD \cdot (H_2O)n$.

Les résultats n'ont pas été obtenus sans un certain nombre de problèmes techniques. Le plus marquant est certainement le problème de l'orbitale 1s de l'oxygène qui est passée dans l'espace CAS durant les procédures CASSCF lors des calculs multiréférences en phase gazeuse. De plus, il a été difficile de construire une surface α CO modèle. Il n'était pas possible de contourner le fait que le programme CRYSTAL [227] construit des plans d'atomes et non de molecules dans la cellule primitive. C'est pour cette raison que le travail sur le cristal s'est arrêté pour se concentrer sur des agrégats, modèle d'une partie de la surface. Après avoir caractérisé la suite complète de réactions en phase gazeuse en utilisant des méthodes multiréferences, le rôle de l'eau et d'autres molécules de CO ont été considérés pour certaines réactions. Le coût numérique des calculs ainsi que la nécessité d'avoir un degré de précision raisonnable ne nous ont pas permis d'étudier toutes les réactions. A titre d'exemple, concernant plus spécifiquement la formation de HCOH , l'état de transition n'a été mis en évidence qu'avec CCSD(T) ou MRCI+Q, ces deux méthodes étant trop coûteuses pour être utilisées avec des agrégats.

Nous montrons qu'en considérant tous les effets, la formation de HCO et COH en phase gazeuse est peu probable voire impossible pour COH compte tenu de son endothermicité. En revanche, la formation de HCO est rendue difficile non seulement à cause d'une barrière d'activation mais aussi parce que ce processus est dominé dans les conditions interstellaires par une perte d'entropie translationnelle qui conduit à une augmentation de la barrière d'énergie libre. Il est à noter que ce processus, qui tend à empêcher les réactions d'addition présentant une barrière, peut aider les processus qui auraient besoin de perdre de l'énergie pour former un produit stable.

Dans cette thèse, nous présentons également une validation de la formation de HCO. La dernière validation au niveau MRCI+Q a été réalisée par Woon en 1996 [52]. A l'époque, l'effort numérique limitait les calculs et il était nécessaire d'ajouter l'orbitale 2s de l'oxygène dans les orbitales de coeur et la base la plus étendue qui pouvait étre considérée était la base aug-cc-pVQZ. Présentement, nous avons pu inclure l'orbitale 2s dans le CAS et aller jusqu'à la base aug-cc-pV6Z. De plus nous avons également quantifié les effets de corrélation de coeur-valence ainsi que relativistes scalaires. Une telle validation est importante car cette réaction figure parmi les cas servant à tester les methodes DFT et les fonctionnelles. Nous avons d'ailleurs utilisé ces résultats pour valider notre approche utilisant la DFT.

Différentes fonctionnelles ont été testées, donnant une énergie d'activation entre -1.86 kcal.mol^{-1} et 3.50 kcal.mol^{-1} (comparé à 3.94 avec MRCI+Q). Nous avons choisi d'utiliser les fonctionnelles BHLYP et B97D pour les calculs sur les agrégats. BHLYP donne en effet une valeur reproduisant la barrière expérimentale de Wang [57], bien que les travaux récents de Friedrichs [58] et Li [59] remettent en question cette valeur. Par contre, B97D donne un très bon accord avec les résultats MRCI+Q avec un coût numérique significativement moins important. Avec la fonctionnelle B97D, il a donc été possible de considérer les voies de formation sur des agrégats $(CO)_4$, $(CO)_5$, $(H_2O)_3$, et $(H_2O)_5$. A noter que l'exothemicité de la réaction est surestimée avec les deux fonctionelles choises en phase gazeuse. Les résultats sur cette grandeur ne peuvent être utilisés que d'une manière qualitative.

En comparant les résultats de la formation de HCO dans l'agrégat $(H_2O)_3$ avec ceux de Woon [190], il apparait que les fonctionnelles prédisent des valeurs d'énergie d'activation plus faibles. La différence avec les calculs de Woon en MP2 provient probablement de la contamination de spin qui est différente entre les deux calculs.

A contrario, la formation de COH est davantage influensée par la taille et la composition de l'agrégat. Dans les clusters de CO, le mécanisme est inchangé, par contre, en présence de quelques molécules d'eau, la réaction devient légérement exothermique. En augmentant la taille de l'agrégat, la réaction est légèrement endothermique du fait d'un affaiblissement des liaisons hydrogène établies avec l'agrégat.

En considérant la suite des hydrogénations dans les agrégats d'eau, les effets de taille apparaissent. Du fait de la possibilité d'établir une liason hydrogéne dans l'agrégat $CO \cdot (H_2O)_5$, l'addition sur les atomes de carbonne est possible. Ainsi, il est possible de former H_2CO directement de HCO. Toutefois, dans l'agrégat $(H_2O)_3$, pour des raisons stériques, l'attaque sur le carbone de HCO n'est plus possible. Par conséquent, de $HCO \cdot (H_2O)_3$ et $COH \cdot (H_2O)_3$, il est possible de former directement HCOH. Ce résultat est important pour les modèles astrophysiques qui considèrent actuellement que H_2CO peut être formé mais pas HCOH. De plus, ces modèles ne prennent pas en compte le fait que la structure locale peut influencer largement la chimie.

Finalement, on constate que, dans les clusters de CO, l'addition de l'hydrogéne modifie les orientation relatives des units CO. S'il était possible de modéliser une surface $\alpha-$CO réelle, cette réorientation n'apparaîtrait pas et nous avons ici un défaut du modèle d'agrégat qui ne permet pas d'avoir la rigidité d'une surface. Néanmoins, l'approche sur les agrégats nous a permis de montrer que la formation de COH est dépendante de la structure de la surface.

Pour la suite, la formation de H_2CO à partir HCO en phase gazeuse procède sans barrière. Par contre, la formation de chacun des isomères *cis* ou *trans* de HCOH met en jeu des barrières qui sont légèrement plus grandes que celle caractérisant la formation de HCO. L'énergie d'activation à la formation de HCOH peut être interprétée comme l'énergie requise pour le réarrangement électronique dans l'état singulier: pour HCO, l'électron non apparié est situé sur le carbone et l'addition de l'hydrogène conduit à un électron non apparié supplémenatire sur l'atome d'oxygène. Comme un tel réarrangement n'est pas requis pour la formation de l'état triplet ou si l'on forme HCOH à partir COH, ces derniers processus sont sans barrière.

L'énergie des réactifs, HCO + H, est au-dessus de la barrière pour l'isomérisation entre *trans*-HCOH et H_2CO, ainsi que celle de l'état de transition pour l'isomérisation *cis*/*trans* en HCOH. Ce résultat est confirmé par l'existence d'un hydrogène 'tournant' sur la surface comme proposé par Bowman [193–198]. Pour cette raison, la formation de HCOH ne peut

être exclue et dépendra des rapports de branchement des réactions ainsi que du flux d'atomes d'hydrogène.

Lorsque l'isomérisation de *trans*-HCOH en H_2CO se fait en présence de quelques molécules d'eau, l'énergie d'activation est réduite d'au moins 80% par rapport à la phase gaz, la réaction devenant alors possible dans les conditions du milieu interstellaire. Cela suggère que l'addition de H sur HCO conduit finalement à H_2CO, puisque l'isomère HCOH est rapidement converti en H_2CO sur les grains si des molécules d'eau sont présentes.

Si l'on considère le taux obtenu expérimentalement par Schreiner et al. [199], *trans*-HCOH est isomérisé en quelques heures à très basses températures. Cela confirme que *trans*-HCOH ne jouera qu'un rôle limité, la suite de réaction conduisant au méthanol d'autant que même si on considère une surface pure de CO, l'isomérisation se produit sur une échelle de temps identique voire plus courte que l'accumulation d'atomes H sur la surface du grain, typiquement quelques heures à 10 K [206].

Par conséquent, pour que *trans*-HCOH participe dans les réactions d'hydrogénation suivantes, l'addition d'un H sur HCOH doit s'effectuer avec un taux beaucoup plus grand que celui d'isomérisation. Toutefois, si le flux des atomes H est plus important que dans le milieu interstellaire et si la réaction se produit sans eau, la participation de *trans*-HCOH dans les réactions suivantes ne peut pas être absolument écartée et nécessiterait une étude plus complète. Cela ne signifie pas non plus que le *cis*-HCOH n'est pas disponible pour d'autres réactions, puis qu'il pourrait aussi être formé par le mécanisme de l'hydrogène 'tournant'.

Ensuite, la formation de H_2COH en HCOH est sans barrière alors que la formation des 2 radicaux depuis H_2CO met en jeu une barrière. Dans les agrégats d'eau, le taux de réaction du processus d'isomérisation est augmenté d'un facteur 4. Cela signifie qu'en présence d'eau, le méthanol est préférentiellement formé de H_2COH et pas H_3CO. Enfin, notre travail sur la dernière hydrogénation confirme que la formation du méthanol depuis chacune des entaités est sans barrière.

En compilant les résultats obtenus, il semblerait que les mécanismes de formation du méthanol en phase gazeuse et en présence d'eau sont différents. Cela donne le schéma suivant pour la phase gazeuse:

$$H + CO \rightarrow HCO \xrightarrow{+H} H_2CO \xrightarrow{+H} H_3CO \xrightarrow{+H} H_3COH$$

Avec la possibilité que HCOH puisse être formé et détruit par isomérisation en H_2CO ou réaction pour former H_2COH.

A la surface des agrégats d'eau, le schéma est plus complexe. La première hydrogénation conduit certainement vers la formation de HCO, mais la formation de COH ne peut pas être exclue puisque celle-ci dépend fortement de l'environnement et sa formation sera déterminée par la largeur de la barrière et non pas sa hauteur. Pour la seconde étape, c'est également plus compliqué dans la mesure où, dans certains environnements, la formation du *cis*-HCOH peut être favorisée par rapport à H_2CO. A noter que *trans*-HCOH est converti aisément en H_2CO. En considérant les réactions suivantes, il y a deux voies possibles:

$$H_2CO + H \rightarrow H_3CO \rightarrow H_2COH \xrightarrow{+H} H_3COH$$

et

$$\textit{cis}\text{-HCOH} + H \rightarrow CH_2OH \xrightarrow{+H} CH_3OH$$

Ces mécanismes sont importants car actuellement aucune de ces possibilité n'est incluse dans les modéles astrophysiques. De ce fait, les abondances de méthanol qui sont calculées sont sous-estimées par comparaison aux abondances de H_2CO.

Pour les réactions d'abstraction de H_2CO et H_3COH, nos résultats sont en bon accord avec les expériences de Oehelers [219] et [160, 221]. En fait, cet accord entre les résultats G_4 et les expériences de Oehlers pour les abstractions de H_2CO est nettement meilleur que le degré de précision de la méthode de 2 kcal.mol^{-1}. De plus, ce travail donne une meilleure estimation par rapport aux calculs de [54]. L'accord avec les expériences de Hoyermann [221] n'est pas surprenant puisque la méthodologie repose sur le travail de Clary [220], qui avait déjà montré un bon accord de leurs taux avec les données expérimentales.

Finalement, pour la modélisation des échanges de deuterium en lien avec les expériences, l'accord théorie-expériences n'est pas convaincant. Les résultats expérimentaux nécessitent d'être davantage exploités, de même que pour la théorie, les calculs doivent être étendus à des agrégats plus grands et la possibilité d'avoir un échange des groupes CD doit être prise en compte.

Bien que nous ayons répondu à certaines questions, beaucoup d'autres restent encore non résolues et nécessitent que les études soient poursuivies. Une question cruciale qui reste de ce travail se pose quant au rôle de HCOH. Nos résultats indiquent que l'isomère *trans* peut être détruit facilement mais qu'en est-il pour le *cis*? Un travail collaboratif avec les astrophysiciens permettra de clarifier ce point. En effet, si le modèle prédit qu'il peut être formé, les réactions d'abstraction devront être considérées comme cela a été fait pour le formaldéhyde. De plus, les réactions d'abstraction depuis les intermédiaires radicalaires doivent aussi être considérées, de façon à expliquer l'absence de goupement OD.

De manière évidente, le travail futur devra considérer des agrégats plus étendus. Il s'agira alors de réfléchir pour traiter la réactivité via une approche du type QM/MM ou WFT/DFT, le but étant d'avoir une meilleure description des effets stériques propres à une surface. Une autre limitation des modèles de chimie quantique est bien sûr qu'ils n'incluent pas la diffusion des espèces et en particulier des hydrogènes à la surface. Ce paramètre est aussi déterminant pour les modèles astrochimiques mais difficilement accessible expérimentalement. Une autre difficulté pour la modélisation vient du fait que la surface du grain reste mal caractérisée (glace pure, amorphe, cristalline). Une alternative pour cette investigation serait de combiner les approches de chimie quantique valides par nos résultats et de la dynamique moléculaire. Comme première approche, une surface de glace cristalline pourrait être utilisée ou différentes configurations d'une glace désordonnée proche de l'amorphe construite par chauffage puis refroidissement rapide. Les méthodes de DFT permettant d'étudier des sysèmes plus gros ont été utilisées ici et confrontées avec des calculs réalisés avec des méthodes de haut niveau. Cette validation sera certainement utile pour toute étude ultérieure incluant ou non de la dynamique.

BIBLIOGRAPHY

[1] Beichman, C. A.; Myers, P. C.; Emerson, J. P. *Astrophys J* **1986**, *307*, 337.

[2] Shu, F. H. *Astrophys J* **1977**, *214*, 488.

[3] Ebert, R. *Zeit. für Astro.* **1955**, *37*, 217.

[4] Bonnor, W. B. *MNRAS* **1956**, *116*, 351.

[5] Andre, P.; Ward-Thompson, D.; Barsony, M. *Protostars and Planets IV* **2000**, 59.

[6] Maury, A. J.; Andre, P.; Menshikov, A.; Könyves, V.; Bontemps, S. *Astron and Astrophys* **2011**, *535*, A77.

[7] Crimer, N.; Ceccarelli, C.; Maret, S. *Astron and Astrophys* **2010**, *519*, A65.

[8] www.astro.uni-koeln.de/cdms/molecules.

[9] Frerking, M. A.; Langer, W. D.; Wilson, R. W. *Astrophys J* **1982**, *262*, 590.

[10] Herbst, E.; Klemperer, W. *Astrophys J* **1973**, *185*, 505.

[11] Cazaux, S.; Tielens, A. G. G. M.; Ceccarelli, C. *Astron and Astrophys* **2003**, *593*, L51.

[12] Parise, B.; Ceccarelli, C.; Tielens, A. G. G. M. *Astron and Astrophys* **2006**, *453*, 949.

[13] Visser, R.; van Dishoeck, E. F.; Doty, S. D.; Dullemond, C. P. *Astron and Astrophys* **2009**, *495*, 881.

[14] Visser, R.; Doty, S. D.; van Dishoeck, E. *Astron and Astrophys* **2011**, *534*, A132.

[15] Bockelee-Morvan, D.; Lis, D. C.; Wink, J. E. *Astron and Astrophys* **2000**, *353*, 1101.

[16] Mumma, M. J.; Charnley, S. B. *Ann Rev of Astron and Astrophys* **2011**, *49*, 471.

[17] Herbst, E.; van Dishoeck, E. *Ann Rev of Astron and Astrophys* **2009**, *47*, 427.

[18] Draine, B. T. *Ann Rev of Astron and Astrophys* **2003**, *41*, 241.

[19] Henning, T. *Ann Rev of Astron and Astrophys* **2010**, *48*, 21.

[20] Pontoppidan, K. M.; van Dishoeck, E.; Dartois, E. *Astron and Astrophys* **2004**, *426*, 925.

[21] Gibb, E. L.; Whittet, D. C. B.; Boogert, A. C. A.; Tielens, A. G. G. M. *Astrophys J Suplement series* **2004**, *151*, 35.

[22] Pontoppidan, K. M.; Boogert, A. C. A.; Fraser, H. J. *Astrophys J* **2008**, *678*, 1005.

[23] Öberg, K. I.; Boogert, A. C. A.; Pontoppidan, K. M. *Astrophys J* **2011**, *740*, 109.

[24] Whittet, D. C. B.; Bode, M. F.; Longmore, A. J. *MNRAS* **1988**, *233*, 321.

[25] Whittet, D. C. B.; Gerakines, P. A.; Hough, J. H.; Shenoy, S. S. *Astrophys J* **2001**, *547*, 872.

[26] Whittet, D. C. B.; Shenoy, S. S.; Bergin, E. A. *Astrophys J* **2007**, *655*, 332.

[27] Whittet, D. C. B.; Cook, A. M.; Herbst, E.; Chiar, J. E.; Shenoy, S. S. *Astrophys J* **2011**, *742*, 28.

[28] Tielens, A. G. G. M.; Hagen, W. *Astron and Astrophys* **1982**, *114*, 245.

[29] Miyauchi, N.; Hidaka, H.; Chigai, T.; Watanabe, N. *Chem. Phys. Lett.* **2008**, *456*, 27.

[30] Mokrane, H.; Chaabouni, H.; Accolla, M. *Astrophys J lett* **2009**, *705*, L195.

[31] Dulieu, F.; Amiaud, L.; Congiu, E. *Astron and Astrophys* **2010**, *512*, A30.

[32] Allen, M.; Robinson, G. W. *Astrophys J* **1977**, *212*, 396.

[33] Ruffle, D.; Herbst, E. *MNRAS* **2001**, *324*, 1054.

[34] Ceccarelli, C.; Loinard, L.; Castets, A.; Tielens, A. G. G. M.; Caux, E. *Astron and Astrophys* **2000**, *357*, L9.

[35] Bottinelli, S.; Ceccarelli, C.; Lefloch, B. *Astrophys J* **2004**, *615*, 354.

[36] Maret, S.; Ceccarelli, C.; Caux, E.; Tielens, A. G. G. M.; Jorgensen, J. K.; van Dishoeck, E.; Bachmann, A.; Castets, A.; Lefloch, B.; Loinard, L.; Praise, B.; Schöier, F. L. *Astron and Astrophys* **2004**, *416*, 577.

[37] Maret, S.; Ceccarelli, C.; Caux, E.; Tielens, A. G. G. M.; Jorgensen, J. K.; van Dishoeck, E.; Bachmann, A.; Castets, A.; Lefloch, B.; Loinard, L.; Praise, B.; Schöier, F. L. *Astron and Astrophys* **2005**, *416*, 577.

[38] Bottinelli, S.; Ceccarelli, C.; Williams, J.; Lefloch, B. *Astron and Astrophys* **2007**, *463*, 601.

[39] Jorgensen, J. K.; Schöier, F. L.; van Dishoeck, E. *Astron and Astrophys* **2005**, *435*, 177.

[40] Atkins, P.; de Paula, J. *Physical Chemistry*, seventh ed.; Oxford University Press, 2002.

[41] Watanabe, N.; Kouchi, A. *Prog Surf Sci* **2008**, *83*, 439.

[42] Pirim, C.; Krim, L.; Laffon, C.; Parent, P.; Pauzat, F.; Pilme, J.; Ellinger, Y. *J Phys Chem A* **2010**, *114*, 3320.

[43] Pirim, C.; Krim, L. *Chem. Phys.* **2011**, *380*, 67.

[44] Pirim, C.; Krim, L. *Phys Chem Chem Phys* **2011**, *13*, 19454.

[45] Watanabe, N.; Kouchi, A. *Astrophys J* **2002**, *567*, 651.

[46] Watanabe, N.; Shiraki, T.; Kouchi, A. *Astrophys J lett* **2003**, *588*, L121.

[47] Hidaka, H.; Watanabe, N.; Shiraki, T.; Nagaoka, A.; Kouchi, A. *Astrophys J* **2004**, *614*, 1124.

[48] Hidaka, H.; Watanabe, M.; Kouchi, A.; Watanabe, N. *Astrophys J* **2009**, *702*, 291.

[49] Nagaoka, A.; Watanabe, N.; Kouchi, A. *Astrophys J lett* **2005**, *624*, L29.

[50] Nagaoka, A.; Watanabe, N.; Kouchi, A. *J Phys Chem A* **2007**, *111*, 3016.

[51] Fuchs, G. W.; Cuppen, H. M.; Ioppolo, S.; Romanzin, C.; Bisschop, S. E.; Andersson, S.; van Dishoeck, E. F.; Linnartz, H. *Astron and Astrophys* **2009**, *505*, 629–639.

[52] Woon, D. E. *J Chem Phys* **1996**, *105*, 9921.

[53] Andersson, S.; Goumans, T.; Arnaldsson, A. *Chemical Physics Letters* **2011**, *513*, 31–36.

[54] Goumans, T. P. M. *MNRAS* **2011**, *413*, 2615.

[55] Werner, H. J.; Bauer, C.; Rosmus, P.; Keller, H. M.; Stumpf, M.; Schinke, R. *J Chem Phys* **1995**, *102*, 3593.

[56] Keller, H. M.; Floethmann, H.; Dobbyn, A. J.; Schinke, R.; Werner, H. J.; Bauer, C.; Rosmus, P. *J Chem Phys* **1996**, *105*, 4983.

[57] Wang, H.; Eyre, J. A.; Dorfman, L. M. *J Chem Phys* **1973**, *59*, 5199.

[58] Friedrichs, G.; Herbon, J. T.; Davidson, D. F.; Hanson, R. K. *Phys Chem Chem Phys* **2002**, *4*, 5778.

[59] Li, J.; Zhao, Z.; Kazakov, A.; Chaos, M.; Dryer, F. L.; Scire Jr, J. J. *Int. J. Chem. Kine.* **2006**, *39*, 109.

[60] Taquet, V.; Ceccarelli, C.; Kahane, C. *Astron and Astrophys* **2012**, *538*, 42.

[61] Hasegawa, T. I.; Herbst, E. *MNRAS* **1993**, *263*, 589.

[62] Chang, Q.; Cuppen, H. M.; Herbst, E. *Astron and Astrophys* **2005**, *434*, 599.

[63] Cuppen, H. M.; Herbst, E. *MNRAS* **2005**, *361*, 565.

[64] Chang, Q.; Cuppen, H. M.; Herbst, E. *Astron and Astrophys* **2007**, *469*, 973.

[65] Cuppen, H. M.; Herbst, E. *Astrophys J* **2007**, *668*.

[66] Cuppen, H. M.; van Dishoeck, E. F.; Herbst, E.; Tielens, A. G. G. M. *Astron and Astrophys* **2009**, *508*, 275.

[67] Schrödinger, E. *Ann. Phys.* **1926**, *62*, 361.

[68] Cohen-Tannoudji, C.; Diu, B.; Laloë, F. *Quantum Mechanics*; Hermann, 1973.

[69] M.Born,; Oppenheimer, R. *Ann. Phys.* **1927**, *389*, 457.

[70] M.Born, *Göttinger Nachr. Acad. Wiss. Math. Nat. KL.* **1951**, *6*, 1.

[71] M.Born,; Huang, K. *Dynamical Theory of Crystal Lattices*; Claredon, 1954.

[72] Fukui, K. *Acc Chem Res* **1981**, *14*, 363.

[73] Hartree, D. R. *Math. Proc. Cam. Phil. Soc.* **1928**, *24*, 111.

[74] Hartree, D. R. *Math. Proc. Cam. Phil. Soc.* **1928**, *24*, 426.

[75] Pauli, W. *Zeit. Phys.* **1925**, *31*, 373.

[76] Slater, J. C. *Phys. Rev.* **1929**, *34*, 1293.

[77] Fock, V. *Zeit. Phys.* **1930**, *61*, 126.

[78] Fock, V. *Zeit. Phys.* **1930**, *62*, 795.

[79] T. H. Dunning Jr, *J Chem Phys* **1989**, *90*, 1007.

[80] Kendall, R. A.; Dunning Jr, T. H.; Harrison, R. J. *J Chem Phys* **1992**, *96*, 6796.

[81] Ditchfield, R.; Hehre, W. J.; Pople, J. A. *J Chem Phys* **1971**, *54*, 724.

[82] Hehre, W. J.; Ditchfield, R.; Pople, J. A. *J Chem Phys* **1972**, *56*, 2257.

[83] Hariharan, P. C.; Pople, J. A. *Theo. Chem. Accounts* **1973**, *28*, 213.

[84] Hariharan, P. C.; Pople, J. A. *Mol. Phys.* **1974**, *27*, 209.

[85] Gordon, M. S. *Chem. Phys. Lett.* **1980**, *76*, 163.

[86] Binkley, J. S.; Pople, J. A.; Hehre, W. J. *J. Am. Chem. Soc.* **1980**, *102*, 939.

[87] Gordon, M. S.; Binkley, J. S.; Pople, J. A.; Pietro, W. J.; Hehre, W. J. *J. Am. Chem. Soc.* **1982**, *104*, 2797.

[88] Pietro, W. J.; Francl, M. M.; Hehre, W. J.; Defrees, D. J.; Pople, J. A.; Binkley, J. S. *J. Am. Chem. Soc.* **1982**, *104*, 5039.

[89] Francl, M. M.; Pietro, W. J.; Hehre, W. J.; Binkley, J. S.; DeFrees, D. J.; Pople, J. A.; Gordon, M. S. *J Chem Phys* **1982**, *77*, 3654.

[90] Clark, T.; Chandrasekhar, J.; Spitznagel, G. W.; Schleyer, P. V. R. *J Comp Chem* **1983**, *4*, 294.

[91] Frisch, M. J.; Pople, J. A.; Binkley, J. S. *J Chem Phys* **1984**, *80*, 3265.

[92] Dobbs, K. D.; Hehre, W. J. *J Comp Chem* **1986**, *7*, 359.

[93] Dobbs, K. D.; Hehre, W. J. *J Comp Chem* **1987**, *8*, 861.

[94] Dobbs, K. D.; Hehre, W. J. *J Comp Chem* **1987**, *8*, 880.

[95] Ögretir, C.; Csizmadia, I. G. *Computational Advances in Organic Chemistry: Molecular Structure and Reactivity*; Nato Science series; Springer, 1990.

[96] Wigner, E. *Phys. Rev.* **1934**, *46*, 1002.

[97] Löwdin, P. O. *Advances in Chemical Physics*; 1959.

[98] Møller, C.; Plesset, M. S. *Phys. Rev.* **1934**, *46*, 618.

[99] Head-Gordan, M.; Pople, J. A.; Frisch, M. J. *Chem. Phys. Lett.* **1988**, *153*, 503.

[100] Shavitt, I. *Mol. Phys.* **1998**, *94*, 3.

[101] Szabo, A.; Ostlund, N. S. *Modern Quantum Chemistry*, first edition revised ed.; Dover, 1996.

[102] Bartlett, R. J.; Musial, M. *Rev. Mod. Phys* **2007**, *79*, 291.

[103] Christiansen, O. *Theo. Chem. Accounts* **2006**, *116*, 106.

[104] Coester, F. *Nucl. Phys.* **1958**, *7*, 421.

[105] Coester, F.; Kümmel, H. *Nucl. Phys.* **1960**, *17*, 477.

[106] Kümmel, H. *Nucl. Phys.* **1961**, *22*, 177.

[107] Noga, J.; Bartlett, R. J. *J. Chem. Phys.* **1987**, *86*, 7041.

[108] Lee, T. J.; Taylor, P. R. *Int. J. Quant. Chem.* **1989**, *36*, 199.

[109] Siegbahn, P. E. M.; Almlof, J.; Heiberg, A.; Roos, B. O. *J. Chem. Phys.* **1981**, *74*, 2384.

[110] Roos, B. O. *Advances in Chemical Physics*; K. P. Lawley, 1987.

[111] Roos, B. O.; clifford, E. D.; Gernot, F.; Kwang, S. K.; Gustavo, E. S. *Theory and Applications of Computational Chemistry*; Elsvier, 2005.

[112] Ruedenberg, K.; Schmidt, M. W.; Gilbert, M. M. *Chem. Phys.* **1982**, *71*, 51.

[113] Ruedenberg, K.; Schmidt, M. W.; Gilbert, M. M.; Elbert, S. T. *Chem. Phys.* **1982**, *71*, 41.

[114] Ruedenberg, K.; Schmidt, M. W.; Gilbert, M. M.; Elbert, S. T. *Chem. Phys.* **1982**, *71*, 65.

[115] Hartree, D. R.; Hartree, W.; Swirles, B. *Phil. Trans. Royal Soc. London A* **1939**, *238*, 229.

[116] Das, G.; Wahl, A. C. *Phys. Rev. A.* **1971**, *4*, 825.

[117] Shephard, R. *Advances in Chemical Physics*; K. P. Lawley, 2007.

[118] Roos, B. O.; Linse, P.; Siegbahn, P. E. M.; Blomberg, M. R. A. *Chem Phys* **1982**, *66*, 054101.

[119] Andersson, K.; Malmqvist, P. A.; Roos, B. O.; Sadlej, A. J.; Wolinski, K. *J Phys Chem* **1990**, *94*, 5483.

[120] Andersson, K.; Malmqvist, P. A.; Roos, B. O. *J Chem Phys* **1992**, *96*, 1218.

[121] Werner, H. J.; Knowles, P. J. *J Chem Phys* **1988**, *89*, 5803.

[122] Knowles, P. J.; Werner, H. J. *Chem. Phys. Lett.* **1988**, *145*, 514.

[123] Werner, H. J.; Knowles, P. J. *Mol. Phys* **1996**, *89*, 645.

[124] Celani, P.; Werner, H. J. *J Chem Phys* **2000**, *112*, 5546.

[125] Hirao, K. *Chem. Phys. Lett.* **1992**, *190*, 374.

[126] Kato, T. *Comm. Pure App. Math.* **1957**, *10*, 151.

[127] Reinhardt, P.; Hoggan, P. E. *Int. J. Quant. Chem.* **2009**, *109*, 3191.

[128] Morrell, M. M.; Parr, R. G.; Levy, M. *J. Chem. Phys.* **1975**, *62*, 549.

[129] Thomas, L. H. *Math. Proc. Cam. Phil. Soc.* **1927**, *23*, 542.

[130] Fermi, E. *Rend. Accad. Naz. Lincei* **1927**, *6*, 602.

[131] Slater, J. C. *Phys. Rev.* **1951**, *81*, 385.

[132] Bloch, F. *Zeit. Phys.* **1929**, *57*, 545.

[133] Dirac, P. A. M. *Proc. Royal Soc.* **1929**, *123*, 714.

[134] Hohenberg, P.; Kohn, W. *Phys. Rev.* **1964**, *136*, 864.

[135] Kohn, W.; Sham, L. J. *Phys. Rev.* **1965**, *140*, 1133.

[136] Burke, K. *The Journal of Chemical Physics* **2012**, *136*, 150901.

[137] Becke, A. D. *J. Chem. Phys.* **1993**, *98*, 5648.

[138] Wu, X.; Vargas, M. C.; Nayak, S.; Lotrich, V.; Scoles, G. *J. Chem. Phys.* **2001**, *115*, 8748.

[139] Wu, Q.; Yang, W. *J. Chem. Phys.* **2002**, *116*, 515.

[140] Zimmerli, U.; Parrinello, M.; Koumoutsakos, P. *J. Chem. Phys.* **2004**, *120*, 2693.

[141] Grimme, S. *J. Comp. Chem.* **2004**, *25*, 1463.

[142] Grimme, S. *J Comp Chem* **2006**, *27*, 1787.

[143] Curtiss, L. A.; Refern, P. C.; Raghavachari, K. *J. Chem. Phys.* **2007**, *126*, 084108.

[144] Frisch, M. J. et al. Gaussian 03 Revision D.0.1. 2003.

[145] Frisch, M. J. et al. Gaussian 09 Revision A. 02. 2009.

[146] Schmidt, M. W.; Baldridge, K. K.; Boatz, J. A.; Elbert, S.; Gordon, M. S.; Jensen, J. H.; Koseki, S.; Matsunaga, N.; Nguyen, K. A.; Su, S.; Windus, T. L.; Dupuis, M.; Jr, J. A. M. *J Comp Chem* **1993**, *14*, 1347.

[147] Gordon, M. S.; Schmidt, M. W. In *Theory and Applications of Computational Chemistry: The First Forty Years*; Dykstra, C., Ed.; Elsvier, 2005.

[148] Werner, H.-J. et al. MOLPRO, version 2010.1, a package of ab initio programs. 2010.

[149] TURBOMOLE V6.4 2012, a development of University of Karlsruhe and Forschungszentrum Karlsruhe GmbH. 1989-2007; TURBOMOLE GmbH, since 2007; available from `http://www.turbomole.com`.

[150] Weigend, F.; Häser, M. *Theor. Chem. Acc.* **1997**, *97*, 331.

[151] Bader, R. F. W. *Atoms in Molecules: A Quantum Theory*; Claredon Press, 1994.

[152] Biegler-Konig, F.; Schonbohn, J.; Bayles, D. *J Comp Chem* **2001**, *22*, 545.

[153] Biegler-Konig, F.; Schonbohn, J. *J Comp Chem* **2002**, *23*, 1489.

[154] Messiah, A. *Quantum Mechanics*; Dover, 1999; Vol. 1 and 2.

[155] Eckart, C. *Phys Rev* **1930**, *35*, 1303.

[156] Landau, L. D.; Lifshitz, E. M. *Quantum Mechanics*; Pergamon Press: New York, 1965.

[157] Skodje, R. T.; Truhlar, D. G.; Garrett, B. C. *J Phys Chem* **1981**, *85*, 3019.

[158] McQuarrie, D. A.; Simon, J. D. *Molecular Thermodynamics*; University Science Books, 1999.

[159] Jursic, B. S. *J. Mol. Struc.* **1998**, *427*, 157.

[160] Baulch, D. L.; Bowman, C. T.; Cobos, C. J.; Cox, R. A.; Just, T.; Kerr, J. A.; Pilling, M. J.; Stocker, D.; Troe, J.; Tsang, W.; Walker, R. W.; Warnatz, J. *J. Phys. Chem. Ref. Data* **2005**, *34*, 757.

[161] Zanchet, A.; Bussery-Honvault, B.; Honvault, P. *J Phys Chem A* **2006**, *110*, 12017.

[162] Bowman, J. M.; Bittman, J. S.; Harding, L. B. *J Chem Phys* **1986**, *85*, 911.

[163] Salazar, M. C.; Hernández, A. J. *Theo. Chem. Accounts* **2009**, *122*, 43.

[164] Wilson, A. K.; van Mourik, T.; Dunning Jr, T. H. *J. Mol. Struc.:THEOCHEM* **1996**, *388*, 339.

[165] Langhoff, S. R.; Davidson, E. R. *Int. J. Quant. Chem.* **1974**, *8*, 61.

[166] Senekowitsch, J. 1988.

[167] Peterson, K. A.; Woon, D. E.; Dunning Jr, T. H. *J Chem Phys* **1994**, *100*, 7410.

[168] van Mourik, T.; Dunning, T. H.; Peterson, K. A. *J. Phys. Chem. A* **1999**, *104*, 2287.

[169] de Jong, W. A.; Harrison, R. J.; Dixon, D. A. *J Chem Phys* **2001**, *114*, 48.

[170] Reiher, M.; Wolf, A. *J Chem Phys* **2004**, *121*, 2037.

[171] Reiher, M.; Wolf, A. *J Chem Phys* **2004**, *121*, 10945.

[172] Peterson, K.; Feller, D.; Dixon, D. *Theo. Chem. Accounts: Theory, Comp. and Mod.* **2012**, *131*, 1.

[173] Hamperecht, F. A.; Cohen, A.; Tozer, D. J. *J Chem Phys* **1998**, *109*, 6264.

[174] Kang, J. K.; Musgrove, C. B. *J Chem Phys* **2001**, *115*, 11040.

[175] Adamo, C.; Barone, V. *J Chem Phys* **1999**, *110*, 6158.

[176] Becke, A. D. *J. Chem. Phys.* **1992**, *98*, 1372.

[177] Andersson, S.; Grüning, M. *J Phys Chem A* **2004**, *108*, 7621.

[178] Tao, J. M.; Perdew, J. P.; Staroverov, V. N.; Scuseria, G. E. *Phys Rev Lett* **2003**, *91*, 146401.

[179] Bruna, P. J.; Buenker, R. J.; Peyerimhoff, S. D. *J. Mol. Struc.* **1976**, *32*, 217.

[180] Serrano-Andres, L.; Forsberg, N.; Malmqvist, P. A. *J Chem Phys* **1998**, *108*, 7202.

[181] Kus, T.; Bartlett, R. J. *J Chem Phys* **2008**, *129*, 104301.

[182] Hirota, E. *J. Mol. Struc.* **1986**, *146*, 237.

[183] Austin, J. A.; Levy, D. H.; Gottlieb, C. A.; Radford, H. E. *J Chem Phys* **1974**, *60*, 207.

[184] Ogilvie, J. F. *J. Mol. Struc.* **1976**, *31*, 407.

[185] Chaung, M. C.; Foltz, M. F.; Moore, C. B. *J. Chem. Phys.* **1987**, *87*, 3855.

[186] Walsh, R. Private Communication cited by Werner in [55].

[187] Shepler, B. C.; Yang, B. H.; Kumar, T. J. D.; Stancil, P. C.; Bowman, J. M.; Balakrishnan, N.; Zhang, P.; Bodo, E.; Dalgrano, A. *Astron and Astrophys* **2007**, *475*, L15.

[188] Vegard, L. *Zeitschrift für Physik* **1930**, *61*, 185.

[189] Janssen, W. B. K. M.; Michieis, J.; van der Avoird, A. *J Chem Phys* **1991**, *94*, 8402.

[190] Woon, D. E. *Astrophys J* **2002**, *569*, 541.

[191] Schreiner, P. R.; Reisenauer, H. P. *Chem Phys Chem* **2006**, *7*, 880.

[192] Kiselev, V. G.; Swinnen, S.; Nquyen, V. S.; Grisan, N. P.; Nguyen, M. T. *J Phys Chem A* **2010**, *114*, 5573.

[193] Townsend, D.; Lahankar, S. A.; Lee, S. K.; Chambreau, S. D.; Suits, A. G.; Zhang, X.; Rheinecker, J.; Harding, L. B.; Bowman, J. M. *Science* **2004**, *306*, 5699.

[194] Zhang, X.; Rheinecker, J. L.; Bowman, J. M. *J Chem Phys* **2005**, *122*, 114313.

[195] Bowman, J. M.; Zhang, X. *Phys Chem Chem Phys* **2006**, *8*, 321.

[196] Christoffel, K. M.; Bowman, J. M. *J Phys Chem A* **2009**, *113*, 4138.

[197] Shepler, B. J.; Han, Y.; Bowman, J. M. *J Phys Chem Lett* **2011**, *2*, 834.

[198] Bowman, J. M.; Shepler, B. C. *Ann Rev Phys Chem* **2011**, *62*, 531.

[199] Schreiner, P. R.; Reisenauer, H. P.; Pickard, F. C.; Simmonett, A. C.; Allen, W. D.; Matyus, E.; Csaszar, A. G. *Nature* **2008**, *453*, 906.

[200] Zhang, X.; Zou, S.; Harding, L. B.; Bowman, J. M. *J Phys Chem A* **2004**, *108*, 8980.

[201] Koch, D. M.; Toubin, C.; Xu, S.; Peslherbe, G. H.; Hynes, J. T. *J. Phys. Chem. C* **2008**, *112*, 2972.

[202] Woon, D. E. *Icarus* **1999**, *142*, 550.

[203] Woon, D. E. *J. Phys. Chem. A* **2001**, *105*, 9478.

[204] Woon, D. E. *Icarus* **2001**, *149*, 277.

[205] Woon, D. E. *Int. J. Quant. Chem.* **2002**, *88*, 226.

[206] Vidali, G.; Roser, J.; Manico, G.; Pirronello, V.; Perets, H. B.; Biham, O. *J of Phys: Conf series* **2005**, *6*, 36.

[207] Hoper, U.; Botschwina, P.; Koppel, H. *J Chem Phys* **2000**, *112*, 4132.

[208] Petraco, N. D. K.; Allen, W. D.; Schaefer Iii, H. F. *J Chem Phys* **2002**, *116*, 1022.

[209] Marenich, A. V.; Boggs, J. E. *J Chem Phys* **2005**, *122*, 024308.

[210] Ghigo, G.; Roos, B. O.; Malmqvist, P. *Chem. Phys. Lett.* **2004**, *396*, 142.

[211] Jackels, C. F. *J Chem Phys* **1982**, *76*, 505.

[212] Osborn, D. L.; Leahy, D. J.; Neumark, D. M. *J Phys Chem A* **1997**, *101*, 6583.

[213] Solgadi, D.; Flament, J. P. *Chem Phys* **1985**, *98*, 387.

[214] Kamarchik, E.; Rodrigo, C.; Bowman, J. M.; Reisler, H.; Krylov, A. I. *J Chem Phys* **2012**, *136*, 084304.

[215] Walch, S. P. *J Chem Phys* **1993**, *96*, 3076.

[216] Sosa, C.; Schlegel, H. B. *Int. Quan. Chem* **1986**, *29*, 1001.

[217] Colwell, S. M. *Mol. Phys.* **1984**, *51*, 1217.

[218] Wang, T.; Bowie, J. H. *Organic & Biomolecular Chemistry* **2012**, *10*, 3219.

[219] Oehlers, C.; Wagner, H. G.; Ziemer, H.; Temps, F.; Dóbé, S. *J. Phys. Chem. A* **2000**, *104*, 10500.

[220] Kerkeni, B.; Clary, D. C. *J. Phys. Chem. A* **2004**, *108*, 8966.

[221] Hoyermann, K.; Silvert, R.; Wagner, H. G. *Ber. Bunsen-Ges. Phys. Chem.* **1981**, *85*, 149.

[222] Goumans, T. P. M.; Kästner, J. *J. Phys. Chem. A* **2011**, *115*, 10767.

[223] Meagher, J. F.; Kim, P.; Lee, J. H.; Timmons, R. B. *J. Phys. Chem* **1974**, *78*, 2650.

[224] Ratajczak, A.; Quirco, E.; Faure, A.; Schmitt, B.; Ceccarelli, C. *Astron and Astrophys* **2009**, *496*, L21.

[225] Johnston, H. S.; Heicklen, J. *J Phys Chem* **1962**, *66*, 532.

[226] Taquet, V.; Peters, P. S.; Kahane, C.; Ceccarelli, C.; Lopez-Sepulcre, A.; Toubin, C.; Duflot, D.; Wiesenfeld, L. *Astron and Astrophys* **2012**, *submitted*.

[227] Dovesi, R.; Orlando, R.; Civalleri, B.; Roetti, C.; Saunders, V. R.; Zicovich-Wilson, C. M. *Z. Kristallogr.* **2005**, *220*, 571.

ACKNOWLEDGMENTS

I would like to thank Céline and Denis for all their help and support over the course of the thesis. This includes all the help and support from both the scientific side and also all the work that they put in when dealing with the administration, thanks here should also be given to Georges and Walter without whom the last 3 months in Lille would have been difficult. I would also like to thank Laurent for never failing to provide an interesting discussion in driving the work forwards.

In addition I'd like to thank everyone in the PCMT team for their patience and always being happy to answer questions. Particular thanks should also be given to Maurice for his work on a time independent program for computing rate constants, which were computed after writing this document. But I would also like to particularly thank Florent and Valerie for tolerating my constant requests with regards to the Cluster.

Finally, I would also like to thank all of the Astromol team in Grenoble for their efforts in teaching me something about astrophysics.

Summary

Throughout this work high level quantum chemistry methods have been used to investigate reactive processes involving: H, D, CO, H_2CO, H_3COH and H_2O at model interstellar grains surfaces.

This study has mainly focused upon the formation of the two most abundant Complex Organic Molecules (COMS), H_2CO and H_3COH. For the first time, all of the hydrogenation steps have been considered and treated with reliable methods in the gas phase, and in particular making use of multi-reference approaches such as MRCI+Q and MRMP2.

Following the characterization of all the reactions in the gas phase, the same processes have been investigated within small molecular clusters using various density functionals and MP2. This was done as a preliminary attempt to model the icy grain mantles of interstellar dust grains. For some of the steps, such as the formation of HCO, the activation energy does not vary significantly between the gas phase and the clusters. In contrast, for other processes, such as the formation of COH, and H_3CO, the activation energy is lowered and the exothermicity/endothermicity of the reaction changes. In addition, the isomerizations of some species,as for instance HCOH to H_2CO, are also strongly affected by the presence of water. From the cluster calculations, we conclude that the arrangement of the surface molecules and the H flux may have a significant influence on the chemical routes leading to H_2CO and H_3COH.

Finally, we have also discussed how these results may be incorporated into astrophysical models, as our results suggest that the current route, that is considered, may not include all of the possible steps which may contribute to the actual formation of these COMs.

Keywords: Interstellar molecules, Interstellar grains, ab initio methods (quantum chemistry), Quantum Chemistry, Density functionals, Formaldehyde, Methanol, Extraterrestrial water, Hydrogenation

Résumé

L'objectif de ce mémoire de thèse est de caractériser par des méthodes de chimie quantique de haute qualité les processus réactionnels impliquant H, CO, H_2CO, H_3COH et H_2O à la surface des grains interstellaires. En effet, H_2CO et H_3COH, sont parmi les molécules organiques dites complexes (COM: Complex Organic Molecules en anglais) les plus abondantes dans les nuages moléculaires du milieu interstellaire. Ce travail théorique est la première étude s'attachant à décrire toutes les étapes et les intermédiaires réactionnels intervenant dans la séquence de réactions conduisant au méthanol par hydrogénations successives de CO. Pour la phase gazeuse, des méthodes multi-références (MRCI+Q et MRMP2) ont été appliquées afin d'avoir la description la plus juste des systèmes. Les calculs montrent que certaines étapes cruciales de la synthèse (formation de HCO) en phase gazeuse mettent en jeu des barrières d'activation significatives dans les conditions du milieu interstellaire. La possibilité de réaction par effet tunnel a aussi été envisagée.

Les mêmes processus réactionnels ont ensuite été étudiés sur des agrégats d'eau ou de CO. Ces agrégats ont été choisis comme surfaces modèles pour les grains interstellaires. Compte-tenu de la taille du système, les calculs ont été menés en utilisant la théorie de la fonctionnelle densité et la méthode perturbative MP2. Pour certaines réactions, telle que la formation de HCO, la présence d'un agrégat ne modifie pas l'énergie d'activation. En revanche, pour d'autres (formation de COH et H_3CO), l'énergie d'activation est réduite et l'endothermicité/exothermicité de la réaction change. De plus, l'isomerisation de certains composés, HCOH en H_2CO, est rendue possible en présence d'agrégats d'eau. Les résultats obtenus sur les agrégats indiquent que l'état de surface et le flux d'atomes H peuvent avoir une influence notable sur la séquence réactionnelle, ouvrant d'autres voies non envisageables en phase gazeuse.

Enfin, les résutats de ces calculs seront intégrées dans le modèle astrophysique GRAINOBLE, ce qui permettra de prendre en compte les différents intermédaires qui pourraient potentiellement participer à la synthèse de ces deux molécules ainsi qu'à celle de molécules plus complexes.

Mots clés: Molécules interstellaires, Grains interstellaires, Méthodes ab initio (chimie quantique), Chimie quantique, Fonctionelles densité, Formaldéhyde, Méthanol, Eau extraterrestre, Hydrogénation